Improving the Stability of Halide Perovskites for Photovoltaic Applications and Solar Fuel Generation

Poli, Isabella

Award date:
2019

Awarding institution:
University of Bath

Improving the Stability of Halide Perovskites for Photovoltaic Applications and Solar Fuel Generation

submitted by

Isabella Poli

for the degree of Doctor of Philosophy

of the

University of Bath

Department of Chemistry

October 2019

Abstract

Halide perovskites have become a popular material to fabricate photovoltaic devices for the conversion of sunlight into electricity. Perovskite solar cells have shown extraordinary performance, reaching power conversion efficiencies of over $24\,\%$ in less than a decade. Some of the reasons for their success are the high light absorption and the possibility of using low cost solution-based fabrication. Perovskite devices are notably efficient, but they still suffer from instabilities that challenge their commercialisation. Indeed, perovskite solar cells degrade when exposed to moisture, high temperature and light, causing irreversible loss of efficiency. In this work, different strategies for improving the stability of perovskite solar cells have been studied.

Humidity is one of the most invasive factors that affects perovskite solar cell stability. Water molecules easily penetrate through the extraction layers reaching the perovskite structure and irreversibly degrading the absorber film. Moisture-induced degradation of perovskite solar cells can be minimised by modifying the top perovskite surface with interfacial hydrophobic thin layers and by passivating the grain boundaries. In this work, for example, the perovskite surface is treated with $CH_3NH_3PbI_3$ nanocrystals capped with long chain ligands (oleic acid and oleylamine), significantly enhancing the film's hydrophobicity. Bulkier and larger organic cations, like tetrabutylammonium, are also incorporated through the absorber perovskite thin film, passivating grain boundaries and improving the stability of perovskite solar cells when exposed to ambient conditions without encapsulation (relative humidity higher than $50\,\%$). Another method to limit the moisture-induced degradation of perovskite solar cells is through encapsulation. Here, a flexible and robust graphite sheet is used to protect halide perovskite devices from water.

Instabilities are also manifested as light-induced defect formation and ion migration through the perovskite film, which can lead to material degradation. It has been shown that under-coordinated surface sites and grain boundaries act as defect reservoirs in perovskite films. Photo-instabilities can therefore be limited by passivating the surface of perovskite films. Here, 5-aminovaleric acid iodide is used to effectively passivate the surface defects of methylammonium lead iodide, photostabilising the perovskite film under continuous illumination, eliminating the formation of light-induced defects.
Light-induced ion migration also causes halide segregation in mixed halide (I and Br) perovskite compositions. Here, it is shown that by incorporating 5-aminovaleric

acid iodide in triple cation mixed halide perovskites to passivate grain boundaries, halide segregation is arrested for over $1\,\mathrm{h}$ under continuous illumination.

Finally, perovskite structures are unstable when exposed to high temperatures. Previous reports have shown that methylammonium lead iodide films tend to degrade over time when heated at $85\,^{\circ}\mathrm{C}$ in ambient air through volatilization of the organic cation. In this work, the use of fully inorganic perovskite materials obtained by substituting Cs for the methylammonium cation considerably improve the thermal stability of perovskite films, which are found to be stable during heating in air at temperatures higher than $350\,^{\circ}\mathrm{C}$. Not only the $MAPbI_3$ perovskite film itself, but also the solar cell device as a whole is particularly unstable when exposed to high temperature. The organic hole extraction layers are indeed prone to thermal instability and undesirable side reactions with metal contacts tend to be induced at high temperatures. To avoid degradation of the hole transporting materials and side reactions with metals, hole-conductor free architectures made by infiltrating porous layers of carbon, ZrO_2 and TiO_2 are used. In this work, carbon solar cells with photovoltages as high as $1.45\,\mathrm{V}$ are achieved by using $CsPbBr_3$ as infiltrating absorber material.

Acknowledgements

Firstly, I would like to thank my supervisor Petra Cameron for the immense and continuous support, for all her advice and enthusiasm. When I started, I could not have imagined a better supervisor. Thanks also to all PJC group members for their friendship and support, my second supervisor Salvador Eslava and the Eslava group.

The Centre for Sustainable Chemical Technology (grant agreement EP/L016354/1) and the European Union's Horizon 2020 research and innovation programme (H2020-MSCA-CO-FUND- 2014. 665992, MSCA FIRE: Fellows with Industrial Research Enhancement) have been absolutely fundamental, providing funding for research and conference attendance. Janet Scott deserves special thanks for the support given to Marie Curie fellows.

Thanks to SPECIFIC and Ulrich Hintermair (University of Bath) for the exciting collaborations that helped in getting results for this thesis. Trystan Watson (SPECIFIC) gave me access to the laboratory facilities at Swansea University and Jenny Baker (SPECIFIC) personally contributed to the experimental research.

Thanks also to Annamaria Petrozza, who provided me an opportunity to join her team at the Centre for Nanoscience and Technology, IIT, giving me access to the laboratory and research facilities.

Thanks to everyone else who helped me out with a wise word, nice gesture, a chat, a beer, a night out. This goes especially to Giulia - she has been my family in Bristol and it would not have been the same without her, and to my whole family that constantly supported me from abroad - they have never made me feel lonely and I could not have managed to go through these years without them.

Finally to Fede for the immense support he has always given me and for being my biggest fan, life without him would not be as happy.

Contents

List of Figures

List of Tables

List of Abbreviations

5AVA	5-ammoniumvaleric acid
ABPACl	Butylphosphonic acid 4-ammonium chloride
AET	Aminoethanethiol
AFM	Atomic force microscopy
ALD	Atomic layer deposition
AM	Air mass
AO	Atomic orbitals
BA	Butylammonium
CB	Conduction band
CE	Counter electrode
CV	Cyclic voltammetry
CW	Continuous wave
DAI	Diethylammonium iodide
DFT	Density functional theory
DI	Deionized
DMF	N,N-dimethylformamide
DMSO	Dimethyl sulfoxide
EDX	Energy dispersive X-ray
EL	Electroluminescence
ETM	Electron transport material
EtOH	Ethanol
FA	Formamidinium
FM	Field's metals
FTIR	Fourier transformed infrared spectroscopy
FTO	Fluorine-doped tin oxide
GS	Graphite sheet
GUA	Guanidinium
HER	Hydrogen evolution reaction
HTM	Hole transport material
HTP	3-hexylthiophene
IPA	Isopropyl alcohol
IPCE	Incident photon to current efficiency
IS	Impedance spectroscopy
ITO	Indium-doped tin oxide
LED	Light emitting device

LSV	Linear sweep voltammetry
MA	Methylammonium
mC	Mesoporous carbon
MetOH	Methanol
MO	Molecular orbital
mp	Mesoporous
NC	Nanocrystal
NIR	Near infrared
OA	Oleic acid
OC	Open circuit
OCP	Open circuit potential
OER	Oxidation evolution reaction
OLA	Oleylamine
P3HT	Poly-3-hexylthiophene
PCBM	Phenyl-C61-butyric acid methyl ester
PCE	Power conversion efficiency
PEA	Phenetylammonium
PEC	Photoelectrochemical
PEDOT:PSS	Poly(ethylene-3,4-dioxythiophene):poly(styrenesulfonic acid)
PL	Photoluminescence
PLQY	Photoluminescence quantum yield
PMMA	Poly(methyl methacrylate)
PSC	Perovskite solar cell
PTAA	Poly-triarylamine
PV	Photovoltaic
PVP	Poly-vinylpyrrolidone
QD	Quantum dots
Ref	Reference electrode
RH	Relative humidity
RHE	Reversible hydrogen electrode
SC	Short circuit
SEM	Scanning electron microscopy
SHE	Standard hydrogen electrode
Spiro-OMeTAD	2,2′,7,7′-tetrakis-(N,N-di-p-methoxyphenylamine)9,9′-spirobifluorene
SQ	Shockley-Quisser
SRH	Shockley Read Hall
SS	Shelf stability
TBA	Tetrabutylammonium
***t*-BA**	Tert-butylammonium
TCO	Transparent conductive oxide
TCSPC	Time correlated single photon counting
TEA	Tetraethylammonium

TMA	Tetramethylammonium
TPA	Terephtalic acid
TRPL	Time resolved photoluminescence
UV-Vis	UV-Visible
VB	Valence band
WE	Working electrode
WF	Work function
WOC	Water oxidation catalyst
XPS	X-ray photoelectron spectroscpy
XRD	X-ray diffraction

Physical Constants

Boltzmann's constant	$k_B = 1.380\,648\,8 \times 10^{-23}\,\mathrm{J\,K^{-1}}$
Elementary charge	$q = 1.602\,176\,62 \times 10^{-19}\,\mathrm{C}$
Farady's constant	$F = 9.648\,533\,29 \times 10^{4}\,\mathrm{s\,A\,mol^{-1}}$
Gas constant	$R = 8.314\,462\,618\,153\,24\,\mathrm{J\,K^{-1}\,mol^{-1}}$
Planck's constant	$h = 6.626\,070\,04 \times 10^{-34}\,\mathrm{J\,s}$
Speed of light	$c = 2.997\,924\,58 \times 10^{8}\,\mathrm{m\,s^{-1}}$

List of Symbols

A	Absorbance	$\%$
B	Full width at half maximum	
C_{geo}	Geometric capacitance	F
C_{μ}	Chemical capacitance	F
d	Lattice spacing	$\mathrm{\AA}$
D	Diffusion coefficient	$\mathrm{cm\,s^{-1}}$
$E^{0'}$	Formal potential	V
E_F	Energy Fermi level	eV
E_g	Energy bandgap	eV
E_{vac}	Energy vacuum level	eV
f	Frequency	Hz
FF	Fill factor	
I_0	Dark saturation current	A
J_m	Maximum current density	$\mathrm{mA\,cm^{-2}}$
J_{sc}	Short circuit current density	$\mathrm{mA\,cm^{-2}}$
K	Shape factor	
k_1	Monomolecular recombination rate constant	$\mathrm{s^{-1}}$
k_2	Bimolecular recombination rate constant	$\mathrm{cm^3\,s^{-1}}$
k_3	Three-body recombination rate constant	$\mathrm{cm^6\,s^{-1}}$
L	Diffusion length	cm
m	Diode ideality factor	
n	Number of electrons involved in redox reaction	
n_e	Free electron density	$\mathrm{cm^{-3}}$
n_p	Free hole density	$\mathrm{cm^{-3}}$
R	Reflectance	$\%$
R_{rec}	Recombination resistance	Ω
R_{ser}	Series resistance	Ω
R_{sh}	Shunt resistance	Ω
T	Transmittance	$\%$
t	Film thickness	nm
V_m	Maximum voltage	V
R	Reflectance	$\%$
V_{oc}	Open circuit voltage	V
Z	Impedance	Ω
α	Absorption coefficient	$\mathrm{cm^{-1}}$

β_{rad}	Radiative recombination	$\mathrm{cm^3\,s^{-1}}$
ΔV_{ph}	Photovoltage	V
θ	Diffraction angle	$^\circ$
θ_z	Zenith angle	$^\circ$
λ	Wavelength	nm
μ	Carrier mobility	$\mathrm{cm\,V^{-1}\,s^{-1}}$
μ_O^0	Standard chemical potential of products	$\mathrm{J\,kg^{-1}}$
μ_R^0	Standard chemical potential of reactants	$\mathrm{J\,kg^{-1}}$
ν	Frequency	Hz
τ	Carrier lifetime	s
ω	Radial frequency	$\mathrm{rad\,s^{-1}}$

Preface

Sustainable Chemical Technologies

A growing awareness of environmental issues pushed the need of introducing the concept of new development models based on preserving natural resources for future generations. Such development is known as *sustainable development* and aims to the long-term stability of the economy and environment, obtained by integrating economic, environmental, and social concerns throughout the decision making process. This concept was popularised for the first time in the Brundtland Report in 1987 at the World Commission on World Environment and Development and provided the fundamentals for the Rio Summit in 1992 that laid to the foundation of a global plan of action to improve human lives and protect the environment. [1, 2]

In order to achieve a better and more sustainable future for all, 17 Sustainable Development Goals have been defined to address the global challenges that humans are currently facing. These goals include climate and environmental degradation, poverty, inequity, prosperity, peace and justice. [3] The 7 th sustainable development goal ensures clean and affordable energy for all. [4]

Energy is a primary need that drives both economical and social development. At the moment, worldwide energy production is mainly based on non-renewable energy sources, which cause several environmental concerns, such as global warming, air pollution and acid precipitation. [4] After the oil crisis in the 1970s, the use of energy conversion systems based on renewable energy sources became very attractive. [5] An energy transition that moves away from the primary use of fossil fuels demands research into new materials and chemical technologies to make energy conversion from renewable energy sources efficient, cheap, reliable and applicable. [6] In addition, human-related factors also need to be addressed and efforts to change the consumer and user behaviours need to be considered for a successful energy transition.

Nowadays, most of the developed technologies that harvest renewable energy produce electricity. Along with the development of such technologies, it is necessary to develop storage solutions to deal with the intermittency of renewable energy sources. [7] Moreover, electricity cannot be the only available energy carrier. In fact, there are sectors which will continue relying on liquid fuels, for example the transport sector with the use of planes and ships. [8] An attractive solution would be the development of processes to produce liquid fuels from renewable sources ('renewable fuels'). One of the most investigated renewable fuel is hydrogen, which could

be potentially used as alternative liquid fuel instead of fossil fuels and as a chemical storage system. [9]

Solar Energy

Solar energy is a renewable primary source of energy, meaning that it requires only capture prior to its use. Electricity and fuels, such as hydrogen, are instead secondary sources of energy, also called energy carriers, because they have to be transformed from a primary source into some other forms prior to use. Energy carriers are considered fully renewable only when they are obtained from renewable primary sources of energy.

At the moment, most hydrogen and electricity are derived from fossil non-renewable resources. However, sustainable production technologies to derive electricity and hydrogen directly from solar energy are being investigated using photovoltaic (PV) technologies.

Electricity - photovoltaic systems

PV uses semiconductor materials to convert solar radiation (photons) into electricity. Technical challenges in the field have origins in the chemical and electrochemical characteristics of the material used to harvest sunlight and convert it into electricity. Once a suitable system has been identified, engineering must optimise its cost, efficiency and reliability.

The efficiency and cost of technologies currently available make PV electricity generation very attractive. At the moment, it is used for both major installations (solar-farms) and smaller local installations (rooftop-solar PV). PV systems can be grid-connected or stand-alone systems depending on whether the electricity produced is fed into the national grid or only used by the property/household. At the end of 2018 the cumulative global PV installed capacity reached $480.3\,\mathrm{GW}$, an increase of about $20\,\%$ with respect to the total installed PV capacity of 2017. [10]

Large-scale *versus* lab-scale The current photovoltaic large-scale market is dominated by mature silicon based technologies. In contrast, lead halide perovskites have been of great interest in the lab-scale PV research area because of the use of low cost materials and inexpensive and convenient solution-based fabrication methods. Most importantly, halide perovskite solar cells can achieve very high power conversion efficiencies, which increased from about $3\,\%$ to over $20\,\%$ in less than a decade, showing an unprecedented improvement in PV technologies. [11]

Fuels - H_2 production

Hydrogen is considered a clean fuel as water is the only product of its combustion and for this reason it became particularly attractive as a transportation fuel for cars and in fuel cells for electricity production. A major challenge that goes along with

hydrogen is associated to its storage and transmission arising from its volatility and diffusivity. [12]

Large-scale *versus* lab-scale About $95\,\%$ of the current H_2 production comes from fossil fuel sources by steam reforming and water-gas shift reactions. [13] One of the most studied processes to obtain hydrogen from renewable sources is direct photocatalytic splitting of water using photovoltaic devices to capture solar radiation. Hydrogen produced from renewable energy sources is nowadays two to three times more expensive than hydrogen from fossil fuels, limiting its large scale manufacturing. [9]

Thesis objectives and contents

Sunlight can be directly converted into electricity using photovoltaic energy. Among the new generation of photovoltaic materials, halide perovskites have been in the spotlight thanks to the high power conversion efficiencies achieved in photovoltaics. Some of the main reasons for their success are the use of abundant materials and low cost solution-based fabrication, high absorption coefficients and defect tolerance. On the other hand, one of the main challenges for the fabrication of reliable commercial perovskite applications is the material and device instability.

This thesis explores some of the degradation mechanisms of perovskite photovoltaics and looks at different approaches and solutions to improve their stability. Below the contents of the following chapters are summarised:

Chapter 1 introduces basic concepts and materials that will be discussed in the following chapters. It also gives an overview of the behaviour of perovskite materials and the degradation mechanisms that challenge their application.

Chapter 2 describes the methods for materials and sample fabrication and the techniques and theories applied to the studies presented in this thesis.

Chapter 3 investigates the use of surface treated perovskite films for higher moisture resistance solar cells. Different materials are used for thin film surface passivation and the photoinstabilities of perovskite films with and without surface treatment are discussed by studying the photoluminescence properties.

Chapter 4 looks at the incorporation of large and bulky cations in standard perovskite absorber films to passivate the grain boundaries for the generation of solar cells with improved moisture resistance.

Chapter 5 presents the use of fully-inorganic $CsPbBr_3$ perovskite for the production of solar cells with higher thermal stability. The use of alternative architectures (metal-free and hole transport material-free) based on carbon is demonstrated, resulting in improved solar cell devices stability and potential scalability.

Chapter 6 describes the use of compact graphite sheets for the generation of water resistant perovskite-based devices. The high water stability of these encapsulated devices is demonstrated by developing $CsPbBr_3$-based photoanodes to drive the oxygen evolution reaction in photoelectrochemical water splitting.

Chapter 7 briefly explores the fabrication of multi cation and mixed halide perovskite materials for the fabrication of wide-bandgap semiconductors which are stable under illumination.

Chapter 8 summarises the conclusions taken form the observations and results presented in the thesis.

Bibliography

[1] G. H. Brundtland, "Our Common Future - Call for Action," *Environ. Conserv.*, vol. 14, no. 4, pp. 291–294, 1987.

[2] M. Keating, "The Earth Summit's agenda for change: a plain language version of Agenda 21 and the other Rio Agreements," 1993.

[3] M. Nilsson, D. Griggs, and M. Visbeck, "Map the interactions between Sustainable Development Goals," *Nature*, vol. 534, pp. 320–322, 2016.

[4] I. Dincer, "Renewable Energy and Sustainable Development: a crucial review," *Renew. Sust. Energ. Rev.*, vol. 4, pp. 157–175, 2000.

[5] N. L. Brown, "Renewable Energy Resources for Developing Countries," *Ann. Rev. Energy*, vol. 5, pp. 389–413, 1980.

[6] G. Centi, G. Iaquaniello, and S. Perathoner, "Chemical engineering role in the use of renewable energy and alternative carbon sources in chemical production," *BMC Chem. Eng.*, vol. 1, no. 5, pp. 1–16, 2019.

[7] M. Raugei and P. Frankl, "Life cycle impacts and costs of photovoltaic systems: Current state of the art and future outlooks," *Energy*, vol. 34, no. 3, pp. 392–399, 2009.

[8] R. J. Detz, J. N. Reek, and B. C. Van Der Zwaan, "The future of solar fuels: When could they become competitive?," *Energy Environ. Sci.*, vol. 11, no. 7, pp. 1653–1669, 2018.

[9] M. Yekini Suberu, M. Wazir Mustafa, and N. Bashir, "Energy storage systems for renewable energy power sector integration and mitigation of intermittency," *Renew. Sust. Energ. Rev.*, vol. 35, pp. 499–514, 2014.

[10] IRENA International Renewable Energy Agency, "Renewable Capacity Statistics 2019," tech. rep., IRENA, 2019.

[11] NREL, "National Renewable Energy Laboratory (NREL)," 2019.

[12] J. O. Bockris, "Hydrogen," *Materials*, vol. 4, no. 12, pp. 2073–2091, 2011.

[13] N. Z. Muradov and T. N. Veziroglu, "From hydrocarbon to hydrogen-carbon to hydrogen economy," *Int. J. Hydrog. Energy*, vol. 30, no. 3, pp. 225–237, 2005.

Chapter 1

Introduction

Halide perovskite solar cells have been of great interest in the past decade due to the high performance achieved, with conversion efficiencies that have now reached over $24\,\%$. A brief summary of the current literature on the stability of halide perovskite solar cells will be provided in this chapter. Section 1.1 will introduce structural properties of halide perovskites and their use in photovoltaic applications. Section 1.2 will outline the main degradation mechanisms and introduce strategies to improve the stability of perovskite solar cells. Finally, section 1.3 will introduce the production of solar hydrogen via photoelectrochemical water splitting, highlighting the material properties needed for the fabrication of efficient photoelectrodes.

1.1 Halide perovskites

The first observations and considerations on halide perovskites were published by Topsoe in 1884, [1] however their extraordinary opto-electronic properties were discovered in the 90s, when Mitzi *et al.* demonstrated that perovskites could be used in light emitting devices (LEDs) and thin-film transistors. [2, 3] Interest in perovskites increased considerably after they were used in solar cells. The first halide perovskite-based solar cell was reported in 2009 and had an efficiency of $3.8\,\%$. [4] Perovskite solar cells (PSC) achieved over $20\,\%$ efficiency in only a decade with the current world record set at $24.2\,\%$. [5] Most of the initial research focused on pursuing higher conversion efficiencies. Recently, attention has turned to issues that hinder the commercial viability of perovskite solar cells, in particular their instabilities and degradation mechanisms.

1.1.1 Crystal structure

The name perovskite indicates a family of materials with a crystal structure characterised by a ABX_3 formula. A is a monovalent cation, X is a monovalent anion

and B is a cation, generally with a 2+ oxidation state. The typical perovskite lattice structure is shown in figure 1.1 and consists in a network of corner-sharing BX_6 octahedra.

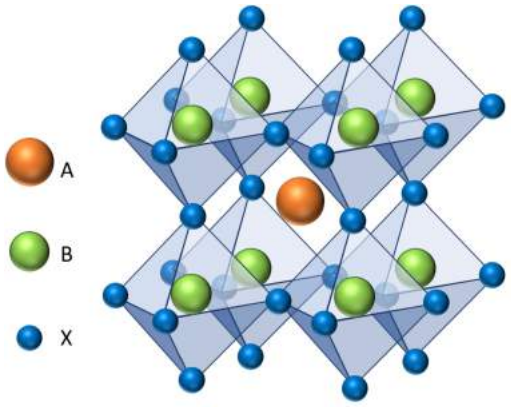

Figure 1.1: Typical perovskite lattice structure characterised by a ABX_3 formula.

In halide perovskites, B is typically Sn^{2+} or Pb^{2+} or a mixture of the two and X is typically I^- or Br^- or Cl^- or a mixture. The central cation A balances the charge and it can be an inorganic ion or a molecular organic cation. The selection of the cation A is limited by the rigid structure shown in figure 1.1. A tolerance factor t (Goldschmidt factor) is defined from:

$$t = \frac{R_A + R_X}{\sqrt{2}(R_B + R_X)} \tag{1.1}$$

R_A, R_B and R_X are the ionic radii of A, B and X, respectively. [6] In order to have a stable, three dimensional perovskite structure, t must be a value between 0.8 and 1. [7]

In the archetypal halide perovskite, methylammonium leadtriiodide ($CH_3NH_3PbI_3$ or $MAPbI_3$), the A site is occupied by the organic cation $CH_3NH_3^+$ (MA^+), B is the metal cation Pb^{2+} and X is I^-. $MAPbI_3$ has a tolerance factor t of 0.91 and it has a black and photoactive tetragonal structure at room temperature. [8]

Other molecules that have been widely investigated as central cations A are formamidinium ($NH_2CH{=}NH_2^+$ or FA^+) and caesium (Cs^+), which are respectively larger and smaller than MA^+. Figure 1.2 shows the correlation between the ionic radius of the cation, the tolerance factor of the structure and the crystal structure of the material. Due to larger and smaller t, $FAPbI_3$ and $CsPbI_3$ tend to form non photoactive yellow perovskites at room temperature with hexagonal and orthorombic crystal structures, respectively. [7] However, as shown in figure 1.2, the tolerance factor can be tuned by mixing FA^+ and Cs^+. If pure $FAPbI_3$ and $CsPbI_3$ are not stable at room temperature, mixed $(FA,Cs)PbI_3$ instead shows a stable black phase with a cubic structure. [7]

The choice of the A-site cation has the largest effect on the thermal stability of the perovskite material. [8] Many reports show that perovskite structures that use

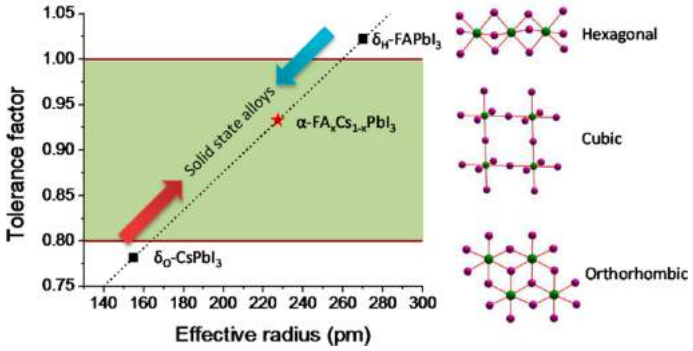

Figure 1.2: Correlation between the perovskite structure and the tolerance factor t. Image taken from Li *et al.*. [7]

triple cations (Cs,FA,MA) in the A-site show stable black photoactive phases with considerably higher thermal stability than single-cation structures. [9, 10, 11] The choice of the X-site, in contrast, has the largest effect on the optical bandgap of the material. Br substitution in $MAPb(I_{1-x}Br_x)_3$ has been reported to tune the bandgap of the material to cover almost the entire visible spectrum. [12]

1.1.2 Photovoltaic application

One of the main advantages of perovskite solar cells is that very high efficiencies can be achieved through solution-process techniques, which are much less expensive than any other methods used for other PV technologies. An aspect that significantly affects the device's electronic and optical properties and efficiency is the solar cell architecture.

Device architectures

Perovskite solar cells can be classified as regular (n-i-p) and inverted (p-i-n) structures depending on which transport material (electron or hole) is deposited on the transparent conductive oxide (TCO) substrate, being therefore the first material encountered by the sunlight. These two structures can then be classified in mesoporous or planar structures.
The mesoporous n-i-p architecture (figure 1.3 a) comprises a compact electron transport material (ETM) on top of the TCO and a mesoporous (mp) ETM scaffold with nanoscale pores. The perovskite penetrates into the scaffold and covers it creating a capping layer. Finally the compact hole transport material (HTM) and the top electrode are sequentially deposited on top. This structure was the first architecture tested for perovskite devices and the most efficient reported mesoporous cell up to date has a PCE of 22.1 %. [13] This structure led to the development of a planar n-i-p architecture (figure 1.3 b), where the perovskite absorber layer is sandwiched between a compact ETM and a compact HTM. [14, 15, 16] The advantage of using a planar architecture is that it is more favourable for scaling up, as the deposition of the

mesoporous layer represents one extra step to the fabrication. [17, 18] The most common materials used for ETM and HTM in mesoporous and planar n-i-p structures are TiO_2 and 2,2',7,7'-tetrakis-(N,N-di-p-methoxyphenylamine)9,9'-spirobifluorene (spiro-OMeTAD), respectively. [19, 20] An alternative ETM material is SnO_2, which requires lower annealing temperature (up to 180 °C) and has better band alignment, [21, 22, 23] while other polymeric hole conductors that have been demonstrated to be effective as HTM are poly-3-hexylthiophene (P3HT) and poly-triarylamine (PTAA). [24, 25] The most common TCO used in n-i-p structures is fluorine-doped tin oxide (FTO).

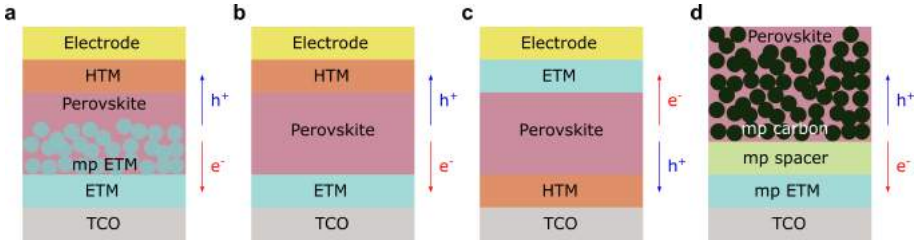

Figure 1.3: a Schematic showing the mesoporous n-i-p structure. **b** Schematic showing the planar n-i-p structure. **c** Schematic showing the planar inverted p-i-n structure. **d** Schematic showing the fully printed HTM- and metal-free carbon based structure.

In the case of the inverted p-i-n structure (figure 1.3 c), the HTM is first deposited on the TCO, which commonly is indium-doped tin oxide (ITO), and the ETM and the top contact are sequentially deposited on top of the perovskite. [26] Devices with inverted p-i-n architecture are usually constructed with planar structures, however examples of mesoporous inverted p-i-n devices have been reported. [27, 28] Common materials used for the HTM in inverted p-i-n architectures are poly(ethylene-3,4-dioxythiophene): poly(styrenesulfonic acid) (PEDOT:PSS) and NiO_x, while the most used material for ETM is phenyl-C61-butyric acid methyl ester (PCBM).

For practical application, PV technologies need to be efficient but also scalable. The architecture that is most compatible with roll-to-roll and other high volume manufacturing techniques is the fully-printable triple mesoscopic carbon architecture, which is shown in figure 1.3 d. This structure was first reported by Ku *et al.* in 2013 and consists of three screen printed mesoporous layers which are then infiltrated with the perovskite solution. [29] The ETM and HTM are mp TiO_2 and mp carbon, respectively. A layer of mp ZrO_2 is screen printed between the ETM and HTM, serving as a spacer layer. Another spacer material that can be used is Al_2O_3. [30]

Hysteresis

One of the most critical issues in perovskite solar cells is the presence of a high hysteric behaviour when the current-voltage (IV) curve is measured. The hysteresis consists of a mismatch of measured current between forward and reverse scan and it was first reported in 2014. [31] Such phenomenon is critical for both the conversion

efficiency and stability of perovskite solar cells, therefore its causes and solutions have been widely investigated over the past few years. [32] Hysteresis in perovskite solar cells was observed to be affected not only by the voltage scan direction, but also by preconditioning effects, like delay time and voltage applied prior to measurement, and by the device architecture. [33, 34] For example, it has been reported that mesoporous n-i-p structures and inverted p-i-n structures show considerably less-hysteresis than planar n-i-p devices. [35, 36]

One phenomenon that possibly relates to hysteresis is the ferroelectric polarisation of perovskites. Spontaneous polarisation of $MAPbI_3$ was reported and self-organised ferroelectric domains were observed to affect charge extraction and to relate to hysteresis. [37, 38, 39] However, other reports disputed the ferroelectric properties of perovskite materials and their effect on hysteresis, which means that the link between ferroelectric polarisation and hysteresis is still open to debate. [40, 41] Instead, it is commonly accepted that the hysteric behaviour is mainly caused by ion migration and non radiative recombination processes occurring near the interface. [42, 43, 44]

Both ion migration and non radiative recombination processes are associated with defects in perovskites. [44, 45] Clear evidence of ion migration was first reported in 2015 and it is believed to cause ion accumulation at the interface, [46] causing ionic screening and affecting the photogenerated charge carriers collection. [47, 48] Van Reenen *et al.* demonstrated that ion migration only cannot explain the hysteresis measured in perovskite solar cells, but electronic charge traps must be included in the model to explain such phenomenon. Both ion migration and charge trapping cause accumulation of electrons and holes at the interface. If the perovskite solar cell is allowed to stabilise at a bias voltage $V<V_{oc}$ prior to performing the IV sweep, a large density of trapped electrons and free holes accumulate at the ETM/perovskite interface, causing strong non-radiative recombination. In contrast, when the cell is stabilised at $V>V_{oc}$, a low density of trapped electrons and free holes accumulate at the ETM/perovskite interface, reducing non-radiative recombination. [44]

It has been reported that defects associated with non radiative recombination processes are most likely originated by iodide vacancies. [49] Such defects are mainly found at the perovskite/ETM and perovskite/HTM interface and at the surface or grain boundaries. [50] Therefore, in order to remove hysteric behaviour both interfacial and bulk defect engineering is required. The former includes change of the device architecture and passivation of the interface, [26, 51] for example, it was shown that the hysteric behaviour could be reduced by modifying the surface of ETM with an ionic-liquid (both TiO_2 and PCBM in standard and inverted architectures, respectively). [16, 52] The latter looks at different perovskite compositions and passivation of grain boundaries, for example by potassium doping. [53, 54, 55, 56]

1.2 Perovskite device stability

Perovskite solar cells have shown a tremendous improvement in their conversion efficiency, reaching a PCE of over $24\,\%$ in just a decade. However, perovskite films and solar cells degrade very quickly. Generally, a warranty of 25 years is required for a commercial photovoltaic technology. [57] Therefore, emergent solar cells need to last throughout this time without loosing too much performance. In order to assess whether a new technology could potentially be transformed into a commercial PV product, accelerated tests are used. Even though perovskite solar cells adopted the IEC 61464 qualification standards that require no more than $20\,\%$ decrease in the PCE after $1000\,\mathrm{h}$ of testing at $85\,^{\circ}\mathrm{C}$ under continuous 1 sun illumination, [58] different stability test conditions have been reported in the literature. It is therefore difficult to compare different works. However, the main stability stressors have been identified and are commonly accepted.

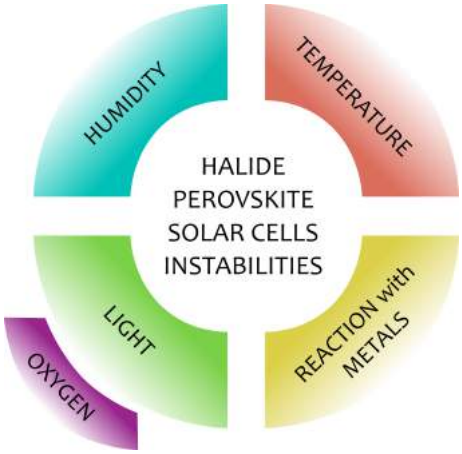

Figure 1.4: Main factors causing halide perovskite solar cells degradation.

Figure 1.4 shows all the external factors that affect perovskite solar cell stability. Cells exposed to moisture degrade very quickly because humidity induces irreversible degradation to the perovskite material. Due to the high volatily of organic species used in perovskites, thin-films and devices are very sensitive to temperatures higher than $65\,^{\circ}\mathrm{C}$. Light exposure induces the creation of defects in the material. Moreover, a combination of oxygen and light causes rapid decomposition of the perovskite active layer. Finally, metals used as top contacts tend to react with halide perovskites, especially in the presence of humidity, light, oxygen and heat.

1.2.1 Humidity

Halide perovskites are highly sensitive to moisture. The presence of H_2O impacts both the perovskite composition and structure, severely affecting the performance and stability of solar cells. It has been proposed that water diffuses into $MAPbI_3$ films through the grain boundaries. [59] H_2O molecules cause deprotonation of MA^+ and protonation of iodide, resulting in weakened bonds between the cation

and PbI_6 and creation of volatile HI. A yellow-coloured PbI_2 film is therefore left behind after exposure of $MAPbI_3$ to high humidity. [8]

Leguy *et al.* studied the hydration process using X-ray diffraction and the following equations have been suggested to describe the process: [59]

$$\begin{aligned} 4CH_3NH_3PbI_3 + 4H_2O &\rightleftharpoons 4[CH_3NH_3PbI_3 \cdot H_2O] \\ &\rightleftharpoons (CH_3NH_3)_4PbI_6 \cdot 2H_2O + 3PbI_2 + 2H_2O \end{aligned} \tag{1.2}$$

$$(CH_3NH_3)_4PbI_6 \cdot 2H_2O \rightarrow 4CH_3NH_3I + PbI_2 + 2H_2O \tag{1.3}$$

The monohydrate $CH_3NH_3PbI_3{\cdot}H_2O$ (figure 1.5 b) and dihydrate $(CH_3NH_3)_4PbI_6{\cdot}2H_2O$ (figure 1.5 c) species are intermediate products that can be converted back to $CH_3NH_3PbI_3$ (figure 1.5 a) upon exposure to dry air (equation 1.2). The former has a 1 dimensional (1D) structure, where isolated $[PbI_3]^-$ chains are balanced by the intercalated $CH_3NH_3{}^+$ cations, which are stabilised by hydrogen bonds between H atoms of H_2O molecules and N atoms of methylammonium. The latter instead is a zero dimensional (0D) structure with isolated $[PbI_6]^-$ neutralised by surrounding $CH_3NH_3{}^+$ cations. If the hydration process is not blocked, the structure is irreversibly degraded and $CH_3NH_3PbI_3$ decomposes into CH_3NH_3I and PbI_2 (equation 1.3). [59, 60]

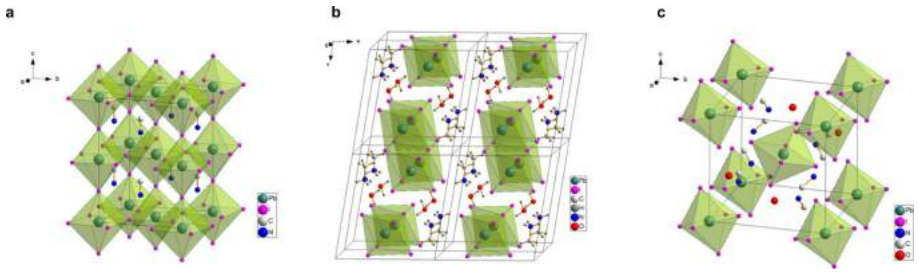

Figure 1.5: a Structure of $CH_3NH_3PbI_3$ in its cubic phase **b** Structure of the monohydrate phase, $CH_3NH_3PbI_3{\cdot}H_2O$. **c** Structure of the dihydrate phase, $(CH_3NH_3)_4PbI_6{\cdot}2H_2O$. Image taken from reference [59].

Recently, Schlipft *et al.* monitored the capability of $MAPbI_3$ to incorporate water when films are exposed to high humidity using in situ grazing incident small angle neutron scattering. [61] They observed that at low humidity levels ($\leq 58\,\%$ RH) water molecules adsorb on the outside of the crystals but they start to be integrated into the crystal structure forming monohydrates only at humidity levels $\leq 73\,\%$ RH. The dihydrated phase formed at humidities $\leq 93\,\%$ RH, when the film ends up containing about 50 vol% of water. The incorporation of water into the perovskite crystal lattice can also reduce the activation energy for ion migration (both I^- and MA^+) through vacancy defects, facilitating the removal of volatile species which leave PbI_2 behind. [62]

The approaches used to improve the stability of perovskite solar cells towards humidity can be categorised as compositional tuning of the perovskite active layer

and modification of the device structure.

Compositional tuning Perovskite stability towards moisture can be improved by strengthening the interaction between the cation and the halide anion. This can be achieved by replacing MA^+ with alternative protonated cations or by modification of the halide anion with more electronegative and smaller elements, such as F, Cl and Br. [63] Perovskite solar cells that use mixed compositions of FA^+ and Cs^+ or MA^+ and FA^+ are more stable due to weaker hydrogen bonds between H_2O molecules and FA and Cs cations. [64, 65] Another way of improving the moisture stability is by reducing the protonation of iodine, for example by incorporating thiocyanate ions in the crystal structure. [66]

The organic cation MA^+ can be also substituted with much larger cations, like phenylethylammonium (PEA^+) or n-butylammonium (BA^+) cations, [67, 68] to form 2D/3D hybrid structures with general formula $A_2(MA)_{n-1}PbX_{3n+1}$ (A=larger cation, X=halide anion). n is an integer that indicates the number of layers of 3D $MAPbI_3$, surrounded by the bulky organic cation A that acts as a spacer. Figure 1.6 shows examples of $A_2(MA)_{n-1}PbI_{3n+1}$ structures with A=PEA and n=1,2,3 and ∞. [67]

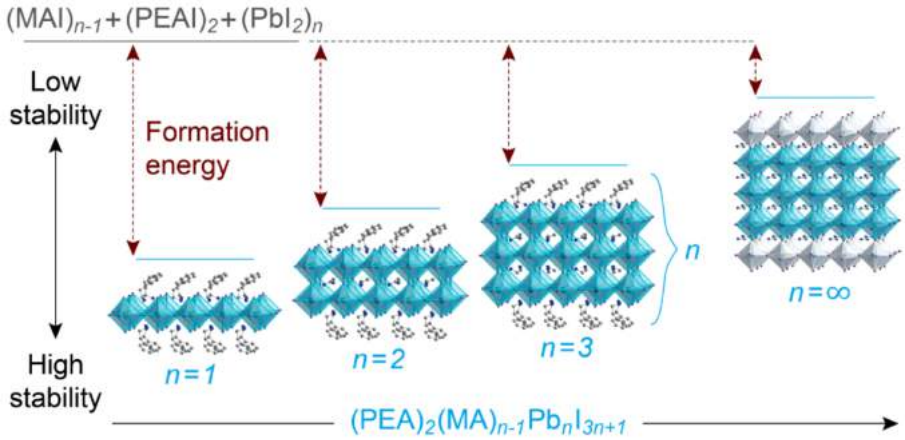

Figure 1.6: Unit cell structure of $A_2(MA)_{n-1}PbI_{3n+1}$ with perovskites A=PEA and with different n values. The perovskite structure evolves from a 2D phase (n=1) to a 3D phase (n=∞). Image taken from reference [67].

The incorporation of 2D materials in 3D perovskite structures considerably increases the stability of perovskite materials thanks to the hydrophobicity of the larger cation A. [69] Moisture-induced decomposition is believed to be reduced thanks to the stronger van der Walls interaction between the large organic cations. [67] Moreover, 3D perovskite grains were observed to grow with higher orientation when surrounded by 2D perovskite platelets, considerably reducing non-radiative charge recombination. [68]

Modification of the device structure The device structure can be altered in order to make the perovskite device more stable towards moisture. Different strategies have been developed and reported, such as passivation of the grain boundaries, perovskite surface passivation through interlayers and modification of the charge transport material to make it more hydrophobic. Grain boundaries have been successfully passivated with bifunctional conjugated cations, 2D molecules like PEA, insulating molecules such as tetraethyl orthosilicate and carbon quantum dots. [70, 71, 72, 73] The added component was found to bond to the uncoordinated Pb in $MAPbI_3$ structures, reducing the contact between H_2O molecules and $MAPbI_3$ and enhancing the moisture stability of perovskite solar cells.
Extensive work has been done on treating the perovskite top surface to minimize the interaction with water and improve moisture stability. Alkyl ammonium salts, long chain polymers and Al_2O_3 films deposited by atomic layer deposition are just some of the materials used to treat the surface of perovskite films, enhancing their moisture resistivity. [74, 75, 76, 77] Passivation of the top perovskite surface and grain boundaries will be extensively discussed in chapters 3 and 4.

Finally, the device structure can be also modified by substituting the charge transport layer with more hydrophobic materials. For example, poly(3-hexylthiophene) (P3HT), which is a hydrophobic polymer, less permeable than the commonly used Spiro-OMeTAD, or the insulating poly(methyl methacrylate) (PMMA) combined with carbon nanotubes have been used as hole transport materials inhibiting the intrusion of moisture through the structure. [78, 79]

1.2.2 Temperature

The typical perovskite ABX_3 structure undergoes phase changes with temperature. The archetypal $MAPbI_3$ shifts from an orthorombic to a tetragonal phase at $-110\,^{\circ}\mathrm{C}$ and from the tetragonal to a cubic phase at $55\,^{\circ}\mathrm{C}$. [80, 81] Even though this phase change does not seem to particularly affect the photovoltaic properties of the device, it is still not clear whether repeated phase transitions may damage the material in the long term. [82] If the black photoactive phase of $MAPbI_3$ is stable at room temperature, pure $FAPbI_3$ and $CsPbI_3$ materials are instead considerably less structurally stable and yellow-non photoactive phases dominate over the black photoactive phase at room temperature. [83, 84, 85, 86]

Thermal treatment at temperatures $> 60\,^{\circ}\mathrm{C}$ does not only affect the structure, but it also induces chemical decomposition of the material. Thermal decomposition consists in the sublimation of the organic and halide components, followed by decomposition of the remaining metal halides. [87]

$$\mathrm{CH_3NH_3PbI_3} \rightarrow \mathrm{PbI_2} + [\mathrm{CH_3NH_3}^+ + \mathrm{I}^-] \tag{1.4}$$

The exact products released upon thermal decomposition of $MAPbI_3$ have been debated and the following reactions have been proposed. [88, 89, 90]

$$CH_3NH_3{}^+ + I^- \rightarrow CH_3I + NH_3 \tag{1.5}$$

$$CH_3NH_3{}^+ + I^- \rightarrow CH_3NH_2 + HI \tag{1.6}$$

Halide perovskite solar cells are particularly sensitive to temperature because of the high volatility of halide species and organic cations. [87] $MAPbI_3$ films showed induced degradation already after annealing treatment at $85\,^{\circ}C$ in the dark and under ambient atmosphere. [91] Annealing treatment at $85\,^{\circ}C$ induces morphological and structural changes, resulting in the conversion of the 3D perovskite structure $MAPbI_3$ into PbI_2 with loss of MAI. It has been reported that thermal degradation is initiated at the grain boundaries of $MAPbI_3$ through surface-mediated decomposition and formation of defects. [92] Therefore, a way to improve the thermal stability of perovskite devices is through passivation of grain boundaries. For example, adding materials, like n-butylammine and phenetylammonium, have been demonstrated to create thin 2D layers at grain boundaries that suppressed defect formation at high temperature, enhancing the thermal stability. [71, 93, 94]

An alternative route to enhance the thermal stability is through the use of alternative cations, like Cs^+, or mixed compositions. The thermodynamic stability of $MAPbI_3$ is enhanced by A-site cation substitution. For example, small positive or very low negative formation enthalpy of pure $MAPbI_3$ has been reported in the literature. [95, 96] In contrast, mixed compositions, such as FA/MA perovskites, exhibit negative formation enthalpy, therefore higher stability against temperature and chemical degradation. [97] The inorganic cation Cs^+ is much less volatile than the MA^+. [10, 98] The thermal stability of $CsPbBr_3$ perovskite films and the effect of temperature on the photovoltaic performance will be discussed more in details in chapter 5.

Finally, thermal instabilities of the perovskite devices can also be caused by thermal degradation of the charge transport materials or diffusion of the mobile ions into transport layers induced by high temperature. [99, 100] Organic hole transport materials, such as PEDOT and Spiro-OMeTAD, tend to be highly unstable at temperatures $> 80\,^{\circ}C$, particularly when additives are added to improve the conductivity. [101, 102] In contrast, oxide transport layers like TiO_2 and NiO_x are much more stable at higher temperatures. Different strategies have been used to enhance thermal stability of perovskite solar cells, like the use of novel HTM with higher glass transition temperature, [103] hole-conductor free devices or barrier layers to prevent the diffusion of mobile ions. The latter two cases will be further discussed in section 1.2.4 and chapter 5.

1.2.3 Light exposure

Long-term reliability of halide perovskite materials under light exposure must be assured to fabricate stable solar cells. It is commonly accepted that perovskites manifest light-induced ion migration when exposed to illumination. However, it is still debated whether ion migration under illumination has a beneficial or detrimental role on the material's stability. Indeed some works reported that ion migration under illumination enhanced the material through defect healing. [104, 105, 106] Mobile iodide was reported to fill vacancies in the material, reducing the density of defects responsible for non-radiative recombination mechanisms. [104, 105] In contrast, other reports showed the generation of photoinduced trap states in the material, which caused severe degradation. [107, 108, 109] Both phenomena showed the beneficial role of oxygen. Tian *et al.* observed a photo-induced healing effect only in the presence of oxygen [104] and Motti *et al.* reported a reduced photo-induced trap states generation when samples were tested in ambient air. [108]

Very recently Motti *et al.* reported a new model, claiming the coexistance and competition of both phenomena of degradation and enhancement of perovskites under illumination. [110] On the one hand, annihilation of Frenkel defects, which led to healed crystal lattice, was predominantly observed at low temperatures and when the film was uniformly illuminated through the thickness. [109] On the other hand, higher temperatures and high initial trap density concentrations induced the formation of I_2 molecules, which preferentially migrated to the surface, creating an iodine imbalance through the film and triggering reactions that generated defects in the bulk. Figure 1.7 shows dynamics in $MAPbI_3$ that describe the photo-induced enhancement and degradation mechanisms modelled by Motti *et al.*.

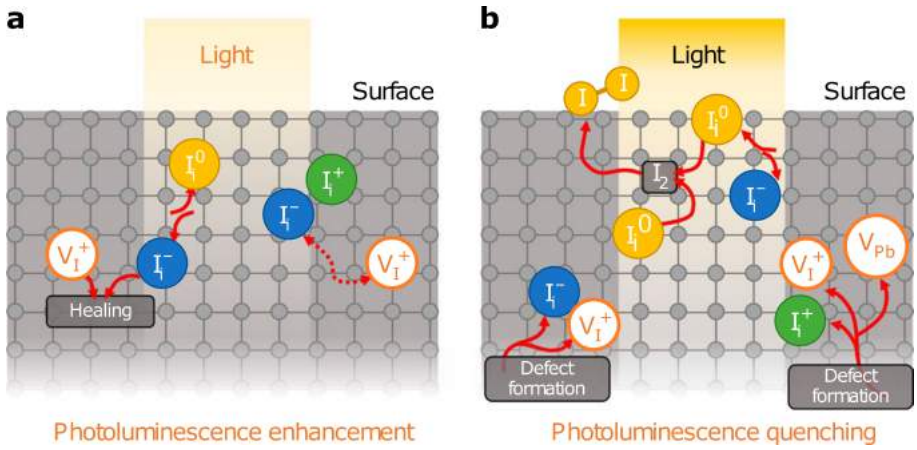

Figure 1.7: **a** Ion dynamics in $CH_3NH_3PbI_3$ film promoting a light induced enhancement of the material by Frenkel defect annihilation. This phenomenon prevails when probability of I_0 species encounters is small. **b** Ion dynamics in $CH_3NH_3PbI_3$ film promoting a light induced degradation of the material by formation of I_2 molecules on the surface. This phenomenon prevails when probability of I_0 species encounters is high. Figure taken from [110].

According to this model, degradation is expected to be caused by the formation

of I_2 molecules, which can be originated by the reaction of two filled traps at the surface and grain boundaries. It has previosuly been reported that grain boundaries exhibit faster non radiative recombination and act as defect reservoir. [111] Therefore, the best way to trigger the photo induced enhancement of the material, avoiding light induced degradation effects and leaving room for the induced enhancement to prevail, was to block undercoordinated surface Pb atoms by using passivating agents. For example, surface passivation by tri-n-octylphosphine oxide or poly(ethylene oxide) layers (demonstrated to be efficient surface passivating agents) has been shown to minimize the formation of I_2 degradation products. [112, 75] Another suggested approach to reduce iodide diffusion through the film is via partial A-site substitution. Recently, it was demonstrated that partial guanidinium substitution into $MAPbI_3$ considerably suppressed iodide ion transport. [97]

Oxygen and light effect

The presence of oxygen has been reported to reduce the generation of trap states observed under illumination and to enhance the photo-induced structural enhancement. [104, 108] Recently it was found that oxygen molecules could strongly bind to surface iodide vacancies resulting in passivation of carrier trap states. [113] However, it has also been reported that the presence of both oxygen and light could be highly detrimental for perovskites, causing rapid decomposition of the material. [114, 115] Molecular oxygen was found to diffuse through the bulk and be adsorbed at vacancy sites, which act as electron traps, forming reactive superoxide O_2^-. O_2^- could react with methylammonium in the material, quickly decomposing the $CH_3NH_3PbI_3$ perovskite absorber to CH_3NH_2, PbI_2 and I_2. [114] Thin-film passivation with iodide salts was found to enhance both the film and the device stability. [116]

1.2.4 Interaction with metals

One issue that concerns the long-term stability of perovskite solar cells is the interaction between the perovskite active layer and the metal contacts. The reaction of metals with halide perovskites is particularly accelerated in the presence of light, heat and humid air. [8, 117, 118, 119] Metal contact-induced degradation might occur through two different mechanisms: diffusion of iodine species through the transporting material to the metal contacts (figure 1.8 a) or migration of metals to the perovskite active layer (figure 1.8 b).

Diffusion of iodine species was observed in both n-i-p and p-i-n structures through HTM Spiro-OMeTAD and ETM PCBM. [117, 118] Degraded $MAPbI_3$ products diffused through the transport materials, reaching the Ag electrode and forming AgI products. The decrease in PCE of cells was mainly caused by: lower conductivity of Ag, partially degraded to AgI; band alignment mismatch between AgI/transport material; and deficiency of I in the perovskite active layer. [117] Such phenomena

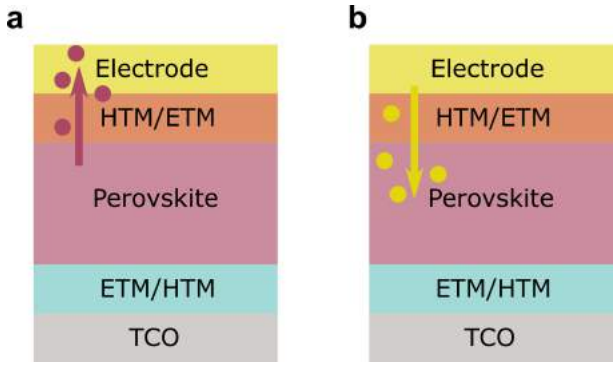

Figure 1.8: Diagram of perovskite devices showing possible degradation mechanisms due to interaction with metal contacts. **a** Diffusion of metals into the active layer. **b** Migration of iodide species into metal contacts through the transport material.

were accelerated by exposure to air or high temperature (85 °C), but were also observed when solar cells were stored in the dark and at room temperature in N_2.

Kato *et al.* reported the presence of AgI at the surface but they did not observe Ag migration to the active layer. In contrast, McGehee and Correa-Baena and coworkers found that both Ag and Au can diffuse through the transport materials, reaching the perovskite absorber layer. [119, 120] Ag migration was identified by XPS spectroscopy techniques and similar results were reported using different perovskite compositions ($MAPbI_3$, $FA_{0.83}Cs_{0.17}Pb(I_{0.83}Br_{0.17})_3$ and $FA_{0.75}Cs_{0.25}Pb_{0.5}Sn_{0.5}I_3$). Boyd *et al.* speculated that metals diffused through the ETM, reacting with the perovskite at the grain boundaries and creating insulating layers that hindered charge extraction. [119]

Potential solutions to prevent iodine species escaping from the active layer and metal diffusion into the active layer consist of forming dense, channel-free barrier layers between the perovskite and metal contacts and designing new architectures that do not require metals to extract charges. The former approach has been widely investigated, for example aluminum doped zinc oxide and tin oxide layers proved to be successful. [121, 122] While an alternative Ag/Au free perovskite solar cell architecture is the triple mesoscopic porous TiO_2/ZrO_2/carbon cell.

The mesoscopic triple carbon solar cell was first reported in 2013 by Ku *et al.* [29] TiO_2 and m-carbon layers are used as ETM and HTM, respectively and ZrO_2 is used as a spacer layer between the transport materials to avoid recombination of photogenerated charges. The advantages of this kind of cells are that metal contacts do not need to be evaporated on top of carbon and that the device is fully-printable trough inexpensive and scalable screen-printed techniques. The perovskite active material in fact is not spin coated, but it is simply infiltrated through the mesoscopic stack with little waste. [123] Carbon is inert to ion migration and its hydrophobic nature reduces the contact between water molecules and the perovskite active material, boosting the moisture stability of the device. [124, 125] The use of such triple mesoscopic carbon architecture will be further investigated in chapter 5.

1.3 Solar hydrogen generation

The current production of hydrogen highly relies on fossil fuels through steam methane reforming and coal gasification processes. Clean hydrogen can be produced through the electrolysis of water. However, high energy needs and costs limit its large-scale application. A straightforward way of reducing the cost consists of combining traditional photovoltaic devices with standard electrolysers. While this route may lead to sustainable production of solar hydrogen, at the moment it is not economically competitive with traditional methods that use fossil fuels. [126] Photovoltaics combined with electrolysis is not the only way of producing solar hydrogen. Two novel alternative routes that have been investigated recently are particulate photocatalyst systems and photoelectrochemical (PEC) water splitting. [127] PEC water splitting is a promising alternative method, which contains a direct-semiconductor/liquid interface. The semiconductor harvests solar energy and converts it into excited charges (electrons and holes) which can directly be used to produce molecular hydrogen and oxygen from the reduction and oxidation of water. To enable practical PEC production of hydrogen, inexpensive, efficient and robust semiconductor materials are needed.

Water splitting into H_2 and O_2 is an up-hill reaction which requires a potential of $1.23\,\mathrm{eV}$ per electron. Two electrons and 4 holes are needed to produce molecular H_2 and O_2, respectively according to:

$$2H_2O + 4h^+ \rightarrow O_2 + 4H^+ \tag{1.7}$$

$$2H^+ + 2e^- \rightarrow H_2 \tag{1.8}$$

where 1.7 is the oxygen evolution reaction (OER) and 1.8 is the hydrogen evolution reaction (HER). A PEC cell can contain a single semiconductor photoelectrode (either a photoanode or a photocathode) combined with a standard metallic electrode or two semiconductor photoelectrodes (a photoanode and a photocathode) in a tandem configuration. [128] The photoanode is a n-type semiconductor and is responsible for the OER, while the photocathode is a p-type semiconductor and looks at the HER. In order to develop unbiased systems, where no potential is applied through the electrodes, sufficient photopotentials $> 1.6\,\mathrm{V}$ must be generated to overcome kinetic limitations and thermodynamic losses. [129]

1.3.1 Photoelectrode material requirements

The most critical aspect in PEC water splitting is the photoelectrode material choice. The energy bandgap must be wide enough to drive the water splitting reaction ($>1.8\,\mathrm{eV}$) but still allow sufficient absorption in the visible range of the solar spectrum. [130] Materials must be chemically stable, without dissolving nor forming thin oxide layers on the surface that prevent charge transfer at the interface. [128]

The band edges of the chosen semiconductor must be properly aligned with the water reduction and oxidation potentials. More specifically, the conduction band edge must be more negative than the reduction potential and the valence band edge must be more positive than the oxidation potential. [130] Once the light has been harvested by the photoelectrode and electron/hole pairs have been generated, charges must be properly transported and extracted at the interfaces. Moreover, the OER and HER require low overpotentials, which means that once charges reach the interface, they must transfer across the semiconductor/electrolyte interface fast enough. [131] Finally, the materials used to fabricate the electrodes must be abundant, non toxic and cheap. [130]

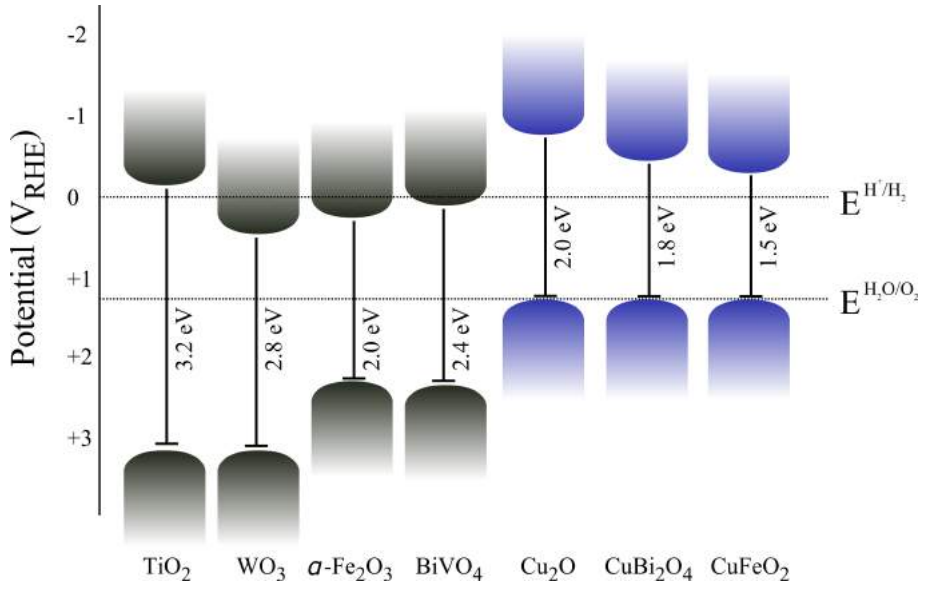

Figure 1.9: Bandgap structures of the most common photoanodes (black) and photocathodes (blue) with respect to the reversible hydrogen electrode and water reduction and oxidation energy levels.

Figure 1.9 shows the bandgap structures of the most common materials used for the fabrication of photoanodes (TiO_2, WO_3, α-Fe_2O_3, $BiVO_4$) and photocathodes ($CuBi_2O_4$ and $CuFeO_2$). TiO_2 and WO_3 are non-toxic, stable materials with good electronic properties, however, they have limited absorption due to their wide energy bandgap. [132, 133] α-Fe_2O_3 and $BiVO_4$ instead have more suitable energy bandgap that allows absorption of light in the visible range, but their PEC performance is limited by poor charge transport. [133, 134] Fewer metal-oxide materials are available for the fabrication of photocathodes, such as Cu_2O, $CuBi_2O_4$ and $CuFeO_2$. Cu_2O is one of the most investigated, however it is unstable in aqueous solution and needs to be protected to avoid photocorrosion during operation. [135] $CuFeO_2$ is more stable in water, however it is challenging to process and is not compatible with large-scale production. [136] In contrast, $CuBi_2O_4$ thin films can be prepared using scalable methods like electrodeposition and spray pyrolysis, but its PEC performance is limited by poor charge transport. [135]

Some of the strategies used to enhance the properties of these materials are: doping to narrow the bandgap, [137] use of co-catalysts to promote charge separation and facilitate OER and HER, [138] surface modification to enhance light absorption, [139] and protection of the electrode to avoid surface recombination and degradation of the material in solution. [140]

Lead halide perovskites are excellent absorber materials which have been widely investigated in the photovoltaic sector for the generation of clean electricity. Their limited stability, particularly in the presence of moisture, initially prevented them from being exploited in aqueous solution for PEC applications. In common with many other metal oxides that are sensitive to photocorrosion, halide perovskites also need proper surface protection to avoid dissolution in water. Research into different encapsulation strategies to protect perovskite materials from water has been undergoing for the past 4 years and successful implementation of halide perovskite-based photoelectrodes has been reported. [141, 142, 143] These works will be extensively discussed in chapter 6.

Bibliography

[1] Topsoe, A. Arzruni, and G. Bath, "XVI.Auszuge," *Z. Kristallogr. Cryst. Mater.*, vol. 8, no. 1-6, pp. 246–320, 1884.

[2] C. R. Kagan, D. B. Mitzi, and C. D. Dimitrakopoulos, "Organic-Inorganic Hybrid Materials as Semiconducting Channels in Thin-Film Field-Effect Transistors," *Science*, vol. 286, pp. 945–948, 1999.

[3] K. Chondroudis and D. B. Mitzi, "Electroluminescence from an Organic-Inorganic Perovskite Incorporating a Quaterthiophene Dye within Lead Halide Perovskite Layers," *Chem. Mater.*, vol. 11, pp. 3028–3030, 1999.

[4] A. Kojima, K. Teshima, Y. Shirai, and T. Miyasaka, "Organometal halide perovskites as visible-light sensitizers for photovoltaic cells.," *J. Am. Chem. Soc.*, vol. 131, pp. 6050–1, may 2009.

[5] NREL, "National Renewable Energy Laboratory (NREL)," 2019.

[6] M. a. Green, A. Ho-Baillie, and H. J. Snaith, "The emergence of perovskite solar cells," *Nat. Photonics*, vol. 8, no. 7, pp. 506–514, 2014.

[7] Z. Li, M. Yang, J. S. Park, S. H. Wei, J. J. Berry, and K. Zhu, "Stabilizing Perovskite Structures by Tuning Tolerance Factor: Formation of Formamidinium and Cesium Lead Iodide Solid-State Alloys," *Chem. Mater.*, vol. 28, no. 1, pp. 284–292, 2016.

[8] C. C. Boyd, R. Cheacharoen, T. Leijtens, and M. D. McGehee, "Understanding Degradation Mechanisms and Improving Stability of Perovskite Photovoltaics," *Chem. Rev.*, vol. 119, no. 5, pp. 3418–3451, 2019.

[9] N. J. Jeon, J. H. Noh, W. S. Yang, Y. C. Kim, S. Ryu, J. Seo, and S. I. Seok, "Compositional engineering of perovskite materials for high-performance solar cells," *Nature*, vol. 517, no. 7535, pp. 476–480, 2015.

[10] D. P. McMeekin, G. Sadoughi, W. Rehman, G. E. Eperon, M. Saliba, M. T. Hörantner, A. Haghighirad, N. Sakai, L. Korte, B. Rech, M. B. Johnston, L. M. Herz, and H. J. Snaith, "A mixed-cation lead mixed-halide perovskite absorber for tandem solar cells," *Science*, vol. 351, no. 6269, pp. 151–155, 2016.

[11] M. Saliba, T. Matsui, J.-Y. Seo, K. Domanski, J.-P. Correa-Baena, M. K. Nazeeruddin, S. M. Zakeeruddin, W. Tress, A. Abate, A. Hagfeldt, and M. Grätzel, "Cesium-containing triple cation perovskite solar cells: improved stability, reproducibility and high efficiency," *Energy Environ. Sci.*, vol. 9, no. 6, pp. 1989–1997, 2016.

[12] J. H. Noh, S. H. Im, J. H. Heo, T. N. Mandal, and S. I. Seok, "Chemical management for colorful, efficient, and stable inorganic-organic hybrid nanostructured solar cells," *Nano Lett.*, vol. 13, no. 4, pp. 1764–1769, 2013.

[13] Woon Seok Yang, Byung-Wook Park, Eui Hyuk Jung, Nam Joong Jeon, Young Chan Kim, Dong Uk Lee, Seong Sik Shin, Jangwon Seo, Eun Kyu Kim, Jun Hong Noh, and Sang Il Seok, "Iodide management in formamidinium-lead-halide-based perovskite layers for efficient solar cells," *Science*, vol. 356, no. 6345, pp. 1376–1379, 2017.

[14] W. Zhang, M. Saliba, D. T. Moore, S. K. Pathak, M. T. Horantner, T. Stergiopoulos, S. D. Stranks, G. E. Eperon, J. A. Alexander-Webber, A. Abate, A. Sadhanala, S. Yao, Y. Chen, R. H. Friend, L. A. Estroff, U. Wiesner, and H. J. Snaith, "Ultrasmooth organic-inorganic perovskite thin-film formation and crystallization for efficient planar heterojunction solar cells," *Nat. Commun.*, vol. 6, p. 6142, 2015.

[15] Y. Hou, C. O. R. Quiroz, S. Scheiner, W. Chen, T. Stubhan, A. Hirsch, M. Halik, and C. J. Brabec, "Low-temperature and hysteresis-free electron-transporting layers for efficient, regular, and planar structure perovskite solar cells," *Adv. Energy Mater.*, vol. 5, no. 20, 2015.

[16] D. Yang, X. Zhou, R. Yang, Z. Yang, W. Yu, X. Wang, C. Li, S. Liu, and R. P. Chang, "Surface optimization to eliminate hysteresis for record efficiency planar perovskite solar cells," *Energy Environ. Sci.*, vol. 9, no. 10, pp. 3071–3078, 2016.

[17] Z. Li, T. R. Klein, D. H. Kim, M. Yang, J. J. Berry, M. F. Van Hest, and K. Zhu, "Scalable fabrication of perovskite solar cells," *Nat. Rev. Mater.*, vol. 3, pp. 1–20, 2018.

[18] I. Hussain, H. P. Tran, J. Jaksik, J. Moore, N. Islam, and M. J. Uddin, "Functional materials, device architecture, and flexibility of perovskite solar cell," *Emergent Materials*, vol. 1, no. 3-4, pp. 133–154, 2018.

[19] J. M. Ball, M. M. Lee, A. Hey, and H. J. Snaith, "Low-temperature processed meso-superstructured to thin-film perovskite solar cells," *Energy Environ. Sci.*, vol. 6, p. 1739, 2013.

[20] M. Liu, M. B. Johnston, and H. J. Snaith, "Efficient planar heterojunction perovskite solar cells by vapour deposition.," *Nature*, vol. 501, no. 7467, pp. 395–8, 2013.

[21] J. P. Correa Baena, L. Steier, W. Tress, M. Saliba, S. Neutzner, T. Matsui, F. Giordano, T. J. Jacobsson, A. R. Srimath Kandada, S. M. Zakeeruddin, A. Petrozza, A. Abate, M. K. Nazeeruddin, M. Grätzel, and A. Hagfeldt, "Highly efficient

planar perovskite solar cells through band alignment engineering," *Energy Environ. Sci.*, vol. 8, no. 10, pp. 2928–2934, 2015.

[22] E. H. Anaraki, A. Kermanpur, L. Steier, K. Domanski, T. Matsui, W. Tress, M. Saliba, A. Abate, M. Grätzel, A. Hagfeldt, and J.-P. Correa-Baena, "Highly efficient and stable planar perovskite solar cells by solution-processed tin oxide," *Energy Environ. Sci.*, vol. 9, no. 10, pp. 3128–3134, 2016.

[23] J. Barbé, M. L. Tietze, M. Neophytou, B. Murali, E. Alarousu, A. E. Labban, M. Abulikemu, W. Yue, O. F. Mohammed, I. McCulloch, A. Amassian, and S. Del Gobbo, "Amorphous Tin Oxide as a Low-Temperature-Processed Electron-Transport Layer for Organic and Hybrid Perovskite Solar Cells," *ACS Appl. Mater. Interfaces*, vol. 9, no. 13, pp. 11828–11836, 2017.

[24] J. H. Heo, S. H. Im, J. H. Noh, T. N. Mandal, C. S. Lim, J. A. Chang, Y. H. Lee, H. J. Kim, A. Sarkar, M. K. Nazeeruddin, M. Grätzel, and S. I. Seok, "Efficient inorganic-organic hybrid heterojunction solar cells containing perovskite compound and polymeric hole conductors," *Nat. Photonics*, vol. 7, no. 6, pp. 486–491, 2013.

[25] D. Bi, G. Boschloo, and A. Hagfeldt, "High-Efficient Solid-State Perovskite Solar Cell Without Lithium Salt in the Hole Transport Material," *Nano*, vol. 09, no. 05, p. 1440001, 2014.

[26] J. H. Heo, M. S. You, M. H. Chang, W. Yin, T. K. Ahn, S.-J. Lee, S.-J. Sung, D. H. Kim, and S. H. Im, "Hysteresis-less mesoscopic $CH_3NH_3PbI_3$ perovskite hybrid solar cells by introduction of Li-treated TiO_2 electrode," *Nano Energy*, vol. 15, pp. 530–539, 2015.

[27] K. Wang, J.-y. Jeng, P. Shen, Y. Chang, E. W. Diau, C.-h. Tsai, T.-y. Chao, H. Hsu, P. Lin, P. Chen, and T. Guo, "p-type Mesoscopic Nickel Oxide/ Organometallic Perovskite Heterojunction Solar Cells," *Sci. Rep.*, vol. 4, no. 4756, pp. 1–8, 2014.

[28] J. H. Park, J. Seo, S. Park, S. S. Shin, Y. C. Kim, N. J. Jeon, H. W. Shin, T. K. Ahn, J. H. Noh, S. C. Yoon, C. S. Hwang, and S. I. Seok, "Efficient $CH_3NH_3PbI_3$ Perovskite Solar Cells Employing Nanostructured p-Type NiO Electrode Formed by a Pulsed Laser Deposition," *Adv. Mater.*, vol. 27, no. 27, pp. 4013–4019, 2015.

[29] Z. Ku, Y. Rong, M. Xu, T. Liu, and H. Han, "Full Printable Processed Mesoscopic $CH_3NH_3PbI_3/TiO_2$ Heterojunction Solar Cells with Carbon Counter Electrode," *Sci. Rep.*, vol. 3, no. 1, p. 3132, 2013.

[30] S. Liu, W. Huang, P. Liao, N. Pootrakulchote, H. Li, J. Lu, J. Li, F. Huang, X. Shai, X. Zhao, Y. Shen, Y. B. Cheng, and M. Wang, "17% efficient printable

mesoscopic PIN metal oxide framework perovskite solar cells using cesium-containing triple cation perovskite," *J. Mater. Chem. A*, vol. 5, no. 44, pp. 22952–22958, 2017.

[31] H. J. Snaith, A. Abate, J. M. Ball, G. E. Eperon, T. Leijtens, N. K. Noel, S. D. Stranks, J. T. W. Wang, K. Wojciechowski, and W. Zhang, "Anomalous hysteresis in perovskite solar cells," *J. Phys. Chem. Lett.*, vol. 5, no. 9, pp. 1511–1515, 2014.

[32] N. Park, M. Grätzel, T. Miyasaka, K. Zhu, and K. Emery, "Towards stable and commercially available perovskite solar cells," *Nat. Energy*, vol. 1, no. 16152, 2016.

[33] E. L. Unger, E. T. Hoke, C. D. Bailie, W. H. Nguyen, A. R. Bowring, M. G. Christoforo, and M. D. Mcgehee, "Hysteresis and transient behavior in current-voltage measurements of hybrid-perovskite absorber solar cells," *Energy Environ. Sci.*, vol. 7, pp. 3690–3698, 2014.

[34] H. Kim, I. Jang, N. Ahn, M. Choi, A. Guerrero, J. Bisquert, and N. Park, "Control of I-V Hysteresis in $CH_3NH_3PbI_3$ Perovskite Solar Cell," *J. Phys. Chem. Lett.*, vol. 6, pp. 4633–4639, 2015.

[35] N. J. Jeon, J. H. Noh, Y. C. Kim, W. S. Yang, S. Ryu, and S. I. Seok, "Solvent engineering for high-performance inorganic-organic hybrid perovskite solar cells.," *Nat. Mater.*, vol. 13, pp. 897–903, 2014.

[36] J. H. Heo, H. J. Han, D. Kim, T. K. Ahn, and S. H. Im, "Hysteresis-less inverted $CH_3NH_3PbI_3$ planar perovskite hybrid solar cells with 18.1% power conversion efficiency," *Energy Environ. Sci.*, vol. 8, no. 5, pp. 1602–1608, 2015.

[37] H. Kim, S. K. Kim, B. J. Kim, K.-s. Shin, M. K. Gupta, H. S. Jung, S.-w. Kim, and N.-g. Park, "Ferroelectric Polarization in $CH_3NH_3PbI_3$ Perovskite," *J. Phys. Chem. Lett.*, vol. 6, pp. 1729–1735, 2015.

[38] H. Rohm, T. Leonhard, M. J. Hoffmann, and A. Colsmann, "Ferroelectric domains in methylammonium lead iodide perovskite thin-films," *Energy Environ. Sci.*, vol. 10, pp. 950–955, 2017.

[39] H. Chen, N. Sakai, M. Ikegami, and T. Miyasaka, "Emergence of Hysteresis and Transient Ferroelectric Response in Organo-Lead Halide Perovskite Solar Cells," *J. Phys. Chem Lett.*, vol. 6, pp. 164–169, 2015.

[40] S. Meloni, T. Moehl, W. Tress, M. Franckeviius, M. Saliba, Y. H. Lee, P. Gao, M. K. Nazeeruddin, S. M. Zakeeruddin, U. Rothlisberger, and M. Graetzel, "Ionic polarization-induced current-voltage hysteresis in $CH_3NH_3PbX_3$ perovskite solar cells," *Nat. Commun.*, vol. 7, no. 10334, 2016.

[41] J. Beilsten-Edmands, G. E. Eperon, R. D. Johnson, H. J. Snaith, and P. G. Radaelli, "Non-ferroelectric nature of the conductance hysteresis in $CH_3NH_3PbI_3$ perovskite-based photovoltaic devices," *Appl. Phys. Lett.*, vol. 106, no. 173502, 2015.

[42] D. Kang and N. Park, "On the Current-Voltage Hysteresis in Perovskite Solar Cells : Dependence on Perovskite Composition and Methods to Remove Hysteresis," *Adv. Mater.*, no. 1805214, pp. 1–23, 2019.

[43] P. Calado, A. M. Telford, D. Bryant, X. Li, J. Nelson, B. C. O'Regan, and P. R. Barnes, "Evidence for ion migration in hybrid perovskite solar cells with minimal hysteresis," *Nat. Commun.*, vol. 7, pp. 1–10, 2016.

[44] S. V. Reenen, M. Kemerink, and H. J. Snaith, "Modeling Anomalous Hysteresis in Perovskite Solar Cells," *J. Phys. Chem Lett.*, vol. 6, pp. 3808–3814, 2015.

[45] C. Li, S. Tscheuschner, F. Paulus, P. E. Hopkinson, J. Kießling, A. Köhler, Y. Vaynzof, and S. Huettner, "Iodine Migration and its Effect on Hysteresis in Perovskite Solar Cells," *Adv. Mater.*, vol. 28, pp. 2446–2454, 2016.

[46] Z. Xiao, Y. Yuan, Y. Shao, Q. Wang, Q. Dong, C. Bi, P. Sharma, A. Gruverman, and J. Huang, "Giant switchable photovoltaic effect in organometal trihalide perovskite devices," *Nat. Mater.*, vol. 14, pp. 193–197, 2015.

[47] W. Tress, N. Marinova, T. Moehl, S. M. Zakeeruddin, N. Mohammad K., M. Grätzel, M. K. Nazeeruddin, and M. Grätzel, "Understanding the rate-dependent J-V hysteresis, slow time component, and aging in $CH_3NH_3PbI_3$ perovskite solar cells: the role of a compensated electric field," *Energy Environ. Sci.*, vol. 8, no. 3, pp. 995–1004, 2015.

[48] C. Eames, J. M. Frost, P. R. F. Barnes, B. C. O'Regan, A. Walsh, and M. S. Islam, "Ionic transport in hybrid lead iodide perovskite solar cells," *Nat. Commun.*, vol. 6, p. 7497, jun 2015.

[49] T. S. Sherkar, C. Momblona, L. Gil-Escrig, J. Ávila, M. Sessolo, H. J. Bolink, and L. J. A. Koster, "Recombination in Perovskite Solar Cells: Significance of Grain Boundaries, Interface Traps, and Defect Ions," *ACS Energy Lett.*, vol. 2, no. 5, pp. 1214–1222, 2017.

[50] V. D'Innocenzo, G. Grancini, M. J. Alcocer, A. R. S. Kandada, S. D. Stranks, M. M. Lee, G. Lanzani, H. J. Snaith, and A. Petrozza, "Excitons versus free charges in organo-lead tri-halide perovskites," *Nat. Commun.*, vol. 5, pp. 1–6, 2014.

[51] J. W. Lee, S. G. Kim, S. H. Bae, D. K. Lee, O. Lin, Y. Yang, and N. G. Park, "The Interplay between Trap Density and Hysteresis in Planar Heterojunction Perovskite Solar Cells," *Nano Lett.*, vol. 17, no. 7, pp. 4270–4276, 2017.

[52] M. Li, C. Zhao, Z. K. Wang, C. C. Zhang, H. K. Lee, A. Pockett, J. Barbé, W. C. Tsoi, Y. G. Yang, M. J. Carnie, X. Y. Gao, W. X. Yang, J. R. Durrant, L. S. Liao, and S. M. Jain, "Interface Modification by Ionic Liquid: A Promising Candidate for Indoor Light Harvesting and Stability Improvement of Planar Perovskite Solar Cells," *Adv. Energy Mater.*, vol. 8, no. 24, pp. 1–8, 2018.

[53] C. Wang, C. Xiao, Y. Yu, D. Zhao, R. A. Awni, C. R. Grice, K. Ghimire, I. Constantinou, W. Liao, A. J. Cimaroli, P. Liu, J. Chen, N. J. Podraza, C. S. Jiang, M. M. Al-Jassim, X. Zhao, and Y. Yan, "Understanding and Eliminating Hysteresis for Highly Efficient Planar Perovskite Solar Cells," *Adv. Energy Mater.*, vol. 7, no. 17, pp. 1–9, 2017.

[54] M. Abdi-jalebi, Z. Andaji-garmaroudi, S. Cacovich, C. Stavrakas, B. Philippe, E. M. Hutter, A. J. Pearson, S. Lilliu, T. J. Savenije, J. M. Richter, M. Alsari, P. Edward, H. Rensmo, G. Divitini, C. Ducati, R. H. Friend, and S. D. Stranks, "Maximizing and stabilizing luminescence from halide perovskites with potassium passivation," *Nature*, vol. 555, no. 7697, pp. 497–501, 2018.

[55] M. Abdi-Jalebi, Z. Andaji-Garmaroudi, A. J. Pearson, G. Divitini, S. Cacovich, B. Philippe, H. Rensmo, C. Ducati, R. H. Friend, and S. D. Stranks, "Potassium and rubidium passivated alloyed perovskite films: Optoelectronic properties and moisture stability," *ACS Energy Lett.*, vol. 3, no. 11, pp. 2671–2678, 2018.

[56] D. Y. Son, S. G. Kim, J. Y. Seo, S. H. Lee, H. Shin, D. Lee, and N. G. Park, "Universal Approach toward Hysteresis-Free Perovskite Solar Cell via Defect Engineering," *J. Am. Chem. Soc.*, vol. 140, no. 4, pp. 1358–1364, 2018.

[57] J. P. Correa-Baena, M. Saliba, T. Buonassisi, M. Grätzel, A. Abate, W. Tress, and A. Hagfeldt, "Promises and challenges of perovskite solar cells," *Science*, vol. 358, pp. 739–744, 2017.

[58] G. Grancini and M. K. Nazeeruddin, "Dimensional tailoring of hybrid perovskites for photovoltaics," *Nat. Rev. Mater.*, vol. 4, no. 1, pp. 4–22, 2019.

[59] A. M. A. Leguy, Y. Hu, M. Campoy-Quiles, M. I. Alonso, O. J. Weber, P. Azarhoosh, M. van Schilfgaarde, M. T. Weller, T. Bein, J. Nelson, P. Docampo, and P. R. F. Barnes, "Reversible Hydration of $CH_3NH_3PbI_3$ Films, Single Crystals, and Solar Cells," *Chem. Mater.*, vol. 27, no. 9, pp. 3397–3407, 2015.

[60] J. Huang, S. Tan, P. D. Lund, and H. Zhou, "Impact of H_2O on organic-inorganic hybrid perovskite solar cells," *Energy Environ. Sci.*, vol. 10, no. 11, pp. 2284–2311, 2017.

[61] J. Schlipf, L. Bießmann, L. Oesinghaus, E. Berger, E. Metwalli, J. A. Lercher, L. Porcar, and P. Mu, "In Situ Monitoring the Uptake of Moisture into Hybrid Perovskite Thin Films," *J. Phys. Chem Lett.*, vol. 9, pp. 2015–2021, 2018.

[62] U.-g. Jong, C.-j. Yu, G.-c. Ri, and A. P. Mcmahon, "Influence of water intercalation and hydration on chemical decomposition and ion transport in methylammonium lead halide perovskites," *J. Mater. Chem. A*, vol. 6, pp. 1067–1074, 2018.

[63] F. El-Mellouhi, A. Marzouk, E. T. Bentria, S. N. Rashkeev, S. Kais, and F. H. Alharbi, "Hydrogen Bonding and Stability of Hybrid Organic–Inorganic Perovskites," *ChemSusChem*, vol. 9, no. 18, pp. 2648–2655, 2016.

[64] J. W. Lee, D. H. Kim, H. S. Kim, S. W. Seo, S. M. Cho, and N. G. Park, "Formamidinium and cesium hybridization for photo- and moisture-stable perovskite solar cell," *Adv. Energy Mater.*, vol. 5, no. 20, 2015.

[65] M. R. Leyden, M. V. Lee, S. R. Raga, and Y. Qi, "Large formamidinium lead trihalide perovskite solar cells using chemical vapor deposition with high reproducibility and tunable chlorine concentrations," *J. Mater. Chem. A*, vol. 3, no. 31, pp. 16097–16103, 2015.

[66] Q. Tai, P. You, H. Sang, Z. Liu, C. Hu, H. Chan, and F. Yan, "Efficient and stable perovskite solar cells prepared in ambient air irrespective of the humidity," *Nat. Commun.*, vol. 7, pp. 1–8, 2016.

[67] L. N. Quan, M. Yuan, R. Comin, O. Voznyy, E. M. Beauregard, S. Hoogland, A. Buin, A. R. Kirmani, K. Zhao, A. Amassian, D. H. Kim, and E. H. Sargent, "Ligand-Stabilized Reduced-Dimensionality Perovskites," *J. Am. Chem. Soc.*, vol. 138, no. 8, pp. 2649–2655, 2016.

[68] Z. Wang, Q. Lin, F. P. Chmiel, N. Sakai, L. M. Herz, and H. J. Snaith, "Efficient ambient-air-stable solar cells with 2D-3D heterostructured butylammonium-caesium-formamidinium lead halide perovskites," *Nat. Energy*, vol. 2, no. 9, 2017.

[69] J. Rodríguez-Romero, B. Clasen Hames, P. Galar, A. Fakharuddin, I. Suarez, L. Schmidt-Mende, J. P. Martínez-Pastor, A. Douhal, I. Mora-Seró, and E. M. Barea, "Tuning optical/electrical properties of 2D/3D perovskite by the inclusion of aromatic cation," *Phys. Chem. Chem. Phys.*, vol. 20, no. 48, pp. 30189–30199, 2018.

[70] Y. Hu, Z. Zhang, A. Mei, Y. Jiang, X. Hou, Q. Wang, and K. Du, "Improved Performance of Printable Perovskite Solar Cells with Bifunctional Conjugated Organic Molecule," *Adv. Mater.*, vol. 30, p. 1705786, 2018.

[71] D. S. Lee, J. S. Yun, J. Kim, A. M. Soufiani, S. Chen, Y. Cho, X. Deng, J. Seidel, S. Lim, S. Huang, and A. W. Ho-Baillie, "Passivation of Grain Boundaries by Phenethylammonium in Formamidinium-Methylammonium Lead Halide Perovskite Solar Cells," *ACS Energy Lett.*, vol. 3, no. 3, pp. 647–654, 2018.

[72] B. A. De Carvalho, S. Kavadiya, S. Huang, D. M. Niedzwiedzki, and P. Biswas, "Highly Stable Perovskite Solar Cells Fabricated under Humid Ambient Conditions," *IEEE J. Photovolt.*, vol. 7, no. 2, pp. 532–538, 2017.

[73] Q. Guo, F. Yuan, B. Zhang, S. Zhou, J. Zhang, Y. Bai, L. Fan, T. Hayat, A. Alsaedi, and Z. Tan, "Passivation of the grain boundaries of $CH_3NH_3PbI_3$ using carbon quantum dots for highly efficient perovskite solar cells with excellent environmental stability," *Nanoscale*, vol. 11, no. 1, pp. 115–124, 2019.

[74] S. Yang, Y. Wang, P. Liu, Y.-B. Cheng, H. J. Zhao, and H. G. Yang, "Functionalization of perovskite thin films with moisture-tolerant molecules," *Nat. Energy*, vol. 1, pp. 1–7, 2016.

[75] M. Kim, S. G. Motti, R. Sorrentino, and A. Petrozza, "Enhanced Solar Cells Stability by Hygroscopic Polymer Passivation of Metal Halide Perovskite Thin Film," *Energy Environ. Sci.*, vol. 11, pp. 2609–2619, 2018.

[76] B. Li, Y. Zhang, L. Fu, T. Yu, S. Zhou, L. Zhang, and L. Yin, "Surface passivation engineering strategy to fully-inorganic cubic $CsPbI_3$ perovskites for high-performance solar cells," *Nat. Commun.*, vol. 9, no. 1, pp. 1–8, 2018.

[77] D. Koushik, W. J. Verhees, Y. Kuang, S. Veenstra, D. Zhang, M. A. Verheijen, M. Creatore, and R. E. Schropp, "High-efficiency humidity-stable planar perovskite solar cells based on atomic layer architecture," *Energy Environ. Sci.*, vol. 10, no. 1, pp. 91–100, 2017.

[78] S. N. Habisreutinger, T. Leijtens, G. E. Eperon, S. D. Stranks, R. J. Nicholas, and H. J. Snaith, "Carbon nanotube/polymer composites as a highly stable hole collection layer in perovskite solar cells," *Nano Lett.*, vol. 14, no. 10, pp. 5561–5568, 2014.

[79] Y. C. Kim, T. Y. Yang, N. J. Jeon, J. Im, S. Jang, T. J. Shin, H. W. Shin, S. Kim, E. Lee, S. Kim, J. H. Noh, S. I. Seok, and J. Seo, "Engineering interface structures between lead halide perovskite and copper phthalocyanine for efficient and stable perovskite solar cells," *Energy Environ. Sci.*, vol. 10, no. 10, pp. 2109–2116, 2017.

[80] Y. Kawamura, H. Mashiyama, and K. Hasebe, "Structural Study on Cubic-Tetragonal Transition of $CH_3NH_3PbI_3$," *J. Phys. Soc. Jpn.*, vol. 71, no. 7, pp. 1694–1697, 2002.

[81] M. T. Weller, O. J. Weber, P. F. Henry, A. M. D. Pumpo, and T. C. Hansen, "Complete structure and cation orientation in the perovskite photovoltaic methylammonium lead iodide between 100 and 352 K," *Chem. Commun.*, vol. 51, pp. 4180–4183, 2015.

[82] C. Quarti, E. Mosconi, J. M. Ball, V. D. Innocenzo, C. Tao, S. Pathak, H. J. Snaith, and F. D. Angelis, "Environmental Science Structural and optical properties of methylammonium lead iodide across the tetragonal to cubic phase transition : implications for perovskite solar cells," *Energy Environ. Sci.*, vol. 9, no. 155, 2016.

[83] M. T. Weller, O. J. Weber, J. M. Frost, and A. Walsh, "Cubic Perovskite Structure of Black Formamidinium Lead Iodide, α-[$HC(NH_2)_2$]PbI_3, at 298 K," *J. Phys. Chem Lett.*, vol. 6, no. 16, pp. 3209–3212, 2015.

[84] C. C. Stoumpos, C. D. Malliakas, and M. G. Kanatzidis, "Semiconducting tin and lead iodide perovskites with organic cations: Phase transitions, high mobilities, and near-infrared photoluminescent properties," *Inorg. Chem.*, vol. 52, no. 15, pp. 9019–9038, 2013.

[85] G. E. Eperon, G. M. Paternò, R. J. Sutton, A. Zampetti, A. A. Haghighirad, F. Cacialli, and H. J. Snaith, "Inorganic caesium lead iodide perovskite solar cells," *J. Mater. Chem. A*, vol. 3, no. 39, pp. 19688–19695, 2015.

[86] I. Lignos, V. Morad, Y. Shynkarenko, C. Bernasconi, R. M. Maceiczyk, L. Protesescu, F. Bertolotti, S. Kumar, S. T. Ochsenbein, N. Masciocchi, A. Guagliardi, C. J. Shih, M. I. Bodnarchuk, A. J. Demello, and M. V. Kovalenko, "Exploration of Near-Infrared-Emissive Colloidal Multinary Lead Halide Perovskite Nanocrystals Using an Automated Microfluidic Platform," *ACS Nano*, vol. 12, no. 6, pp. 5504–5517, 2018.

[87] A. Dualeh, P. Gao, S. I. Seok, M. K. Nazeeruddin, and M. Grätzel, "Thermal behavior of methylammonium lead-trihalide perovskite photovoltaic light harvesters," *Chem. Mater.*, vol. 26, no. 21, pp. 6160–6164, 2014.

[88] M. Sawicka, P. Storoniak, P. Skurski, J. Blazejowski, and J. Rak, "TG-FTIR, DSC and quantum chemical studies of the thermal decomposition of quaternary methylammonium halides," *Chem. Phys.*, vol. 324, no. 2-3, pp. 425–437, 2006.

[89] A. E. Williams, P. J. Holliman, M. J. Carnie, M. L. Davies, D. A. Worsley, and T. M. Watson, "Perovskite processing for photovoltaics: A spectro-thermal evaluation," *J. Mater. Chem. A*, vol. 2, no. 45, pp. 19338–19346, 2014.

[90] E. J. Juarez-Perez, Z. Hawash, S. R. Raga, L. K. Ono, and Y. Qi, "Thermal degradation of $CH_3NH_3PbI_3$ perovskite into NH_3 and CH_3I gases observed by coupled thermogravimetry-mass spectrometry analysis," *Energy Environ. Sci.*, vol. 9, no. 11, pp. 3406–3410, 2016.

[91] B. Conings, J. Drijkoningen, N. Gauquelin, A. Babayigit, J. D. Haen, L. D. Olieslaeger, A. Ethirajan, J. Verbeeck, J. Manca, E. Mosconi, F. D. Angelis, and H.-g. Boyen, "Intrinsic Thermal Instability of Methylammonium Lead Trihalide Perovskite," *Adv. Energy Mater.*, no. 1500477, 2015.

[92] Z. Fan, H. Xiao, Y. Wang, Z. Zhao, Z. Lin, H. Cheng, S.-j. Lee, G. Wang, Z. Feng, W. A. Goddard, Y. Huang, and X. Duan, "Layer-by-Layer Degradation of Methylammonium Lead Tri-iodide Perovskite Microplates," *Joule*, vol. 1, no. 3, pp. 548–562, 2017.

[93] I. C. Smith, E. T. Hoke, D. Solis-Ibarra, M. D. McGehee, and H. I. Karunadasa, "A Layered Hybrid Perovskite Solar-Cell Absorber with Enhanced Moisture Stability," *Angew. Chem. Int. Ed.*, vol. 53, no. 42, pp. 11232–11235, 2014.

[94] D. H. Cao, C. C. Stoumpos, O. K. Farha, J. T. Hupp, and M. G. Kanatzidis, "2D Homologous Perovskites as Light-Absorbing Materials for Solar Cell Applications," *J. Am. Chem. Soc.*, vol. 137, no. 24, pp. 7843–7850, 2015.

[95] A. Buin, R. Comin, J. Xu, A. H. Ip, and E. H. Sargent, "Halide-Dependent Electronic Structure of Organolead Perovskite Materials," *Chem. Mater.*, vol. 27, no. 12, pp. 4405–4412, 2015.

[96] A. S. Thind, X. Huang, J. Sun, and R. Mishra, "First-Principles Prediction of a Stable Hexagonal Phase of $CH_3NH_3PbI_3$," *Chem. Mater.*, vol. 29, no. 14, pp. 6003–6011, 2017.

[97] D. Ferdani, S. Pering, D. Ghosh, P. Kubiak, A. Walker, S. E. Lewis, A. L. Johnson, P. J. Baker, S. Islam, and P. J. Cameron, "Partial Cation Substitution Reduces Iodide Ion Transport in Lead Iodide Perovskite Solar Cells," *Energy Environ. Sci.*, vol. 12, p. 2264, 2019.

[98] M. Kulbak, S. Gupta, N. Kedem, I. Levine, T. Bendikov, G. Hodes, and D. Cahen, "Cesium Enhances Long-Term Stability of Lead Bromide Perovskite-Based Solar Cells," *J. Phys. Chem. Lett.*, vol. 7, no. 1, pp. 167–172, 2016.

[99] J. Yang, B. D. Siempelkamp, E. Mosconi, F. De Angelis, and T. L. Kelly, "Origin of the Thermal Instability in $CH_3NH_3PbI_3$ Thin Films Deposited on ZnO," *Chem. Mater.*, vol. 27, no. 12, pp. 4229–4236, 2015.

[100] G. Divitini, S. Cacovich, F. Matteocci, L. Cinà, A. Di Carlo, and C. Ducati, "In situ observation of heat-induced degradation of perovskite solar cells," *Nat. Energy*, vol. 1, jan 2016.

[101] M. Jorgensen, K. Norrman, S. A. Gevorgyan, T. Tromholt, B. Andreasen, and F. C. Krebs, "Stability of polymer solar cells," *Adv. Mater.*, vol. 24, no. 5, pp. 580–612, 2012.

[102] A. K. Jena, M. Ikegami, and T. Miyasaka, "Severe Morphological Deformation of Spiro-OMeTAD in $(CH_3NH_3)PbI_3$ Solar Cells at High Temperature," *ACS Energy Lett.*, vol. 2, no. 8, pp. 1760–1761, 2017.

[103] N. J. Jeon, H. Na, E. H. Jung, T.-Y. Yang, Y. G. Lee, G. Kim, H.-W. Shin, S. Il Seok, J. Lee, and J. Seo, "A fluorene-terminated hole-transporting material for highly efficient and stable perovskite solar cells," *Nat. Energy*, vol. 3, no. 8, pp. 682–689, 2018.

[104] Y. Tian, M. Peter, E. Unger, M. Abdellah, K. Zheng, T. Pullerits, A. Yartsev, V. Sundström, and I. G. Scheblykin, "Mechanistic insights into perovskite photoluminescence enhancement: light curing with oxygen can boost yield thousandfold," *Phys. Chem. Chem. Phys.*, vol. 17, no. 38, pp. 24978–24987, 2015.

[105] D. W. DeQuilettes, W. Zhang, V. M. Burlakov, D. J. Graham, T. Leijtens, A. Osherov, V. Bulović, H. J. Snaith, D. S. Ginger, and S. D. Stranks, "Photo-induced halide redistribution in organic-inorganic perovskite films," *Nat. Commun.*, vol. 7, p. 11683, 2016.

[106] S. D. Stranks, V. M. Burlakov, T. Leijtens, J. M. Ball, A. Goriely, and H. J. Snaith, "Recombination Kinetics in Organic-Inorganic Perovskites : Excitons , Free Charge , and Subgap States," *Phys. Rev. Appl*, vol. 2, p. 034007, 2014.

[107] E. T. Hoke, D. J. Slotcavage, E. R. Dohner, A. R. Bowring, H. I. Karunadasa, and M. D. Mcgehee, "Reversible photo-induced trap formation in mixed-halide hybrid perovskites for photovoltaics," *Chem. Sci.*, vol. 6, pp. 613–617, 2015.

[108] S. G. Motti, M. Gandini, A. J. Barker, J. M. Ball, A. R. Srimath Kandada, and A. Petrozza, "Photoinduced Emissive Trap States in Lead Halide Perovskite Semiconductors," *ACS Energy Lett.*, vol. 1, no. 4, pp. 726–730, 2016.

[109] E. Mosconi, D. Meggiolaro, H. J. Snaith, S. D. Stranks, and F. De Angelis, "Light-induced annihilation of Frenkel defects in organo-lead halide perovskites," *Energy Environ. Sci.*, vol. 9, p. 3180, 2016.

[110] S. G. Motti, D. Meggiolaro, A. J. Barker, E. Mosconi, C. A. R. Perini, J. M. Ball, M. Gandini, M. Kim, F. De Angelis, and A. Petrozza, "Controlling competing photochemical reactions stabilizes perovskite solar cells," *Nat. Photonics*, vol. 13, pp. 532–539, 2019.

[111] D. W. de Quilettes, S. M. Vorpahl, S. D. Stranks, H. Nagaoka, G. E. Eperon, M. E. Ziffer, H. J. Snaith, and D. S. Ginger, "Impact of microstructure on local carrier lifetime in perovskite solar cells," *Science*, vol. 348, no. 6235, pp. 683–686, 2015.

[112] D. W. Dequilettes, S. Koch, S. Burke, R. K. Paranji, A. J. Shropshire, M. E. Ziffer, and D. S. Ginger, "Photoluminescence Lifetimes Exceeding 8 μs and Quantum Yields Exceeding 30% in Hybrid Perovskite Thin Films by Ligand Passivation," *ACS Energy Lett.*, vol. 1, no. 2, pp. 438–444, 2016.

[113] R. Brenes, C. Eames, V. Bulović, M. S. Islam, and S. D. Stranks, "The Impact of Atmosphere on the Local Luminescence Properties of Metal Halide Perovskite Grains," *Adv. Mater.*, vol. 30, no. 15, pp. 1–8, 2018.

[114] N. Aristidou, I. Sanchez-Molina, T. Chotchuangchutchaval, M. Brown, L. Martinez, T. Rath, and S. A. Haque, "The Role of Oxygen in the Degradation of Methylammonium Lead Trihalide Perovskite Photoactive Layers," *Angew. Chem. Int. Ed.*, vol. 54, no. 28, pp. 8208–8212, 2015.

[115] A. D. Sheikh, A. Bera, A. Haque, R. B. Rakhi, S. Del, H. N. Alshareef, and T. Wu, "Atmospheric effects on the photovoltaic performance of hybrid perovskite solar cells," *Sol. Energy Mater. Sol. Cells*, vol. 137, pp. 6–14, 2015.

[116] N. Aristidou, C. Eames, I. Sanchez-molina, X. Bu, J. Kosco, M. S. Islam, and S. A. Haque, "Fast oxygen diffusion and iodide defects mediate oxygen-induced degradation of perovskite solar cells," *Nat. Commun.*, vol. 8, no. May, pp. 1–40, 2017.

[117] Y. Kato, L. K. Ono, M. V. Lee, S. Wang, S. R. Raga, and Y. Qi, "Silver Iodide Formation in Methyl Ammonium Lead Iodide Perovskite Solar Cells with Silver Top Electrodes," *Adv. Mater. Interfaces*, vol. 2, no. 13, pp. 2–7, 2015.

[118] J. Li, Q. Dong, N. Li, and L. Wang, "Direct Evidence of Ion Diffusion for the Silver-Electrode-Induced Thermal Degradation of Inverted Perovskite Solar Cells," *Adv. Energy Mater.*, vol. 7, no. 14, pp. 1–8, 2017.

[119] C. C. Boyd, R. Cheacharoen, K. A. Bush, R. Prasanna, T. Leijtens, and M. D. McGehee, "Barrier Design to Prevent Metal-Induced Degradation and Improve Thermal Stability in Perovskite Solar Cells," *ACS Energy Lett.*, vol. 3, no. 7, pp. 1772–1778, 2018.

[120] K. Domanski, J. P. Correa-Baena, N. Mine, M. K. Nazeeruddin, A. Abate, M. Saliba, W. Tress, A. Hagfeldt, and M. Grätzel, "Not All That Glitters Is Gold: Metal-Migration-Induced Degradation in Perovskite Solar Cells," *ACS Nano*, vol. 10, no. 6, pp. 6306–6314, 2016.

[121] K. Brinkmann, J. Zhao, N. Pourdavoud, T. Becker, T. Hu, S. Olthof, K. Meerholz, L. Hoffmann, T. Gahlmann, R. Heiderhoff, M. F. Oszajca, N. A. Luechinger, D. Rogalla, Y. Chen, B. Cheng, and T. Riedl, "Suppressed decomposition of organometal halide perovskites by impermeable electron-extraction layers in inverted solar cells," *Nat. Commun.*, vol. 8, p. 13938, 2017.

[122] T. Hu, T. Becker, N. Pourdavoud, J. Zhao, K. O. Brinkmann, R. Heiderhoff, T. Gahlmann, Z. Huang, S. Olthof, K. Meerholz, D. Többens, B. Cheng, Y. Chen, and T. Riedl, "Indium-Free Perovskite Solar Cells Enabled by Impermeable Tin-Oxide Electron Extraction Layers," *Adv. Mater.*, vol. 29, p. 1606656, 2017.

[123] H. Lakhiani, T. Dunlop, F. De Rossi, S. Dimitrov, R. Kerremans, C. Charbonneau, T. Watson, J. Barbé, and W. C. Tsoi, "Variations of Infiltration and Electronic Contact in Mesoscopic Perovskite Solar Cells Revealed by High-Resolution Multi-Mapping Techniques," *Adv. Funct. Mater.*, vol. 1900885, pp. 1–10, 2019.

[124] H. Chen and S. Yang, "Carbon-Based Perovskite Solar Cells without Hole Transport Materials : The Front Runner to the Market ?," *Adv. Mater.*, vol. 29, p. 1603994, 2017.

[125] F. Matteocci, L. Cinà, E. Lamanna, S. Cacovich, G. Divitini, P. A. Midgley, C. Ducati, and A. Di Carlo, "Encapsulation for long-term stability enhancement of perovskite solar cells," *Nano Energy*, vol. 30, pp. 162–172, 2016.

[126] C. Acar and I. Dincer, "Comparative assessment of hydrogen production methods from renewable and non-renewable sources," *Int. J. Hydrog. Energy*, vol. 39, pp. 1–12, 2014.

[127] J. R. McKone, N. S. Lewis, and H. B. Gray, "Will solar-driven water-splitting devices see the light of day?," *Chem. Mater.*, vol. 26, no. 1, pp. 407–414, 2014.

[128] K. Sivula and R. Van De Krol, "Semiconducting materials for photoelectrochemical energy conversion," *Nat. Rev. Mater.*, vol. 1, no. 15010, 2016.

[129] H. Dotan, N. Mathews, T. Hisatomi, M. Grätzel, and A. Rothschild, "On the solar to hydrogen conversion efficiency of photoelectrodes for water splitting," *J. Phys. Chem. Lett.*, vol. 5, no. 19, pp. 3330–3334, 2014.

[130] C. Jiang, S. J. A. Moniz, A. Wang, T. Zhang, and J. Tang, "Photoelectrochemical devices for solar water splitting-materials and challenges," *Chem. Soc. Rev.*, vol. 46, p. 4645, 2017.

[131] L. M. Peter and K. G. Upul Wijayantha, "Photoelectrochemical water splitting at semiconductor electrodes: Fundamental problems and new perspectives," *ChemPhysChem*, vol. 15, no. 10, pp. 1983–1995, 2014.

[132] X. Liu, F. Wang, and Q. Wang, "Nanostructure-based WO_3 photoanodes for photoelectrochemical water splitting," *Phys. Chem. Chem. Phys.*, vol. 14, no. 22, pp. 7894–7911, 2012.

[133] S. Kment, F. Riboni, S. Pausova, L. Wang, L. Wang, H. Han, Z. Hubicka, J. Krysa, P. Schmuki, and R. Zboril, "Photoanodes based on TiO_2 and α-Fe_2O_3 for solar water splitting-superior role of 1D nanoarchitectures and of combined heterostructures," *Chem. Soc. Rev.*, vol. 46, pp. 3716–3769, 2017.

[134] H. S. Han, S. Shin, D. H. Kim, I. J. Park, J. S. Kim, P. S. Huang, J. K. Lee, I. S. Cho, and X. Zheng, "Boosting the solar water oxidation performance of

a $BiVO_4$ photoanode by crystallographic orientation control," *Energy Environ. Sci.*, vol. 11, no. 5, pp. 1299–1306, 2018.

[135] W. Yang and J. Moon, "Recent Advances in Earth-Abundant Photocathodes for Photoelectrochemical Water Splitting," *ChemSusChem*, pp. 1889–1899, 2018.

[136] M. S. Prévot, N. Guijarro, and K. Sivula, "Enhancing the Performance of a Robust Sol-Gel-Processed p-Type Delafossite $CuFeO_2$ Photocathode for Solar Water Reduction," *ChemSusChem*, vol. 8, no. 8, pp. 1359–1367, 2015.

[137] M. Regue, K. Armstrong, D. Walsh, A. L. Johnson, S. Eslava, and E. Richards, "Mo-doped TiO2 photoanodes using $[Ti_4Mo_2O_8(OEt)_{10}]_2$ bimetallic oxo cages as a single source precursor," *Sustain. Energ. Fuels*, vol. 2, pp. 2674–2686, 2018.

[138] J. W. Moir, E. V. Sackville, U. Hintermair, and G. A. Ozin, "Kinetics versus Charge Separation: Improving the Activity of Stoichiometric and Non-Stoichiometric Hematite Photoanodes Using a Molecular Iridium Water Oxidation Catalyst," *J. Phys. Chem. C*, vol. 120, no. 24, pp. 12999–13012, 2016.

[139] Y. J. Jang, Y. B. Park, H. E. Kim, Y. H. Choi, S. H. Choi, and J. S. Lee, "Oxygen-Intercalated $CuFeO_2$ Photocathode Fabricated by Hybrid Microwave Annealing for Efficient Solar Hydrogen Production," *Chem. Mater.*, vol. 28, no. 17, pp. 6054–6061, 2016.

[140] M. Crespo Quesada and E. Reisner, "Emerging Approaches to Stabilise Photocorrodible Electrodes and Catalysts for Solar Fuel Applications," *Energy Environ. Sci.*, vol. 10, pp. 1116–1127, 2017.

[141] M. Crespo-Quesada, L. M. Pazos-Outón, J. Warnan, M. F. Kuehnel, R. H. Friend, and E. Reisner, "Metal-encapsulated organolead halide perovskite photocathode for solar-driven hydrogen evolution in water," *Nat. Commun.*, vol. 7, p. 12555, 2016.

[142] S. Nam, C. T. K. Mai, and I. Oh, "Ultrastable Photoelectrodes for Solar Water Splitting Based on Organic Metal Halide Perovskite Fabricated by Lift-Off Process," *ACS Appl. Mater. Interfaces*, vol. 10, no. 17, pp. 14659–14664, 2018.

[143] R. Tao, Z. Sun, F. Li, W. Fang, and L. Xu, "Achieving Organic Metal Halide Perovskite into a Conventional Photoelectrode: Outstanding Stability in Aqueous Solution and High-Efficient Photoelectrochemical Water Splitting," *ACS Appl. Energy Mater.*, vol. 2, pp. 1969–1976, 2019.

Chapter 2

Methodology and Theory

Different techniques have been developed to fabricate perovskite solar cells, including one-step and two-step spin-coating, solvent-assisted solution processes, dual-source vacuum deposition and sequential vapour deposition. Once fabricated, perovskite thin films and devices can be electrically and optically characterised through many different techniques. A brief theoretical background of the semiconductors used in photovoltaic applications, and more specifically of perovskites, will be provided in this chapter, together with an overview of the fabrication and characterisation methods used in this work. Section 2.1 will introduce the semiconductor physics and optoelectronic properties of perovskites. Section 2.2 will list all experimental procedures used to fabricate perovskite thin films and full devices. Finally, section 2.3 will give a brief theoretical background of the characterisation techniques used to measure the properties of perovskite materials and devices.

2.1 Theory

2.1.1 Electronic structure

When two atoms are put together into a molecule, their atomic orbitals (AO) combine to form pairs of molecular orbitals (MO), with energies that are higher and lower than the initial energy levels (figure 2.1 a). In a solid, large number of atoms come together, forming many MO very close in energy to effectively form a band (figure 2.1 b). The highest occupied band that contains valence electrons is called the valence band (VB), while the lowest unoccupied band is called the conduction band (CB). The VB and CB are separated by a forbidden energy gap, called energy band gap E_g. [1]

The density of states that describe the valence and conduction bands are usually complicated functions (sketch in figure 2.1 c), which approach simple parabolic functions near the edges (figure 2.1 d). For simplicity, the band diagram is usually represented with flat conduction and valence bands near the surface. [2] The band

structure of a semiconductor can form either a direct or an indirect bandgap depending on the conservation of the momentum. For example, silicon is an indirect bandgap semiconductor, which means that the bottom of the CB and the top of the VB are not aligned, therefore they have different electron crystal momentum. [3] In contrast, GaAs is a direct bandgap semiconductor and the bottom of the CB and the top of the VB lie for the same momentum. [4] Several experimental data and computational calculations determined that halide perovskites are commonly direct bandgap semiconductors. [5, 6, 7] However, this property has been recently questioned and evidence of a slightly indirect bandgap in halide perovskites has now become widely accepted. [8, 9]

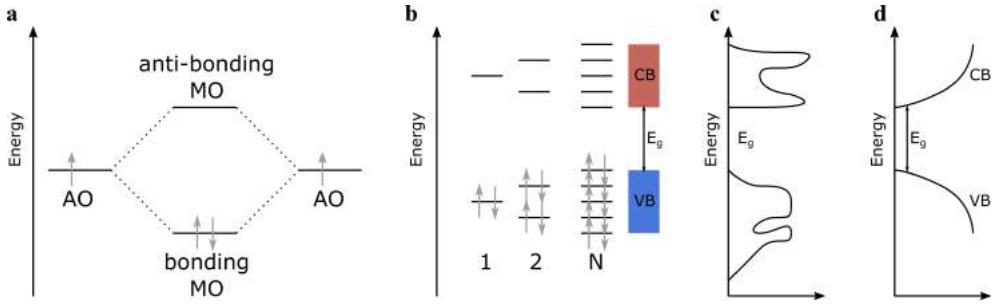

Figure 2.1: a Combination of two atomic orbitals to form pairs of molecular orbitals. **b** N atomic orbitals split to form bands. **c** Sketch of the density of states for a semiconductor. **d** Parabolic approximation of VB and CB near band edges.

The electrons in the valence band are involved in chemical bondings, therefore they require at least an energy equivalent to the energy bandgap to be removed from the VB and jump to the nearest unoccupied level in the CB. When an electron is removed from the VB, a positively charged vacancy is left behind. If the vacancy is filled by an electron involved in a neighbouring bond, the vacancy moves. The movement of valence electrons is therefore equivalent to a movement of positive holes, which can be characterised with mobility and mass in the same way as conduction electrons. Conventionally, it is said that the absorption of photons with energy higher than E_g leads to the excitation of electron-hole pairs.

The occupation of the bands follow the Fermi-Diract distribution, and the probability of finding an electron in a band with energy E, at a certain temperature T is given by:

$$f(E) = \frac{1}{1 + \exp(\frac{E - E_F}{k_B T})} \tag{2.1}$$

E_F is the Fermi level and k_B is the Boltzmann constant. The Fermi level is the energy state with $50\,\%$ chance of being occupied by an electron. The work function (WF) of a material is an important parameter for electronic materials. It is the energy required to remove the least tightly bound electron to a state corresponding to a free electron in the vacuum and it is defined by:

$$WF = E_{vac} - E_F \tag{2.2}$$

E_{vac} is the energy level of a free electron in the vacuum (at rest, positioned outside the solid material considered). [10] The energy Fermi level position depends upon doping. In the ideal ground state of an intrinsic semiconductor at a temperature of 0 K, the E_F lies exactly in the center of the bandgap, the *VB* is completely filled up and the *CB* completely empty. A p-type semiconductor is defined as a material where the majority carriers are holes and electrons are the minority carriers. In this case, the Fermi energy level is closer to the VB. In contrast, in n-type semiconductors, the majority carriers are electrons and the Fermi level is closer to the CB. Consequently, the WF of a p-type semiconductor is larger than the WF of a n-type semiconductor (figure 2.2 a).

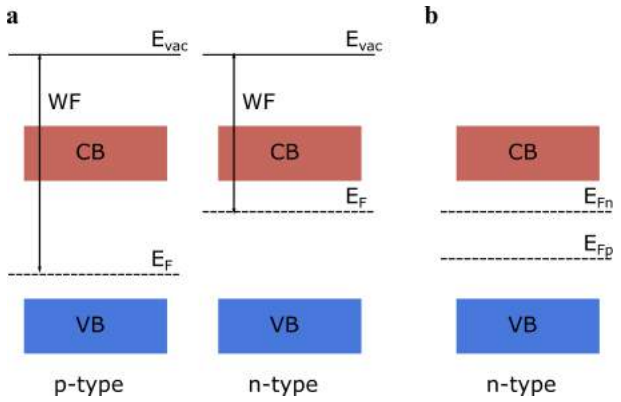

Figure 2.2: a Fermi energy levels and WF in p-type and n-type semiconductors. **b** Splitting of the Fermi energies in quasi-Fermi energies upon illumination.

The generation of electron-hole pairs under illumination perturbs the thermal equilibrium described by the Fermi energy. Indeed, the concentrations of holes and electrons under illumination depend on the rates at which electron-hole pairs are generated and recombine (see section 2.1.3 for recombination processes) and the distribution of electrons and holes can be described by quasi-Fermi energies E_{Fn} and E_{Fp}. As illustrated in figure 2.2 b for a n-type semiconductor, the Fermi level for the majority carriers (electrons) remains essentially the same, while the Fermi energy of the minority carriers (holes) is considerably affected by illumination. The difference between the quasi Fermi energies gives the energy of electron-hole pairs.

2.1.2 Absorption

The absorption of a photon with energy $E \geq E_g$ induces the excitation of one electron from the VB to the CB, resulting in a free electron in the conduction band and a free hole in valence band. Immediately after the absorption, the photogenerated carriers are out of equilibrium and free electrons and holes quickly thermalise to the conduction and valence band edges to reach the equilibrium. After this first

regime of relaxation, the excess photogenerated carriers return to the ground state via radiative or non-radiative recombination processes, which will be explained in detail in the next section.

The free electron-hole pair generation is not the only absorption mechanism present in perovskite semiconductors. Another possible photoexcitation is given by excitonic absorption. [11] An exciton is a quasi-particle resulting from the Coulomb interaction between an electron and hole pair. The magnitude of the Coloumb attraction between the positive and the negative charge is indicated by the exciton binding energy E_b. E_b in perovskites ranges between 2 and $60\,\mathrm{meV}$ and it is higher in wide bandgap materials like $MAPbBr_3$ and $MAPbCl_3$ than $MAPbI_3$. [11]

Excitonic absorption results in an absorption enhancement which is beneficial for solar light harvesting and PV applications. [12, 13] However, the exciton binding energies reported for halide perovskites are still low enough to let free carriers to prevail over bound exciton transmission at room temperature, therefore the population of excitons in the solar cell operating regime at room temperature is usually neglected. [14]

2.1.3 Recombination mechanisms

After generation and relaxation of carriers to the band edges (figure 2.3 a), the system relaxes back to the ground state through an electron-hole recombination process. Such recombination can occur through a radiative or a non-radiative process. In a radiative recombination mechanism (figure 2.3 b) the energy resulting from the recombination of an electron-hole pair is released in a form of a photon with energy E=$h\nu$. This process is a bimolecular recombination because two carriers (an electron and a hole) are needed. Radiative recombination can be directly observed as photoluminescence (PL), and for a direct bandgap semiconductor the energy of the emitted photons is centred right at the bandgap E_g.

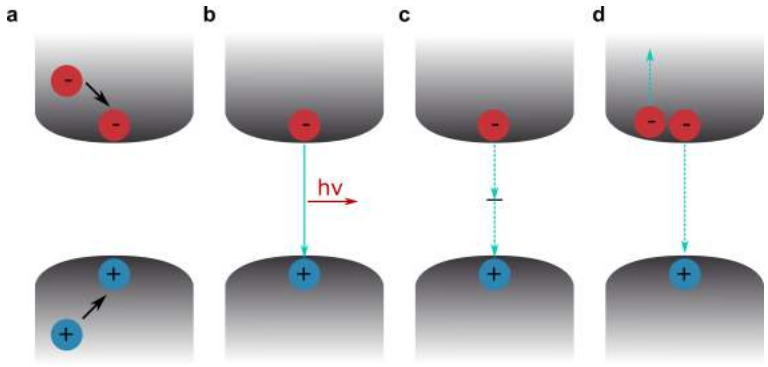

Figure 2.3: a Thermalisation of electron and hole carriers after photoexcitation. **b** Carrier decay to the ground state by radiative recombination. **c** Carrier decay to the ground state trap-assisted recombination (Shockley-Read-Hall recombination). **d** Carrier decay to the ground state by Auger recombination.

Non-radiative recombination processes are trap-assisted (figure 2.3 c) and Auger recombination (figure 2.3 d). Trap-assisted recombination, also known as Shockley-Read-Hall (*SRH*), occurs when a carrier gets trapped in an intra-gap energy state and then recombines with a carrier of opposite charge. This process is a monomolecular decay mechanism because it requires only one carrier (either positive or negative) to get trapped/released. Finally, Auger recombination involves three different charges: the energy from the recombination of an electron-hole pair is transferred to a third charge, which is excited to a higher state. This excess energy is then released in a form of heat through thermalisation.

At low excitation densities, the photoexcited carriers recombine mainly through interactions with sub-bandgap trapping states at a monomolecular rate. At higher excitation densities, these traps saturate and the bimolecular band-to-band radiative recombination becomes the dominant decay. Finally at very high excitaton densities the three body interaction becomes more probable and Auger recombination becomes the dominant decay process. The time dependent carrier depopulation in a semiconductor can be described with: [15]

$$\frac{dn}{dt} = -k_1 n - k_2 n^2 - k_3 n^3 \tag{2.3}$$

n is the photoexcited carrier density, k_1, k_2 and k_3 are the monomolecular, bimolecular and three-body recombination rate constant, respectively. These recombination rates can be experimentally calculated by using time-resolved photoluminescence spectroscopy techniques. [13]

2.1.4 Defects

Defects in semiconductors are identified as crystallographic defects, which means interruptions to a perfect crystal lattice and impurities (foreign atoms in the lattice). Figure 2.4 a is an illustration of a perfect perovskite crystal lattice, while figure 2.4 b-d show different point crystallographic defects: vacancies, interstitials and anti-site substitutions, respectively.

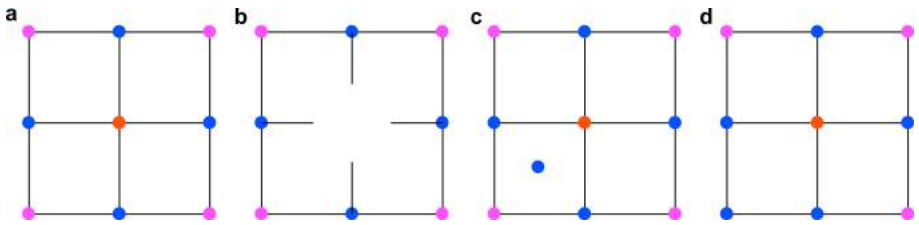

Figure 2.4: Illustration of perovskite crystal lattice with orange, pink and blue dots representing A-, B- and X-site ions, respectively. **a** Perfect lattice. **b** Atomic vacancy, atom is missing from the lattice **c** Interstitial, atom is occupying the space between atoms in the lattice. **d** Anti-site substitutions, atom is occupying the wrong site in the lattice.

Other defects that can be found in ionic crystals are Frenkel defects, a vacancy and an interstitial of the same ion in a unit cell, and Schottky defects, two vacancies

of oppositely charged ions in a unit cell. [16] Conventionally, defects can be studied by calculating their theoretical enthalpy of formation using density functional theory (DFT) calculations. The formation energy of defects is calculated by taking into account both the chemical energy required to form a defect and the energy associated with the exchange of electrons with the Fermi level of the sysytem. If a defect is located within the semiconductor bandgap, it can act as a trapping state, being detrimental for the photovoltaic performance of the semiconductor. [17] In fact, trap defects can significantly contribute to non-radiative recombination processes, which are strictly related to the open circuit voltage of the solar cell. [18]

The density of trap states in halide perovskites have been calculated to be between 1×10^{15} and $1 \times 10^{16}\,\mathrm{cm}^{-3}$. [19] These numbers are considerably higher than the values reported for polycrystalline silicon, which instead range between 1×10^{13} and $1 \times 10^{14}\,\mathrm{cm}^{-3}$. [20] Halide perovskites are indeed known to be highly defect tolerant. One explanation may be that many defects have energy levels which are very close to the conduction and valence band edges, acting as shallow trap defects. [21] Meggiolaro *et al.* recently reported that among all native point defects in perovskites, the only one that may act as a deep trap is interstitial iodine. [17]
Confocal photoluminescence and scanning electron microscopy have been used to study the structure and homogeneity of perovskite films, revealing that grain boundaries act as reservoir of defects and exhibit faster non-radiative decay. [22]. Recently, it was found that also strained regions in films act as driving force for defect formation, considerably reducing the local carrier lifetime. [23] For example, one of the reasons causing the generation of local strains in perovskite films is the cubic-to-tetragonal phase transition occurring at $57\,^{\circ}\mathrm{C}$. [24]

2.1.5 Semiconductor junctions

Semiconductor junctions are very important to separate charges in many electronic devices, including solar cells. The simplest type of junction is the semiconductor-metal contact, also known as Schottky barrier. [1] Figure 2.5 a and b shows the band energies of a n-type semiconductor and a metal in isolation and when they are brought together, respectively. When the two materials are isolated, the Fermi levels are independent from each other, while when they are put together, the Fermi levels line up. If the work function of the metal is higher than the one of the semiconductor, electrons will spontaneously move from the semiconductor to the metal, leaving a layer of fixed positive space charges near the surface, until thermal equilibrium is reached. The region where the semiconductor carries a net fixed charge is defined as space charge region. At this point an electrostatic field exists, which results in effective charge separation, driving electrons to the left and holes to the right.

A barrier similar to the Schottky barrier can be established at the interface between a semiconductor and a liquid electrolyte. If the electrolyte contains a redox couple, the electronic equilibrium described above can be achieved by electron transfer across the semiconductor/electrolyte interface (one-electron reaction:

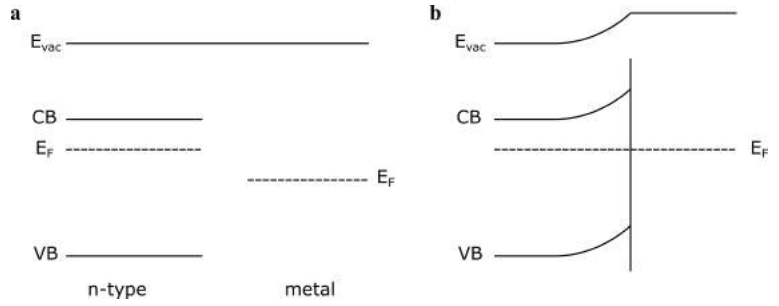

Figure 2.5: a Band profiles of n-type semiconductor and a metal in isolation. **b** Band profiles of the n-type semiconductor-metal junction at equilibrium.

O+e^- $\rightarrow$R). Like metals, the redox couple has a Fermi level ($E_{F,redox}$), which can be defined in terms of chemical potentials:

$$E_{F,redox} = (\mu_R^0 - \mu_O^0) - k_B T ln \left[\frac{N_R}{N_O}\right] \tag{2.4}$$

$(\mu_R^0 - \mu_O^0)$ is the difference between the standard chemical potentials of reactants and products, k_B is the Boltzmann constant, T is the temperature and N_R and N_O are the number densities of reactants and products, respectively. [2] Under equilibrium, the charge in the space charge region is balanced by an ionic charge of opposite sign in the electrolyte, developed in a region called the Helmholtz layer.

2.1.6 Photoelectrochemical process

When photons with energy $> E_g$ are absorbed, electrons are excited creating electron hole pairs. Under illumination, the local concentrations of holes and electrons are perturbed from the equilibrium (dark) giving rise to a splitting of the Fermi level. At this point, assuming a n-type semiconductor is in contact with an electrolyte, electrons flow through the junction from the species R to the semiconductor and a photocurrent is produced. Such photocurrent will depend on the generation, collection and reaction of holes in the junction regions. In the ideal case, where all holes generated in the space charge reach the surface and fast reaction at the surface occurs, three important length scales can be defined to describe the generation-collection and generation-recombination problem (as illustrated in figure 2.6 a).

α^{-1} is the wavelength dependent penetration depth of the incident light, W_{sc} is the space charge width and L_{min} is the minority carrier diffusion length, which can be calculated as:

$$L_{min} = \sqrt{D_{min}\tau_{min}} = \sqrt{\frac{k_B T}{q}\mu_{min}\tau_{min}} \tag{2.5}$$

D_{min} is the diffusion coefficient, μ_{min} is the mobility and τ_{min} is the minority carrier lifetime. If holes are generated within the space charge region, they drift to the surface where they accept electrons from the species R. If carriers are generated within

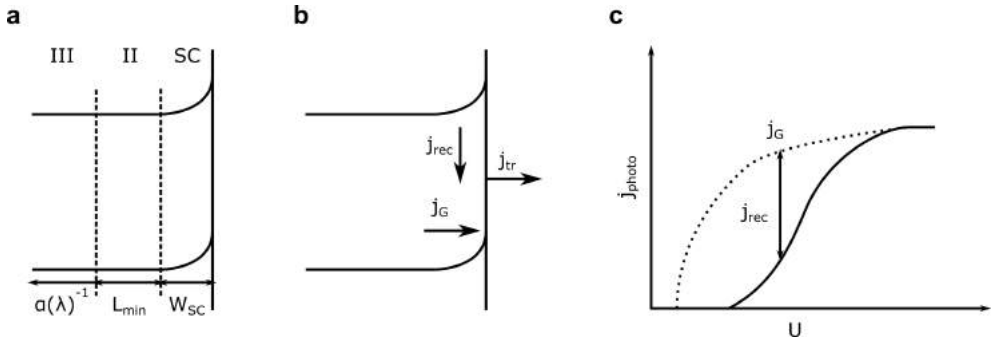

Figure 2.6: **a** Characteristic length scale important to solve the generation-recombination generation-collection problem in an ideal case (no recombination in the space charge and at the surface). **b** Simple kinetic scheme describing the competition between the arrival of holes at the surface and their removal after recombination in the space charge and at the surface and in the transfer process. Figure adapted from [25]. **c** Sketch of the delayed onset of photocurrent density due to the recombination in the space charge region and at the surface (solid line). Dotted line shows the photocurrent density in the ideal case where recombination in the space charge and at the surface is neglected.

region II, holes diffuse to the space charge region before recombining. If light penetrates and is absorbed in region III, electron-hole pairs recombine before reaching the space charge region. [26]

The assumptions made above are not valid in real systems, where recombination at the surface and in the space charge play an important role. All real semiconductors contain defect sites, such as impurities or imperfections, which cause localised energy levels, where carriers can be trapped. Slow reactions cause build-up of charges at the interface and recombination becomes dominant, especially for low band bending. [27] Figure 2.6 b shows a simple kinetic scheme of the hole concentration involved in the redox reaction, which is determined by the difference between the holes rate of arrival (j_G) and their rate of removal by recombination (j_{rec}) and transfer (J_{tr}). Both surface recombination and recombination in the space charge cause a delay in the onset of the photocurrent, as sketched in figure 2.6 c.

2.2 Experimental section

2.2.1 Device fabrication

Devices were built on FTO coated glass (TEC 7 and TEC 15, Sigma-Aldrich). Prior deposition, substrates were etched with Zn powder (99%, Sigma-Aldrich) and 2 M HCl. Substrates were cleaned in 2 vol% Hellmanex solution in DI water, DI water, acetone, isopropyl alcohol (IPA) and ethanol, the slides were placed in each solution for 15 minutes and sonicated. The cleaned FTO coated glass substrates were treated with UV-ozone cleaner for $20\,\mathrm{min}$ before any further deposition. Samples were prepared inside the drybox under N_2 atmosphere (unless differently specified).

Photovoltaic solar cells

This work focused on mesoporous standard devices and planar standard and inverted devices. The photoactive material was placed between the charge-selective transport layers. On top of the final transporting layers, metal contacts were thermally evaporated ($100\,\mathrm{nm}$, Au in standard devices and Ag in inverted devices) using an evaporation mask to have 6 pixels of $0.0625\,\mathrm{cm}^2$. In planar carbon solar cells, Ag paste was used to create the contact. The methods for preparing the photoactive perovskite material, ETM and HTM are described below.

Photoanodes

Photoanodes were built as planar carbon solar cells. A graphite thermal sheet (RS, Panasonic, $1600\,\mathrm{W\,m^{-1}\,K^{-1}}$, 180 x $115\,\mathrm{mm}$, $0.025\,\mathrm{mm}$, self-adhesive on one side) was stuck by hand onto the mesoporous carbon top layer. The device was sealed (except an active area of $0.25\,\mathrm{cm}^2$) with commercial silicone and epoxy resin left to harden out at room temperature overnight.

2.2.2 Materials

Organic solvents (methanol, acetone, IPA and ethanol) were purchased from VWR. Deionized water was supplied from a centralised purification system (Dept. of Chemistry, Bath University). All chemicals were purchased from major commercial suppliers and were used without any further purification.

Electron transport layers

TiO_2 Compact TiO_2 layer was deposited by spray pyrolysis, using a hand held atomiser. 0.2 M solution of titanium diisopropoxide bis(acetylacetonate) (75 wt%, Sigma-aldrich) in ethanol was sprayed onto the substrates held at $500\,^\circ\mathrm{C}$ (one spray every $30\,\mathrm{s}$ for 10 times). Substrates were then annealed at this temperature for $10\,\mathrm{min}$. Mesoporous TiO_2 layer (2:7 weight mixture of Dyesol's 30NRD TiO_2 paste in ethanol) was spun onto the TiO_2 compact layer (6000 rpm for $45\,\mathrm{s}$) and annealed for $15\,\mathrm{min}$ on a hot plate and further $30\,\mathrm{min}$ at $500\,^\circ\mathrm{C}$ in air.

SnO_2 SnO_2 solution was prepared by mixing Tin(IV) oxide in H_2O colloidal dispersion (Afla Aesar) in DI H_2O (volume ration 1:5) and sonicated for $10\,\mathrm{min}$. The solution was then filtered through a $0.22\,\mu\mathrm{m}$ filter and spun onto the substrates at 3000 rpm for $30\,\mathrm{s}$. Substrates were then annealed at $180\,^\circ\mathrm{C}$ for $1\,\mathrm{h}$.

PCBM When used as ETM in inverted devices, a $20\,\mathrm{mg\,ml^{-1}}$ solution of PCBM (95%, Ossila) in chlorobenzene (anhydrous, Sigma-Aldrich) was stirred at $60\,^\circ\mathrm{C}$ to ensure complete dissolution and filtered through a $0.45\,\mu\mathrm{m}$ PTFE filter prior use. Solution was spun onto the perovskite film at 3000 rpm for $30\,\mathrm{s}$ and left dry at room

temperature. $0.5\,\mathrm{mg\,ml^{-1}}$ solution of bathocuproine (96%, Sigma-Aldrich) in ethanol was spun onto the PCBM film at 6000 rpm for $30\,\mathrm{s}$.
When used as interlayer on top of SnO_2 in standard devices, a $10\,\mathrm{mg\,ml^{-1}}$ solution of $PC_{70}BM$ in chlorobenzene was spun onto the SnO_2 film at 6000 rpm for $30\,\mathrm{s}$ and left dry at room temperature.

Hole transport layers

Spiro A $73\,\mathrm{mg\,ml^{-1}}$ solution of spiro-OMeTAD (Sigma-Aldrich) in anhydrous chlorobenzene was stirred at $60\,^{\circ}\mathrm{C}$ to ensure complete dissolution. $28.8\,\mu\mathrm{l\,ml^{-1}}$ of 4-*tert*-butyl pyridine (96%, Sigma-Aldrich) and $17.5\,\mu\mathrm{l\,ml^{-1}}$ of Li-TFSI solution ($520\,\mathrm{mg}$ LiTFSI in $1\,\mathrm{ml}$ acetonitrile, 99.8%, Sigma-Aldrich) were added to the solution prior use. Spiro-OMeTAD was spin coated onto the perovskite film at 4000 rpm for $30\,\mathrm{s}$.

NiO_x A 0.2 M solution of nickel acetate tetrahydrate (98%, Sigma-Aldrich) in 2-methoxyethanol was prepared and stirred at $60\,^{\circ}\mathrm{C}$ until complete dissolution. $12\,\mu\mathrm{l\,ml^{-1}}$ of ethanolamine (ACS reagent, Sigma-Aldrich) was added to the solution, which was then filtered using a $0.45\,\mu\mathrm{m}$ PTFE filter. NiO_x was spin coated onto the substrates at 4000 rpm for 30 s and annealed at $400\,^{\circ}\mathrm{C}$ for $30\,\mathrm{min}$.

m-carbon The carbon paste used to make mesoporous carbon layers was given by our collaborators SPECIFIC, Swansea University (Gwent Electronic Materials). When planar devices were fabricated, the carbon paste was doctor bladed onto the perovskite film and annealed at $380\,^{\circ}\mathrm{C}$ for $30\,\mathrm{min}$. In mesoporous devices it was screen printed onto ZrO_2 films and sintered at $400\,^{\circ}\mathrm{C}$ for $30\,\mathrm{min}$.

Perovskite absorber films

$CH_3NH_3PbI_3$ Two different recipes were used to deposit $CH_3NH_3PbI_3$ films depending on whether the antisolvent treatment was used. Perovskite deposition was performed in a N_2 filled dry-box. When no antisolvent treatment was used, the perovskite precursor solution was prepared by dissolving MAI (Dyesol), PbI_2 (99%, Sigma-Aldrich) and $PbCl_2$ (Sigma-Aldrich) in N,N-dimethylformamide (DMF, anhydrous, Sigma-Aldrich) to get 40 wt% solution (MAI:PbI_2:$PbCl_2$–4:1:1). The solution was spin coated onto the substrate at 4000 rpm for $30\,\mathrm{s}$, and then dried at $100\,^{\circ}\mathrm{C}$ for $90\,\mathrm{min}$. When the antisolvent treatment was carried out, a 1.25 M:1.25 M solution of PbI_2 and MAI in 4:1 volume ration of DMF:DMSO (Dimethyl sulfoxide anhydrous, Sigma-Aldrich) was prepared. The solution was spin coated onto the substrate at 4000 rpm fro $30\,\mathrm{s}$ and $7\,\mathrm{s}$ after the start of the spin $200\,\mu\mathrm{l}$ of ethyl acetate (anhydrous, Sigma-Aldrich) was deposited directly onto the centre of the spinning sample. Substrates were then dried at $100\,^{\circ}\mathrm{C}$ for $10\,\mathrm{min}$.

$CsPbBr_3$ 1 M of $PbBr_2$ (98%, Sigma-Aldrich) in DMF was prepared and stirred at $60\,^{\circ}\mathrm{C}$ until complete dissolution. The solution was spin coated onto the substrate that was pre-heated at $70\,^{\circ}\mathrm{C}$ at 2500 rpm for $30\,\mathrm{s}$ and further annealed at $70\,^{\circ}\mathrm{C}$ for $30\,\mathrm{min}$. The substrate was then immersed in CsBr (99.999%, Sigma-Aldrich) solution in methanol ($17\,\mathrm{mg\,ml^{-1}}$) kept at $50\,^{\circ}\mathrm{C}$ in a vertical staining jar. After $30\,\mathrm{min}$ immersion, the sample was annealed at $380\,^{\circ}\mathrm{C}$ in air for $30\,\mathrm{min}$.

$(MAFACs)Pb(Br_{0.4}I_{0.6})_3$ The mixed cation MA/FA/Cs perovskite solution was prepared by dissolving different molar quantities of 0.85 M PbI_2, 0.85 M FAI, 0.56 M MABr, 0.56 M$PbBr_2$ in DMF:DMSO (4:1). The solution was spin coated onto the substrate at 4000 rpm for $30\,\mathrm{s}$ and $7\,\mathrm{s}$ after the start of the spin $300\,\mu\mathrm{l}$ of ethyl acetate (anhydrous, Sigma-Aldrich) was deposited directly onto the centre of the spinning sample. Substrates were annealed at $100\,^{\circ}\mathrm{C}$ for $30\,\mathrm{min}$.

Ir catalyst synthesis

The iridium precursor [Cp*Ir(pyalc)Cl] was synthesised by Dr Ulrich Hintermair according to previous literature reports. [28] $48\,\mathrm{mg}$ (0.1 mmol) were added to $20\,\mathrm{ml}$ of DI water in an open beaker and the clear orange solution was stirred vigorously for $5\,\mathrm{min}$. Under constant stirring, $540\,\mathrm{mg}$ (2.5 mmol) of $NaIO_4$ were added to the beaker and the dark blue solution was allowed to stir overnight at room temperature. A piece of GS was floated on the unstirred, blue Ir-water oxidation catalyst (WOC) solution overnight to bind the catalyst. It was then rinsed with DI water and left to dry at room temperature.

2.3 Characterisation

This section gives an explanation of the techniques used throughout this thesis and their basic working principles. The characterisation techniques used include standard PV methods to measure the performance parameters of solar cells, microscopy techniques to investigate the morphology in nano and micro scale, spectroscopy analysis to quickly characterise materials and structural properties of thin-films and electrochemical measurements to measure the performance of photoanode devices.

2.3.1 Solar cell analysis

The extraterrestrial spectrum of solar radiation is characteristic of the radiation emitted from a black body at $5762\,\mathrm{K}$, its spectrum extends from 200 to $3000\,\mathrm{nm}$, with a peak in the invisible light region at $480\,\mathrm{nm}$. [29] During its passage through the atmosphere, the sun radiation is affected by reflection, absorption and scattering due to the presence of particulates and gas molecules. These processes are wavelength dependent and the intensity of their effects depends on the thickness of the atmosphere penetrated. The air mass (AM) quantifies the reduction in the power of light

as it passes through the atmosphere and it is defined as the ratio between the optical thickness of the atmosphere and the optical thickness if the sun was at zenith:

$$AM = \frac{1}{\cos\theta_z} \tag{2.6}$$

where θ_z is zenith angle. For example, AM 1.0 refers to the the solar radiation at the equator.

The efficiency of a solar cell varies with the power of incident light, which changes at different times, and its spectrum, which is affected by the location. To allow an efficient comparison between solar cells measured at different times and locations, a standard spectrum and power density have been defined. The standard spectrum at the Earth's surface is AM 1.5 G (G stands for global radiation, consisting of both beam radiation and diffuse radiation) normalised to give $100\,\mathrm{mW\,cm^{-2}}$ (1 Sun intensity).

Current-voltage curves Current density-voltage (JV) curves are one of the most fundamental characterisation techniques for solar cells and measure the current density (J) as a function of the potential (V) applied between the two terminals of the device (herein the FTO electrode and the metallic electrode). Typical JV curve of a solar cell is represented in figure 2.7.

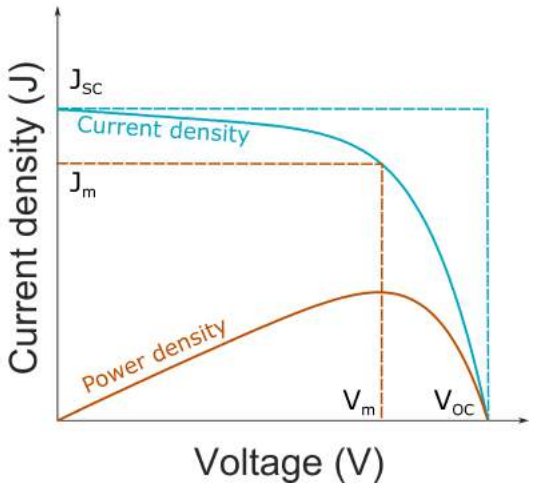

Figure 2.7: Typical current density voltage curve of a solar cell with main photovoltaic parameters.

The maximum power is reached at the maximum voltage V_m and the maximum current density J_m. The maximum current density output is the short circuit current density J_{sc} and is obtained when zero bias is applied (short circuit condition), while the maximum device photovoltage is the open circuit voltage V_{oc} and corresponds to the point in which the current equals zero (open circuit condition). The fill factor

FF is a measure of the shape of the JV curve and is given by:

$$FF = \frac{J_m V_m}{J_{sc} V_{oc}} \tag{2.7}$$

The power conversion efficiency *PCE* is the ratio between the maximum power density and the standard power density P_s (AM 1.5 G, $100\,\mathrm{mW\,cm^{-2}}$). J_{sc}, V_{oc}, FF and PCE are the most important parameters that describe the quality of a solar cell.

In this thesis, photo-electrical measurements were performed at room temperature, in air, under standard AM 1.5 G conditions and 1 Sun intensity with a solar simulator (TS SPACE SYSTEMS) and a Keithley 2601A potentiostat. Instrument calibration was performed with a WPVS reference monocrystalline Si cell with a KG3 filter (Ser. No. 031-2012). The solar cell was pre-poled for $5\,\mathrm{s}$ at the initial bias V_0 (larger than the V_{oc}) and then swept from V_0 to $0\,\mathrm{V}$ (reverse scan) and back to V_0 (forward scan) with a scan speed of $100\,\mathrm{mV\,s^{-1}}$.

Stabilised power output Despite the easy acquisition of JV characterisation, this measurement can be uncertain due to hysteresis when measuring in forward and reverse directions, which is affected by preconditioning effects. [30] It is therefore useful to combine JV scans with other methods, such as the stabilised power output over time. This measurement is determined by holding the tested device at a constant voltage and tracking the power-output over time.

In this thesis, stabilised power output measurements were performed at room temperature, in air, under standard AM 1.5 G conditions and 1 Sun intensity with a solar simulator (TS SPACE SYSTEMS) and a Keithley 2601A potentiostat. The solar cell's current density was tracked for $60\,\mathrm{s}$ while the device was held at V_m.

2.3.2 Microscopy

Microscopy is a technique that uses microscopes to view areas of objects that cannot be seen with the naked eye. In this thesis scanning probe and electron microscopy techniques were used.

Atomic Force Microscopy Atomic Force Microscopy (AFM) is a scanning probe microscopy technique, which involves the interaction of a scanning probe with the surface of the sample. This technique provides three-dimensional images of the surface by sensing the force changes as the surface sample is scanned. [31] The force is monitored by attaching the probe to a cantilever and detecting its deflection. The larger the cantilever deflection, the higher the force experienced by the the probe.

In this thesis, AFM images were used for the analysis of surface patterns and crystal growth of crystalline perovskite thin films and transporting layers. AFM images were collected with a Nanosurf easyScan 2 FlexAFM system in tapping mode. The dynamic force mode was used, in which the deflection of the cantilever was detected by measuring changes in its vibration amplitude. The probe was excited externally with a sinusoidal signal with a frequency close to the cantilever's free resonance frequency. A force of $20\,\mathrm{nN}$ and ContAl-G Tip were used for measurements.

Scanning Electron Microscopy Scanning Electron Microscopy (SEM) is a an electron microscopy technique that involves the interaction of a high energy electron beam with the specimen, which generates a number of signals that are then detected by appropriate detectors to generate an image. Electrons have much shorter wavelength than light, enabling higher resolution images with respect to light microscopes.
Top-view SEM characterisation is useful to study thin film structures, determining the surface roughness, the grain size and the presence of voids and cracks. [32] Cross-sectional SEM images are used to study single and multilayer heterostructure devices and to determine crystal growth properties and thickness of each layer. SEM can be also used in conjunction with other techniques, like Energy Dispersive X-ray (EDX), to study the chemical composition. EDX will be further discussed in section 2.3.4.

In this thesis, SEM images were taken on a JEOL JSM-6480LV at an acceleration voltage of $10\,\mathrm{kV}$. Higher resolution images were taken with a field emission JEOL JSM-6301F FESEM at an acceleration voltage of $5\,\mathrm{kV}$. An electrical bridge from the sample surface to the sample holder stub was made using double-sided conductive carbon tape. $5\,\mathrm{nm}$ of Cr was sputtered onto the surface prior scanning.

2.3.3 Structural analysis

X-Ray Diffraction X-ray Diffraction (XRD) is a technique for characterising crystalline materials and is based on the resonant interaction of electromagnetic radiation with the lattice of crystalline materials. It provides useful information on the structure, phase and the preferred crystal orientations of the material.
X-ray diffraction is the scattering of X-ray photons by atoms in a periodic crystal lattice. Since in phase scattered X-rays give construction interference, the characteristic lattice spacing between crystal planes of a given material can be derived by studying the diffraction of X-rays using the Bragg's law: [33]

$$n\lambda = 2dsin(\theta) \tag{2.8}$$

n is a positive integer, λ is the wavelength of X-rays, d is the lattice spacing and

θ is the diffraction angle. During measurement, the beam is directed towards the sample at various angles, resulting in the diffraction of X-rays. Each diffracted X-ray corresponds to a certain interstitial lattice spacing d that can be calculated using Eq. 2.8. The recorded intensities are plotted as a function of the diffraction angle 2θ. Each mineral has a set of unique d-spacings, therefore it is possible to identify the tested material by comparing the intensities measured with standard reference patterns.

In this thesis, XRD characterisation was used on known structures (halide perovskite films), therefore the parameters that were particularly interesting were the peaks' position and shape. The peaks' position is studied to confirm the correct film's crystal structure and the presence of any residual precursor materials. The peaks' shape gives useful information about the crystallinity of the sample and the grain size, as defined by the Scherrer formula: [34]

$$B = \frac{K\lambda}{Lcos(\theta)} \tag{2.9}$$

where, B is the full width at half maximum of the diffracted beam, K is the shape factor, L is the linear dimension of the particle and θ is the diffraction angle. According to Eq. 2.9, the sharper and narrower the peak, the larger the crystal.

In this thesis, a Bruker Advance D8 X-ray diffractometer with a Cu Ka source was used and measurements were taken from 2θ values of 5 to $70°$.

2.3.4 Spectroscopy

Impedance Impedance spectroscopy (IS) technique measures changes in current of an electrode material as modulated voltage is applied and can be used to study intrinsic properties, such as mobilities of charges and bulk generation-recombination. [35] The electrical impedance indicates the amount of opposition that a system presents to a current or voltage change and it is expressed in a form of a complex number $Z = Z' + jZ''$, with the impedance Z being frequency-dependent. Conventional impedance measures Z as a function of the radial frequency ω over a range of frequencies f. Impedance data reported in this thesis were measured by applying $10\,\mathrm{mV}$ single-frequency sinusoidal perturbation around the open circuit and measuring the phase shift and the amplitude at different frequencies. The excitation signal has the form

$$V_t = V_0 \sin(\omega t) \tag{2.10}$$

where V_t is the voltage at time t and V_0 is the amplitude of the signal. The relationship between the radial frequency ω and the frequency f is:

$$\omega = 2\pi f \tag{2.11}$$

A common way to represent impedance data is by plotting the real part on the X-axis and the imaginary part on the Y-axis of a chart; such plot is known as Nyquist Plot. On the Nyquist Plot the impedance is represented as a vector of length $|Z|$. Impedance plots usually contain one or more semicircles and the intrinsic properties of the material studied can be obtained by fitting the semicircles using simple equivalent electrical circuits. Nyquist plots of halide perovskite devices usually present two or three semicircles. [36, 37] A simple equivalent circuit that can be used to fit the high frequency semicircle is shown in Figure 2.8.

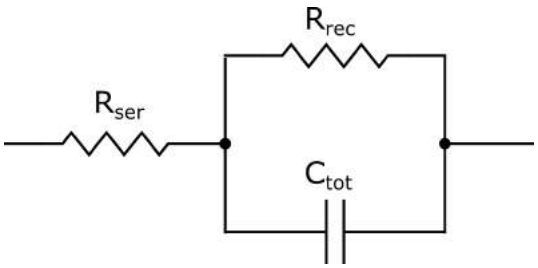

Figure 2.8: Equivalent circuit used to fit the high frequency impedance data represented as a semicircle in Nyquist plots, with elements representing the recombination resistance R_{rec}, the cell capacitance C_{tot} and the series resistance R_{ser}.

R_{ser} is the series resistance of the cell, usually largely associated with the FTO substrate, while R_{rec} is the voltage-dependent recombination resistance. The total capacitance C_{tot} reflects the overall charge storage in the device, which is the sum of the charge in the contacts (geometric capacitance C_{geo}) and the charge associated with photogenerated electrons and holes in the perovskite layer (chemical capacitance C_μ). C_{geo} is expected to be practically constant across a range of voltages measured. In contrast, C_μ is expected to increase exponentially with voltage due to higher accumulation of free carriers in the perovskite layer. [37] Previous works in the group showed that the high frequency semi-circle measured by IS was dominated by the value of geometric capacitance and that the resistance extracted was indeed a measure of recombination. [36]

In this thesis, impedance measurements for different illumination intensities were made at the corresponding open-circuit voltage using an Autolab PGSTAT30 over a frequency range of $1\,\mathrm{MHz}$ and $5\,\mathrm{mHz}$. Impedance data were fitted using ZView software (Scribner Associates).

Photoluminescence Photluminescence (PL) spectroscopy is an effective approach used to gather information about the optoelectronic properties of a semiconductor. [38] Steady state PL intensity (I_{PL}) can be obtained by:

$$I_{PL} = \beta_{rad} n_e n_h \tag{2.12}$$

where β_{rad} is the radiative recombination coefficient and n_e and n_h are the population of free electrons and holes. The PL intensity is directly related to the radiative recombination processes occurring in a semiconductor, and it is extremely sensitive to small variations in the material properties that normally could not be perceived by other optical techniques. In this thesis, variations in the defect composition that induce structural instabilities in the perovskite films were investigated by monitoring the dynamics of PL.

Relative PL quantum yield (PLQY) was obtained from the measured integrated PL at varying excitation intensities *I* and plotted as:

$$RelativePLQY = \frac{I_{PL}}{I_{pump}} \tag{2.13}$$

where, I_{punp} is the excitation intensity.

Steady state Photoluminescence (PL) spectra reported in this thesis, as well as the evolution of steady state PL intensities over time were acquired with a fiber coupled spectrometer (Ocean Optics Maya Pro 2000) that operated with a silicon photodetector array. The samples were mounted in a chamber under vacuum. The excitation source was provided by 405 and $450\,\mathrm{nm}$ lasers (specified for each experiment reported). A software with a graphic interface built in Python was used for communicating with the spectrometer and acquiring spectra and recording the emission of the samples over time.

Time-resolved PL (TRPL) measurements were performed with a Time Correlated Single Photon Counting (TCSPC) setup. The excitation source was an unamplified tunable Ti:Sapphire laser (Coherent Chameleon Ultra II, temporal and spectral bandwidths of 140 fs and $5\,\mathrm{nm}$, respectively), which was tuned to a central wavelength of $700\,\mathrm{nm}$. The measurements were performed with excitation at $2\,\mathrm{MHz}$, which was achieved using an acousto-optical modulator pulse picker (APE Pulse Select). The sample was excited with an excitation density of about $7 \times 10^{-15}\,\mathrm{cm}^{-3}$. The samples were mounted in a chamber under vacuum, and PL was collected in reflection mode and focused onto a spectrometer coupled to a N_2 cooled photomultiplier.

UV-Visible UV-Visible spectroscopy (UV-Vis) is a technique that measures the part of the solar spectrum that a material absorbs. Optical properties can be measured on both solids (powder or films) and solutions. When measured on solutions, a light beam with a varying wavelength passes through a solution in a cuvette. A direct parameter that can be measured is the transmittance *T* as a function of the wavelength of incoming light λ, which is given by

$$T(\lambda) = \frac{I(\lambda)}{I_0(\lambda)} \tag{2.14}$$

where I is the intensity of the light transmitted through the sample and I_0 is the intensity of the incoming light. The transmittance is often measured as a percentage $T\%$. If the amount of light reflected can be neglected, the absorbance A of the solution is calculated as

$$A = log\left(\frac{100}{T\%}\right) \tag{2.15}$$

and it depends on the concentration of the solution, the path length of the light through the cuvette and how well the analyte absorbs the light at a certain wavelength. If the material studied is a film, the absorbance depends on the thickness of the film.

The equation that relates the energy state E with the frequency ν of the electromagnetic radiation is

$$E = h\nu \tag{2.16}$$

where h is the Plank's constant ($6.626 \times 10^{-34}\,\mathrm{J\,s}$). The optical bandgap of a semiconductor can be determined by using the Tauc plot, [39] which shows the quantity $(\alpha h\nu)^{\frac{1}{a}}$ as a function of E, where α is the absorption coefficient. The factor a denotes the nature of the semiconductor (i.e. $a = \frac{1}{2}$ for direct semiconductors and $a = 2$ for indirect semiconductors). The resulting plot has a distinct linear region and the energy bandgap can be measured by extrapolating the linear region to the x-axis. The absorption coefficient can be approximated as [40]

$$\alpha = \frac{1}{t} ln\left(\frac{(1-R)^2}{T}\right) \tag{2.17}$$

where t is the thickness of the film.
Methylammonium lead iodide perovskites have been widely considered direct bandgap semiconductors, however a weak indirect bandgap transition was also reported. [41] Therefore, the Tauc plot of halide perovskite materials is not considered an absolute accurate method to calculate the energy bandgap.

The UV-Vis data present in this thesis were measured on thin films with a Perkin-Elmer Lambda 750S UV/Vis/NIR spectrometer and spectra were acquired from 900 to $300\,\mathrm{nm}$. The values were shown in arbitrary units because the thickness of the films were not measured everytime. Before acquiring the UV-Vis spectra, a 100% T calibration was performed. Tauc plots were calculated assuming the perovskite material to be a direct semiconductor.

X-Ray Photoelectron X-ray Photoelectron Spectroscopy (XPS) is a surface quantitative technique that measures the elemental composition, chemical state and electronic state of the elements that exist within a material. In a typical XPS experiment the surface of the sample is irradiated with photons of a X-ray source (monochromated or not) that interact directly with the core electrons of the material's atoms.

As a result of this interaction, ionized states are created and a photoelectron is emitted with a kinetic energy that is detected and analysed. The kinetic energy is given approximately by the difference between the incoming photon energy and the binding energy. The kinetic energy is usually plotted as a function of the binding energy (which increases from right to left). [42]
The small attenuation length of photoelectrons restricts the chemical information obtained to the first few atomic layers. Therefore this technique is not appropriate for bulk analysis but only surface analysis.

XPS characterisation reported in this thesis was carried out in Swansea University by Dr James McGettrick on a Kratos Axis Supra (Kratos Analytical, Manchester) instrument with samples connected to the ground. Control XPS spectra of precursor powders were also collected. XPS was performed at an X-ray power of $225\,\mathrm{W}$ using a monochromated Al Ka source. Step size and pass energy used were 0.1 eV and 20 eV respectively. XPS data were analysed using CasaXPS and the Kratos sensitivity factor library.

Fourier-transform infrared Fourier-transform infrared spectroscopy (FTIR) is used to collect high-spectral-resolution data over a spectral range. It is a quick measurement to identify the presence of certain functional groups in a molecule and the absorption bands in a material to detect the presence of specific impurities. Most of the molecules absorb light in the infra-red region of the electromagnetic spectrum. This absorption is characteristic of the bonds present in the molecule. The frequency range are measured as wave numbers. An infrared source beam passes through the sample, which emits signals that are acquired by a detector, and compared to a blank sample to correct the response for air. The information are translated into a plot with wave numbers on the X-axis and intensity measured as the percent transmittance of the IR radiation.

In this thesis, a Perkin Elmer Frontier FTIR instrument was used to measure the relative transmittance of halide perovskite films in air. Spectra were acquired between 1000 and $3500\,\mathrm{cm}^{-1}$ wave numbers.

Energy Dispersive X-Ray Energy Dispersive X-Ray (EDX) spectroscopy is a technique that measures the elemental composition and chemical characterisation of a sample. [43] EDX makes use of the X-ray spectrum produced by the atoms of a solid sample which is bombarded with an electron beam. The emitted X-ray energy is detected and the related spectral peaks are generated. Each element has a unique atomic structure allowing a particular set of peaks, therefore the elemental composition can be derived by analysing the position of the emission spectrum. X-Ray spectrometers that measure EDX can be added to standard SEM microscopes allowing to obtain elemental composition coloured maps of SEM images, revealing

the surface topography. Moreover, quantitative elemental concentrations of selected areas of SEM images can be obtained.

EDX used to acquire data reported in this thesis is mounted to the 6480LV SEM microscope described above.

2.3.5 Electrochemistry

Electrochemistry is used to probe reactions that involve electron transfers. [44] For example, the observed electron flow can correspond to a chemical change which results from the oxidation or reduction of the studied material. By definition, the electrode where the oxidation reaction occurs is called anode, while the electrode where the reduction reaction occurs is called cathode. [45] Electrons are transferred between the electrical conductor (electrode) and the electrolyte solution, which consists of a solvent in which the active species to be reduced or oxidised are dissolved. In electrochemical measurements a potentiostat is used as an external source to apply a voltage to modulate the energy of the electrons in the working electrode. When studying reactions occurring at the surface of the working electrode, the applied potential is a key parameter that needs to be measured with respect to a fixed reference potential. Therefore, the electrochemical cell used for any quantitative research study in electrochemistry is a three-electrode system. The three electrodes used are the working electrode (WE), that can act as either a cathode or anode, the counter electrode (CE) and a reference (Ref). The voltage is therefore applied between the WE and the Ref and the generated current is measured between the WE and the CE. Some of the common references used in electrochemistry are the reversible hydrogen electrode (RHE), the standard hydrogen electrode (SHE), the silver/silver chloride elctrode (Ag/AgCl) and the calomel electrode (Hg/Hg_2Cl_2). In order to compare results obtained with different references, it is common to convert the measured potential V_{ref} to the RHE scale V_{RHE} by using the following expression: [46]

$$V_{RHE} = V_{ref} + E_{0vsSHE} + 0.059pH \tag{2.18}$$

where E_{0vsSHE} is the potential of the reference electrode with respect to the SHE.

Most of the electrochemical characterisation present in this thesis is used to measure the photoelectrochemical (PEC) water splitting performance of halide perovskite based photoelectrodes. The reactions that take place during PEC water splitting are driven by the capture of photogenerated carriers at the interface between an electrolyte and the illuminated semiconductor electrode. The electrolyte used in PEC systems is indeed water. Since pure water is poorly conducting, supporting ions are commonly added to ensure that the generated current can be carried. Aqueous H_2SO_4 and KOH solutions are commonly used as acid and alkaline electrolytes, respectively. [46]

The electrochemical experiments and PEC performance measurements presented in this thesis were conducted in aqueous solutions $0.1\,\mathrm{M}$ KNO_3, with the pH adjusted by using H_2SO_4 or KOH. The electrolyte was exposed to air during measurement. The pH of the solution was measured prior to each experiment using a jenway pH meter. When specified, a buffered solution of K-borate at pH 9 was used.

Cyclic Voltammetry Cyclic voltammetry (CV) is used to study reduction and oxidation processes. One of its application for example consists of evaluating the performance of molecular catalysts. [47] CV measures the current in an electrochemical cell as the potential is linearly ramped up and down between two potentials E_1 and E_2. Figure 2.9 show a typical CV scan of the reversible reduction and re-oxidation of $1\,\mathrm{mM}$ Fc^+ solution as the applied potential is changed over time.

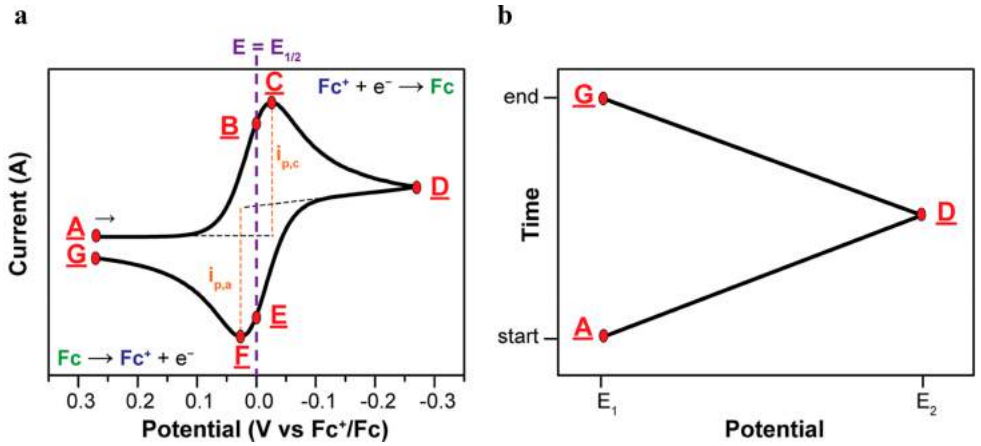

Figure 2.9: a Typical CV scan of the reversible reduction of $1\,\mathrm{mM}$ Fc^+ solution to Fc. **b** Applied potential in a typical CV scan as a function of time. Figure taken from [44].

Considering a fast single electron transfer reaction: $Red \rightarrow Ox + e^-$, the concentration of the two species *Ox* and *Red* can be described by the Nerst equation, which provides a powerful way to predict how the studied system will respond to a change in the electrode potential. Under the assumption of rapid electrode kinetics, the concentration of the oxidized and reduced species can be considered at equilibrium and the potential is given by:

$$E = E_0' + \frac{RT}{nF} ln \frac{[Ox]}{[Red]} \tag{2.19}$$

where, E_0' is the formal potential of the electrode, *[Ox]* and *[Red]* are the surface concentration of the oxidised and reduced species respectively, *R* is the gas constant, *F* is the Faraday's constant and *n* is the number of electrons involved in the reaction. Figure 2.9 shows the half wave potential $E_{1/2}$, which corresponds to the halfway potential between the oxidation and reduction peaks C and F. Assuming that the diffusion coefficients of *Ox* and *Red* are equal, $E_{1/2}$ can be approximated to the formal potential E_0'.

In this thesis, CV data were measured in a three-electrode system, in the dark by using a Compactstat IVIUM potentiostat, with a scan rate of $50\,\mathrm{mV\,s^{-1}}$. Pt and Ag/AgCl were used as counter electrode and reference, respectively.

Linear Sweep Voltammetry Linear Sweep Voltammetry is a technique that measures the current at a working electrode while the potential between the working electrode and a reference electrode is swept linearly with time. In this thesis it is used to study the PEC water splitting performance. During the measurement, an external bias is applied with respect to the reference. Typical PEC current-voltage curves see the current increase with applied bias. [27] The potential at which the current starts to increase indicates the reaction start point and it is called the onset potential V_{on}. Conventionally, V_{on} is defined as the potential that corresponds to the intercept between the dark current and the tangent to the maximum slope of the current rise under illumination. [48]

LSV data shown in this thesis were measured by using a Compactstat IVIUM potentiostat under simulated solar illumination (AM 1.5 G filtered $100\,\mathrm{mW\,cm^{-2}}$) with $300\,\mathrm{W}$ Xe source (Lot-QD). The intensity of the light at the working electrode position was measured by certified and calibrated SEL033/U photodetector (International Light Technologies).

Chronoamperometry Chronoamperometry is an electrochemical technique in which the applied potential is stepped and the current measured at the working electrode is monitored as a function of time. A typical chronoamperometry test consists of initially holding the working electrode at a potential where no faradaic processes occur and then stepping it to a value at which redox reactions occur. This technique can be used to monitor the processes occurring at the working electrode over time.

In this thesis chronoamperometry is used to study the stability of the current generated by the photoanode in both three-electrode and two-electrode PEC configurations.

Chronoamperometric data in three-electrode configuration were measured by using a Compactstat IVIUM potentiostat under simulated solar illumination (AM 1.5 G filtered $100\,\mathrm{mW\,cm^{-2}}$) with $300\,\mathrm{W}$ Xe source (Lot-QD), applying a constant bias of $1.23\,\mathrm{V_{RHE}}$. Unbiased measurements were conducted in two-electrode configurations, with $0\,\mathrm{V}$ applied between the working and the counter electrodes.

Incident Photon-to-Current Efficiency The Incident Photon-to-Current Efficiency (IPCE) is a useful parameter that can be used to identify the performance-limiting factors in PEC photoelectrodes. It is defined as the fraction of the incident photons that is converted to electrons that can be measured by the outer circuit. IPCE is given

by: [46]

$$IPCE = \frac{hc}{q}\left(\frac{j_{photo}(\lambda)}{\lambda P(\lambda)}\right) \tag{2.20}$$

where h is the Plank's constant, c is the speed of light, q is the elemental charge, j_{photo} is the measured photocurrent as a function of wavelength λ and P is the power density of the incident photons. IPCE is indicated as a percentage value and plotted as a function of the wavelength of incident light.

IPCE data shown in this thesis were measured in aqueous solution in a three-electrode system at an applied potential of $1.23\,\mathrm{V_{RHE}}$. A monochromator (MSH-300F LOT QuantumDesign) without the AM 1.5 G filter was used to change the wavelength of the light source from 300 to $900\,\mathrm{nm}$ with a wavelength increment of $5\,\mathrm{nm}$ every $5\,\mathrm{s}$. The intensity of the monochromatic light was measured by a SEL033/U photodetector (International Light Technologies).

Bibliography

[1] J. Nelson, *The physics of solar cells*. London: Imperial college press, 2003.

[2] S. Gimenez and J. Bisquert, *Photoelectrochemical solar fuel production*. Springer International Publishing Switzerland, 2016.

[3] R. Rajkanan, R. Singh, and J. Shewchun, "Absorption Coefficient of Silicon for Solar Cell Calculations," *Solid State Electron.*, vol. 22, pp. 793–795, 1979.

[4] I. Balslev, "Direct edge piezo-reflectance in Ge and GaAs," *Solid State Commun.*, vol. 5, no. 4, pp. 315–317, 1967.

[5] H. Kim, C.-R. Lee, J.-H. Im, K. Lee, T. Moehl, A. Marchioro, S. Moon, R. Humphry-Baker, J. Yum, J. E. Moser, M. Grätzel, and N. Park, "Lead iodide perovskite sensitized all-solid-state submicron thin film mesoscopic solar cell with efficiency exceeding 9%.," *Sci. Rep.*, vol. 2, no. 591, 2012.

[6] T. Baikie, Y. Fang, J. M. Kadro, M. Schreyer, F. Wei, S. G. Mhaisalkar, M. Graetzel, and T. J. White, "Synthesis and crystal chemistry of the hybrid perovskite $(CH_3NH_3)PbI_3$ for solid-state sensitised solar cell applications," *J. Mater. Chem. A*, vol. 1, no. 18, pp. 5628–5641, 2013.

[7] V. Sarritzu, N. Sestu, D. Marongiu, X. Chang, Q. Wang, S. Masi, S. Colella, A. Rizzo, A. Gocalinska, E. Pelucchi, M. L. Mercuri, F. Quochi, M. Saba, A. Mura, and G. Bongiovanni, "Direct or Indirect Bandgap in Hybrid Lead Halide Perovskites?," *Adv. Opt. Mater*, vol. 6, no. 10, pp. 1–8, 2018.

[8] T. Wang, B. Daiber, J. M. Frost, S. A. Mann, E. C. Garnett, A. Walsh, and B. Ehrler, "Indirect to direct bandgap transition in methylammonium lead halide perovskite," *Energy Environ. Sci.*, vol. 10, no. 2, pp. 509–515, 2017.

[9] E. M. Hutter, M. C. Gélvez-Rueda, A. Osherov, V. Bulović, F. C. Grozema, S. D. Stranks, and T. J. Savenije, "Direct-indirect character of the bandgap in methylammonium lead iodide perovskite," *Nat. Mater.*, vol. 16, no. 1, pp. 115–120, 2017.

[10] A. Kahn, "Fermi level, work function and vacuum level," *Mater. Horiz.*, vol. 3, no. 1, pp. 7–10, 2016.

[11] M. Saba, F. Quochi, A. Mura, and G. Bongiovanni, "Excited State Properties of Hybrid Perovskites," *Acc. Chem. Res*, vol. 49, no. 1, pp. 166–173, 2016.

[12] M. a. Green, A. Ho-Baillie, and H. J. Snaith, "The emergence of perovskite solar cells," *Nat. Photonics*, vol. 8, no. 7, pp. 506–514, 2014.

[13] M. Saba, M. Cadelano, D. Marongiu, F. Chen, V. Sarritzu, N. Sestu, C. Figus, M. Aresti, R. Piras, A. Geddo Lehmann, C. Cannas, A. Musinu, F. Quochi,

A. Mura, and G. Bongiovanni, "Correlated electron-hole plasma in organometal perovskites," *Nat. Commun.*, vol. 5, no. May, pp. 1–10, 2014.

[14] V. D'Innocenzo, G. Grancini, M. J. Alcocer, A. R. S. Kandada, S. D. Stranks, M. M. Lee, G. Lanzani, H. J. Snaith, and A. Petrozza, "Excitons versus free charges in organo-lead tri-halide perovskites," *Nat. Commun.*, vol. 5, pp. 1–6, 2014.

[15] J. M. Ball and A. Petrozza, "Defects in perovskite-halides and their effects in solar cells," *Nat. Energy*, vol. 1, no. 11, 2016.

[16] P. D. Schulze and J. R. Hardy, "Frenkel Defects in Alkali Halides," *Phys. Rev. B*, vol. 6, no. 4, pp. 1580–1584, 1972.

[17] D. Meggiolaro, S. G. Motti, E. Mosconi, A. J. Barker, J. Ball, C. Andrea Riccardo Perini, F. Deschler, A. Petrozza, and F. De Angelis, "Iodine chemistry determines the defect tolerance of lead-halide perovskites," *Energy Environ. Sci.*, vol. 11, no. 3, pp. 702–713, 2018.

[18] U. Rau, "Reciprocity relation between photovoltaic quantum efficiency and electroluminescent emission of solar cells," *Phys. Rev. B*, vol. 76, no. 085303, 2007.

[19] T. Leijtens, G. E. Eperon, A. J. Barker, G. Grancini, W. Zhang, J. M. Ball, R. Srimath, J. Snaith, and A. Petrozza, "Carrier trapping and recombination : the role of defect physics in enhancing the open circuit voltage of metal halide perovskite solar cells," *Energy Environ. Sci.*, vol. 9, no. 3472, pp. 3472–3481, 2016.

[20] J. R. Ayres, "Characterization of trapping states in polycrystalline-silicon thin film transistors by deep level transient spectroscopy," *J. Appl. Phys.*, vol. 74, no. 3, pp. 1787–1792, 1993.

[21] W. J. Yin, T. Shi, and Y. Yan, "Unusual defect physics in $CH_3NH_3PbI_3$ perovskite solar cell absorber," *Appl. Phys. Lett.*, vol. 104, no. 6, 2014.

[22] D. W. de Quilettes, S. M. Vorpahl, S. D. Stranks, H. Nagaoka, G. E. Eperon, M. E. Ziffer, H. J. Snaith, and D. S. Ginger, "Impact of microstructure on local carrier lifetime in perovskite solar cells," *Science*, vol. 348, no. 6235, pp. 683–686, 2015.

[23] T. W. Jones, A. Osherov, M. Alsari, M. Sponseller, B. C. Duck, Y. K. Jung, C. Settens, F. Niroui, R. Brenes, C. V. Stan, Y. Li, M. Abdi-Jalebi, N. Tamura, J. E. MacDonald, M. Burghammer, R. H. Friend, V. Bulović, A. Walsh, G. J. Wilson, S. Lilliu, and S. D. Stranks, "Lattice strain causes non-radiative losses in halide perovskites," *Energy Environ. Sci.*, vol. 12, no. 2, pp. 596–606, 2019.

[24] S. M. Vorpahl, R. Giridharagopal, G. E. Eperon, I. M. Hermes, S. A. L. Weber, and D. S. Ginger, "Orientation of Ferroelectric Domains and Disappearance

upon Heating Methylammonium Lead Triiodide Perovskite from Tetragonal to Cubic Phase," *ACS Appl. Energy Mater.*, vol. 1, pp. 1534–1539, 2018.

[25] K. G. Upul Wijayantha, S. Saremi-Yarahmadi, and L. M. Peter, "Kinetics of oxygen evolution at a-Fe_2O_3 photoanodes: a study by photoelectrochemical impedance spectroscopy," *Phys. Chem. Chem. Phys.*, vol. 13, pp. 5264–5270, 2011.

[26] L. M. Peter and K. G. Upul Wijayantha, "Photoelectrochemical water splitting at semiconductor electrodes: Fundamental problems and new perspectives," *ChemPhysChem*, vol. 15, no. 10, pp. 1983–1995, 2014.

[27] H. J. Lewerenz and L. Peter, *Photoelectrochemical Water Splitting: Materials, Processes and Architectures*. RSC Energy and Environment Series, 2013.

[28] U. Hintermair, S. M. Hashmi, M. Elimelech, and R. H. Crabtree, "Particle Formation during Oxidation Catalysis with Cp* Iridium Complexes," *J. Am. Chem. Soc.*, vol. 134, pp. 9785–9795, 2012.

[29] N. D. Kaushika, A. Mishra, and A. K. Rai, *Solar photovoltaics: Technology, system design, reliability and viability*. Springer, 2018.

[30] M. Bliss, A. Smith, T. R. Betts, J. Baker, F. De Rossi, S. Bai, T. Watson, H. Snaith, and R. Gottschalg, "Spectral Response Measurements of Perovskite Solar Cells," *IEEE J. Photovolt.*, vol. 9, pp. 220–226, 2019.

[31] Y. F. Dufre, "Atomic Force Microscopy , a Powerful Tool in Microbiology," *J. Bacteriol.*, vol. 184, pp. 5205–5213, 2002.

[32] T. E. Everhart, "Thin-Film Measurements in the Scanning Electron Microscope," *J. Vac. Sci. Technol.*, vol. 7, pp. 322–322, 2002.

[33] A. K. Chatterjee, "X-Ray Diffraction," in *Analytical Techniques in Concrete Science and Technology*, Rowman and Littlefield Publishers, 2001.

[34] A. L. Patterson, "The scherrer formula for X-ray particle size determination," *Phys. Rev.*, vol. 56, pp. 978–982, 1939.

[35] E. Barsoukov and J. R. Macdonald, *Impedance Spectroscopy Theory , Experiment , and Applications*. John Wiley and Sons. Inc., 2005.

[36] A. Pockett, G. E. Eperon, T. Peltola, H. J. Snaith, A. B. Walker, L. M. Peter, and P. J. Cameron, "Characterization of Planar Lead Halide Perovskite Solar Cells by Impedance Spectroscopy, Open Circuit Photovoltage Decay and Intensity-Modulated Photovoltage/Photocurrent Spectroscopy," *J. Phys. Chem. C*, vol. 119, pp. 3456–3465, 2015.

[37] A. Pockett, G. E. Eperon, N. Sakai, H. J. Snaith, L. M. Peter, and P. J. Cameron, "Microseconds, milliseconds and seconds: deconvoluting the dynamic behaviour of planar perovskite solar cells," *Phys. Chem. Chem. Phys.*, vol. 19, pp. 5959–5970, 2017.

[38] I. Pelant and J. Valenta, *Luminescence Spectroscopy of Semiconductors*. Oxford University Press, 2012.

[39] J. Tauc, "Optical Properties and Electronic Structure of Amorphous Ge and Si," *Mat. Res. Bull.*, vol. 3, pp. 37–46, 1968.

[40] J. I. Pankove, *Optical Processes in Semiconductors*. Dover Publications, 1975.

[41] T. Wang, B. Daiber, J. M. Frost, S. A. Mann, E. C. Garnett, and B. Ehrler, "Indirect to direct bandgap transition in methylammonium lead halide perovskite," *Energy Environ. Sci.*, vol. 10, pp. 509–515, 2016.

[42] S. Hofmann, *Auger- and X-Ray Photoelectron Spectroscopy in Materials Science*. Springer, 2013.

[43] S. K. Sharma, *X-Ray Spectroscopy*. InTech, 2011.

[44] N. Elgrishi, K. J. Rountree, B. D. Mccarthy, E. S. Rountree, T. T. Eisenhart, and J. L. Dempsey, "A Practical Beginner 's Guide to Cyclic Voltammetry," *J. Chem. Educ.*, vol. 95, pp. 197–206, 2018.

[45] C. Lefrou, P. Fabry, and J.-C. Poignet, *Electrochemistry*. Springer, 2012.

[46] R. Van de Krol and M. Grätzel, *Photoelectro-chemical Hydrogen Production*. Springer, 2012 ed., 2012.

[47] E. S. Rountree, B. D. Mccarthy, T. T. Eisenhart, and J. L. Dempsey, "Evaluation of Homogeneous Electrocatalysts by Cyclic Voltammetry," *Inorg. Chem.*, vol. 53, pp. 9983–10002, 2014.

[48] D. Cao, W. Luo, J. Feng, X. Zhao, Z. Li, and Z. Zou, "Cathodic shift of onset potential for water oxidation on a Ti^{4+} doped Fe_2O_3 photoanode by suppressing the back reaction," *Energy Environ. Sci.*, vol. 7, pp. 752–759, 2014.

Chapter 3

Surface treatment techniques to enhance the stability of perovskite solar cells

Water has been identified as one of the key reasons for irreversible degradation of perovskite solar cells. This chapter investigates several surface treatment techniques to enhance the stability of perovskite devices. Section 3.1 demonstrates the application of $MAPbI_3$ nanocrystals capped with oleic acid as a hydrophobic protection to repel water from getting to the perovskite layer and improve the moisture stability of the solar cell. Section 3.2 shows the effect of protecting the perovskite absorber with large organic cations to simultaneously reduce the moisture-induced degradation and improve the photo-stability of the material.

3.1 Moisture-induced degradation

The elements that compose halide perovskites are mainly alkylammonium salts and lead salts, which are both soluble in water. [1, 2] Water molecules easily penetrate the perovskite structure, changing the stoichiometry of $CH_3NH_3PbI_3$ into CH_3NH_3I and PbI_2, [3] and leaving behind yellow-coloured PbI_2 films as a decomposition product. Such degradation does not only have effects on the conversion efficiency of the device, but issues concerning toxicology become of primary importance, as the product PbI_2 is highly toxic and soluble in water. [4]

One simple route to effectively minimize the moisture-induced degradation of the perovskite absorber is by coating its surface with an interfacial layer. Such a layer needs to be thick enough to protect the perovskite from moisture-induced degradation and thin enough to allow charge tunneling without insulating the perovskite absorber. [5] Some of the interlayers that demonstrated to enhance the moisture stability are summarised in Table 3.1.

Table 3.1: Passivation layers reported in the literature to reduce moisture-induced degradation of perovskite solar cells

Passivation layer	Stability test	% degradation	ref
Al_2O_3	SS*, 70 days, RH 40-70%	40%	[5]
dodecyl	SS, 600 h, RH 45%	20%	[6]
tetraethylammonium cations	SS, 500 h, RH 55%	10%	[7]
fluoroalkyl silane	SS, 500 h, RH 30%	20%	[8]
pentafluorobenzenethiol	SS, 250 h, RH 45%	25%	[9]
cyclopropylammonium cation	SS, 200 h, RH 60%	46%	[10]

*SS: Shelf Stability, solar cells stored in the dark at open circuit between data collection points.

Several reports showed that coating the perovskite absorber with thin hydrophobic layers by spin coating effectively changed the hydrophilic properties of the perovskite film surface, reducing the tendency of undesirable chemical reactions with water. [6, 7, 8, 10] Fluoroalkyl silane coating layers [8], long alkyl chains [6] and alkyl ammonium salts [7, 10] were successfully assembled on the perovskite surface and two times larger water contact angles were measured for treated perovskite films. Solar cells based on these treated films were fabricated and improved shelf stability was measured for unsealed devices for over $500\,\mathrm{h}$, under relative humidity $>45\,\%$. Improved stability towards high humidity and more efficient devices were also obtained by protecting the perovskite absorber films by directly depositing Al_2O_3 thin layers on the surface via ALD [5] and hydrophobic thiols via dip-coating. [9]

3.1.1 Enhancing the hydrophobicity of perovskite solar cells using C18 capped $CH_3NH_3PbI_3$ nanocrystals

In this work, the poor humidity resistance of $MAPbI_3$ perovskite films was enhanced by treating the surface with $\sim 10\,\mathrm{nm}$ size $MAPbI_3$ nanocrystals (NCs). The nanoscale size of these particles was controlled by the long chain ligands oleic acid (OA) and oleylamine (OLA) that sourrounded the NC's surface. When $MAPbI_3$ NCs were introduced onto the perovskite films, the hydrophobicity of the surface was improved by over $75\,\%$ with respect to untreated $MAPbI_3$ perovskites. When the pristine perovskite film was exposed to a water droplet, the black colour quickly changed to yellow, indicating immediate formation of PbI_2. In contrast, the surface treated $MAPbI_3$ film did not change its aspect and it did not turn yellow even when completely submerged in water for over $30\,\mathrm{s}$. XRD measurements confirmed that the tetragonal perovskite crystalline phase was dominating in films coated with $MAPbI_3$ NCs after complete immersion in water for $10\,\mathrm{s}$. In contrast, only PbI_2 was identified in reference $MAPbI_3$ films. When only ligands were deposited onto the perovskite film, a maximum water contact angle of 60° was measured, $40\,\%$ lower than what has been measured for NCs treated films. Lower hydrophobicity was probably caused by poorer coverage of the ligands on the film.

The presence of organic hydrophobic long side chains like OA and OLA at the perovskite/transporting layer interface may affect the charge extraction. Devices

with both inverted and standard architectures and different transporting layers were fabricated to study the effect of capped-$MAPbI_3$ NCs on the photovoltaic properties of solar cells. $MAPbI_3$ NCs were deposited at the perovskite/spiro-OMeTAD interface in standard cells and at the perovskite/PCBM interface in inverted devices. Inverted solar cells with NCs incorporated at the perovskite/PCBM interface showed the presence of inverted hysteresis, suggesting that the thin layer of $MAPbI_3$ NCs acted as an extraction barrier. In contrast, reduced normal hysteresis was observed when $MAPbI_3$ NCs were deposited at the perovskite/spiro-OMeTAD interface in standard mesoporous devices, suggesting improved charge extraction. It was proposed that the presence of $MAPbI_3$ NCs at the interface improved the band alignment between the perovskite absorber layer and the hole transporting layer, enhancing the hole extraction. Standard mesoporous solar cells with treated perovskite surface showed similar conversion efficiencies to the reference $MAPbI_3$, but with considerably enhanced moisture stability observed for unsealed devices for over 70 days, under relative humidity $>60\,\%$. Larger-area solar cells ($0.25\,\mathrm{cm}^2$) were also fabricated achieving PCEs of $\sim 8\,\%$.

This approach allowed us to easily treat the surface of halide perovskites with highly hydrophobic long chain ligands-capped $MAPbI_3$ NCs deposited via solution-based processes to enhance moisture stability and charge extraction of final devices. $MAPbI_3$ NCs were synthesised in a flow reactor, in ambient conditions and at room temperature, through a process which could be easily scaled-up for large-scale manufacturing. [11]

The results summarised in this section have been published by Poli et al. (2018). [12] The statement of authorship is given below.

This declaration concerns the article entitled:					
Enhancing the Hydrophobicity of Perovskite Solar Cells using C18 Capped $CH_3NH_3PbI_3$ Nanocrystals					
Publication status (tick one)					
Draft manuscript		**Submitted**		**In review**		**Accepted**		**Published**	X
Publication details (reference)	The article has been published in: *J. Mater. Chem. C*, Vol. 6, 7149-7156 (2018)				
Copyright status (tick the appropriate statement)					
I hold the copyright for this material		Copyright is retained by the publisher, but I have been given permission to replicate the material here	X		
Candidate's contribution to the paper (provide details, and also indicate as a percentage)	The candidate **predominantly** executed the work presented in the paper. **Formulation of ideas:** The objectives, analysis and conclusions of the paper were formulated by the candidate, with the support of the lead supervisor Petra Cameron. [IP=80%, XL=5%, RB=0%, SE=0%, PJC=15%] **Design of methodology:** The methodology was designed by the candidate with the support of the lead supervisor Dr Petra Cameron. [IP=83%, XL=2%, RB=0%, SE=0%, PJC=15%] **Experimental work:** The fabrication of thin-film perovskites and full devices was carried out by the candidate along with the characterisation of both films and devices. The synthesis of MAPI NCs and TEM and PL characterisation of MAPI NCs was carried out by Dr Xinxing Liang and Robert Baker. [IP=85%, XL=10%, RB=5%, SE=0%, PJC=0%] **Presentation of data in journal format:** Data were analysed by the candidate and plots and figures in journal format were generated by the candidate. The writing of the manuscript was done by the candidate. The lead supervisor Petra Cameron and second supervisor Salvador Eslava reviewed and corrected the writing of the paper and gave assistance in the submission and peer reviewing process. [IP=75%, XL=3%, RB=0%, SE=2%, PJC=20%]				
Statement from Candidate	This paper reports on original research I conducted during the period of my Higher Degree by Research candidature.				
Signed	X Isabella Poli Isabella Poli		**Date**	03/06/2019	

Journal of
Materials Chemistry C

PAPER

View Article Online
View Journal | View Issue

Cite this: J. Mater. Chem. C, 2018, 6, 7149

Enhancing the hydrophobicity of perovskite solar cells using C18 capped $CH_3NH_3PbI_3$ nanocrystals†

Isabella Poli, *[ab] Xinxing Liang,[a] Robert Baker,[ab] Salvador Eslava [bc] and Petra J. Cameron *[ab]

Received 23rd April 2018,
Accepted 14th June 2018

DOI: 10.1039/c8tc01939h

rsc.li/materials-c

An important limitation in the commercialisation of perovskite solar cells is lack of stability towards moisture due to fast degradation of the absorber perovskite layer. One approach to improve the stability is effective interface engineering by adding materials that can protect the underlying perovskite film. In this work, we look at the incorporation of C18 capped $CH_3NH_3PbI_3$ nanocrystals (MAPI NCs) in perovskite solar cells with both standard and inverted architecture. Three different solution-processing techniques were investigated and compared. We show that solar cells with MAPI NCs integrated at the perovskite–Spiro interface can reach over 10% efficiency. The presence of long chain ligands bound to the MAPI NCs does not appear to damage hole extraction. Most importantly, the hydrophobicity of the surface is significantly enhanced, leading to a much higher device stability towards moisture.

Introduction

Recent years have seen remarkable developments in perovskite solar cells (PSCs) due to their outstanding optoelectronic properties and the numerous cost-efficient processing techniques explored.[1] The great potential of perovskites has been reflected by a very rapid growth in power conversion efficiencies (PCEs), from 10.9% in 2012[2] to the current world record of 22.1% in small cells and 19.7% in 1 cm^2 cells.[3] The high power conversion efficiency, the cheap fabrication and the fast development achieved over very few years make this technology one of the most promising competitors for silicon based photovoltaics. Despite the high performance, there are currently several difficulties in implementing perovskite solar cells as a viable source of energy. The three most important factors preventing halide perovskite photovoltaics from being commercialised are their ecotoxicity, their lack of stability[1] and the current–voltage hysteresis effect.[4]

Standard perovskite solar cells use the highly toxic Pb^{2+} metal cation.[5–7] The use of Pb raises critical environmental concerns,[8] which are made worse by the device instability. The crystal structure and the chemistry of lead halide perovskite based materials are highly sensitive leading to fast degradation in the presence of moisture, heat, light and oxygen.[9,10] Long-term stability towards moisture is currently the biggest challenge. When exposed to moisture, a hydration process occurs, which causes current and voltage losses.[11] This process is irreversible in high humidity environments, leading to dissolution of the methylammonium cation.[11] A lot of recent research has focused on improving the stability of perovskite devices towards high humidity. Alkyl ammonium salts have been used to improve the humidity tolerance of perovskite solar cells either by functionalising the perovskite surface[12] or by partly substituting the alkyl ammonium cation for methylammonium iodide in the precursor solution.[13] Li *et al.* used 2-aminoethanethiol (2-AET) as an additive to generate a barrier layer at the surface of perovskite films; this protected the perovskite crystal structure for over 10 minutes after immersion in water.[14] However, the use of 2-AET in a complete solar cell was not investigated. Major progress has been achieved by using a hydrophobic insulating fluoro-silane tunneling layer to make water-resistant devices.[15] Very recently perovskite solar cells encapsulated with an ultrathin plasma polymer showed unchanged photovoltaic performance after immersion in water for 60 s.[16] Reduced graphene oxide was used as hole transport material, replacing Spiro-OMeTAD and achieving longer stability under light illumination.[17] Another way of enhancing the moisture stability is through 2D/3D hybrid structures[18–21] and cells stable for over one year have already been reported.[22]

Another big challenge in the halide perovskite field is the hysteresis effect. Hysteresis in perovskite solar cells is believed to be caused by both ion migration and the nature of the contact layers. Careful selection of the hole and electron transport materials (HTM and ETM) can reduce the adverse phenomenon.[23,24] Optimization of interfacial charge transfer by interface engineering may also limit surface recombination and benefit the power conversion efficiency.

[a] Department of Chemistry, University of Bath, Bath BA2 7AY, UK. E-mail: i.poli@bath.ac.uk, p.j.cameron@bath.ac.uk
[b] Centre for Sustainable Chemical Technologies, University of Bath, Bath BA2 7AY, UK
[c] Department of Chemical Engineering, University of Bath, Bath BA2 7AY, UK

† Electronic supplementary information (ESI) available. See DOI: 10.1039/c8tc01939h

Small molecules are often deposited at the interface to passivate the surface, reducing defects that may act as trap states.[25] Several strategies have also been investigated to facilitate electron transfer between the perovskite and the ETM. Recently, $CuInS_2$ quantum dots (QDs) were applied on TiO_2 nanorod arrays, where they were believed to facilitate electron injection from the perovskite absorber layer to the TiO_2 scaffold.[26] However, less work has been done to optimise the interface between the perovskite and the HTM. In 2016, $CH_3NH_3PbBr_{0.9}I_{2.1}$ QDs were incorporated at the $CH_3NH_3PbI_3$–HTM interface, where it was suggested that they facilitated hole transfer.[27] Despite the power conversion efficiency being improved by introducing QDs at the interface, no higher stability towards moisture was observed in this study. Other interface engineering strategies used to improve hole transfer at the perovskite/HTM interface were through the use of thiophene derivatives to passivate surface defects and spray-coating of MoS_2 flakes to achieve higher stability and increased performance.[28,29]

Here, we have simultaneously addressed two important issues: the optimisation of the perovskite/HTM interface and the poor water/humidity resistance of halide perovskite films. C18 capped MAPI NCs were incorporated in both the standard and inverted perovskite architecture. To our surprise the C18 ligands did not appear to negatively affect charge transfer from the perovskite film to the HTM in the standard cells. In contrast, when incorporated in inverted structure devices, inverted hysteresis was observed, suggesting that the MAPI NCs might act as an extraction barrier at the $CH_3NH_3PbI_3$/ETM interface. Standard mesoporous solar cells with MAPI NCs at the $CH_3NH_3PbI_3$/HTM interface reached over 10% efficiency with almost no hysteresis. The perovskite film with integrated MAPI NCs was much more hydrophobic. The C18 long chain ligands bound to the MAPI NCs allowed the cells to have a higher water-resistivity and PSCs with capped C18 MAPI NCs showed much higher stability towards moisture with respect to the reference perovskite cells.

Experimental

Materials

CH_3NH_3I (MAI, Dyesol), PbI_2 (PbI_2, 99%, Sigma-Aldrich), $PbCl_2$ (Sigma-Aldrich), *N*,*N*-dimethylformamide (DMF, anhydrous, Sigma-Aldrich). The electron transport material solution consisted of 200 mm titanium diisopropoxide bis(acetylacetonate) (Sigma-Aldrich) in ethanol. The hole transport material solution consisted of 85 mg ml^{-1} Spiro OMeTAD (Sigma-Aldrich) in chlorobenzene (anhydrous, Sigma-Aldrich), with additives of 30 μm ml^{-1} of *t*-butyl pyridine (Sigma Aldrich) and Li-TFSI.

Solvents used for the flow synthesis of the MAPI NCs: 1-octadecene (ODE, 90%, Acros Organics), 1-butanol (BuOH, 99%, Acros Organics), oleylamine (OLA, 80–90%, Acros Organics), oleic acid (OA, 90%, Alfa Aesar) and toluene (ACS reagent, VWR International).

Preparation of MAPI NCs

PbI_2 was dissolved in ODE (sol. 1) and MAI was dissolved in a mixture of ODE and BuOH (sol. 2) with OA and OLA added as ligands. The two solutions were injected through syringe pumps and mixed through a PFA T-junction. The mixed solution was then flowed through a 3 m long PTFE tube immersed in a water bath at 30 °C. The product was collected into an ice bath and centrifuged at 7000 rpm. The solid material was resuspended in toluene and centrifuged again for 10 min. The supernatant solution, the MAPI NCs suspended in toluene, was then further used to fabricate the devices.[30]

Preparation of MAPI active layer

Perovskite deposition was performed in a nitrogen filled glove box.

Method 1. The standard perovskite precursor solutions were prepared by dissolving MAI, PbI_2 and $PbCl_2$ in DMF to get 40 wt% solution (MAI : PbI_2 : $PbCl_2$ – 4 : 1 : 1). 100 μl of precursor solution was spun onto the substrate at 4000 rpm for 30 s, then dried at 100 °C for 100 min. The MAPI NCs dispersed in toluene was spun coated onto the above perovskite layer at 4000 rpm for 30 s followed by annealing at 100 °C for 2 min, forming the perovskite/MAPI NCs film. In the reference perovskite film, no MAPI NCs dispersed in toluene were spin coated on top.

Method 2. The standard perovskite precursor solutions were prepared by dissolving MAI and PbI_2 in DMSO/GBL (3 : 7 vol ratio) to get 40 wt% solution (MAI : PbI_2 – 1 : 1). 100 μl of precursor solution was spun onto the substrate at 5000 rpm for 50 s. At the 25th second 1 ml of MAPI NCs dispersed in toluene was quickly dropped onto the center of the substrate and then dried at 100 °C for 10 min. The reference perovskite film was fabricated using pure toluene as anti-solvent.

Method 3. The PbI_2 precursor solutions were prepared by dissolving PbI_2 in DMF to get 40 w% solution. 100 μl of PbI_2 solution was spun onto the substrate at 3000 rpm for 30 s, then dried at 100 °C for 30 min. In the second step, substrates were dipped in a solution containing MAI for 30 min to allow the conversion of PbI_2 into $CH_3NH_3PbI_3$. The dipping solution consisted of a mixture of MAPI NCs dispersed in toluene and MAI in anhydrous IPA (10 mg ml^{-1}) (1 : 9 vol ratio). The reference perovskite film was fabricated using a dipping solution with MAI in IPA only.

Preparation of devices

FTO glass TEC 15 (Sigma-Aldrich) was etched with zinc powder and HCl. It was then cleaned in 2 vol% Hellmanex solution in water, followed by deionised water, acetone, propan-2-ol and ethanol.

Standard mesoporous cells. A compact TiO_2 layer was deposited by spray pyrolysis, using a hand held atomiser to spray the solution onto the substrates held at 500 °C. Substrates were then sintered at this temperature for 10 minutes. A mesoporous TiO_2 layer (2 : 7 weight mixture of Dyesol's 30NRD TiO_2 paste in ethanol) was spun onto the TiO_2 compact layer and annealed for 15 min at 150 °C and then a further 30 min at 500 °C. After cooling, substrates were placed in a UV Ozone treatment for 30 min.

A perovskite active layer was deposited onto the mesoporous TiO_2 layer following the three different methods outlined in the Experimental section.

Spiro solution was spun onto the perovskite film at 3000 rpm for 30 s. To establish the contacts, a 2 mm wide channel of perovskite was removed from the centre of the substrate. Finally, a 100 nm thick layer of gold was thermally evaporated using evaporation masks to make 6 pixels of 0.0625 cm^2.

Inverted cells. 0.2 M solution of nickel acetate tetrahydrate (Sigma-Aldrich) in 2-methoxyethanol was prepared and stirred at 60 °C until complete dissolution. 12 μl ml^{-1} of ethanolamine was added to the solution, which was then filtered using a 0.45 μm PTFE filter. NiO_x was spun coated onto the UV-ozone treated FTO substrates at 4000 rpm for 30 s and annealed at 400 °C for 30 min. 1.25 : 1.25 molar solution of PbI_2 and MAI in 4 : 1 vol of DMF : DMSO was prepared. 100 μl of precursor solution was spun onto the substrate at 4000 rpm for 30 s. 10 s after the start of the spin, 200 μl of ethyl acetate was deposited directly onto the centre of the spinning sample. Substrates were then dried at 100 °C for 30 min. The MAPI NCs dispersed in toluene was spun coated onto the above perovskite layer at 4000 rpm for 30 s followed by annealing at 100 °C for 2 min, forming the perovskite/MAPI NCs film. 100 μl of PCBM solution (20 mg ml^{-1} in chlorobenzene) was spun onto the perovskite layer at 3000 rpm for 30 s. Finally, a 100 nm thick layer of silver was thermally evaporated using evaporation masks to make 6 pixels of 0.0625 cm^2. In the control inverted devices, no MAPI NCs dispersed in toluene was spun coated on top.

Characterisation

PXRD. Powder diffraction patterns were collected using a Bruker Advance D8 X-ray diffractometer with a Cu Kα source. Measurements were taken from 2θ values of 5° to 80°.

UV/vis spectroscopy. Thin film optical transmission and reflectance measurements were performed on a Perkin-Elmer Lambda 750S UV/vis spectrometer, from 900 nm to 300 nm. Absorption was calculated as $\alpha = \log\left(\frac{1-R}{T}\right)$

***J–V* curves.** *JV* curves were measured using Keithley 2601A potentiostat, under 1 Sun intensity and AM 1.5. The voltage was swept at 100 mV s^{-1} from 1.2 V to 0 V and back to 1.2 V. The 6 pixels were measured independently using a mask to cover the non-active area.

SEM, TEM and AFM images. Top-view and cross section SEM images were taken on a JEOL SEM 6480LV, at an acceleration voltage of 5 kV. Samples for TEM imaging were prepared by dropping the toluene dispersions of the NCs onto carbon supported copper grids followed by drying overnight under vacuum. The TEM measurements were performed on a JEOL JEM-2100Plus transmission electron microscope with an acceleration voltage of 200 kV. AFM images were taken on a Nanosurf easyscan 2 FlexAFM system in Phase Contrast mode using a force of 2 nN. A ContAl-G Tip was used for measurements.

PL fluorescence. Photoluminescence spectra were obtained on a Gilden photonics fluoroSENS fluorimeter. The dispersions of MAPI NCs in toluene were placed in a 1 cm quartz cuvette and excited at 365 nm. The integrating time was 100 ms. All the data were obtained at room temperature and in the air atmosphere.

Results and discussion

C18 capped MAPI NCs were synthesized in toluene with OLA and OA as coligands in a flow system reactor. A TEM image of the MAPI NCs is shown in Fig. 1(a). The nanoparticles produced were of an average size of 10.5 ± 1.5 nm with a cubic morphology. Normal distribution of the particle size was observed, showing high homogeneity in the measured data.

The band gap of the MAPI NCs was estimated from the photoluminescence (PL) spectrum and the UV-vis absorption spectroscopy, which are both shown in Fig. 1(b). The emission peak and the onset absorption coincide at 745 nm, which corresponds to 1.66 eV.

Three different fabrication methods were investigated to incorporate MAPI NCs in the standard perovskite solar cell architecture, which are shown in Fig. 2. When using method 1 (M1), MAPI NCs were deposited on top of the pre-crystallised perovskite layer and, therefore, introduced just at the perovskite/HTM interface. In contrast, method 2 (M2) used MAPI NCs dispersed in toluene as anti-solvent. It is therefore likely that the NCs partially infiltrated the perovskite layer during crystallisation. Finally, when using method 3 (M3) MAPI NCs were mixed into the MAI solution during conversion of PbI_2 into $CH_3NH_3PbI_3$ and distributed throughout the material. MAPI NCs were also incorporated in inverted perovskite solar cells with NiO_x and PCBM used as HTM and ETM respectively. These devices were fabricated using method 1, where MAPI NCs were deposited on top of the crystallised perovskite, as shown in Fig. 2(d).

MAPI NC are capped by oleic acid (OA) and oleylamine (OLA) surface ligands. It has previously been demonstrated that the COO^- functional group in OA and the lone pair on the nitrogen in OLA can coordinate with Pb^{2+} present at the surface of the MAPI NCs.[31–33]

Hydrophobic properties

In this work, pure MAPI perovskite material was investigated. Perovskite devices with compositions of mixed cations and mixed halides in the active absorber layer are well known to be much more efficient and stable than pure $CH_3NH_3PbI_3$.[3,34] The purpose of this work was not to make the highest efficiency cells, but to have a reproducible baseline where any changes due to the presence of MAPI NCs could clearly be seen. Therefore, the cells were not optimised for efficiency as it was more

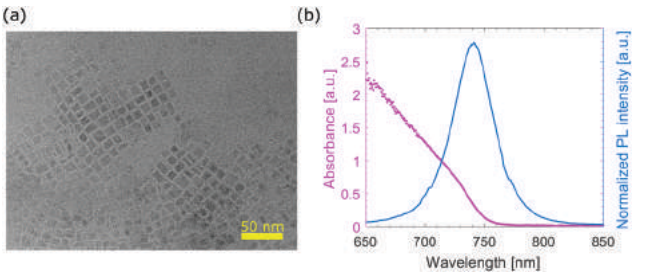

Fig. 1 (a) TEM images of C18 capped MAPI NCs; (b) absorbance and photoluminescence of MAPI NCs in toluene.

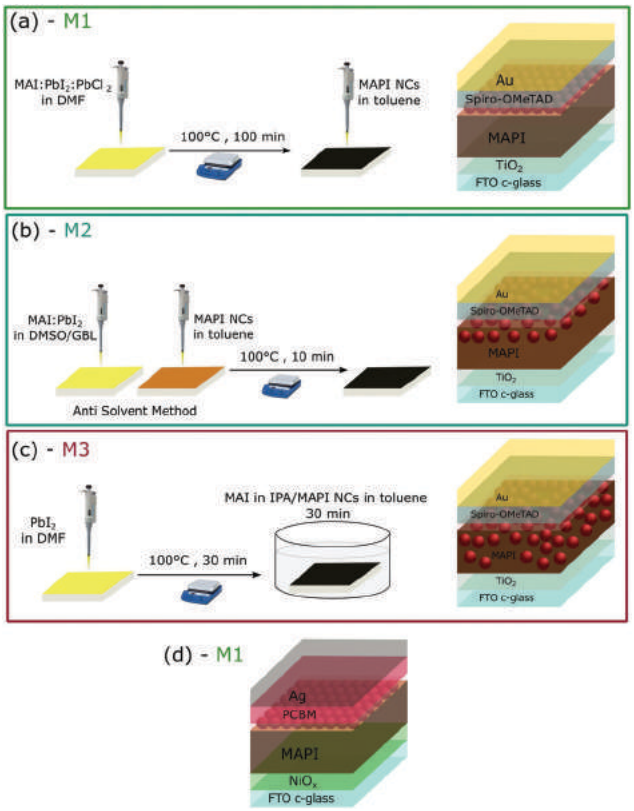

Fig. 2 Schematic illustration of the three fabrication procedures used for the processing of the perovskite solar cells with C18 capped MAPI NCs; (a) method 1 (M1) with MAPI NCs above the perovskite layer; (b) method 2 (M2) with MAPI NCs embedded in the perovskite layer using an anti-solvent deposition technique; (c) method 3 (M3) with MAPI NCs embedded in the perovskite layer using a 2-step deposition technique; (d) inverted architecture deposited using M1 with MAPI NCs above the perovskite layer at the MAPI/PCBM interface.

important to study the influence of MAPI NCs when incorporated in the standard and inverted architecture. Moreover, we were interested in seeing the effect of MAPI NCs on the stability towards moisture and on the water-resistivity of the surface. Therefore we decided to use the least stable perovskite material, which is pure $CH_3NH_3PbI_3$.[35]

Fourier transform infrared (FTIR) spectroscopy was used to verify the presence of the C18 capped MAPI NCs in the perovskite films. All FTIR spectra, shown in Fig. S1 in the ESI,† showed N–H and C–H stretching and bending vibrations for MAPI at around 3130, 2800, 1580 and 1470 cm^{-1}, consistent with previous reports in the literature.[36] When C18 capped MAPI NCs were incorporated in the perovskite film, an new peak at 2925 cm^{-1} was observed, which was assigned to stretching of CH_2,[33] typical of the C18 long chain ligands oleic acid and oleylamine used as surface ligands in the fabrication of MAPI NCs. The peak is particularly visible for films prepared using M1 and M2. The peak intensity is very small compared to the peaks for the bulk MAPI, but confirms the existence of C18 capped MAPI NCs in the materials. The hydrophobic properties of the perovskite films were investigated using contact angle measurements, which are shown in Fig. 3(a). We found that the

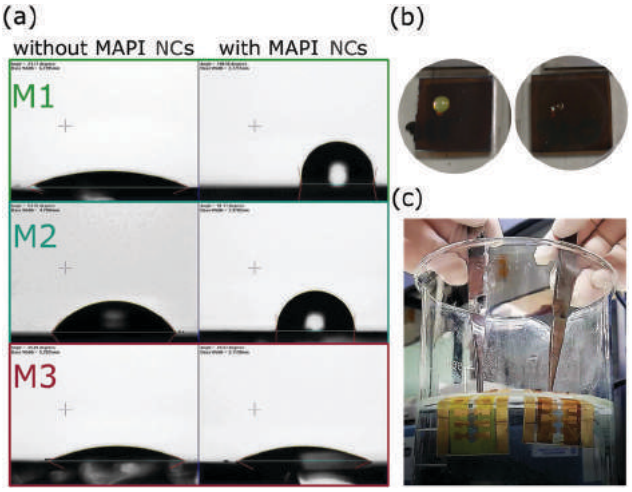

Fig. 3 (a) Contact angle measurements of perovskite films without and with MAPI NCs for perovskite films deposited with methods 1, 2 and 3; from the top to the bottom: 1 – 23° → 101°; 2 – 54° → 92°; 3 – 26° → 26°; (b) picture of perovskite films without and with MAPI NCs deposited on the surface (M1) when one droplet of water is put on the surface; (c) picture of solar cells without (left) and with (right) MAPI NCs after 30 seconds of immersion in water.

surface of perovskite films deposited using M1 and M2 were markedly more hydrophobic when the MAPI NCs were incorporated in the architecture. Contact angles higher than 100° were measured. In contrast, films deposited using M3 did not show improvements in the contact angle, indicating that MAPI NCs were not on its surface.

The presence of long chain C18 OA + OLA ligands stabilised NCs at the perovskite surface clearly enhanced hydrophobicity. In the fabrication of MAPI NCs, the initial concentration of C18 ligands is 15 vol%. The final product is centrifuged and the solid is re-dispersed in toluene in order to obtain equal volume. The exact amount of C18 ligands present in the final solution of MAPI NCs dispersed in toluene is unknown. However, it is expected to be less than 15 vol%. For comparison, the effect of depositing just the long chain ligands OA on the perovskite layer on the surface contact angle was also examined. This was done to investigate if the ligand alone would impart enhanced stability. A solution with different concentration of OA dispersed in toluene, ranging between 10 and 50 vol%, was deposited onto the perovskite film, using method 1. The contact angle, which is shown in Fig. S2 in the ESI,† increased when the long chain ligands were deposited onto the perovskite layer, reaching a maximum value of 60°. However, even when a solution of 50 vol% of OA in toluene was deposited onto the perovskite film, the surface was less hydrophobic than the one obtained by introducing MAPI NCs in the perovskite layer or on the surface (*via* M1 and M2).

Fig. 3(b) shows photographs of perovskite films deposited with method 1 without and with MAPI NCs on the surface when some water was dropped onto the surface. The perovskite films with MAPI NCs (on the right hand side) remained dark brown, while, the reference film became quickly yellow. Similar results were observed when the final solar cells were completely

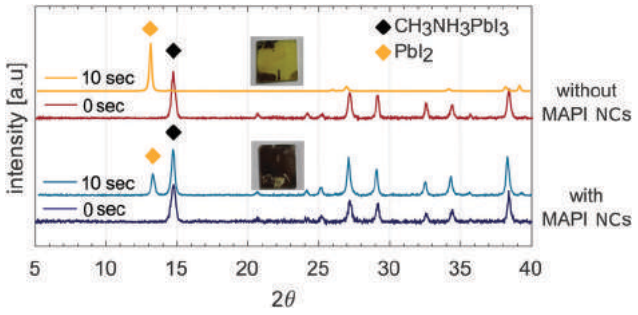

Fig. 4 XRD patterns of films with and without MAPI NCs as soon as deposited and after they have been immersed in water for 10 s.

immersed in water (Fig. 3(c)). The reference perovskite solar cell (left hand side) underwent a rapid colour change from dark brown to yellow, indicating a complete dissociation of the $CH_3NH_3PbI_3$ phase into the PbI_2 phase, while the cell with integrated MAPI NCs remained dark brown.

XRD patterns of perovskite films with and without MAPI NCs above the perovskite layer are shown in Fig. 4 (films fabricated using M1). After the reference perovskite film was immersed in water for 10 seconds, the PbI_2 characteristic peak at 13.2° became the main diffraction peak and the $CH_3NH_3PbI_3$ phase could no longer be detected. The amount of PbI_2 also increased after the perovskite film with MAPI NCs was immersed in water for 10 seconds. However, the tetragonal $CH_3NH_3PbI_3$ phase was still detected and its characteristic peak at 14.7° was identified as the main diffraction peak, indicating that the tetragonal $CH_3NH_3PbI_3$ crystalline phase still dominated.

Photovoltaic performance

Standard and inverted perovskite solar cells with and without MAPI NCs were fabricated using the methods described above. Fig. 5(a) shows the average performing standard mesoporous solar cells fabricated using the three different methods. To examine the reproducibility of photovoltaic performance, different samples were fabricated and measured. Table 1 lists the average values of the main photovoltaic parameters with 95% confidence intervals. The box plots showing the reproducibility of the performance are shown in Fig. S3 in the ESI.† Stabilised power output measurements were collected by monitoring the current when the cell was biased to the maximum power point voltage determined by the *JV* sweep and are shown in Fig. S5 (ESI†). All devices showed a stable output over 60 s. The PCEs of devices with MAPI NCs incorporated at the interface fabricated using M1 were similar to control cells. While, when methods M2 and M3 were used, the control cells showed a superior performance. *JV* curves showing both the forward and reverse scans are shown in Fig. S4 in the ESI.† Cells deposited with method M1 showed consistently reduced hysteresis with respect to cells deposited using M2 and M3. The solar cells deposited using the three different methods have similar V_{OC}, which is slightly larger than the V_{OC} measured in control cells. Films fabricated with the anti-solvent technique (M2) show considerably lower photocurrent density and FF, which are reflected in a decreased PCE. The highest performance is obtained by fabricating cells using the first method M1. Cells with larger active area of 0.25 cm^2 were also fabricated and shown in Fig. S8 in the ESI.† Devices deposited using method M1 showed PCE of 7.8%.

The most efficient cell with a mesoporous standard architecture and integrated MAPI NCs was fabricated using method M1 and gave V_{OC} = 0.74 V, J_{SC} = 20.89 mA cm^{-2}, FF = 68.52 and PCE = 10.6%. Cells fabricated using methods M2 and M3, where MAPI NCs are expected to be embedded in the perovskite active layer, showed consistently lower performance. Previous literature data from Cha *et al.* showed that the introduction of very thin layers of $MAPbBr_xI_{3-x}$ QDs on top of $CH_3NH_3PbI_3$ can change the band edge positions of the material, affecting charge extraction.[27] Similar to what we observe here, they found that QDs embedded in the $CH_3NH_3PbI_3$ perovskite layer produced a PCE of only 6.93%, much lower than what measured when QDs were deposited just at the interface. They attributed the inferior performance to an increased number of recombination centers due to a misalignment of the band edge positions, the hydrophobicity of the films was not investigated.[27]

In the preparation of MAPI NCs, long chain ligands play a crucial role, preventing the aggregation of the perovskite nanocrystals. However, during the fabrication of quantum dot solar cells, organic ligands are usually removed because they can work as insulating barriers to charge transport between the NCs limiting the PCE of the device.[37] Surprisingly, the presence of C18 capped MAPI NCs did not appear to obstruct charge extraction in our standard architecture solar cells.

Photocurrent generation is directly related to the light-harvesting properties of the absorber layer. Gao *et al.* found that $CuInS_2$ QDs integrated at the perovskite/ETM interface could assist light harvesting, increasing the absorbed light and the device performance.[26] To check whether the NCs had an effect on the absorption properties, UV-vis absorption of perovskite films with and without MAPI NCs was measured. The curves, which are shown in Fig. S9 of the ESI,† were found to be very similar, suggesting that the MAPI NCs did not affect light absorption in the active layer. This result is fully consistent with what was previously reported in the literature for perovskite films with $MAPbBr_{3-x}I_x$ QDs on top.[27]

Recently, Yavari *et al.* observed that the incorporation of carbon nanoparticles into the perovskite active layer could boost the surface coverage of the film by enlarging grains compared to reference perovskite films.[38] We investigated possible changes in the morphology through top-view SEM and AFM and cross-sectional SEM images. Fig. 5(b) shows cross section SEM images of perovskite solar cells deposited using method 2 without and with C18 capped MAPI NCs. NCs can not be seen in the active layer and the film thickness does not appear to change. In Fig. 5(c) the surface of perovskite films with and without MAPI NCs deposited on top (M1) is compared through top-view SEM images. These films were deposited by using method 1 to see whether any changes due to the presence of NCs on the surface could clearly be seen. However, changes in the surface morphology are negligible. The influence of the concentration of MAPI NCs on the morphology was also

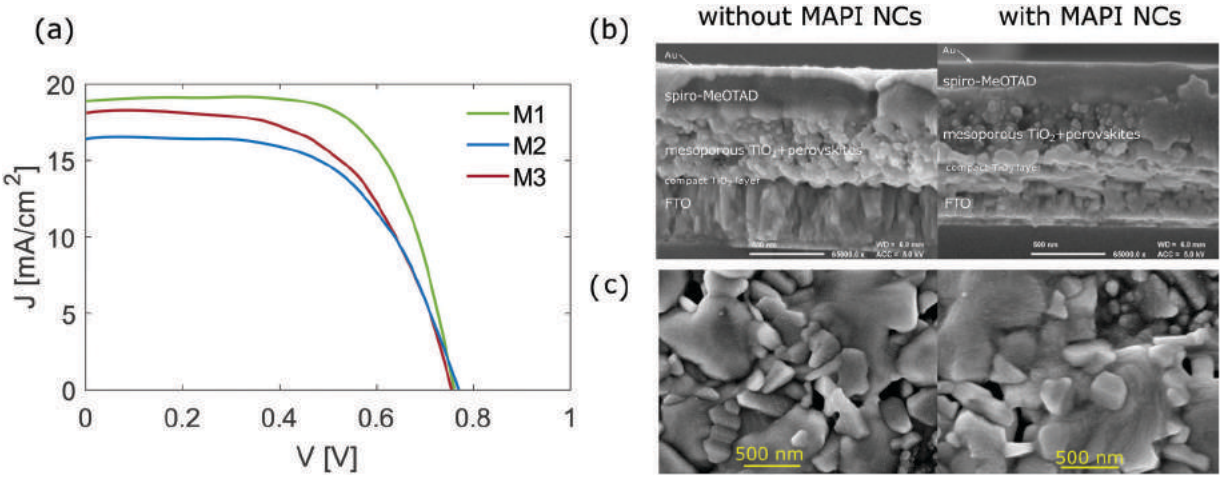

Fig. 5 (a) *JV* curves of average performing solar cells fabricated using the three different deposition method (only the reverse scan is showed, the forward scan is in Fig. S4 in the ESI†); (b) cross-section SEM images of perovskite films without and with C18 capped MAPI NCs. Perovskite solar cells fabricated using the second method M2 *via* the anti-solvent technique, where the NCs are embedded in the perovskite film; (c) top-view SEM images of perovskite films without and with C18 capped MAPI NCs. Perovskite films deposited using the first method M1, where the NCs are above the perovskite film.

Table 1 Average PV parameters for mesoporous cells deposited using the three different methods with 95% confidence intervals

Param.	Control	M1	M2	M3
J_{SC} [mA cm^{-2}]	19.98 ± 0.26	18.48 ± 0.76	15.40 ± 1.01	18.21 ± 1.08
V_{OC} [V]	0.73 ± 0.01	0.76 ± 0.02	0.76 ± 0.01	0.76 ± 0.02
FF [—]	68.57 ± 4.24	68.22 ± 1.37	61.88 ± 2.99	63.54 ± 2.70
PCE [%]	10.05 ± 0.55	9.61 ± 0.32	7.19 ± 0.21	8.80 ± 0.74

investigated and showed in Fig. S11 in the ESI† through AFM images (films deposited using method 1).

To further investigate the effect that MAPI NCs might have at the interface, different contact layers were used. MAPI NCs were integrated in an inverted structure with NiO_x and PCBM used as HTM and ETM respectively by depositing them above the perovskite layer as described in the Experimental section. Fig. 2(d) presents a schematic of the inverted device. Fig. 6(a) shows the *JV* curves of an inverted solar cell with integrated MAPI NCs measured under forward and reverse scan. Interestingly, inverted hysteresis was observed, where the V_{OC} measured during forward scan was much larger than the one measured during the reverse scan. A similar phenomenon was observed for all the inverted cells with MAPI NCs fabricated for this study. Fig. 6(b) shows the V_{OC}

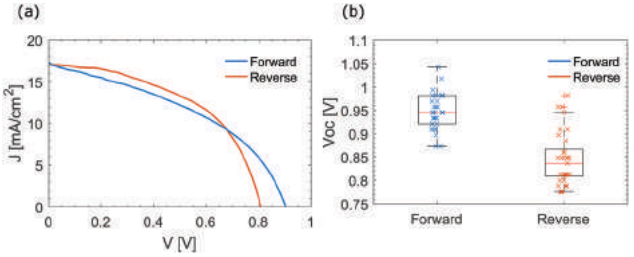

Fig. 6 (a) *JV* curves of an inverted structure perovskite solar cell with MAPI NCs incorporated at the $CH_3NH_3PbI_3$/ETM interface; (b) comparison of the open circuit voltages measured during forward and reverse scan for over 30 devices.

measured by the reverse and forward scan for over 30 different devices fabricated in different days. In contrast, almost no hysteresis was observed in the inverted control devices without MAPI NCs at the $CH_3NH_3PbI_3$/PCBM interface. A typical *JV* curve and box plots of the V_{OC} under forward and reverse scan are shown in the ESI† in Fig. S13. The champion control inverted cell without MAPI NCs exhibited V_{OC} = 0.93 V, J_{SC} = 16.74 mA cm^{-2}, FF = 69.71 and PCE = 10.89%, with very low hysteresis. While, very high inverted hysteresis was measured for the solar cells with MAPI NCs. The most efficient cell with an inverted architecture and integrated MAPI NCs exhibited V_{OC} = 0.85 V, J_{SC} = 18.61 mA cm^{-2}, FF = 68.03 and PCE = 10.75% during reverse scan and V_{OC} = 0.95 V, J_{SC} = 17.67 mA cm^{-2}, FF = 43.01 and PCE = 7.18% during forward scan.

Recent studies have associated the inverted hysteresis phenomenon with the presence of an extraction barrier at the perovskite/ETM interface.[39,40] As suggested by Cha *et al.*, very thin layers of MAPI NCs might change the surface properties of $CH_3NH_3PbI_3$, affecting the charge extraction.[27] Electrochemical experiments can be very useful in understanding the chemical changes occurring at the perovskite/HTM interface.[41] The anodic part of CV scans of a perovskite film and a perovskite/MAPI NCs film are shown in Fig. S14(a) in the ESI.† When MAPI NCs were deposited on the surface, the peak slightly shifted to lower voltages. The position of the first oxidation peak of the $CH_3NH_3PbI_3$ and $CH_3NH_3PbI_3$/MAPI NCs films was calculated from the onset potential of the redox waves and it was found to be −5.32 eV and −5.27 eV respectively. Very recently, Samu *et al.* looked at the reduction and oxidation events that occur in halide perovskites and concluded that CV scans alone can not be used to determine the band edge positions of $CH_3NH_3PbI_3$. Other chemical processes occur in the material within the electrochemical window, therefore the measured currents can not be related to actual carrier injection.[42] Even though the exact band edge positions of $CH_3NH_3PbI_3$ and MAPI NCs can not be determined from CV scans, a consistent difference between the

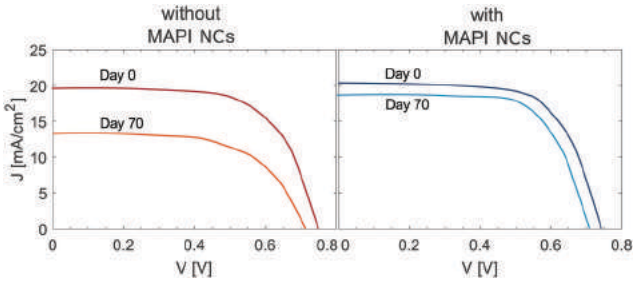

Fig. 7 Shelf-stability of the perovskite devices fabricated using method 1. *JV* curves of solar cells without and with MAPI NCs as soon as fabricated and after 70 days of ageing in ambient atmosphere (method 1 M1 was used to fabricate these cells). Without MAPI NCs – day 0: PCE = 9.57%, day 70: PCE = 5.81%; with MAPI NCs – day 0: PCE = 10.47%, day 70: PCE = 9.27%.

onset potential of the redox events was detected for the studied films, highlighting different material properties. The inverted hysteresis observed in the inverted architecture with MAPI NCs suggested that such interlayer may act as an extraction barrier at the $CH_3NH_3PbI_3$/ETM interface. When the same NC layer was used at the $CH_3NH_3PbI_3$/HTM interface no change in the shape of the *JV* curve was observed suggesting that the NCs are not detrimental at this interface.

Moisture stability

To investigate the stability of the perovskite solar cells, the PCE of two devices with and without C18 capped MAPI NCs was measured 70 days after fabrication. During this time period, the cells were left in an ambient atmosphere without encapsulation, in the dark, at open circuit with relative humidity (RH) measured to be 60 ± 10% (also known as shelf-stability). Two sets of cells were fabricated on the same day and exposed to the same ageing process. Two solar cells with similar initial PCEs were evaluated, the *JV* curves measured on the day of fabrication and after 70 days are shown in Fig. 7. The PCE of the reference cell decreased by over 40%. The main parameter affecting the reduced PCE was the current density. This might be due to a degradation of the perovskite $CH_3NH_3PbI_3$ to PbI_2, due to the presence of moisture which caused a decreased light harvesting. In contrast, the cell with integrated MAPI NCs decreased by only 10%, showing what we believe to be enhanced stability towards moisture due to the hydrophobic nature of $CH_3NH_3PbI_3$/MAPI NCs layers.

Conclusions

We developed standard mesoporous and inverted perovskite solar cells with integrated C18 capped MAPI NCs. Inverted hysteresis was observed in the inverted architecture, suggesting that the MAPI NCs introduced an extraction barrier at the $CH_3NH_3PbI_3$/ETM interface. In contrast, the hole extraction was not affected when the MAPI NCs were deposited at the $CH_3NH_3PbI_3$/HTM interface in standard mesoporous cells.

Three different deposition methods were investigated. MAPI NCs were deposited just at the $CH_3NH_3PbI_3$/HTM interface and embedded in the perovskite active layer. When using method 1, in which MAPI NCs were above the perovskite layer, solar cells with PCEs over 10% were measured. While, when using method 2 with MAPI NCs embedded in the perovskite layer, devices with only 7% conversion efficiency were obtained.

MAPI NCs did not contribute to the light-harvesting, however they gave the perovskite films higher hydrophobicity with surface water contact angles that exceeded 100°. XRD measurements showed that the tetragonal $CH_3NH_3PbI_3$ phase was retained after the film was immersed in water for 10 s. Such hydrophobic properties allowed solar cells with MAPI NCs to be much more stable towards moisture with respect to the reference perovskite solar cells.

MAPI NCs were fabricated in a flow reactor, in ambient conditions and at room temperature, therefore, no complex production steps were added to the PSC fabrication. Flow chemistry allows fast reactions, clean products and it is a technique that is very easy to scale-up, which is crucial for viable and commercial photovoltaic technologies.

Conflicts of interest

There are no conflicts to declare.

Acknowledgements

We acknowledge the MAS staff at University of Bath for their assistance in SEM acquisition. We would like to thank the EPSRC Centre for Doctoral Training in Sustainable Chemical Technologies (EP/L016354/1). This project has received funding from the European Union's Horizon 2020 research and innovation programme H2020-MSCA-CO-FUND-2014 (# 665992, MSCA FIRE: Fellows with Industrial Research Enhancement).

References

1 M. A. Green, A. Ho-Baillie and H. J. Snaith, *Nat. Photonics*, 2014, **8**, 506–514.
2 M. M. Lee, J. Teuscher, T. Miyasaka, T. N. Murakami and H. J. Snaith, *Science*, 2012, **338**, 643–647.
3 W. S. Yang, B.-W. Park, E. H. Jung, N. J. Jeon, Y. C. Kim, D. U. Lee, S. S. Shin, J. Seo, E. K. Kim, J. H. Noh and S. I. Seok, *Science*, 2017, **356**, 1376–1379.
4 G. A. Nemnes, C. Besleaga, V. Stancu, D. E. Dogaru, L. N. Leonat, L. Pintilie, K. Torfason, M. Ilkov, A. Manolescu and I. Pintilie, *J. Phys. Chem. C*, 2017, **121**, 11207–11214.
5 N. K. Noel, S. D. Stranks, A. Abate, C. Wehrenfennig, S. Guarnera, A.-A. Haghighirad, A. Sadhanala, G. E. Eperon, S. K. Pathak, M. B. Johnston, A. Petrozza, L. M. Herz and H. J. Snaith, *Energy Environ. Sci.*, 2014, **7**, 3061.
6 F. Hao, C. C. Stoumpos, D. H. Cao, R. P. Chang and M. G. Kanatzidis, *Nat. Photonics*, 2014, **8**, 489–494.
7 C. Liu, J. Fan, H. Li, C. Zhang and Y. Mai, *Sci. Rep.*, 2016, **6**, 35705.
8 F. Giustino and H. J. Snaith, *ACS Energy Lett.*, 2016, **1**, 1233–1240.

9 D. Wang, M. Wright, N. K. Elumalai and A. Uddin, *Sol. Energy Mater. Sol. Cells*, 2016, **147**, 255–275.
10 N. Aristidou, C. Eames, I. Sanchez-molina, X. Bu, J. Kosco, M. S. Islam and S. A. Haque, *Nat. Commun.*, 2017, **8**, 1–40.
11 A. M. A. Leguy, Y. Hu, M. Campoy-Quiles, M. I. Alonso, O. J. Weber, P. Azarhoosh, M. van Schilfgaarde, M. T. Weller, T. Bein, J. Nelson, P. Docampo and P. R. F. Barnes, *Chem. Mater.*, 2015, **27**, 3397–3407.
12 S. Yang, Y. Wang, P. Liu, Y.-B. Cheng, H. J. Zhao and H. G. Yang, *Nat. Energy*, 2016, **1**, 1–7.
13 I. Poli, S. Eslava and P. Cameron, *J. Mater. Chem. A*, 2017, **5**, 22325–22333.
14 B. Li, C. Fei, K. Zheng, X. Qu, T. Pullerits, G. Cao and J. Tian, *J. Mater. Chem. A*, 2016, **4**, 17018–17024.
15 Q. Wang, Q. Dong, T. Li, A. Gruverman and J. Huang, *Adv. Mater.*, 2016, **28**, 6734–6739.
16 J. Idigoras, F. J. Aparicio, L. Contreras-Bernal, S. Ramos-Terrón, M. Alcaire, J. R. Sanchez-Valencia, A. Borras, A. Barranco and J. A. Anta, *ACS Appl. Mater. Interfaces*, 2018, **10**, 11587–11594.
17 A. Palma, L. Cinà, S. Pescetelli, A. Agresti, M. Raggio, R. Paolesse, F. Bonaccorso and A. Di Carlo, *Nano Energy*, 2016, **22**, 349–360.
18 C. Ma, C. Leng, Y. Ji, X. Wei, K. Sun, L. Tang, J. Yang, W. Luo, C. Li, Y. Deng, S. Feng, J. Shen, S. Lu, C. Du and H. Shi, *Nanoscale*, 2016, **338**, 643–647.
19 H. Tsai, W. Nie, J.-C. Blancon, C. C. Stoumpos, R. Asadpour, B. Harutyunyan, A. J. Neukirch, R. Verduzco, J. J. Crochet, S. Tretiak, L. Pedesseau, J. Even, M. A. Alam, G. Gupta, J. Lou, P. M. Ajayan, M. J. Bedzyk, M. G. Kanatzidis and A. D. Mohite, *Nature*, 2016, **536**, 312–316.
20 D. H. Cao, C. C. Stoumpos, T. Yokoyama, J. L. Logsdon, T.-B. Song, O. K. Farha, M. R. Wasielewski, J. T. Hupp and M. G. Kanatzidis, *ACS Energy Lett.*, 2017, **2**, 982–990.
21 I. C. Smith, E. T. Hoke, D. Solis-Ibarra, M. D. McGehee and H. I. Karunadasa, *Angew. Chem., Int. Ed.*, 2014, **53**, 11232–11235.
22 G. Grancini, I. Zimmermann, E. Mosconi, D. Martineau and S. Narbey, *Nat. Commun.*, 2017, **8**, 1–8.
23 D. A. Jacobs, Y. Wu, H. Shen, C. Barugkin, F. J. Beck, T. P. White, K. Weber and K. R. Catchpole, *Phys. Chem. Chem. Phys.*, 2017, **19**, 3094–3103.
24 S. V. Reenen, M. Kemerink and H. J. Snaith, *J. Phys. Lett.*, 2015, **6**, 3808–3814.
25 W. Deng, X. Liang, P. S. Kubiak and P. J. Cameron, *Adv. Energy Mater.*, 2018, **8**, 1–20.
26 F. Gao, H. Dai, H. Pan, Y. Chen, J. Wang and Z. Chen, *J. Colloid Interface Sci.*, 2017, **513**, 693–699.
27 M. Cha, P. Da, J. Wang, W. Wang, Z. Chen, F. Xiu, G. Zheng and Z.-S. Wang, *J. Am. Chem. Soc.*, 2016, **138**, 8581–8587.
28 T. Y. Wen, S. Yang, P. F. Liu, L. J. Tang, H. W. Qiao, X. Chen, X. H. Yang, Y. Hou and H. G. Yang, *Adv. Energy Mater.*, 2018, **1703143**, 1–7.
29 A. Capasso, F. Matteocci, L. Najafi, M. Prato, J. Buha, L. Ciná, V. Pellegrini, A. D. Carlo and F. Bonaccorso, *Adv. Energy Mater.*, 2016, **6**, 1–12.
30 X. Liang, W. Deng, K. Wu, R. Baker, D. Ferdani, L. Torrente-Murciano and P. Cameron, 2018, submitted.
31 A. Pan, B. He, X. Fan, Z. Liu, J. J. Urban, A. P. Alivisatos, L. He and Y. Liu, *ACS Nano*, 2016, **10**, 7943–7954.
32 S. Sun, D. Yuan, Y. Xu, A. Wang and Z. Deng, *ACS Nano*, 2016, **10**, 3648–3657.
33 Y. Zhao, X. Xu and X. You, *Sci. Rep.*, 2016, **6**, 1–8.
34 A. D. Jodlowski, C. Roldán-Carmona, G. Grancini, M. Salado, M. Ralaiarisoa, S. Ahmad, N. Koch, L. Camacho, G. De Miguel and M. K. Nazeeruddin, *Nat. Energy*, 2017, **2**, 972–979.
35 T. Leijtens, K. Bush, R. Cheacharoen, R. Beal, A. Bowring and M. D. McGehee, *J. Mater. Chem. A*, 2017, **5**, 11483–11500.
36 Y. Wang, T. Mahmoudi, W. Y. Rho, H. Y. Yang, S. Seo, K. S. Bhat, R. Ahmad and Y. B. Hahn, *Nano Energy*, 2017, **40**, 408–417.
37 J. Peng, Y. Chen, X. Zhang, A. Dong and Z. Liang, *Adv. Sci.*, 2016, **3**, 1500432.
38 M. Yavari, M. Mazloum-Ardakani, S. Gholipour, N. Marinova, J. L. Delgado, S.-H. Turren-Cruz, K. Domanski, N. Taghavinia, M. Saliba, M. Grätzel, A. Hagfeldt and W. Tress, *Adv. Energy Mater.*, 2018, **8**, 1702719.
39 W. Tress, J. P. Correa Baena, M. Saliba, A. Abate and M. Graetzel, *Adv. Energy Mater.*, 2016, **6**, 1–11.
40 H. Shen, D. A. Jacobs, Y. Wu, T. Duong, J. Peng, X. Wen, X. Fu, S. K. Karuturi, T. P. White, K. Weber and K. R. Catchpole, *J. Phys. Chem. Lett.*, 2017, **8**, 2672–2680.
41 L. Zhao, R. A. Kerner, Z. Xiao, Y. L. Lin, K. M. Lee, J. Schwartz and B. P. Rand, *ACS Energy Lett.*, 2016, **1**, 595–602.
42 G. F. Samu, R. A. Scheidt, P. V. Kamat and C. Janáky, *Chem. Mater.*, 2018, **30**, 561–569.

Supporting Information for

Enhancing the hydrophobicity of perovskite solar cells using C18 capped $CH_3NH_3PbI_3$ nanocrystals

Isabella Poli,[§] [‡] *Xinxing Liang,* [§] *Robert Baker,* [§] [‡] *Salvador Eslava,*[¶] [‡] *and Petra Cameron*[§] [‡]

[§]*Department of Chemistry, University of Bath, Bath BA2 7AY, United Kingdom*

[¶]*Department of Chemical Engineering, University of Bath, Bath BA2 7AY, United Kingdom*

[‡]*Centre for Sustainable Chemical Technologies, University of Bath, Bath BA2 7AY, United Kingdom*

Experimental

Characterisation

Cyclic Voltammetry Cyclic Volatmmetry (CV) scans were performed in a dichloromethane (DCM) solution of 0.1 M Bu_4NPF_6 at a scan rate of $20\,mV\,s^{-1}$. Ag/AgCl was used as reference electrode and Pt as counter electrode. The oxidative peak potential of Ag/AgCl *vs* the normal hydrogen electrode (NHE) is set to 0.197 V and the NHE *vs* the vacuum level to 4.5 V [1]. The VB level was calculated according to the formula VB=-(E^{ox}+4.697) eV. The oxidation potential E^{ox} was calculated from the onset potential of the redox wave.

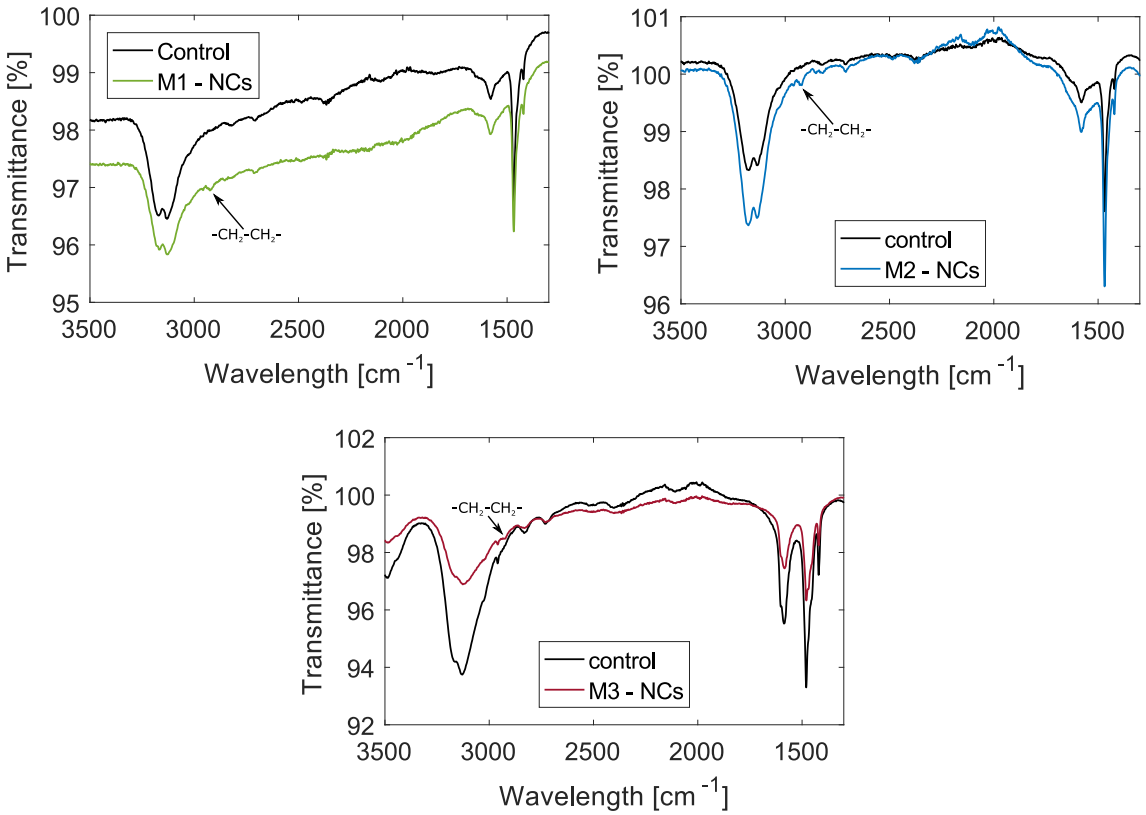

Fig. S1: FTIR spectra of perovskite films with and without MAPI NCs incorporated using methods M1, M2 and M3

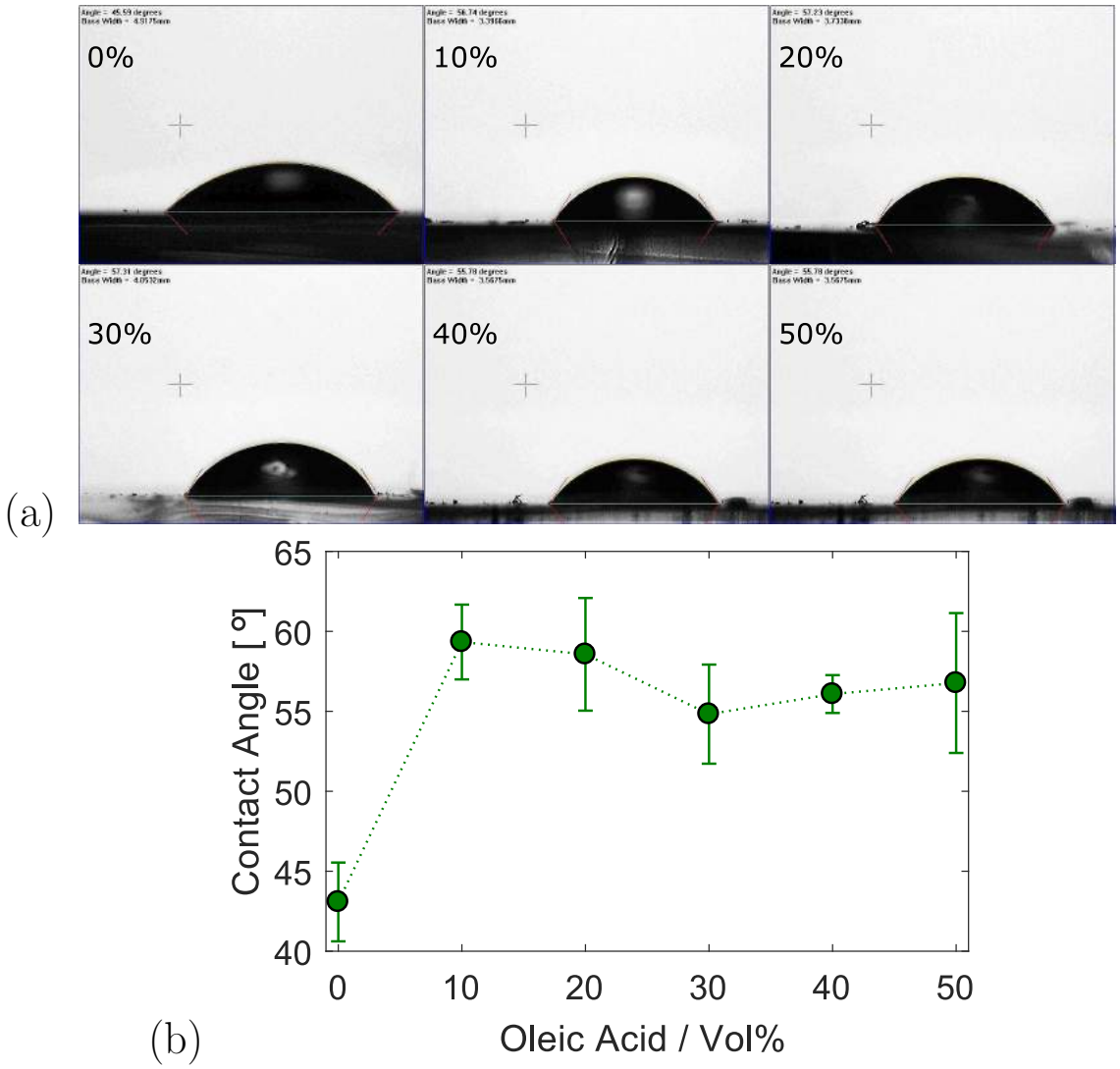

Fig. S2: (a) Surface water contact angles of perovskite films with different concentration of OA in toluene; (b) variation of the contact angle with the concentration of OA in toluene.

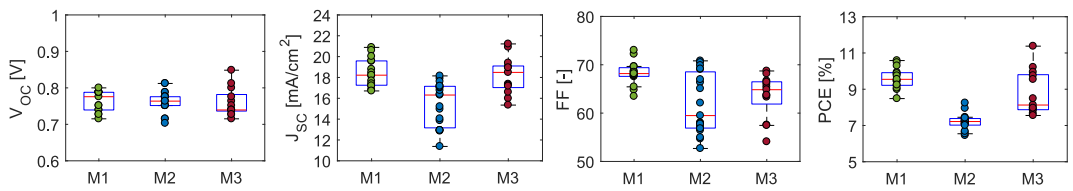

Fig. S3: Photovoltaic parameters shown as box plots for efficiency distributions of standard perovskite solar cells fabricated using three different deposition techniques. Cells have been tested under AM 1.5 and 1 sun illumination. The reproducibility is evaluated by characterising 15, 19 and 13 cells for M1, M2 and M3 respectively

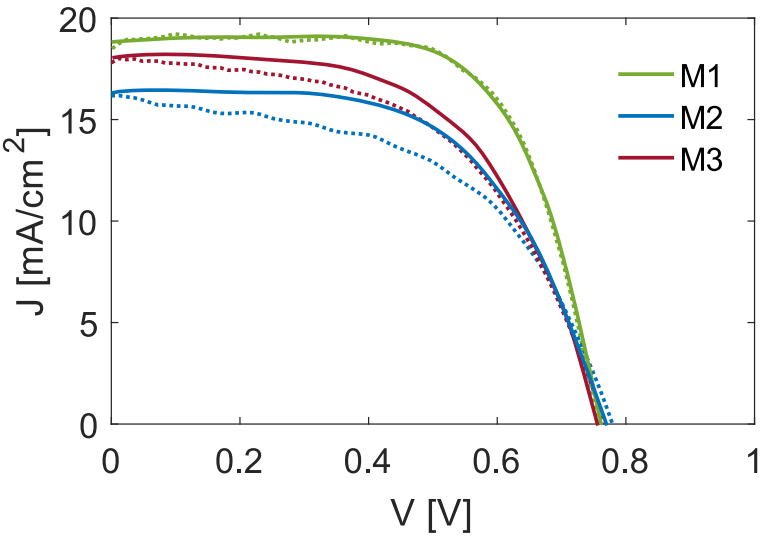

Fig. S4: JV curves of average performing solar cells deposited via the three different methods M1, M2 and M3. The solid line is the curve measured under reverse scan, while the dotted line is the one measured under forward scan.

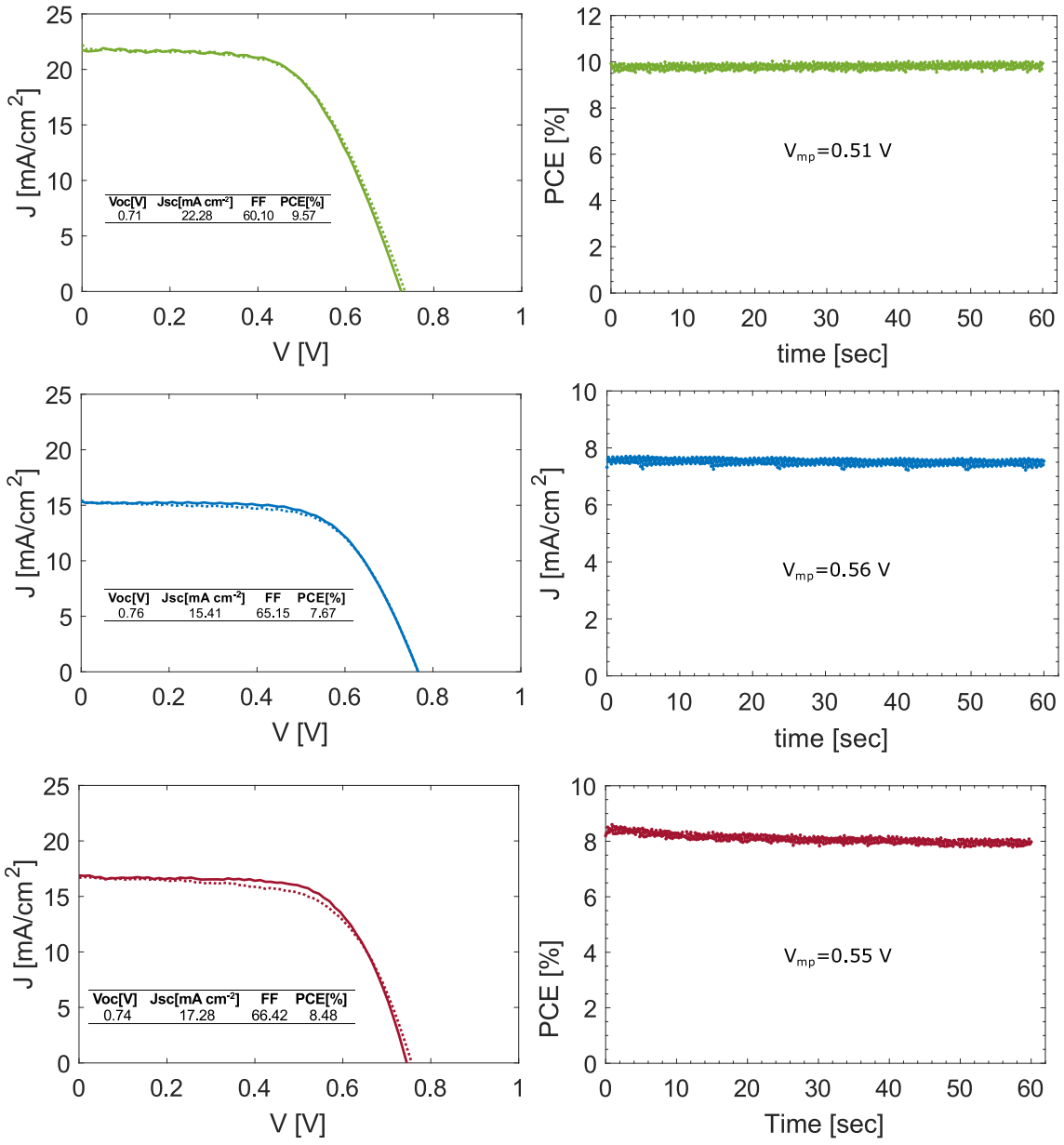

Fig. S5: JV curves of solar cells deposited via the three different methods M1, M2 and M3 (from top to bottom). Stabilised power conversion efficiency was measured by applying the maximum voltage point calculated during the JV scan for 60 seconds

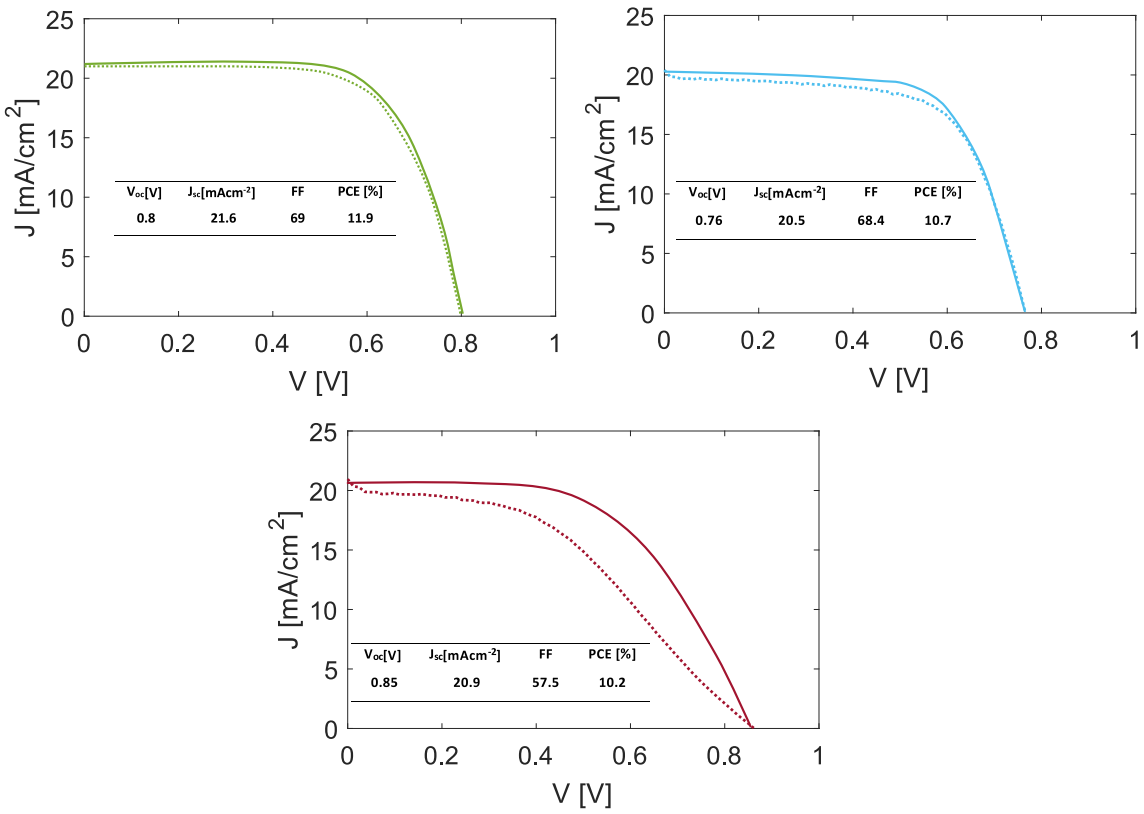

Fig. S6: JV curves of control mesoporous devices (without MAPI NCs) deposited via the three different methods M1, M2 and M3 (from top to bottom)

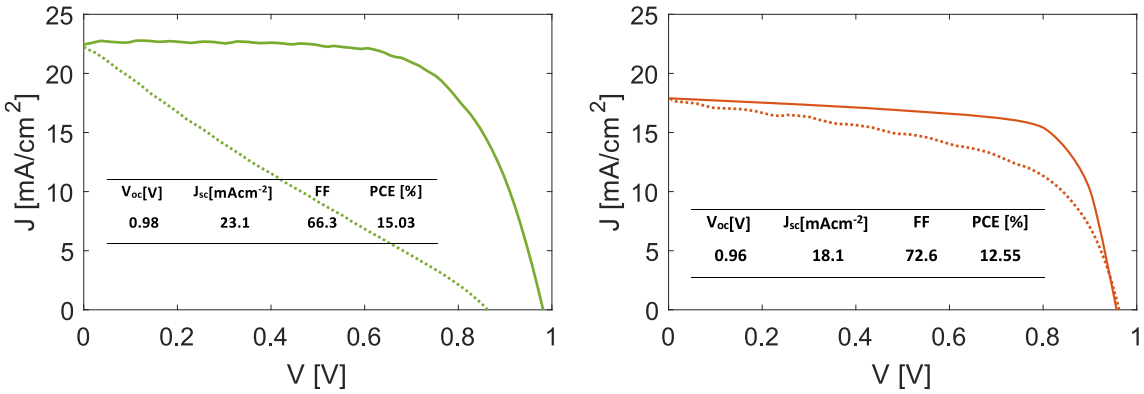

Fig. S7: JV curves of control standard planar device (left) and inverted cell (right)

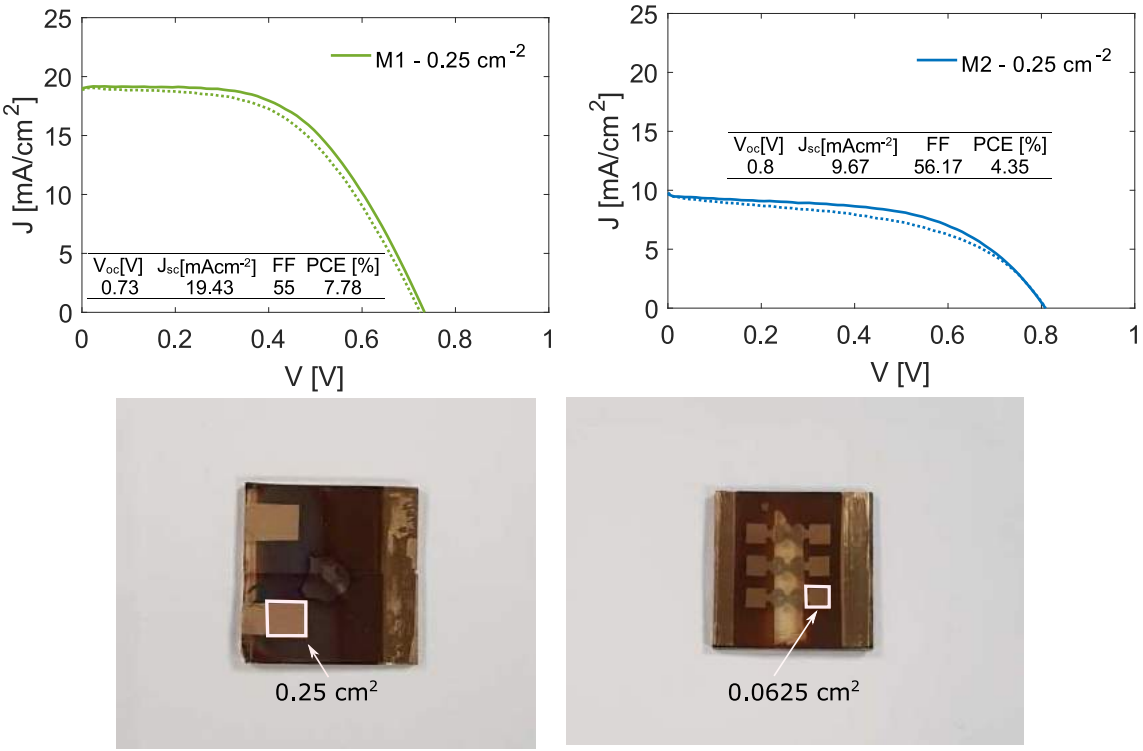

Fig. S8: JV curves and pictures of perovskite solar cells fabricated using method M1 and M2. The active area is 0.25 cm^2.

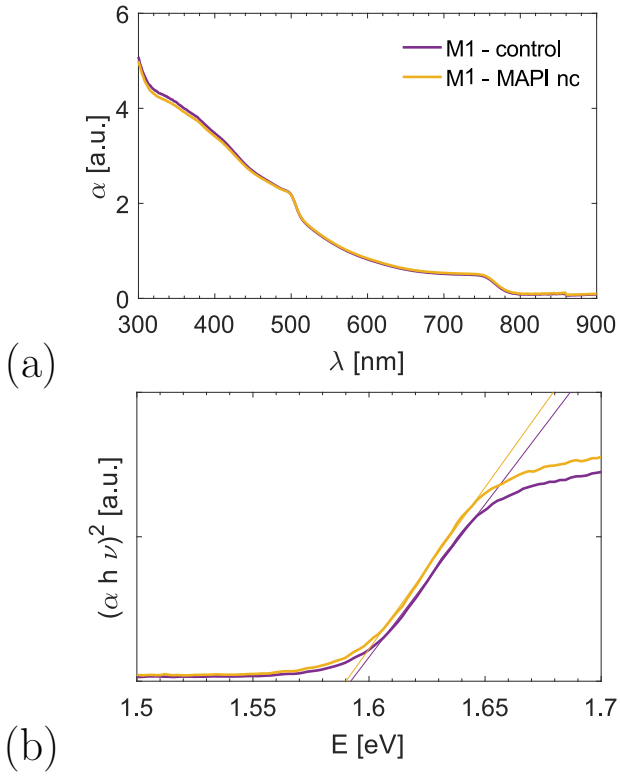

Fig. S9: (a) UV-vis absorption and (b) Tauc plot of perovskite films without and with the incorporated MAPI NCs

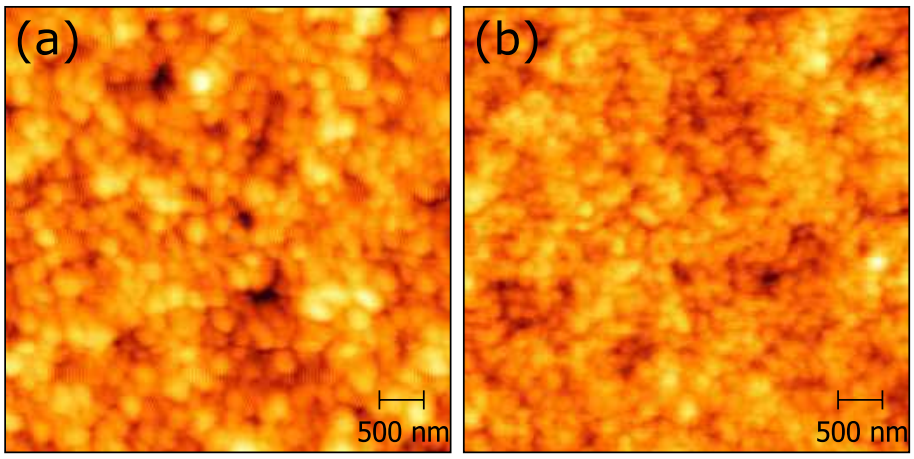

Fig. S10: AFM images of perovskite films (a) without and (b) with integrated MAPI NCs. Films deposited by using the second deposition method M2

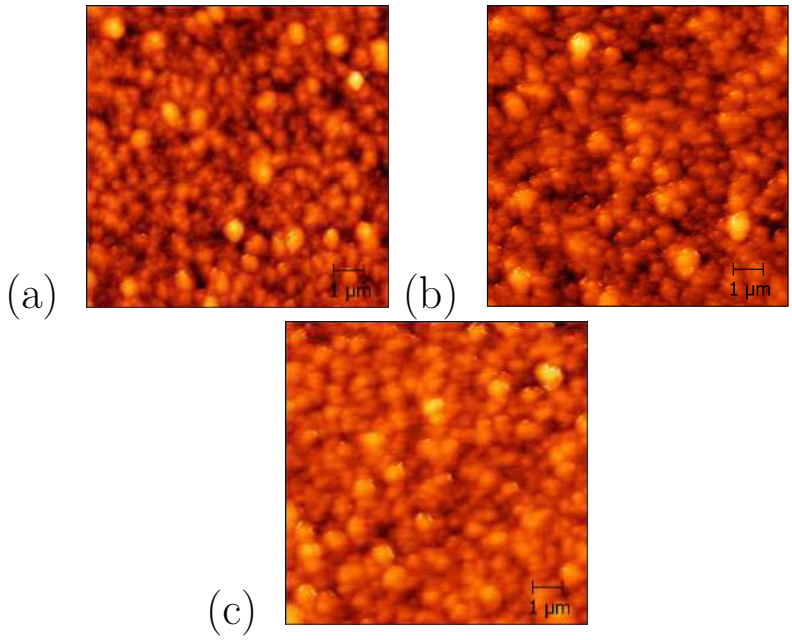

Fig. S11: AFM images of perovskite films with integrated MAPI NCs. The MAPI NCs dispersed in toluene solution was diluted in order to obtain less concentrated solutions (NCs+toluene:toluene-65:35 and NCs+toluene:toluene-30:70) (a) NCs+toluene:toluene - 30:70 (b) NCs+toluene:toluene - 65:35 (c) NCs+toluene:toluene - 100:0

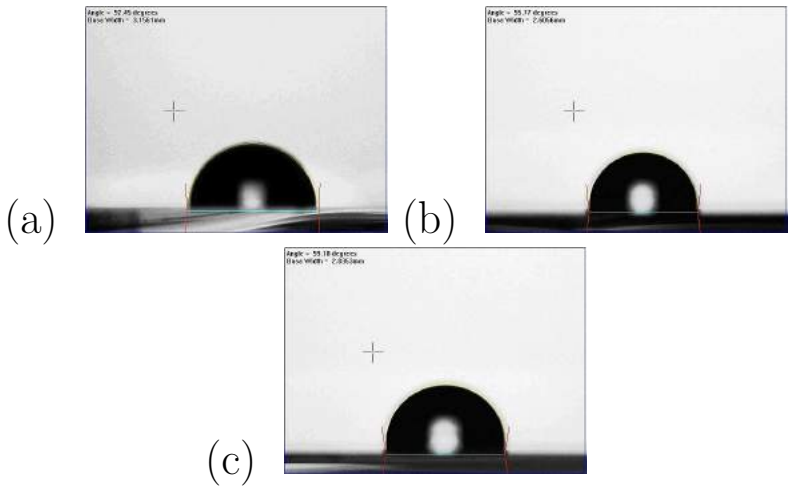

Fig. S12: Surface water contact angle of perovskite films with integrated MAPI NCs. Different concentration of the MAPI NCs solution is used: (a) NCs+toluene:toluene - 30:70 (92°) (b) NCs+toluene:toluene - 65:35 (96°) (c) NCs+toluene:toluene - 100:0 (99°)

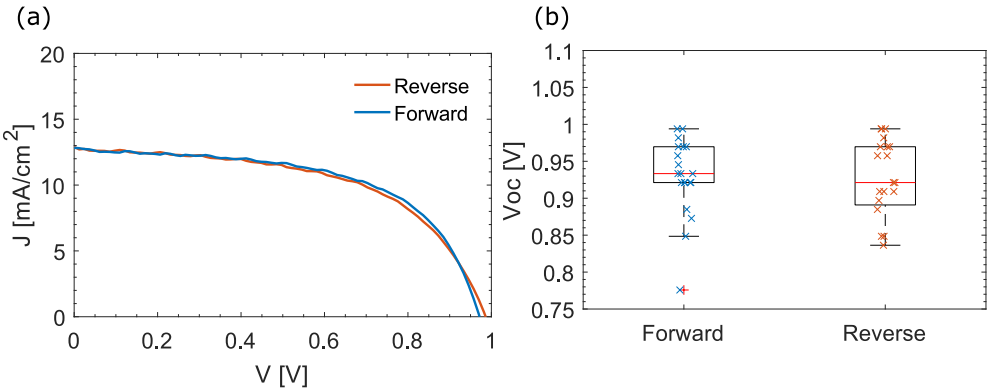

Fig. S13: (a) JV curves of an inverted structure perovskite solar cell without MAPI NCs incorporated at the $CH_3NH_3PbI_3$/PCBM interface; (b) Comparison of the open circuit voltages measured by the forward and reverse scan for control cells with inverted architecture

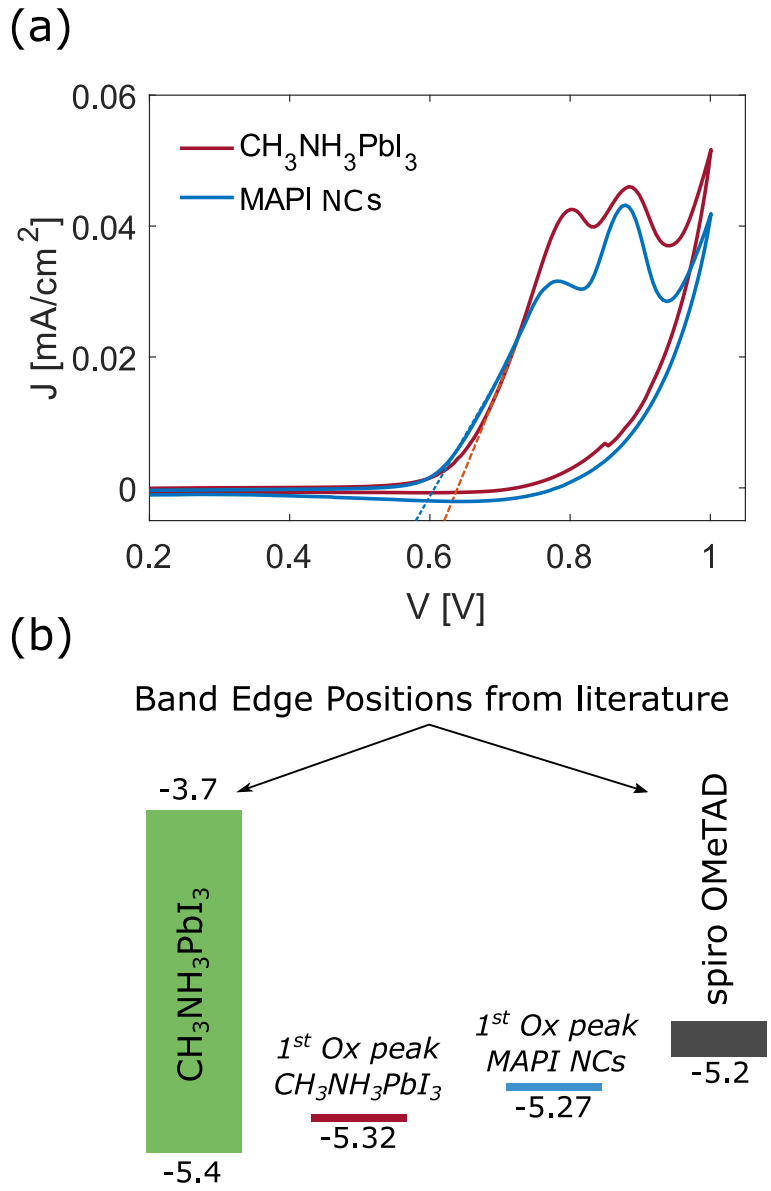

Fig. S14: (a) cyclic voltammetry data of perovskite and perovskite/MAPI NCs (fabricated by using M1) in a DCM solution of 0.1 M Bu_4NPF_6 at a scan rate of 20 mV/s; (b) Comparison of the band edge positions of $CH_3NH_3PbI_3$ and spiro-OMeTAD and the position of the first oxidation peaks detected for the studied materials

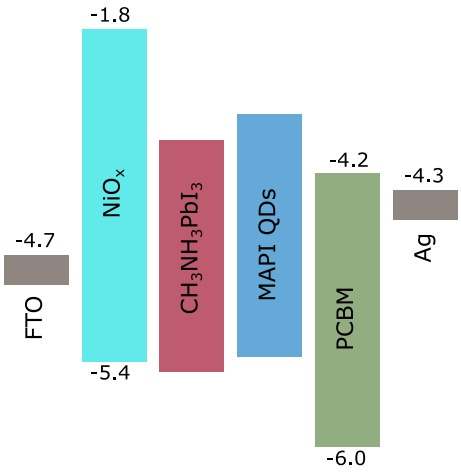

Fig. S15: sketch of the energy band diagram of an inverted architecture. Higher CB position of MAPI NCs might create an extraction barrier at the interface that could cause the inverted hysteresis phenomenon

(a) 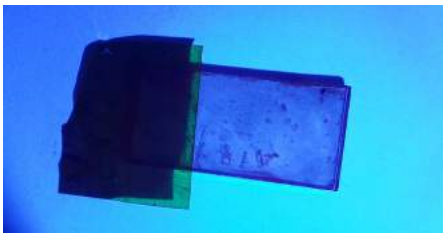 (b) 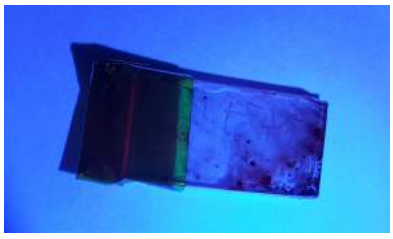

Fig. S16: Photos of C18 capped MAPI NCs deposited on a FTO coated glass under UV-light illumination; (a) Film with no annealing step (b) Film after thermal annealing at 100°C for 10 min. The photoluminescence properties of the films did not change

Bibliography

[1] E. Wang, Z. Ma, Z. Zhang, P. Henriksson, O. Inganäs, F. Zhang, and M. R. Andersson, "An isoindigo-based low band gap polymer for efficient polymer solar cells with high photo-voltage," *Chemical Communications*, vol. 47, no. 17, p. 4908, 2011.

3.1.2 Post-publication commentary

The energy band positions calculated by cyclic voltammetry and discussed in the paper published by Poli *et al.* showed that the first oxidation peak of the absorber $MAPbI_3$ film shifted to lower potentials when MAPI NCs were deposited on the surface. These results suggested a variation in the VB position, which might have induced an extraction barrier at the PCBM/perovskite interface. This extraction barrier could have been the cause of the inverted hysteresis effect observed in devices fabricated with an inverted architecture.

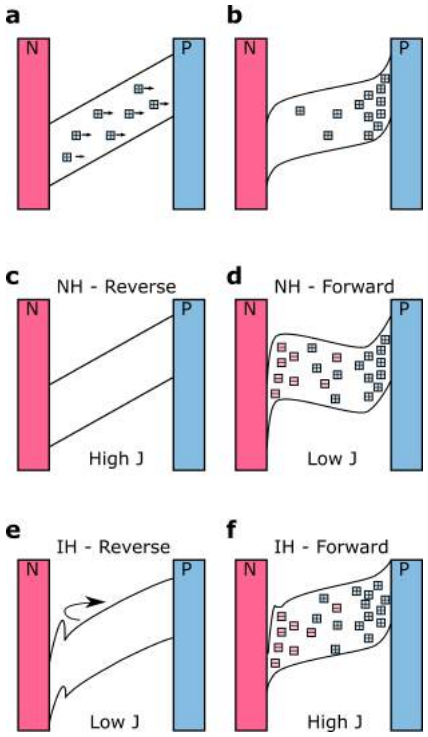

Figure 3.1: a-b Schematic diagrams indicating the influence of iodide vacancy (squares with + sign) drift on the band energies at short circuit. The vacancies are balanced by immobile cations with negative charges. **c-d** Schematic diagrams of a perovskite thin film solar cell at different scan direction conditions giving rise to normal hysteresis (NH). **e-f** Schematic diagrams of a perovskite thin film solar cell at different scan direction. The presence of an extraction barrier gives rise to an inverted hysteresis (IH).

Figure 3.1 shows the influence that iodide vacancies have on the energy band diagram of a perovskite N-i-P device under the effect of an electric field ('N'=electron transport material, 'P'=hole transport material and 'i'=perovskite absorber layer). At short circuit, a built-in electric field exists in the perovskite layer due to the difference in the work functions of the P and N contacts. The built-in electric field results in the migration of iodide ion vacancies towards the HTM/perovskite interface (figure 3.1 a), which partially screen the internal field (figure 3.1 b). [13, 14] Figure 3.1 c and d show schematic diagrams of the band energies under reverse and forward scan direction, respectively. The built-in field is not screened under reverse scan and all photogenerated electrons/holes can drift to the N and P contacts, except for some carriers that recombine radiatively or through defects. In contrast,

when the cell is scanned in forward direction, the internal field within the device is screened due to accentuated migration of ions, leading to less efficient collection of charge carriers. Therefore, the solar cell generates lower photocurrent densities when scanned in forward direction, leading to an effect referred to as *normal hysteresis* (NH). [13] Figure 3.1 e shows a case scenario where an extraction barrier is present at the ETM/perovskite interface, which can drive photogenerated electrons to the wrong direction with respect to charge collection. Ion migration accentuated under forward scan may reduce the extraction barrier at the ETL/perovskite interface, leading to more efficient charge collection (figure 3.1 f). In contrast to what expected in 'normal conditions' (diagrams shown in figure 3.1 c and d), higher photocurrent densities and photovoltages are measured under forward scan directions, giving rise to a phenomenon referred to as *inverted hysteresis* (IH).

3.1.3 Contemporary assessment

The paper 'Enhancing the hydrophobicity of perovskite solar cells using C18 capped $CH_3NH_3PbI_3$ nanocrystals' by Poli *et al.* demonstrated a facile technique to enhance the moisture stability of solar cells and extraction of charges by tailoring the perovskite surface. In 2016, Cha *et al.* reported the use of $CH_3NH_3PbBr_{0.9}I_{2.1}$ quantum dots (QDs) at the perovskite/HTM interface. In line with our conclusions, they claimed that the incorporation of $CH_3NH_3PbBr_{0.9}I_{2.1}$ QDs enhanced the charge extraction at the interface due to improved band alignment. They also reported steady-state PL data, claiming that the presence of QDs acted as a passivation layer and reduced the defect density at the interface. However, the PL spectra presented in the manuscript exhibited the opposite trend and showed that QDs treatment quenched the PL intensity, implying the formation of defect states. Moreover, the authors did not investigate the moisture-induced degradation of $MAPbI_3$ films, nor the stability of the devices.

Other examples to improve the charge extraction at the perovskite/transport layer interface used MoS_2 flakes, which also prevented metal electrode migration, [15] and 3-hexylthiophene (HTP) molecules. [16] The latter, in particular, showed that the transfer of carriers from the perovskite absorber to the HTM Spiro-OMeTAD was faster with the addition of HTP and that HTP could also passivate surface traps. However, data about the hydrophobicity of the treated surface were not provided. Moreover, HTP-treated solar cells degraded by $20\,\%$ after 30 days of exposure to RH=$40\,\%$ (shelf-stability) even if the triple cation mixed halide perovskite was used as absorber material, which is intrinsically more stable than $MAPbI_3$. [17, 18]

Finally, while the paper by Poli *et al.* was under review and consideration for publication, the use of oleic acid was reported as hydrophobic material to passivate the perovskite absorber and enhance its moisture resistivity. [19] A mixture of oleic acid and toluene was spin coated on the prepared $MAPbI_3$ films, and the shelf-stability of the devices was investigated over 4 weeks, showing considerably reduced moisture-induced degradation with OA-treated perovskites. However the

fabricated devices showed poor performances, with FF<0.45 already after deposition. The authors also claimed that oleic acid effectively passivated the surface defect sites, but no evidence was provided.

3.2 Large organic cations as passivation layers

As discussed in the previous section, moisture induces irreversible degradation of perovskite films. Modification of the surface by inserting a layer between the perovskite absorber and the charge transport layer is an option to improve device stability. This section studies the effect that large organic cations deposited on the perovskite absorber have on moisture-related degradation mechanisms and density of surface defects.

3.2.1 Experimental methods

The experiments presented in this section were carried out by the candidate at the Centre for Nano Science and Technology (CNST), Italian Institute of Technology (IIT), Milan. Perovskite films were deposited on non-conductive glass. The substrates cleaning and deposition of $MAPbI_3$ were done in the same way as described in Chapter 2. However, the fabrication of the samples was carried out in a nitrogen filled glove box. $MAPbI_3$ surfaces were treated by spin coating 25 mM of ammonium iodine isopropanol solution at 3000 rpm for $30\,\mathrm{s}$ (anhydrous IPA was used). The products were then dried at $30\,^{\circ}\mathrm{C}$ for $2\,\mathrm{min}$ and annealed at $100\,^{\circ}\mathrm{C}$ for $10\,\mathrm{min}$. The same concentration of ammonium iodide solution was used to aim to the same coverage of the passivation film on the perovskite surface. The forms of ammonium iodide used in this work are phenylethylammonium iodide, tetrabutylammonium iodide, tert-butylammonium iodide, 5-aminovaleric acid iodide and n-butylammonium iodide.

For the steady-state PL analysis, excitation light was provided by a continuous wave CW diode laser (Oxxius laserboxx, wavelength 405 nm). $MAPbI_3$ films were mounted inside a vacuum chamber and measured under constant pumping (pressure $< 1 \times 10^{-5}\,\mathrm{mbar}$), and PL was collected in reflection mode and focused into a fiber coupled to a spectrometer (Ocean Optics Maya Pro 2000).

3.2.2 Moisture degradation

Moisture-induced degradation of $MAPbI_3$ films was investigated by functionalising the perovskite surface with different forms of ammonium iodide. The five different organic cations assembled on the perovskite surface are listed in Table 3.2: phenyelthylammonium (PEA), tetrabutylammonium (TBA), tert-butylammonium (t-BA), 5-aminovaleric acid (5AVA) and n-butylammonium (n-BA). The reason for using these particular large organic cations is that they have been reported to form

low-dimensional 2D materials when added to the precursor solution (see ref in Table 3.2).

Table 3.2: Organic cations used to treat the $MAPbI_3$ surface. The table lists literature report examples of using such cations to incorporate 2D structures into 3D perovskites.

Organic cations	Molecular structure	ref
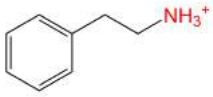	PEA^+	[20, 21]
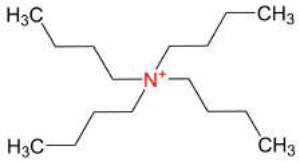	TBA^+	[22, 23]
	t-BA^+	[24]
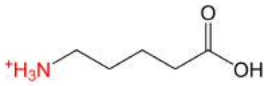	5 AVA^+	[25]
	n-BA^+	[26, 27, 28]

The compositional tuning of the absorber layer with integration of 2D phases into the 3D structure has been successfully proposed as an approach to increase stability and lifetime of perovskite solar cells. [20, 25, 27, 28] The presence of 2D layers induces a vertically graded structure of highly oriented 3D perovskites, reducing grain boundaries, which act as defect reservoirs. [29] Moreover, the hydrophobic nature of the large cation used can lead to considerably higher moisture stability. [30] Recently, PEA was used to treat the perovskite surface, showing that improved device stability could be achieved even if the cation was not directly added to the precursor solution. [31, 32, 33] Recently, Schlipf *et al.* studied the interaction between water and 3D/2D films ($MAPbI_3$ films with a 2D top layer of PEA) using in situ neutron X-ray scattering, revealing that the 2D layer does not prevent the ingress of water but it inhibits the formation of PbI_2 blocking MAI escape. [21]

The large cation used to passivate the surface can diffuse into the perovskite film and partially convert the perovskite 3D to 2D, in some cases. In others, the 3D-to-2D phase transition does not occur and the large cation limits itself to be distributed at

the perovskite surface. The tendency of inducing 3D-to-2D phase transition highly depends on the activation energy of the process itself. [34] For example, Zhao *et al.* found that C4 diammonium iodides induced 3D-to-2D perovskite phase transition, while C8 diammonium iodides stayed on the perovskite surface because of the high activation energy arising from its anti-gauche isomeration. [34] Hu *et al.* demonstrated that the top layer of a $MAPbI_3$ film could be converted into a layered perovskite by spin coating an IPA solution containing MAI and PEAI. The presence of MAI in the solution was crucial to form the layered perovskite and avoid formation of crystallised PEAI. [31] Finally, fullerenes have been widely investigated to passivate surface charge trap states in perovskite films. [35, 36, 37] PCBM was first reported as perovskite surface passivator by Shao *et al.*, who claimed that PCBM could diffuse into the perovskite film along the grain boundaries after prolonged thermal annealing. In contrast, without temperature treatments PCBM was found to remain on the surface of the perovskite film. [38]

Figure 3.2 a shows the UV-Vis spectra of $MAPbI_3$ films right after deposition. Surface treatments did not induce changes in the optical properties of the absorbers. All films had the same onset absorption wavelength, which corresponded to an optical energy bandgap of $1.6\,\mathrm{eV}$ (3.2 b).

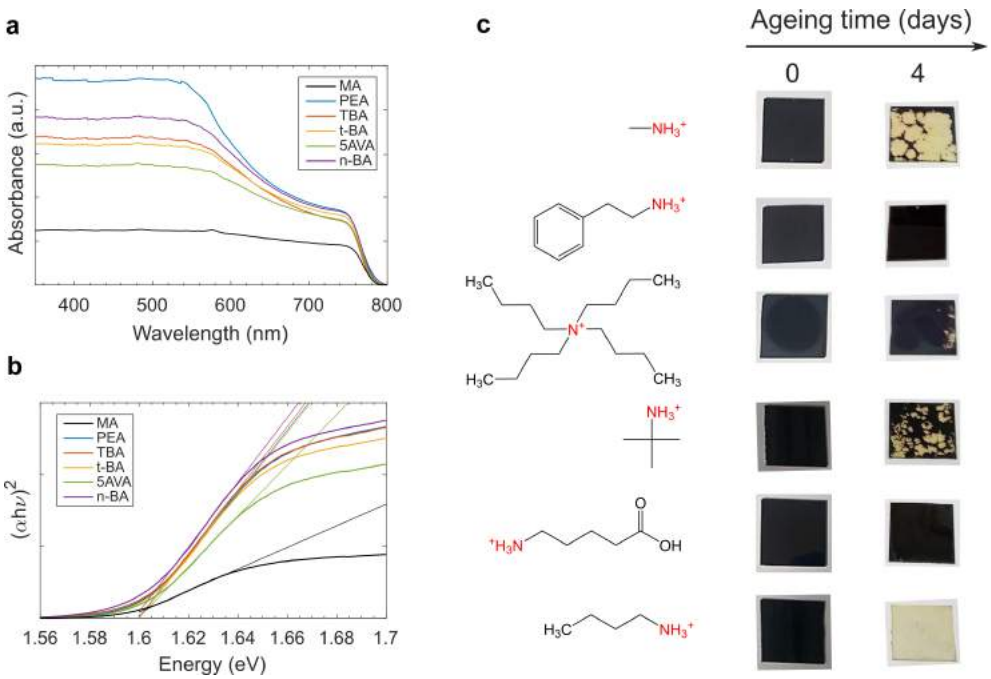

Figure 3.2: **a** UV-Vis absorbance of $MAPbI_3$ perovskite films with and without surface treatments. **b** Tauc plots of $MAPbI_3$ perovskite films, indicating an energy bandgap of 1.6 eV. **c** Photographs of $MAPbI_3$ perovskite films with and without surface treatments during exposure to relative humidity of $70\,\%$ over 4 days.

Figure 3.2 c shows the appearance of the perovskite films with and without surface treatments after exposure to high humidity (70%) over 4 days. The bare perovskite film turned transparent over time due to hydration of the lattice. t-BA and n-BA covered films did not efficiently avoid this process, and they similarly

turned transparent over time. The perovskite film covered with n-BA degraded even faster than the reference $MAPbI_3$, suggesting that n-BA at the surface accelerate the moisture-induced degradation. In contrast, PEA, TBA and 5AVA covered perovskites showed significantly higher stability and films did not change their aspect after 4 days of exposure at high humidity. Small hydrated areas appeared at the edges of the TBA treated film and they may have been caused by uncovered areas. However, these areas did not grow on larger scale over the 4 days.

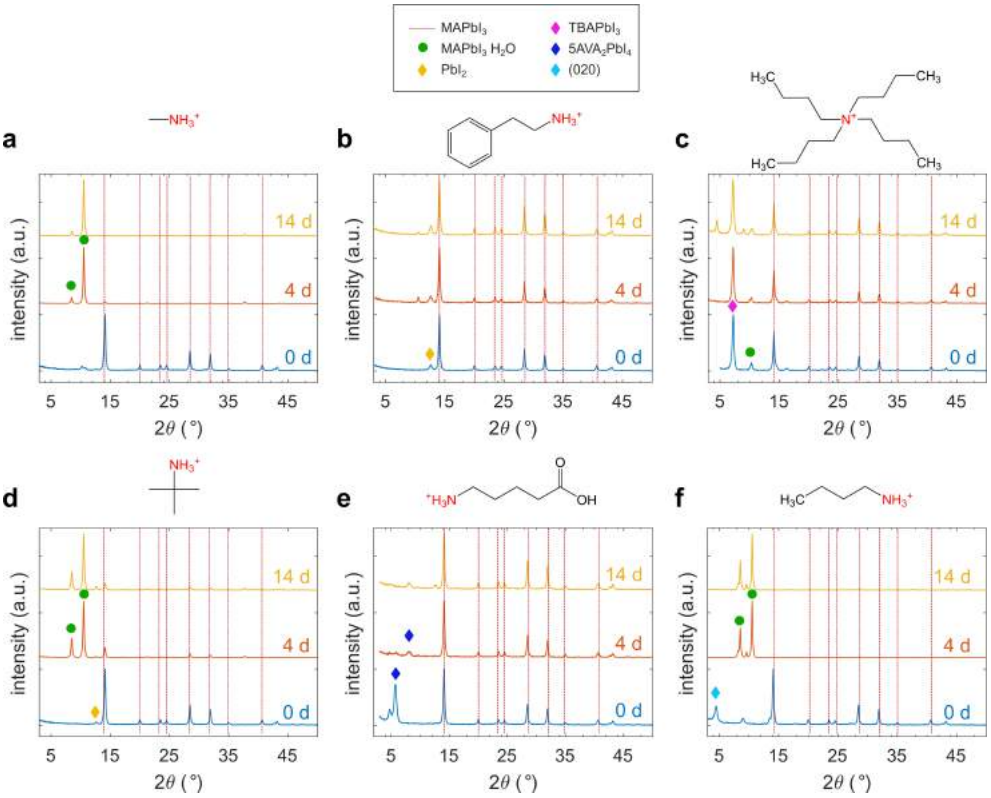

Figure 3.3: XRD of as-prepared $MAPbI_3$ films after exposure to relative humidity of 70 % over 4 and 14 days. The positions of the XRD peaks for $MAPbI_3$, PbI_2, $MAPbI_3{\cdot}H_2O$, $TBAPbI_3$ and 2D materials are marked in the graphs. **a** Untreated $MAPbI_3$. **b** PEA-covered $MAPbI_3$. **c** TBA-covered $MAPbI_3$. **d** t-BA-covered $MAPbI_3$. **e** 5AVA-covered $MAPbI_3$. **f** n-BA-covered $MAPbI_3$.

XRD data were collected to provide more detailed information on structural phase changes of perovskite films on exposure to high humidity. The XRD patterns of thin films with and without surface functionalisation before and after moisture exposure for 4 and 14 days are shown in Figure 3.3. All diffraction patterns of the as prepared films ('0 d') exhibit the tetragonal crystal structure, for example characteristic peaks at 2θ=14.10°, 28.50° and 31.95° are assigned to (110), (220) and (310) diffraction planes. [39] Diffraction peaks at low angles 2θ <10° may be assigned to the (0l0) lattice planes, typical of 2D materials. [10, 40, 31] The initial 5AVA-coated perovskite film shows additional peaks at 5.35° and 5.75°, which become considerably less intense after exposure to high RH for 4 days. Instead, a new peak emerges

at 2θ=8.3°, indicating that the structural properties of the film changed with exposure to moisture. A similar structural transformation with humidity has been reported in PEA and n-BA based 2D perovskites. [41, 21]
The TBA-coated perovskite film exhibited a very strong diffraction peak at 2θ=7.2°, which is assigned to the presence of 1 dimensional 1D $TBAPbI_3$ structure within thin-film (see Chapter 4 for further details). The diffraction patterns of untreated $MAPbI_3$ films considerably changed after exposure to high humidity. Moreover, as a consequence of hydration, additional peaks at 2θ=8.6° and 10.5° appeared, which were assigned to the presence of hydrated $MAPbI_3$. [42, 1] As expected from the appearance of the films shown in Figure 3.2 c, also n-BA and t-BA coated films showed complete degradation with the formation of peaks indicating hydration of the material. In contrast, films passivated with PEA, TBA and 5AVA did not show any change of the 3D perovskite phases into hydrated or decomposed phases, which indicated that $MAPbI_3$ treated with these cations are highly durable even under high RH of 70 % over at least 14 days (Figure 3.3 b, c and e).

Unexpectedly, only traces of PbI_2 were detected in the XRD patterns, while reflections of the monohydrate form $MAPbI_3{\cdot}H_2O$ were more intense. Similar results were reported by Leguy *et al.*, who claimed that PbI_2 may have been formed in an amorphous or nanocrystalline form and pushed out of the hydrate crystals and therefore not detected with XRD. [1] Another possible explanation about the appearance of monohydrate $MAPbI_3{\cdot}H_2O$ characteristic peaks in bare $MAPbI_3$ films and *t*-BA and *n*-BA treated films may be the excess of MAI, t-BAI and n-BAI present in the film. Petrus *et al.* studied the influence of moisture on perovskite films with different distribution of the precursor material excess and found that MAI-excess samples did not show the formation of PbI_2, instead only the monohydrate $MAPbI_3{\cdot}H_2O$ appeared. [43] In contrast, perovskite films prepared from stoichiometric solutions or PbI_2 excess solutions showed the formation of crystalline PbI_2 upon exposure to moisture. They inferred that the excess cation material AI (either MAI or bulkier cations, such as *t*-BAI or *n*-BAI) may be distributed homogeneously at the grain boundaries. Upon moisture exposure, A^+ and I^- vacancies are created as a result of hydration. Initially, these vacancies are refilled by the excess of AI that is distributed at the grain boundaries, resulting in improved crystallinity. Once reservoir of excess AI has been consumed, degradation starts occurring by the formation of hydrated perovskite species. [43]

3.2.3 Photostability

Surface treatment by PEA, TBA and 5AVA showed reduced moisture-induced degradation upon exposure to high humidity. The modification of the surface by introducing passivation layers directly on the absorber can lead to the formation of defects and new electronic states, which can affect the optoelectronic quality of the interface. Therefore, it is important to optically characterise surface treated perovskite

films by monitoring the quantum yields and dynamics of photoluminescence to investigate the suppression/formation of new defects at the interface. For example, poly(ethylene oxide) and tri-n-octylphosphine oxide layers on $MAPbI_3$ have been reported to effectively suppress non-radiative recombination paths at the surface, showing longer carrier lifetimes and higher PL intensities than untreated $MAPbI_3$ films. [42, 44] In contrast, surface modification of $MAPbI_3$ with $MAPbBr_{0.9}I_{2.1}$ quantum dots and with cyclopropylammonium cation induced a PL quenching. [45, 10] Quenching of the PL may be caused by an increased defect density at the interface, which would reduce the radiative recombination mechanisms, or by effective charge transfer.

Dynamics and quantum yields of photoluminescence are very sensitive to defects that affect radiative and non-radiative recombinations. PL dynamics were studied by exciting the samples with a monochromatic CW laser with different power densities. Figure 3.4 shows the relative photoluminescence quantum yield (PLQY) of $MAPbI_3$ thin films as a function of power density. The solid lines show data collected with increasing excitation intensity, while the dotted lines show data collected from high to low power densities. All perovskite films showed an increasing trend of PLQY with power density, indicating that trap states have been filled up with higher carrier densities. [46]

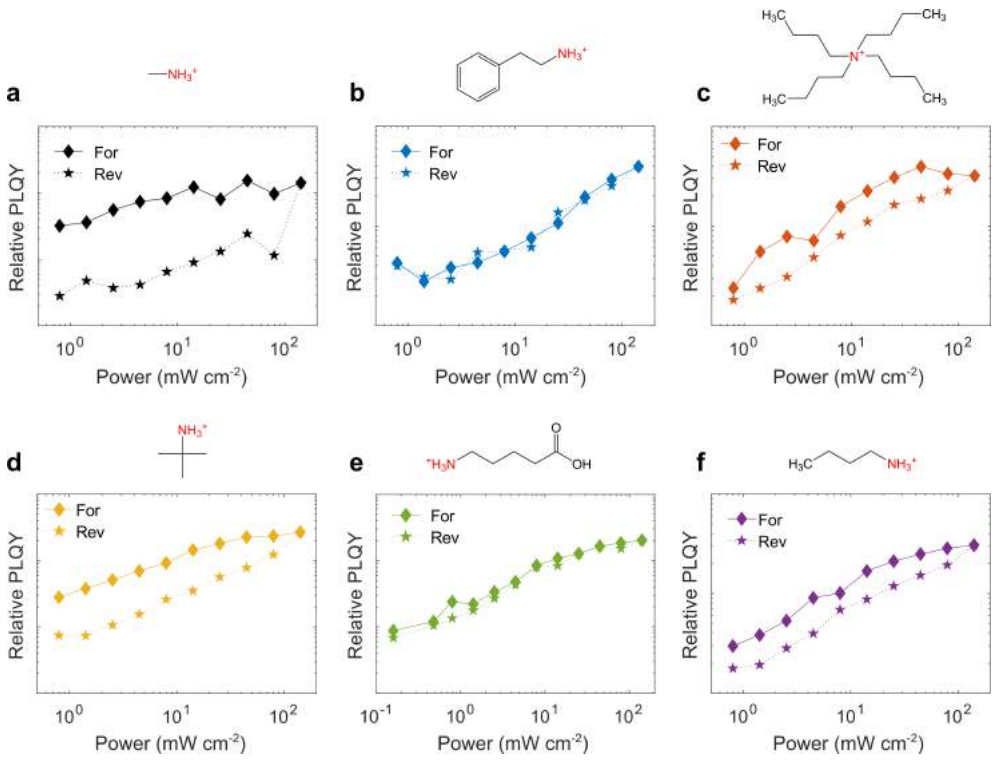

Figure 3.4: Relative PLQY curves of $MAPbI_3$ films in active vacuum, taken with increasing (solid lines) or decreasing (dotted lines) excitation densities. **a** Untreated $MAPbI_3$. **b** PEA-covered $MAPbI_3$. **c** TBA-covered $MAPbI_3$. **d** t-BA-covered $MAPbI_3$. **e** 5AVA-covered $MAPbI_3$. **f** n-BA-covered $MAPbI_3$.

The PLQY curves of the bare $MAPbI_3$ perovskite film showed high hysteric behaviour (Figure 3.4 a). When the perovskite film was characterised from high to low power densities, a reduced band-to-band radiative emission was measured, indicating the formation of emissive sub-band gap states under photoexcitation. [47] All capped perovskite films (Figure 3.4 b-f) behaved differently from the reference $MAPbI_3$. The PLQY still increased with power densities, but the hysteric effect was considerably reduced. These results inferred that photo-induced non-radiative recombination pathways could be reduced by treating the perovskite surface with different large organic molecules. Particularly, using PEA and 5AVA cations, the hysteric behaviour totally disappeared, indicating suppression of photo-induced trap states.

The photoluminescence spectra of $MAPbI_3$ films were compared to evaluate the emission properties of thin films (Figure 3.5 a). t-BA-capped perovskite films were less emissive than the reference $MAPbI_3$, indicating that once in contact with the perovskite film, t-BA might have created loss channels for photogenerated carriers. [42] PL spectra of n-BA and PEA passivated perovskite films were similar to the reference sample, while the film coated with TBA was about 1.5 times more emissive than the reference untreated $MAPbI_3$. Excitingly, the 5AVA-capped $MAPbI_3$ film was about 100 times more emissive than all the other perovskite absorbers, indicating that 5AVA thin passivation layers significantly healed defect states on the perovskite surface by suppression of non-radiative recombination paths.

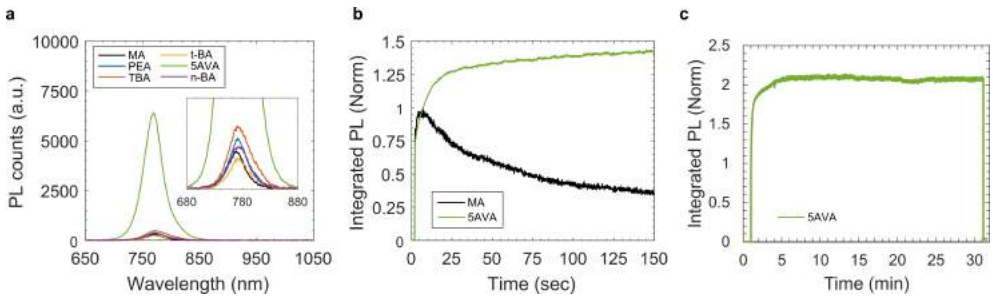

Figure 3.5: **a** PL spectra of bare $MAPbI_3$ and surface treated $MAPbI_3$ films. The inset shows a close-up of the wavelength axis. **b** Integrated PL signal of $MAPbI_3$ and 5AVA-capped $MAPbI_3$ films over time measured at $10\,\mathrm{mW\,cm^{-2}}$. **c** Integrated PL signal of 5AVA-capped $MAPbI_3$ over time measured under continuous photoexcitation at $10\,\mathrm{mW\,cm^{-2}}$.

The integrated PL intensity of $MAPbI_3$ and surface treated $MAPbI_3$ was monitored over long period of time under continuous photoexcitation; Dynamics are shown in figure 3.5 b. The integrated PL of bare $MAPbI_3$ decreased over time, indicating the formation of photo-induced sub-band gap defect states that quenched the band-to-band radiative emission. [47] In contrast, the PL intensity of $MAPbI_3$ film treated with 5AVA showed an enhancement over time. Figure 3.5 c shows the dynamics of the $MAPbI_3$ film treated with 5AVA measured under continuous photoexcitation for over $30\,\mathrm{min}$. These results suggest that the presence of 5AVA on the

surface blocks the formation of photo-induced sub-band gap states that act as defects. Indeed, band-to-band radiative recombination mechanisms, herein directly measured by PL, rise over time and reach a plateau after $300\,\mathrm{s}$. Excitingly, the integrated PL intensity remains invariable for more than $30\,\mathrm{min}$, showing that passivating the perovskite thin film surface prevents the detrimental generation of defects that lead to photoluminescence decrease and improves the thin-film stability.

3.3 Chapter conclusions

Surface treatment of the perovskite absorber layer was proposed as an effective strategy to improve the stability of perovskite solar cells. The perovskite layer was functionalised by coating the surface with $MAPbI_3$ NCs capped with long chain ligands OA and OLA. Thanks to the presence of OA and OLA, the thin layer of $MAPbI_3$ NCs became highly hydrophobic and water contact angles $>90°$ were measured on treated $MAPbI_3$ films. The hydrophobic capping layer slowed down the hydration process, preventing degradation even when the treated-film was completely immersed in water for $30\,\mathrm{s}$. Applying MAPI NCs as an interlayer between the perovskite and the HTM Spiro-OMeTAD in solar cell devices may have improved the charge extraction, leading to reduced normal hysteresis. Solar cells with $MAPbI_3$ NCs incorporated at the interface showed enhanced moisture stability for devices stored in the dark, at open circuit, in ambient conditions with RH $> 50\,\%$.

Large organic ammonium cations were also investigated as hydrophobic molecules to effectively passivate the perovskite absorber surface. In particular, applying thin layers of PEA, TBA and 5AVA to coat the perovskite surface allowed for reduced moisture-degradation. Spectroscopic studies demonstrated that the presence of bulky ammonium cation thin layers on the surface improved the photo-stability of $MAPbI_3$ films, reducing the generation of photo-induced sub-band gap states at the interface. The passivation of surface defects was observed when the surface was treated with 5AVA, leading to a substantial enhancement of the PL intensity. This study looked at surface treatment as an effective technique to simultaneously protect the perovskite absorber from moisture-degradation and passivate surface defects, therefore improving the stability of perovskite solar cells.

3.4 Future work

The $MAPbI_3$ perovskite surface has been treated with different molecules to enhance the photostability and moisture-stability of the material. The hydrophobicity of perovskite films was improved by depositing C18 capped $MAPbI_3$ NCs on the surface and higher moisture-stability was measured on full devices. In the published article, it was speculated that the $MAPbI_3$ NCs may have improved the band alignment, enhancing the charge extraction and reducing the hysteric behaviour. The valence

band edge was estimated using cyclic voltammetry (CV). However, electrochemical studies with halide perovskites may be difficult to interpret. It has been previously reported that the measured currents in CV scans might correspond to Faradaic events, like oxidation and reduction of ions, rather than charge carrier injection in the material. [48] Other spectroscopy techniques, such as XPS, may be more informative to give absolute values of the VB and CB edge positions. The optoelectronic quality of the $CH_3NH_3PbI_3$/$MAPbI_3$ NCs interface should be further investigated by looking at the photoluminescence dynamics and radiative and non-radiative defect density.

Different bulky cations have been used to treat the $MAPbI_3$ surface making the perovskite thin films more stable towards moisture. The presence of 5AVA may have passivated undercoordinated defect sites at the surface enhancing the photostability of the material. Further understanding of the chemical interaction between the perovskite and the bulky cation may be gained using XPS characterisation. Moreover, photovoltaic devices with and without 5AVA cation passivation should be fabricated to see the effects on the photovoltaic performance.

Bibliography

[1] A. M. A. Leguy, Y. Hu, M. Campoy-Quiles, M. I. Alonso, O. J. Weber, P. Azarhoosh, M. van Schilfgaarde, M. T. Weller, T. Bein, J. Nelson, P. Docampo, and P. R. F. Barnes, "Reversible Hydration of $CH_3NH_3PbI_3$ Films, Single Crystals, and Solar Cells," *Chem. Mater.*, vol. 27, no. 9, pp. 3397–3407, 2015.

[2] J. Huang, S. Tan, P. D. Lund, and H. Zhou, "Impact of H_2O on organic-inorganic hybrid perovskite solar cells," *Energy Environ. Sci.*, vol. 10, no. 11, pp. 2284–2311, 2017.

[3] J. Frost, K. Butler, and F. Brivio, "Atomistic origins of high-performance in hybrid halide perovskite solar cells," *Nano Lett.*, vol. 14, pp. 2584–90, may 2014.

[4] H. L. Clever and F. J. Johnston, "The solubility of some sparingly soluble lead salts: An evaluation of the solubility in water and aqueous electrolyte solution," *J. Phys. Chem. Ref. Data*, vol. 9, no. 3, pp. 751–784, 1982.

[5] D. Koushik, W. J. Verhees, Y. Kuang, S. Veenstra, D. Zhang, M. A. Verheijen, M. Creatore, and R. E. Schropp, "High-efficiency humidity-stable planar perovskite solar cells based on atomic layer architecture," *Energy Environ. Sci.*, vol. 10, no. 1, pp. 91–100, 2017.

[6] J. Zhang, Z. Hu, L. Huang, G. Yue, J. Liu, X. Lu, Z. Hu, M. Shang, L. Han, and Y. Zhu, "Bifunctional alkyl chain barriers for efficient perovskite solar cells," *Chem. Commun.*, vol. 51, no. 32, pp. 7047–7050, 2015.

[7] S. Yang, Y. Wang, P. Liu, Y.-B. Cheng, H. J. Zhao, and H. G. Yang, "Functionalization of perovskite thin films with moisture-tolerant molecules," *Nat. Energy*, vol. 1, pp. 1–7, 2016.

[8] H. Xiong, Y. Rui, Y. Li, Q. Zhang, and H. Wang, "Hydrophobic coating over a $CH_3NH_3PbI_3$ absorbing layer towards air stable perovskite solar cells," *J. Mater. Chem. C*, vol. 4, no. 28, pp. 6848–6854, 2016.

[9] J. Cao, J. Yin, S. Yuan, Y. Zhao, J. Li, and N. Zheng, "Thiols as interfacial modifiers to enhance the performance and stability of perovskite solar cells," *Nanoscale*, vol. 7, no. 21, pp. 9443–9447, 2015.

[10] C. Ma, C. Leng, Y. Ji, X. Wei, K. Sun, L. Tang, J. Yang, W. Luo, C. Li, Y. Deng, S. Feng, J. Shen, S. Lu, C. Du, and H. Shi, "2D/3D perovskite hybrids as moisture-tolerant and efficient light absorbers for solar cells," *Nanoscale*, vol. 338, pp. 643–647, 2016.

[11] X. Liang, R. W. Baker, K. Wu, W. Deng, D. Ferdani, P. S. Kubiak, F. Marken, L. Torrente-Murciano, and P. J. Cameron, "Continuous low temperature synthesis of $MAPbX_3$ perovskite nanocrystals in a flow reactor," *React. Chem. Eng.*, pp. 640–644, 2018.

[12] I. Poli, X. Liang, R. Baker, S. Eslava, and P. J. Cameron, "Enhancing the Hydrophobicity of Perovskite Solar Cells using C18 Capped $CH_3NH_3PbI_3$ Nanocrystals," *J. Mater. Chem. C*, vol. 6, pp. 7149–7156, 2018.

[13] C. Eames, J. M. Frost, P. R. F. Barnes, B. C. O'Regan, A. Walsh, and M. S. Islam, "Ionic transport in hybrid lead iodide perovskite solar cells," *Nat. Commun.*, vol. 6, p. 7497, jun 2015.

[14] D. A. Jacobs, Y. Wu, H. Shen, C. Barugkin, F. J. Beck, T. P. White, K. Weber, and K. R. Catchpole, "Hysteresis phenomena in perovskite solar cells: the many and varied effects of ionic accumulation," *Phys. Chem. Chem. Phys.*, vol. 19, no. 4, pp. 3094–3103, 2017.

[15] A. Capasso, F. Matteocci, L. Najafi, M. Prato, J. Buha, L. Cina, V. Pellegrini, A. D. Carlo, and F. Bonaccorso, "Few-Layer MoS_2Flakes as Active Buffer Layer for Stable Perovskite Solar Cells," *Adv. Energy Mater.*, vol. 6, no. 16, pp. 1–12, 2016.

[16] T. Y. Wen, S. Yang, P. F. Liu, L. J. Tang, H. W. Qiao, X. Chen, X. H. Yang, Y. Hou, and H. G. Yang, "Surface Electronic Modification of Perovskite Thin Film with Water-Resistant Electron Delocalized Molecules for Stable and Efficient Photovoltaics," *Adv. Energy Mater.*, vol. 1703143, pp. 1–7, 2018.

[17] D. P. McMeekin, G. Sadoughi, W. Rehman, G. E. Eperon, M. Saliba, M. T. Hörantner, A. Haghighirad, N. Sakai, L. Korte, B. Rech, M. B. Johnston, L. M. Herz, and H. J. Snaith, "A mixed-cation lead mixed-halide perovskite absorber for tandem solar cells," *Science*, vol. 351, no. 6269, pp. 151–155, 2016.

[18] M. Saliba, T. Matsui, J.-Y. Seo, K. Domanski, J.-P. Correa-Baena, M. K. Nazeeruddin, S. M. Zakeeruddin, W. Tress, A. Abate, A. Hagfeldt, and M. Grätzel, "Cesium-containing triple cation perovskite solar cells: improved stability, reproducibility and high efficiency," *Energy Environ. Sci.*, vol. 9, no. 6, pp. 1989–1997, 2016.

[19] G. Abdelmageed, H. R. Sully, S. Bonabi Naghadeh, A. El-Hag Ali, S. A. Carter, and J. Z. Zhang, "Improved Stability of Organometal Halide Perovskite Films and Solar Cells toward Humidity via Surface Passivation with Oleic Acid," *ACS Appl. Energy Mater.*, vol. 1, no. 2, pp. 387–392, 2018.

[20] K. Z. Du, Q. Tu, X. Zhang, Q. Han, J. Liu, S. Zauscher, and D. B. Mitzi, "Two-Dimensional Lead(II) Halide-Based Hybrid Perovskites Templated by Acene Alkylamines: Crystal Structures, Optical Properties, and Piezoelectricity," *Inorg. Chem.*, vol. 56, no. 15, pp. 9291–9302, 2017.

[21] J. Schlipf, Y. Hu, S. Pratap, L. Bießmann, N. Hohn, L. Porcar, T. Bein, P. Docampo, and P. Müller-Buschbaum, "Shedding Light on the Moisture Stability of

3D/2D Hybrid Perovskite Heterojunction Thin Films," *ACS Appl. Energy Mater.*, vol. 2, no. 2, pp. 1011–1018, 2019.

[22] I. Poli, S. Eslava, and P. Cameron, "Tetrabutylammonium cations for moisture-resistant and semitransparent perovskite solar cells," *J. Mater. Chem. A*, vol. 5, pp. 22325–22333, 2017.

[23] P. Kour, M. Chenna Reddy, R. Naphade, and S. Ogale, "Quaternary alkylammonium salt incorporated 2D/3D mixed halide perovskite with highly enhanced photoluminescence and arrested iodide/bromide phase segregation," *APL Materials*, vol. 6, no. 8, p. 086107, 2018.

[24] D. Ramirez, K. Schutt, Z. Wang, A. J. Pearson, E. Ruggeri, H. J. Snaith, S. D. Stranks, and F. Jaramillo, "Layered Mixed Tin-lead Hybrid Perovskite Solar Cells with High Stability," *ACS Energy Lett.*, p. acsenergylett.8b01411, 2018.

[25] G. Grancini, I. Zimmermann, E. Mosconi, D. Martineau, and S. Narbey, "One-Year stable perovskite solar cells by 2D/3D interface engineering," *Nat. Commun.*, vol. 8, pp. 1–8, 2017.

[26] H. Tsai, W. Nie, J.-C. Blancon, C. C. Stoumpos, R. Asadpour, B. Harutyunyan, A. J. Neukirch, R. Verduzco, J. J. Crochet, S. Tretiak, L. Pedesseau, J. Even, M. A. Alam, G. Gupta, J. Lou, P. M. Ajayan, M. J. Bedzyk, M. G. Kanatzidis, and A. D. Mohite, "High-efficiency two-dimensional Ruddlesden–Popper perovskite solar cells," *Nature*, vol. 536, no. 7616, pp. 312–316, 2016.

[27] D. H. Cao, C. C. Stoumpos, O. K. Farha, J. T. Hupp, and M. G. Kanatzidis, "2D Homologous Perovskites as Light-Absorbing Materials for Solar Cell Applications," *J. Am. Chem. Soc.*, vol. 137, no. 24, pp. 7843–7850, 2015.

[28] C. C. Stoumpos, D. H. Cao, D. J. Clark, J. Young, J. M. Rondinelli, J. I. Jang, J. T. Hupp, and M. G. Kanatzidis, "Ruddlesden-Popper Hybrid Lead Iodide Perovskite 2D Homologous Semiconductors," *Chem. Mater.*, vol. 28, no. 8, pp. 2852–2867, 2016.

[29] D. W. de Quilettes, S. M. Vorpahl, S. D. Stranks, H. Nagaoka, G. E. Eperon, M. E. Ziffer, H. J. Snaith, and D. S. Ginger, "Impact of microstructure on local carrier lifetime in perovskite solar cells," *Science*, vol. 348, no. 6235, pp. 683–686, 2015.

[30] G. Grancini and M. K. Nazeeruddin, "Dimensional tailoring of hybrid perovskites for photovoltaics," *Nat. Rev. Mater.*, vol. 4, no. 1, pp. 4–22, 2019.

[31] Y. Hu, J. Schlipf, M. Wussler, M. L. Petrus, W. Jaegermann, T. Bein, P. Muller-Buschbaum, and P. Docampo, "Hybrid Perovskite/Perovskite Heterojunction Solar Cells," *ACS Nano*, vol. 10, no. 6, pp. 5999–6007, 2016.

[32] H. S. Yoo and N. G. Park, "Post-treatment of perovskite film with phenylalkylammonium iodide for hysteresis-less perovskite solar cells," *Sol. Energy Mater. Sol. Cells*, vol. 179, no. February, pp. 57–65, 2018.

[33] P. Chen, Y. Bai, S. Wang, M. Lyu, J.-h. Yun, and L. Wang, "In Situ Growth of 2D Perovskite Capping Layer for Stable and Efficient Perovskite Solar Cells," *Adv. Energy Mater.*, p. 10.1002/adfm.201706923, 2018.

[34] T. Zhao, C. C. Chueh, Q. Chen, A. Rajagopal, and A. K. Jen, "Defect Passivation of Organic-Inorganic Hybrid Perovskites by Diammonium Iodide toward High-Performance Photovoltaic Devices," *ACS Energy Lett.*, vol. 1, no. 4, pp. 757–763, 2016.

[35] Y. Fang and J. Huang, "Resolving Weak Light of Sub-picowatt per Square Centimeter by Hybrid Perovskite Photodetectors Enabled by Noise Reduction," *Adv. Mater.*, vol. 27, pp. 2804–2810, 2015.

[36] P.-w. Liang, C.-c. Chueh, S. T. Williams, and A. K. Jen, "Roles of Fullerene-Based Interlayers in Enhancing the Performance of Organometal Perovskite Thin-Film Solar Cells," *Adv. Energy Mater.*, vol. 5, no. 1402321, 2015.

[37] Y.-c. Shih, L. Wang, H.-c. Hsieh, and K.-f. Lin, "Effect of Fullerene Passivation on the Charging and Discharging Behavior of Perovskite Solar Cells : Reduction of Bound Charges and Ion Accumulation," *ACS Appl. Mater. Interfaces*, vol. 10, pp. 11722–11731, 2018.

[38] Y. Shao, Z. Xiao, C. Bi, Y. Yuan, and J. Huang, "Origin and elimination of photocurrent hysteresis by fullerene passivation in $CH_3NH_3PbI_3$ planar heterojunction solar cells," *Nat. Commun.*, vol. 5, no. 5784, p. 5784, 2014.

[39] C.-W. Chen, H.-W. Kang, S.-Y. Hsiao, P.-F. Yang, K.-M. Chiang, and H.-W. Lin, "Efficient and Uniform Planar-Type Perovskite Solar Cells by Simple Sequential Vacuum Deposition," *Adv. Mater.*, vol. 26, no. 38, pp. 6647–6652, 2014.

[40] K. Yao, X. Wang, F. Li, and L. Zhou, "Mixed Perovskite Based on Methylammonium and Polymeric-ammonium for Stable and Reproducible Solar Cells," *Chem. Commun.*, vol. 51, no. stage IV, pp. 15430–15433, 2015.

[41] C. C. Stoumpos, C. M. M. Soe, H. Tsai, W. Nie, J. C. Blancon, D. H. Cao, F. Liu, B. Traoré, C. Katan, J. Even, A. D. Mohite, and M. G. Kanatzidis, "High Members of the 2D Ruddlesden-Popper Halide Perovskites: Synthesis, Optical Properties, and Solar Cells of $(CH_3(CH_2)_3NH_3)_2(CH_3NH_3)_4Pb_5I_{16}$," *Chem*, vol. 2, no. 3, pp. 427–440, 2017.

[42] M. Kim, S. G. Motti, R. Sorrentino, and A. Petrozza, "Enhanced Solar Cells Stability by Hygroscopic Polymer Passivation of Metal Halide Perovskite Thin Film," *Energy Environ. Sci.*, vol. 11, pp. 2609–2619, 2018.

[43] M. L. Petrus, Y. Hu, D. Moia, P. Calado, and Ø. M. A. Leguy, "The Influence of Water Vapor on the Stability and Processing of Hybrid Perovskite Solar Cells Made from Non-Stoichiometric Precursor Mixtures," *ChemSusChem*, vol. 9, pp. 2699–2707, 2016.

[44] D. W. Dequilettes, S. Koch, S. Burke, R. K. Paranji, A. J. Shropshire, M. E. Ziffer, and D. S. Ginger, "Photoluminescence Lifetimes Exceeding 8 μs and Quantum Yields Exceeding 30% in Hybrid Perovskite Thin Films by Ligand Passivation," *ACS Energy Lett.*, vol. 1, no. 2, pp. 438–444, 2016.

[45] M. Cha, P. Da, J. Wang, W. Wang, Z. Chen, F. Xiu, G. Zheng, and Z.-S. Wang, "Enhancing Perovskite Solar Cell Performance by Interface Engineering Using $CH_3NH_3PbBr_{0.9}I_{2.1}$ Quantum Dots," *J. Am. Chem. Soc.*, vol. 138, no. 27, pp. 8581–8587, 2016.

[46] S. D. Stranks, V. M. Burlakov, T. Leijtens, J. M. Ball, A. Goriely, and H. J. Snaith, "Recombination Kinetics in Organic-Inorganic Perovskites : Excitons , Free Charge , and Subgap States," *Phys. Rev. Appl*, vol. 2, p. 034007, 2014.

[47] S. G. Motti, M. Gandini, A. J. Barker, J. M. Ball, A. R. Srimath Kandada, and A. Petrozza, "Photoinduced Emissive Trap States in Lead Halide Perovskite Semiconductors," *ACS Energy Lett.*, vol. 1, no. 4, pp. 726–730, 2016.

[48] G. F. Samu, R. A. Scheidt, P. V. Kamat, and C. Janáky, "Electrochemistry and Spectroelectrochemistry of Lead Halide Perovskite Films: Materials Science Aspects and Boundary Conditions," *Chem. Mater.*, vol. 30, no. 3, pp. 561–569, 2018.

Chapter 4

Compositional tuning of $MAPbI_3$ absorber layer

The performance of 3D halide perovskites has increased rapidly, however their commercial application is still limited by poor stability. Low-dimensional hybrid perovskites have recently attracted much attention due to higher moisture stability. This chapter investigates the compositional tuning of the absorber material by combining 3D perovskite structures with additional bulky organic cations to overcome the stability issue. Recent achievements in using bulky cations and additives into 3D perovskite structures in the literature and the use of the large cation tetrabutylammonium in 3D $MAPbI_3$ are discussed in Section 4.1. Section 4.2 presents the use of different spectroscopic techniques to confirm the presence of tetrabutylammonium within the absorber layer.

4.1 Perovskite stabilisation via compositional engineering

The intrinsic affinity of halide perovskites for moisture leads to poor stability and fast degradation under ambient conditions. The stability of the absorber material can be enhanced by tuning its compositional engineering. One approach is to use different cation mixtures, such as Cs^+, FA^+ and MA^+, which lead to triple cation perovskites with stabilised 3D structures due to decreased moisture-induced volatilisation of the organic cation. [1, 2]

A different approach consists of combining 3D structures with low dimensional 2D materials forming $A_2(CH_3NH_3)_{n-1}M_nX_{3n+1}$, where A is a large aliphatic or aromatic alkylammonium cation, M is the metal cation and X is the halide anion. n indicates the number of sheets of inorganic PbX_6 octahedra between two organic cation spacers (A). 2D materials show considerably higher moisture resistivity than 3D perovskites due to the hydrophobic nature of the bulky organic cations and the highly oriented structure. [3, 4] However, full-2D devices show considerably poorer performances than cells based on 3D structures due to a wider bandgap, [4] narrow

absorption and limited charge transport. [5, 6] Therefore, 2D/3D structures can potentially merge the high stability of 2D materials with the good performance of 3D perovskites. Phenylethylammonium (PEA) and butylammonium (BA) are two of the most used molecules in 2D and 2D/3D perovskites. Mixed 2D/3D perovskites based on PEA and BA showed not only improved moisture resistivity due to the hydrophobic nature of PEA and BA, but also reduced photoinduced trap formation and ion movement. [5, 3, 7, 8, 9]

A final approach looks at the passivation of moisture-sensitive grain boundaries of 3D perovskites with large molecules. Butylphosphonic acid 4-ammonium chloride (4-ABPACl) was used as an additive in the perovskite precursor solution resulting in devices with improved performance and moisture-stability. [10] 4-ABPACl acted as crosslink between neighbouring grains in the perovskite structure. The additive was shown to improve the infiltration through the mesoporous TiO_2 scaffold and the surface coverage, therefore leading to enhanced carrier transport. Similarly, 2-aminoethanethiol (2-AET) was used as a ligand in $MAPbI_3$ perovskite crystal structures, leading to films with enhanced crystallinity, higher surface coverage and improved intrinsic water-resistance. [11] However, no results on the device performance and stability were reported with 2-AET addition. Poly-vinylpyrrolidone (PVP) has also been reported to efficiently passivate defects at the grain boundaries improving the optoelectronic properties [12, 9] and the moisture-stability of the devices. [13] Finally, terephtalic acid (TPA) was added within the perovskite precursor solution to form interconnected crystal grains thanks to the strong coordination between I^- and the hydrogen bonds of the hydroxyl groups in TPA. [14]

The use of alkyl ammonium salts to treat the surface of $MAPbI_3$ films was briefly introduced in Chapter 3. Table 4.1 shows the water adsorption energy and the surface contact angle of $MAPbI_3$ films as deposited (methylammonium - MA) and functionalised with alkyl ammonium salts with four methyl (tetra-methyl ammonium - TMA) and four ethyl groups (tetra-ethylammonium - TEA) reported by Yang *et al.* in 2016. [15]

Table 4.1: Surface properties of $MAPbI_3$ films functionalised with TMA and TEA. These data have been taken from Yang *et al.* [15]

Surface	Adsorption energy (eV)	Contact angle (°)	Tilt angle (°)
MA	-0.52	44.23	33.4
TMA	-0.68	67.57	59.5
TEA	-0.43	78.28	98.7

The tilt angle was calculated computationally and indicate the angle between the surface I atom coordinated with one Pb atom and the (100) surface. [15] After replacing the surface MA with TEA, the tilt angle increased to $98.7°$, resulting in a more difficult adsorption of water at the surface. These computational results were confirmed experimentally by a higher water contact angle and good shelf stability

under high relative humidity $90\,\%$ for over 30 days. [15] Tetra-butyl ammonium (TBA) is expected to behave similarly to TEA, having similar bulky branched structures along four directions.

The use of TBA to partly replace MA in $MAPbI_3$ absorber materials to improve the moisture-stability of perovskite devices will be investigated in Section 4.1.1.

4.1.1 Tetrabutylammonium cations for moisture-resistant and semitransparent perovskite solar cells

In this work, the moisture stability of $MAPbI_3$ perovskite devices was enhanced by modifying the absorber material by partly substituting MA with TBA cations. TBA was incorporated directly within the precursor solution and perovskite films were deposited via a single-step spin coating procedure.

Films prepared without MA but only TBA showed strong XRD diffraction peaks at low angles $\sim 8^\circ$ and $\sim 10^\circ$, which could be assigned to low-dimensional 2D structures. In mixed TBA/MA films, the XRD diffraction peak at $\sim 8^\circ$ coexisted with (110) and (220) peaks characteristic of the tetragonal phase of the 3D $MAPbI_3$ perovskite structure. These results suggested that when TBA was incorporated in the absorber material, 2D and 3D structural phases coexisted. Larger TBA percentages significantly decreased the diffraction signals of 3D $MAPbI_3$ while the signal of peaks at low angles increased.

The presence of TBA affected the crystallisation and morphology of thin films. Films containing TBA changed colour from yellow to black during annealing more slowly. Top-view SEM images showed improved surface coverage and reduced pinholes density in MA/TBA mixed perovskites. In addition, TBA crystallites were observed at the perovskite/spiro-OMeTAD interface. No changes were observed in the energy bandgap, which was calculated to be $\sim 1.58\,\mathrm{eV}$ irrespective of the presence of TBA. Larger TBA percentages ($\geq 10\,\%$) significantly decreased the optical absorbance, due to much higher transparency of the film.

To demonstrate the applicability and advantage of TBA-containing perovskites, full devices were fabricated by sandwiching the $MA_{1-n}TBA_nPbI_3$ films between a mesoporous TiO_2 electron transporting layer and the spiro-OMeTAD hole transporting layer. The short-circuit current density gradually decreased from about 20 to $10\,\mathrm{mA\,cm^{-2}}$ with increased TBA contents. This behaviour was related to the decreased absorption measured for films with TBA contents $\geq 10\,\%$. The open circuit voltage increased progressively with TBA incorporation, reaching a maximum average value of about $0.85\,\mathrm{V}$ for TBA contents of $5\,\%$.

The device shelf-stability (cells stored in the dark, at room temperature, at open circuit and under $30\,\%\leq$RH$\leq 60\,\%$) was tested for more than $1000\,\mathrm{h}$ and enhanced stability was observed for higher TBA contents, providing evidence of the beneficial effect on the material stability. Indeed, higher water contact angles were measured for mixed MA/TBA perovskite films, resulting in enhanced moisture-stability.

The results summarised in this section have been published by Poli et al. (2017). [16] The statement of authorship is given below.

Few typing mistakes were found in the published article: some of the ° units were printed as °C. These mistakes have been generated when the submitted LaTeX file was converted into the online pdf version by the journal after the article was accepted. Unfortunately, these typing mistakes were not spotted by the authors during the proof reading. For this reason, the accepted submitted version of the article is shown here, which is the same as the published one but without typing mistakes.

This declaration concerns the article entitled:					
Tetrabutylammonium cations for moisture-resistant and semitransparent perovskite solar cells					
Publication status (tick one)					
Draft manuscript		**Submitted**		**In review**		**Accepted**		**Published**	X
Publication details (reference)	The article has been published in: *J. Mater. Chem. A*, Vol. 5, 22325-22333 (2017)				
Copyright status (tick the appropriate statement)					
I hold the copyright for this material		Copyright is retained by the publisher, but I have been given permission to replicate the material here	X		
Candidate's contribution to the paper (provide details, and also indicate as a percentage)	The candidate **predominantly** executed the work presented in the paper. **Formulation of ideas:** The objectives, analysis and conclusions of the paper were formulated by the candidate, with the support of the lead supervisor Petra Cameron. [IP=85%, SE=0%, PJC=15%] **Design of methodology:** The methodology was designed by the candidate with the support of the lead supervisor Dr Petra Cameron. [IP=85%, SE=0%, PJC=15%] **Experimental work:** All experimental work was carried out by the candidate. [IP=100%, SE=0%, PJC=0%] **Presentation of data in journal format:** Data were analysed by the candidate and plots and figures in journal format were generated by the candidate. The writing of the manuscript was done by the candidate. The lead supervisor Petra Cameron, second supervisor Salvador Eslava reviewed and corrected the writing of the paper. Petra Cameron gave assistance in the submission and peer reviewing process. [IP=78%, SE=2%, PJC=20%]				
Statement from Candidate	This paper reports on original research I conducted during the period of my Higher Degree by Research candidature.				
Signed	X Isabella Poli Isabella Poli		**Date**	11/06/2019	

Journal Name

ARTICLE TYPE

Cite this: DOI: 10.1039/xxxxxxxxxx

Tetrabutylammonium cations for moisture-resistant and semitransparent perovskite solar cells†

Isabella Poli,[§ ‡] * Salvador Eslava,[¶ ‡] and Petra Cameron [§ ‡] *

Received Date
Accepted Date

DOI: 10.1039/xxxxxxxxxx

www.rsc.org/journalname

Perovskite solar cells have gained increasing interest, especially after reaching performances which are comparable with mature silicon PV technologies. However, the perovskite crystalline structure $CH_3NH_3PbI_3$ is unstable in the presence of moisture, which leads to fast degradation in ambient conditions. The commercialisation of perovskite solar cells will only be achieved with the engineering of long term stable materials. We report a modified perovskite absorber layer obtained by adding methylammonium iodide (MAI) and tetrabutylammonium (TBA) iodide. The incorporation of TBA improves the film coverage, reducing the number of pinholes. X-ray diffraction analysis suggests that, in common with other mixed larger cation perovskites, two distinct phases coexist: a 3D perovskite material and a 2D layered material. The TBA containing perovskite films showed improved hydrophobicity, which contributed to a significantly higher moisture stability. The cells maintained their original PCE after 45 days in ambient condition without encapsulation. In comparison the $CH_3NH_3PbX_3$ 3D perovskite device lost more than 60% of its original efficiency over the same time.

Introduction

Methylammonium lead halide perovskite is a promising material for the development of cheap, solution processed solar cells. Since the emergence of perovskite solar cells in 2012,[1,2] improvements in film morphology and fabrication technique has lead to a power conversion efficiency (PCE) of 22.1%.[3] Some of the properties that allow halide perovskites to be so efficient in photovoltaic applications are their good absorption of light in the visible range, long electron and hole lifetimes and optoelectronic tunability.[4] A lot of research has focused on thin film fabrication to improve morphology and device reproducibility. Different lead sources have been investigated[5–8] and solvent engineering strategies developed to improve perovskite crystallinity.[9] These approaches have helped to increase the PCE of halide perovskite solar cells rapidly.

A big challenge that remains is to ensure the long term stability of perovskite solar cells under ambient conditions. Perovskite materials suffer from very fast degradation when exposed to water or even moisture in the air.[10] Leguy *et al.* showed that moisture in air induces a hydration process in $CH_3NH_3PbI_3$, which causes strong current drops and voltage losses.[11] These losses can be reversed according to equation 1.

$$4(CH_3NH_3)PbI_3 + 4H_2O \rightleftharpoons 4[CH_3NH_3PbI_3 \cdot H_2O] \rightleftharpoons (CH_3NH_3)_4PbI_6 \cdot 2H_2O + 3PbI_2 + 2H_2O \quad (1)$$

However, high excess of water results in a permanent dissolution of the methylammonium cation and irreversible degradation of the perovskite structure (Eq. 2).[11]

$$(CH_3NH_3)_4PbI_6 \cdot 2H_2O \xrightarrow{H_2O_{(l)}} 4CH_3NH_3I + PbI_2 + 2H_2O \quad (2)$$

Over the last few years a number of strategies, summarised in Fig. 1, have been developed to improve the moisture stability of perovskite solar cells (PSC). The first strategy is encapsulation: a selection of sealing materials with good high temperature performance[19] can protect the PSC and allow it to remain chemically stable[20] under normal working conditions. However, encapsulation leads to considerably higher fabrication costs.

A second strategy to improve stability is by introducing new

[§]*Department of Chemistry, University of Bath, Bath BA2 7AY, United Kingdom*
[¶]*Department of Chemical Engineering, University of Bath, Bath BA2 7AY, United Kingdom*
[‡]*Centre for Sustainable Chemical Technologies, University of Bath, Bath BA2 7AY, United Kingdom*
** Corresponding authors: i.poli@bath.ac.uk; p.j.cameron@bath.ac.uk*
† Electronic Supplementary Information (ESI) available. See DOI: 10.1039/b000000x/

Table 1 Summary of some of the cations used as additives into the perovskite solution found in literature and their impact on the perovskite film and device

Additive	Name	Enhancement	Ref
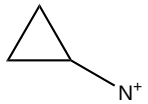	cyclopropylammonium	• 2D/3D interface • higher efficiency and improved moisture resistance	12
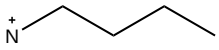	n-butylamine	• 2D/3D layered perovskite absorber layer • 12.52% efficiency and greater tolerance to high RH	13–15
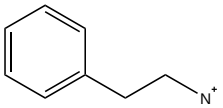	phenylethylammonium	• first 2D/3D layered perovskite absorber layer	16
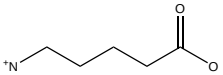	5-ammonium valeric acide	• 2D/3D perovskite junction • 1-year stability	17
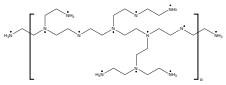	polyethylenimine	• 2D materials in the final structure • higher absorption and slower degradation in air	18

coating layers in the structure. In 2014 the organic HTM Spiro OMeTAD was replaced with a conducting carbon nanotube-poly methylmethacrylate (PMMA) composite for the first time.[21] This novel layer was mainly introduced to mitigate thermal degradation. The adopted PMMA-nanotube composite HTM was found to protect the perovskite structure and seal in volatile components more efficiently than the commonly employed HTM Spiro OMeTAD, due to its nonhygroscopic nature.[21] More recently, fluorinated photo-polymer coatings[22] and hydrophobic polymers, such as poly(4-vinylpyridine),[23] which form strong hydrophobic barriers, have been reported. The coating was deposited on top of the perovskite film once it was dried.

A third way of enhancing moisture stability is through the use of small molecules adsorbed to the surface of the perovskite crystallites in the film. Young *et al.* showed how alkyl ammonium cations can be used to functionalise the perovskite surface. Perovskite films were dipped into alkyl ammonium iodine solution, improving the humidity tolerance and passivating surface defects.[24] Li *et al.* used 2-aminoethanethiol (2-AET) as a ligand for MAI and PbI_2, adding it into the perovskite precursor solution. The strong coordination interaction of PbI_2-2-AET-(MAI) generated a very efficient barrier layer, which protected the perovskite crystal structure for over 10 minutes after immersion in water.[25] A similar approach was reported by Sun *et al.*, who added 2-pyridylthiourea in the perovskite precursor solution, achieving high conversion efficiencies and relatively better stability.[26] The implementation of these interlayers delayed perovskite degradation.

The fourth and final approach is very promising as it has been shown to create perovskite solar cells that are stable for up to one year[17] and importantly achieves comparable performances to standard 3D perovskite device. In this approach 2D/3D perovskite hybrids are prepared. Several cations have been investigated to make these 2D/3D hybrid structures, which are listed in Table 1. The first layered 2D/3D perovskite used as absorber layer was reported in 2014 by Smith *et al.*, using phenylethylammonium (PEA).[16] Devices containining $(PEA)_2(MA)_2Pb_3I_{10}$ showed enhanced moisture stability, but poor power conversion efficiency (the best performing cell had a PCE of 4.73%). Later on, Tsai *et al.* overcame the issue of poor efficiency, reporting a 12.52% efficient device using n-butylammonium (BA) spacer cations in a mixed 2D/3D hybrid structure.[15] Very recently, a protonated salt of aminovaleric acid iodide (AVAI) was added to the precursor solution, showing much higher moisture resistivity in standard device and one-year stability in carbon-based solar cells.[17] Grancini *et al.* suggested that a 2D/3D junction is generated at the TiO_2/perovskite interface when AVAI is added,[17] allowing the creation of carbon-based PSC with impressive stability. It is worth noting that the XRD patterns of the AVAI/MAI mixed perovskites used to fabricate the solar cells do not show evidence of low dimensional perovskite being formed as is seen by others.[12,13] The authors claimed that the 2D layer was too thin to be observed; however, it could also suggest that AVAI is concentrated in the grain boundaries, modifying the crystal structure, instead of generating a 2D/3D junction at the interface. Ma *et al.* reported a 2D perovskite capping layer, which allowed an increase in moisture tolerance while still keeping high conversion efficiency of a 3D absorber layer.[12] A solution of cyclopropylammonium iodide (CAI) was spin coated on top of the formed 3D perovskite layer, generating a 2D/3D $CA_2PbI_4/CH_3NH_3PbI_xCl_{3-x}$ perovksite interface at the perovskite/spiro OMeTAD junction.

Tetrabutylammonium (TBA) and other tetraalkylammonium cations have been extensively exploited for their amphiphillic properties in the crystallisation and templating of zeolites and other porous materials.[27] In perovskite solar cells, TBA is one of the alkyl ammonium cations that has been recently used as a

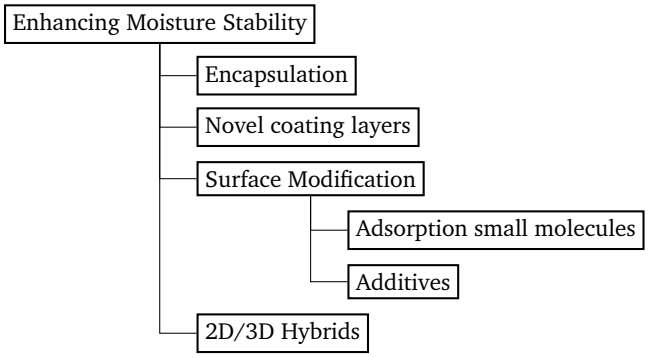

Fig. 1 Diagram which summarizes the approaches found in literature to limit the moisture instability of perovskite solar cells

moisture tolerant small molecule to functionalise the perovskite surface. Pre-formed perovskite films were dipped in solvent containing TBA and the alkyl ammonium cations assembled on top of the perovskite films. The humidity tolerance of the film was improved, although solar cells based these films were not fabricated.[24] Up to now, TBA has been used as processing additive to prepare perovskites only once. It was found that introducing tetrabutylammonium iodide salt into the perovskite precursor solution, increased coverage and reduced pinhole size.[28] It was speculated that TBA formed a layered organic-inorganic structure but no evidence was shown in the XRD pattern. Furthermore, solar cells prepared by adding only 1wt% of TBA into the precursor solution showed very poor PCE of 1.4%.[28]

In this work, MAI is partly substituted with TBA using different molar percentage concentrations. We show that TBA can be used as an ionic additive in the precursor solution to enhance the stability of the final device. X-ray diffraction (XRD) analysis suggests the coexistance of two distinct phases: a 3D perovskite layer and a 2D layered perovskite. TBA might be pushed towards the surface of perovskite grains, generating 2D sheets and intra-layers between the perovskite/spiro interface. Mixed 2D/3D structures show comparable photovoltaic performance to standard 3D $MAPbX_3$, with PCEs over 10%. Above all, they show better stability compared to the reference device. Higher water contact angles were measured for mixed cations films, which might contribute to the greater moisture stability. When aged in the dark, under ambient condition (40± 20% relative humidity), the PCE for the TBA containing devices was found to be unchanged after over 40 days.

Experimental

Materials

CH_3NH_3I (MAI) was bought by Dyesol Australia. PbI_2, $PbCl_2$ and tetrabutylammonium (TBA) iodide were all bought from Sigma-Aldrich. The standard perovskite precursor solutions were prepared by dissolving MAI, PbI_2 and $PbCl_2$ in N,N-dimethylformamide (DMF, anhydrous, Sigma-Aldrich) to get 40w% solution (MAI:PbI_2:$PbCl_2$ - 4:1:1). TBA iodide was added into the perovskite precursor solutions. Cation A was partly substituted with TBA instead of MAI with different molar percentage concentrations TBA%:MAI% (1:99, 3:97, 5:95, 10:90, 30:70, 100:0). As the concentration of I and Cl in the perovskite film is uncertain, the abbreviations $MAPbX_3$, $(TBA)_n(MA)_{1-n}PbX_3$ and $(TBA)PbX_3$ are used in the text.

The electron transport material solution consisted of 200 mM titanium diisopropoxide bis(acetylacetonate) in ethanol. The hole transport material solution consisted of 85mg/ml Spiro OMeTAD (Sigma-Aldrich) in chlorobenzene, with additives of 30 μL/mL of *t*-butyl pyridine (Sigma Aldrich) and Li-TFSI.

Solar cell fabrication

FTO glass (Sigma-Aldrich) was etched with zinc powder and HCl. It was then cleaned in 2vol% Hellmanex solution in water, followed by deionised water, acetone, propan-2-ol and ethanol.

A compact TiO_2 layer was deposited by spray pyrolysis, using a hand held atomiser to spray the solution onto the substrates held at 500°C. Substrates were then sintered at this temperature for 10 minutes. A mesoporous TiO_2 layer (2:7 weight mixture of Dyesol's 30NRD TiO_2 paste in ethanol) was spun onto the TiO_2 compact layer and annealed for 15 minutes at 150°C and then a further 30 minutes at 500°C. After cooling, substrates were placed in a UV Ozone treatment for 30 minutes. Perovskite deposition was performed in a nitrogen filled glove box, following a one-step method. 100 μL of precursor solution was spun onto the substrate at 4000 rpm for 30 seconds, then dried at 100°C for 90 minutes. Spiro solution was spun onto the perovskite film at 3000 rpm for 30 seconds. To establish the contacts, a 2-mm wide channel of perovskite was removed from the centre of the substrate. Finally, 100 nm thin layer of gold was thermally evaporated using evaporation masks to have 6 pixels of 0.0625 cm^{-2}.

Characterisation

PXRD Powder diffraction patterns were collected using a Bruker Advance D8 X-ray diffractometer with a Cu Kα source. Measurements were taken from 2θ values of 5° to 80°.

UV/vis spectroscopy Thin film optical transmission and reflectance measurements were performed on a Perkin-Elmer Lambda 750S UV/Vis spectrometer, from 900 nm to 300 nm. Absorption was calculated as $\alpha = log(\frac{1-R}{T})$

J-V curves JV curves were measured using Keithley 2601A potentiostat, under 1 Sun intensity and AM 1.5. The volatge was sweept at 100 mV/s from 1.2V to 0V and back to 1.2V. The 6 pixels were measured independently using a mask to cover the non-active area.

SEM and AFM images Top-view SEM images were taken on a JEOL SEM 6480LV, at an acceleration voltage of 5kV. AFM images were taken on a Nanosurf easyscan 2 FlexAFM system in Phase Contrast mode using a force of 2 nN. A ContAl-G Tip was used for measurements.

Results and discussion

Perovskite solutions of $(TBA)_n(MA)_{1-n}PbX_3$ with n=0, 0.01, 0.03, 0.05, 0.1, 0.3 and 1 were used to fabricate thin films, in such a way that some of the MA cations are partially or entirely substituted with TBA cations. The growth characteristics, optical properties and film morphology were investigated. Fig. 2 shows

the chemical structure of TBA ion. In Table 2, the ionic radii of cations commonly used in organic-inorganic perovskite materials are listed. Formamidinium (FA) and methylammonium (MA) have similar size and they are considerably bigger than caesium. When one of these cations or mixtures of them are used to generate perovskite materials, a tetragonal 3D structure is created. The ionic radius of $(C_4H_9)_4N^+$ (TBA) is considerably larger. Being such a big cation, it is more likely to form a 2D perovskite structure, like the one created by using n-butylammonium cations.[15]

Table 2 List of ionic radii of cations commonly used in organic-inorganic perovskite materials compared to the ionic radius of 4 $(C_4H_9)N^+$ (TBA)

Cation	name	r_c [Å]	ref
$CH_3NH_3^+$	MA	2.70	[29]
$CH_3(NH_2)_2^+$	FA	2.79	[29]
Cs	Cs	1.81	[29]
$(C_4H_9)_4N^+$	TBA	4.94	[30]

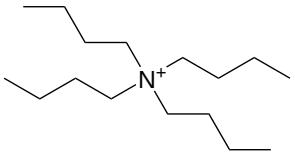

Fig. 2 Chemical structure of tetrabutylammonium (TBA) cation

Structural properties

X-ray diffraction (XRD) measurements of 2D/3D hybrid perovskite films found in literaure showed consistent peaks at low angles ($2\theta < 10°$).[12,13,17,18] Fig. 3 shows XRD patterns of thin films made with $(TBA)_n(MA)_{1-n}PbX_3$ solutions, with n=0, 0.01, 0.03, 0.05, 0.1, 0.3 and 1 (from the bottom to the top).

XRD patterns reveal that the perovskite structure changes considerably when TBA is added to the solution. Diffraction peaks at approx. 14°, 28° and 32° correspond to the (110), (220) and (310) crystal planes, assigned to the tetragonal phase of the 3D $MAPbX_3$ perovskite structure.[9,31] A very strong diffraction peak at 2θ=7.8° appears in films with TBA-only (100% mol - n=1) and remains in the final mixed perovskites. The position of this peak is consistent with the characteristic peak of 2D perovskites observed in literature when 2D/3D hybrids were formed.[12,18]

Ma *et al.*, who reported a 2D perovskite capping layer using a solution of cyclopropylammonium iodide, observed that the intensity of the diffraction increased with the concentration of CAI.[12] Similarly, the intensity of the diffraction peak assigned to the 2D perovskite phase $(TBA)PbX_3$ increases with the concentration of TBA. Fig. S1 shows the integrated intensity of the diffraction peaks with increasing concentration of TBA. In the mixed perovskite films, the 2D perovskite phase $(TBA)PbX_3$ coexists with the 3D $MAPbX_3$ perovskite phase. TBA containing films with concentrations higher than 3mol% show preferential growth along the 2D $(TBA)PbX_3$ perovskite phase direction. The peak at 2θ=7.9°, assigned to the 2D component, slightly decreases when 30mol% of TBA is added to the precursor solution. However, the intensity of the peaks assigned to the 3D components ([110] and [220]) decreases similarly, indicating reduced crystallinity of the film. Figure S2 shows the variation of the ratio between the 2D peak and 3D peak ([110]); For TBA concentration higher than 5%, the ratio is found to be fairly constant.

Cao *et al* have previously reported that in the case of mixed $(BA)_2(MA)_{n-1}Pb_nI_{3n+1}$, with $n > 1$, a competition between BA and MA ions arises in the structure. The former tries to confine the growth on the planar layer; the latter tries to expand the perovskite outside the layer.[13] Assuming TBA behaves similarly to BA, and referring to the intensity of diffraction peaks in Fig. S1, it might be concluded that the vertical growth pushed by TBA cations increases with TBA concentration, suggesting thicker 2D layers are present. On the other hand, the integrated intensity of peaks assigned to the 3D tetragonal phase ([110] and [220]) slightly decreases with the concentration of TBA, suggesting reduced growth of 3D $MAPbX_3$ crystal.

Neat $MAPbX_3$ films show a small peak at 2θ=12.7° (100), which is a characteristic peak of PbI_2, indicating that PbI_2 has not been fully converted. This peak completely disappears as soon as some TBA is added to the structure $((TBA)_n(MA)_{1-n}PbX_3$ solutions with n≥0.01), indicating a full conversion of PbI_2. Even in the XRD pattern of the film with no MAI (100% TBA), there is no detectable peak of unconverted PbI_2, suggesting that a strong interaction between PbI_2 and TBA is formed in DMF solution. On the other hand, peaks at 2θ=9.7° and 2θ=14.7° are observed in the $(TBA)PbX_3$ film. The one at 2θ=14.7° is detected also in mixed perovskite films with TBA concentration higher than 3%.

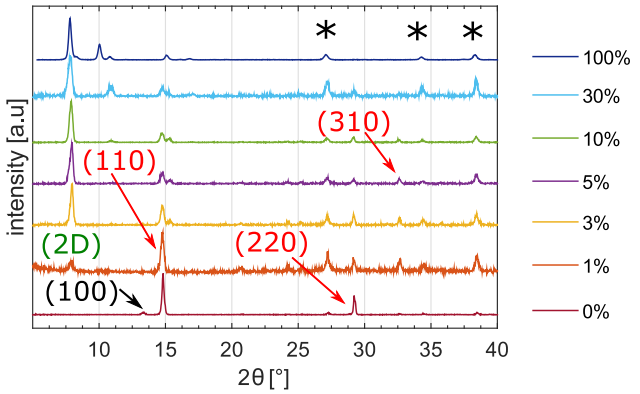

Fig. 3 XRD patterns of $(TBA)_n(MA)_{1-n}PbX_3$, from perovskite precursor solutions with n=0 (0%), 0.01 (1%), 0.03 (3%), 0.5 (5%), 0.1 (10%), 0.3 (30%) and 1 (100%) respectively. Films have spun onto FTO c-glass substrates. Peaks originated by the SnO_2 underlayer are marked by asterisks

Based on XRD measurements, it appears that a 2D phase has been formed in the $(TBA)PbX_3$ films. Similarly, other large size cation, such as the ones listed in Table 1, also formed a low dimensional 2D perovskite phase.[12–18] Mixed perovskite based on methylammonium and polyethyleneimine (PEI), which is a very large cation, showed evidence of the formation of mixed 2D/3D perovskite phase in the XRD pattern.[18] Good evidence of 2D phase coexisting with 3D $MaPbI_3$ phase is given by the presence of diffraction peaks at low angles. It is open to debate whether XRD can conclusively say that a 2D/3D mixed phase structure is

formed, but it is good evidence for the coexistence of 2D and 3D phases.

Optical properties

Fig. 4(a) and (b) show the UV-vis absorption spectra and the Tauc plot of $MAPbX_3$ and $(TBA)_n(MA)_{1-n}PbX_3$ perovskite films prepared with different concentrations of TBA. The film prepared with TBA only looked bright yellow and highly transparent and spectrum is not shown here. The linear regime in the Tauc plot denotes the onset of absorption that translates into an optical bandgap of 1.57±0.02 eV for all the samples. This result is fully consistent with what has previously been reported in literature for $MAPbX_3$ films.[12,32] Measurements were repeated on three different samples prepared in different batches.

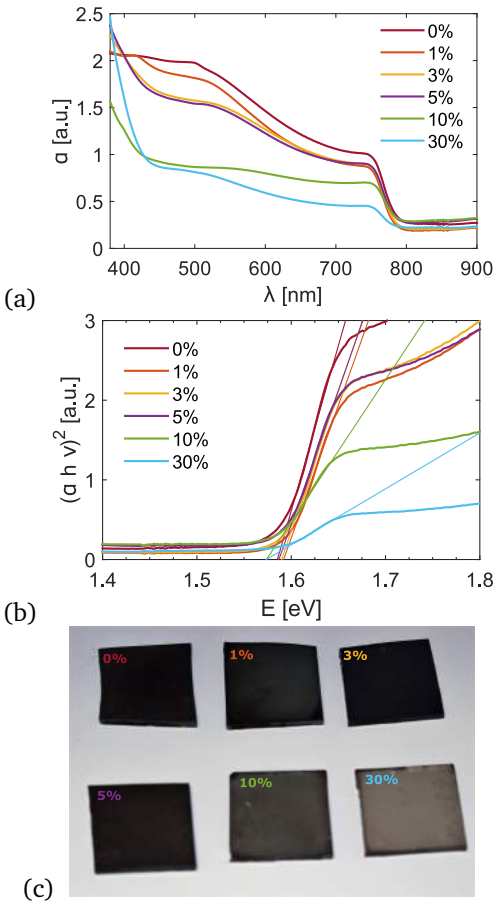

Fig. 4 (a) UV-vis absorption spectra and (b) Tauc plot of $(TBA)_n(MA)_{1-n}PbX_3$ perovskite films prepared on glass substrates with n=0 (0%), 0.01 (1%), 0.03 (3%), 0.5 (5%), 0.1 (10%), 0.3 (30%) and 1 (100%) respectively; (c) images of fabricated $(TBA)_n(MA)_{1-n}PbX_3$ perovskite films deposited on glass substrates

In Fig. 4(c), images of the $(TBA)_n(MA)_{1-n}PbX_3$ annealed perovskite films prepared with n=0, 0.01, 0.03, 0.5, 0.1 and 0.3 are shown. Films with n≤0.05, look fairly similar. They appear to be black and reflective. At higher concentrations of TBA (n≥0.1), the color changes and the film becomes more transparent. However, this net colour change is not related to the thickness of the films, which has been measured by a profilometer and found to be consistently between 300-350 nm (Fig. S4). Despite the films being the same thickness, the absorption of the TBA containing films is lower. However, SEM images, which are discussed in the next section, show that coverage is better and fewer pinholes are observed. The absorption drops when high concentrations of TBA are added to the precursor solution; this reduction is mainly due to greater transparency, as shown in Fig. S5. Although the films prepared with higher concentrations of TBA have higher transmittance, they could be used as semi-transparent PV for window applications.

Morphology

Fig. 5 shows the top-view SEM images of perovskite films without and with different concentrations of TBA. Perovskite films were spin coated on identical substrates and in the same conditions to compare the different SEM images and investigate the effect that TBA has on the crystallisation.

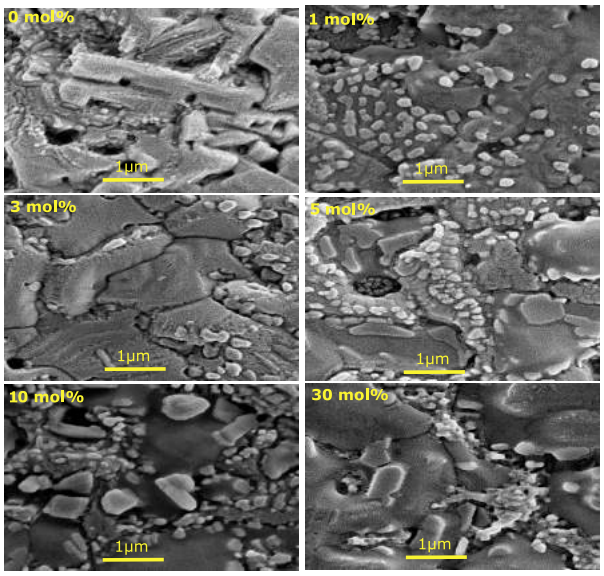

Fig. 5 Top surface SEM images of $(TBA)_n(MA)_{1-n}PbX_3$ perovskite films with different TBA concentration (n=0 (0%), 0.01 (1%), 0.03 (3%), 0.5 (5%), 0.1 (10%), 0.3 (30%) and 1 (100%) respectively); Films were deposited onto a compact layer of TiO_2

Neat $MAPbX_3$ shows the typical branch-like perovskite grains.[33] Particularly large and elongated crystals are observed, fully consistent with what has previously been reported in the literature for $MAPbI_{3-x}Cl_x$.[5] Spin-coating the precursor solution directly onto the compact TiO_2 layer results in a dewetting effect that causes poor surface coverage.[34] Fig. S6 shows larger top view SEM images, and large pinholes on the substrate, which are coloured in red for easier comparison, are emphasized. When TBA is used, the elongated crystals disappear and larger more homogeneous crystallites with enhanced surface perovskite coverage and fewer pinholes were observed. Moreover, the SEM images show that some small crystals start to form on the surface of the film, which may be 2D TBA crystallites. When using more TBA, the number of small 2D TBA crystallites sitting on top of the perovskite grains increases. Top surface AFM images (a) with-

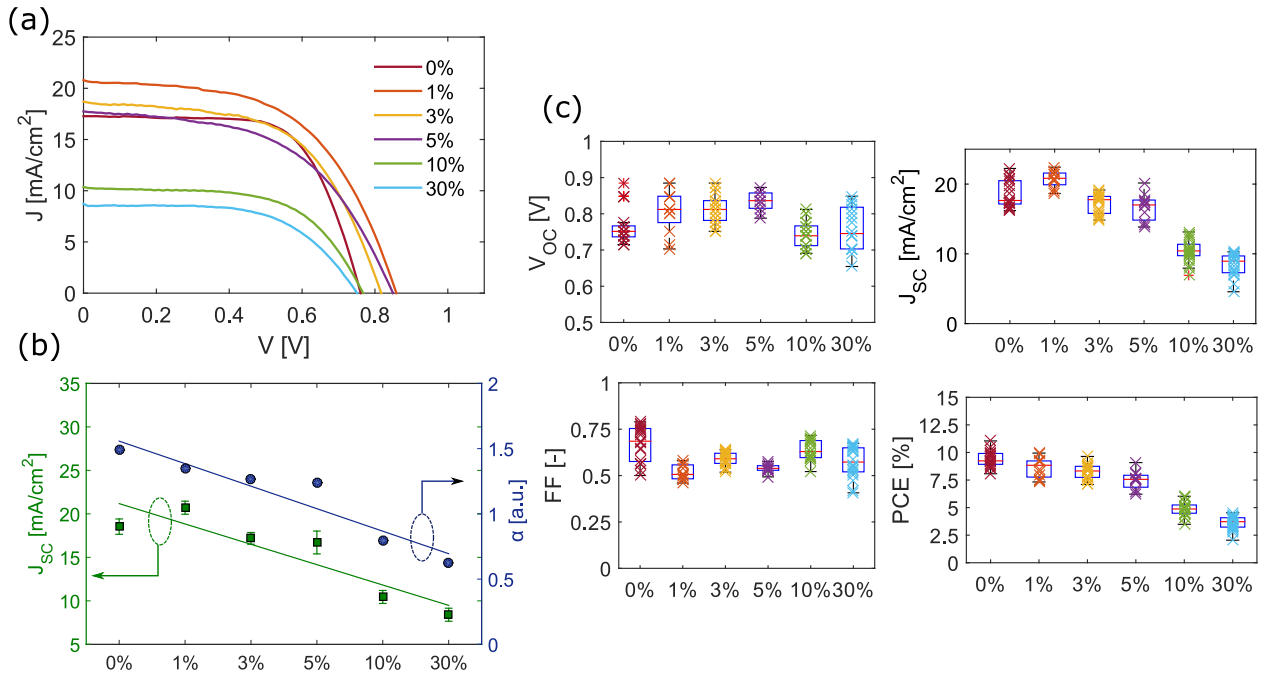

Fig. 6 (a) JV curves of average performed devices based on 3D MAPI perovskites (0%) and mixed 2D/3D $(TBA)_n(MA)_{1-n}PbX_3$ (with n=0 (0%), 0.01 (1%), 0.03 (3%), 0.5 (5%), 0.1 (10%), 0.3 (30%) and 1 (100%) respectively). Typical JV curve obtained by reverse scan from 1.2V to 0V. (b)J_{SC} and average spectral absorption of films (absorption data averaged between 450 and 750 nm) as a function of the concentration of TBA; the error bars indicates upper and lower 95% confidence interval boundaries computed for a normal distribution fitted to the data set (between 11 and 21 different pixels for each TBA concentration) (c) Photovoltaic parameters shown as box plots for efficiency distributions of perovskite solar cells based on 3D and mixed 2D/3D with various TBA concentrations tested under AM 1.5 and 1 sun illumination (reproducibility evaluated by characterising between 11 and 21 different pixels for each TBA concentration)

out and (b-f) with TBA as additive are illustrated in Fig. S7. Neat $MAPbX_3$ film crystals look quite homogeneous, with grains of similar size. When TBA is used, a much larger variety of grain sizes can be seen, with interconnected big crystals and relatively small crystals. As shown in Fig. S7(g), the addition of TBA changes the average roughness of the perovskite films. These values have been measured over 50μm x 50μm size images (Fig. S8) and averaged over 8 different images. The average roughness indicates the microscopic peaks and valleys that can be found on the surface, which is found to increase with TBA concentration.

Recent reports have suggested that additives, such as 2-aminoethanethiol and 2-pyridylthiourea, might slow down crystallisation, allowing the formation of intermidiate phases and pushing additives from grain boundaries throughout the film to the surface of the film itself.[25,26] It is possible that a similar process is also occurring when TBA is added, leading to a high concentration of 2D TBA crystallites on the surface. Looking at the colour change during annealing, it was noticed that when the TBA cation was added to the precursor solution, the reaction between the organic iodide and the PbI_2 was retarded. This delay may cause enhanced surface coverage. From Fig. S6 it can be seen that at the highest TBA concentrations, 2D TBA crystallites are found in between the larger perovskite grains. In the top-view SEM of 30mol% in Fig. 5, it can be clearly seen that some TBA crystallites are found between crystal grains and some of them can be seen underneath, suggesting a mixed 2D/3D structure.

JV performance

To investigate the photovoltaic performance, J-V curves of PSCs with and without TBA were measured and are shown in Fig. 6 (a). The curves were obtained under reverse scan, the forward scan is shown in Fig. S9. The average device performance of each case has been used as the basis of the comparison. The corresponding V_{OC}, J_{SC}, fill factor (FF) and power conversion efficiency (PCE) at reverse and forward voltage scans are summarized in Table 3, together with the champion PCEs obtained. It is important to note that the cells were not optimised for efficiency as it was more important to obtain a reproducible baseline for a standard cell so the effect of TBA could be understood. The efficiency can be pushed to higher values by controlling the crystallization kinetics of perovskites. Several techniques can be used, including anti-solvent methods where solvents, such as toluene or chlorobenzene, are dripped onto spinning perovskite to obtain smooth and compact films.[35] However it was not clear whether the anti-solvent method would change the ratio of 2D to 3D perovskite in the cells with TBA so it was decided to use the simplest preparation method and to sacrifice some efficiency for better comparability.

According to literature, when mixed FA/MA cells and triple cation Cs/FA/MA cells are fabricated, the hysteresis is commonly not pronounced.[29,36] Similarly, the presence of large cations, such as cyclopropylammonium and polymericammonium, seemed to reduce the hysteresis effect with respect to standard $MAPbX_3$ cells.[12,18] It is interesting to note that contrary to

Table 3 V_{OC}, J_{SC}, FF and PCE of average-performing devices without and with TBA at different concentration at reverse (rev.) and forward (for.) voltage scans. The champion PCE (ch. PCE) is also showed.

Concentration of TBA	Dir.	V_{OC} [V]	J_{SC} [mA cm^{-2}]	FF	PCE [%]	ch. PCE [%]
0%	rev.	0.75	17.46	0.68	8.87	11.05
	for.	0.75	16.95	0.62	7.88	
1%	rev.	0.85	20.82	0.56	9.91	9.95
	for.	0.84	20.71	0.51	8.76	
3%	rev.	0.81	18.71	0.58	8.85	9.64
	for.	0.81	18.63	0.54	8.25	
5%	rev.	0.85	17.75	0.53	8.01	9.08
	for.	0.85	17.95	0.49	7.51	
10%	rev.	0.76	10.37	0.61	4.85	6.03
	for.	0.75	10.20	0.55	4.25	
30%	rev.	0.75	8.75	0.59	3.88	4.53
	for.	0.74	8.58	0.56	3.55	

what found in literature, the presence of TBA does not appear to reduce hysteresis.

Final devices demonstrate good reproducibility (Fig. 6(c)). JV curves in Fig. 6(a) shows that initially the average photogenerated current increases when a thin 2D perovskite layer is added (1mol%). This could occur if the 2D perovskite layer passivates the surface of the film. However, when the amount of 2D perovskite in the film is further increased (TBA concentration higher than 3mol%), more transparent films were obtained and the photocurrent decreased. The maximum current that can be extracted from a device strongly depends on the light absorption. The photogenerated current was found to decrease as the transparency of the perovskite films increased. JV curves as well as J_{SC} and film transparency data is shown in Fig. 6 (a) and (c). Similarly, Yao *et al.* observed that the J_{SC} of mixed methylammonium and polymeric-ammonium devices was lower than the J_{SC} of the control $MAPbI_3$.[18] It is possible that the presence of thick 2D perovskite layers reduces carrier mobility, increasing the electron-hole recombination.[10] 1mol% was found to be the optimum TBA concentration to get the maximum extractable current.

The open circuit voltage is improved slightly (by an average of 0.05 V) following the addition of low concentration of TBA. SEM images proved that higher coverage is obtained when TBA is added to the solution, decreasing the pinholes density. Further increasing the concentration of TBA, pushes the V_{OC} to lower values, comparable to the one obtained for the reference solar cell (0% TBA). On the other hand, devices with 10% and 30% of TBA showed higher FF.

The PCE decreases with the concentration of TBA; the main parameter affecting a lower PCE is the J_{SC}. A reduction in the photocurrent was observed for higher transmittance devices, which is fully consistent with what observed in literature.[37,38] Fig. 6(b) shows the J_{SC} and the spectral absorption as a function of the concentration of TBA in the precursor solution. It was found that the reduction of absorption with increasing concentration of TBA was mainly due to higher transparency. When compared to the trend of photocurrent, a linear correlation between optical properties and J_{SC} was found.

Long term stability

An important advantage of the TBA containing perovskite solar cells is that we found them to have a higher resistance to moisture. Fig. 7 shows the long term stability of samples without and with 1mol%, 3mol% and 5mol% of TBA added to the precursor solution.

Solar cells were stored in the dark, at room temperature and ambient relative humidity, which varied between 30% to 60% over time, and tested without encapsulation in an ambient environment. The variation of the other device parameters (V_{OC}, J_{SC} and *FF*) are shown in Fig. S11. V_{OC} and *FF* were not significantly affected by moisture. The photocurrent density of the device without TBA decreases in just a few days. On the other hand, the PCE of devices with some TBA starts to drop after about 45 days, showing much slower degradation. We believe that the bulky organic TBA delays the ingress of water, slowing the degradation of the device when stored under ambient conditions. These results reinforce the conclusion that 2D TBA crystallites are present at the surface. The perovskite structure of mixed cations films decomposed when dipped into water. However, contact angle measurements using water droplets, showed that the mixed cations perovskite films had a more hydrophobic surface (see Fig. 8). This result might significantly contribute to the greater moisture stability reported.

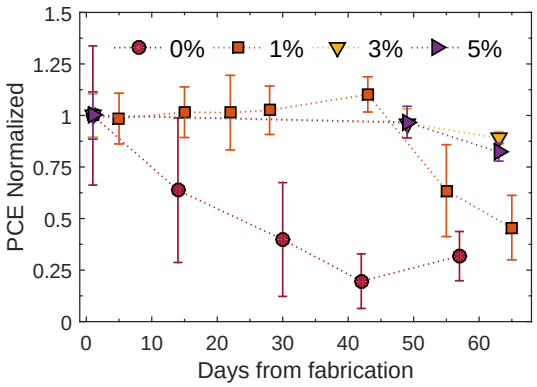

Fig. 7 Evolution of PCE over time for samples without and with different concentrations of TBA ($(TBA)_n(MA)_{1-n}PbX_3$ with n=0 (0%), 0.01 (1%), 0.03 (3%), 0.5 (5%)). Each point is representative of 6 pixels. The marker indicates the mean value of each set of data. The top and the bottom of the error bars are upper and lower 95% confidence interval boundaries computed for a normal distribution fitted to the data set. All the values have been normalised with respect to the mean value obtained after deposition (7.13%, 7.36%, 8.73% and 6.65% for 0%, 1%, 3% and 5% TBA respectively)

After about 45 days the cells with TBA started losing efficiency. However, degradation and decomposition of the solar cells might be affected by other factors, such as damage to the Au contacts due to repeated measurements, corrosion of thin metal layers,[19] degradation of the Spiro HTM due to hygroscopic additives[39] and formation of voids in the perovskite layer due to detachment of the material from the TiO_2 layer.[19] Films with TBA look black after over 100 days, indicating that the formation of PbI_2 may not be the main degradation mechanism (see Fig. S12). Once

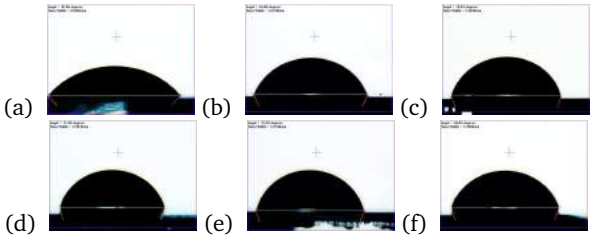

Fig. 8 Water contact angle measurements of perovskite films (a) without and (b-f) with various concentration of TBA added to the solution. (a)0% TBA: 48°; (b)1% TBA: 66°; (c)3% TBA: 71°; (d)5% TBA: 72°; (e)10% TBA: 73°; (f)30% TBA: 69°

water molecules attack the perovskite interface, it has been suggested that CH_3NH_2 and volatile gases are released, enlarging the pinholes and causing delamination, which limits charge collection.[39] As water molecules gain acces through pinholes, smooth and pinhole-free surfaces are expected to show higher stability.[40] By optimizing the device with anti-solvent methods, the stability of mixed TBA-MA perovskite based solar cells is expected to reach greater heights.

Conclusions

In summary, $(TBA)_n(MA)_{1-n}PbX_3$ perovskite films with improved hydrophobicity have been observed. Tetrabutylammonium was added to the perovskite precursor solution in different concentration. The films containing TBA, which is a much larger cation than MA, showed better coverage and fewer pinholes when compared to a $MAPbI_3$ film. The presence of TBA delayed the formation of the perovskite phase, retarding the change in film colour change. X-ray diffraction measurements showed that mixed TBA/MA films lead to the growth of perovskite films, where 2D perovskite phase coexisted with the 3D $MAPbI_3$ phase. Top-view SEM images suggested that 2D $(TBA)PbX_3$ crystallites are deposited on the surface when TBA is added. 2D perovskite layers may result in surface passivation; We estimated that the maximum extractable current was obtained when a TBA concentration of 1mol% was used. The TBA containing perovskite solar cells showed higher moisture stability, with stable PCE after more than 40 days in ambient conditions without encapsulation. We suggest that TBA cations might be driven to the surface of perovskite grains. The bulky alkyl chains could act as a hydrophobic layer on the surface, delaying the degradation of the perovskite film under ambient conditions.

Acknowledgements

We acknowledge Mrs. Ursula Potter for her assistance in SEM acquisition. We would like to thank the EPSRC Centre for Doctoral Training in Sustainable Chemical Technologies (EP/L016354/1). This project has received funding from the European Union's Horizon 2020 research and innovation programme H2020-MSCA-CO-FUND-2014 (# 665992, MSCA FIRE: Fellows with Industrial Research Enhancement). Dataset available - see DOI: https://doi.org/10.15125/BATH-00403

References

1 M. M. Lee, J. Teuscher, T. Miyasaka, T. N. Murakami and H. J. Snaith, *Science*, 2012, **338**, 643–647.

2 H.-S. Kim, C.-R. Lee, J.-H. Im, K.-B. Lee, T. Moehl, A. Marchioro, S.-J. Moon, R. Humphry-Baker, J.-H. Yum, J. E. Moser, M. Grätzel and N.-G. Park, *Scientific reports*, 2012, **2**, 591.

3 M. A. Green, K. Emery, Y. Hishikawa, W. Warta, E. D. Dunlop, D. H. Levi and A. W. Y. Ho-Baillie, *Prog. Photovolt: Res. Appl.*, 2017, 3–13.

4 M. a. Green, A. Ho-Baillie and H. J. Snaith, *Nature Photonics*, 2014, **8**, 506–514.

5 S. T. Williams, F. Zuo, C. C. Chueh, C. Y. Liao, P. W. Liang and A. K. Y. Jen, *ACS Nano*, 2014, **8**, 10640–10654.

6 C.-c. Chueh, C.-z. Li and A. K. Jen, *Energy & Environmental Science*, 2015, **00**, 1–30.

7 W. Zhang, M. Saliba, D. T. Moore, S. K. Pathak, M. T. Horantner, T. Stergiopoulos, S. D. Stranks, G. E. Eperon, J. A. Alexander-Webber, A. Abate, A. Sadhanala, S. Yao, Y. Chen, R. H. Friend, L. A. Estroff, U. Wiesner and H. J. Snaith, *Nat Commun*, 2015, **6**, 6142.

8 R. G. Niemann, A. G. Kontos, D. Palles, E. I. Kamitsos, A. Kaltzoglou, F. Brivio, P. Falaras and P. J. Cameron, *Journal of Physical Chemistry C*, 2016, **120**, 2509–2519.

9 N. J. Jeon, J. H. Noh, Y. C. Kim, W. S. Yang, S. Ryu and S. I. Seok, *Nature materials*, 2014, **13**, 1–7.

10 T. Leijtens, G. E. Eperon, N. K. Noel, S. N. Habisreutinger, A. Petrozza and H. J. Snaith, *Advanced Energy Materials*, 2015, **5**, 1500963.

11 A. M. A. Leguy, Y. Hu, M. Campoy-Quiles, M. I. Alonso, O. J. Weber, P. Azarhoosh, M. van Schilfgaarde, M. T. Weller, T. Bein, J. Nelson, P. Docampo and P. R. F. Barnes, *Chemistry of Materials*, 2015, **27**, 3397–3407.

12 C. Ma, C. Leng, Y. Ji, X. Wei, K. Sun, L. Tang, J. Yang, W. Luo, C. Li, Y. Deng, S. Feng, J. Shen, S. Lu, C. Du and H. Shi, *Nanoscale*, 2016, **338**, 643–647.

13 D. H. Cao, C. C. Stoumpos, O. K. Farha, J. T. Hupp and M. G. Kanatzidis, *Journal of the American Chemical Society*, 2015, **137**, 7843–7850.

14 D. H. Cao, C. C. Stoumpos, T. Yokoyama, J. L. Logsdon, T.-B. Song, O. K. Farha, M. R. Wasielewski, J. T. Hupp and M. G. Kanatzidis, *ACS Energy Letters*, 2017, **2**, 982–990.

15 H. Tsai, W. Nie, J.-C. Blancon, C. C. Stoumpos, R. Asadpour, B. Harutyunyan, A. J. Neukirch, R. Verduzco, J. J. Crochet, S. Tretiak, L. Pedesseau, J. Even, M. A. Alam, G. Gupta, J. Lou, P. M. Ajayan, M. J. Bedzyk, M. G. Kanatzidis and A. D. Mohite, *Nature*, 2016, **536**, 312–316.

16 I. C. Smith, E. T. Hoke, D. Solis-Ibarra, M. D. McGehee and H. I. Karunadasa, *Angewandte Chemie - International Edition*, 2014, **53**, 11232–11235.

17 G. Grancini, I. Zimmermann, E. Mosconi, D. Martineau and S. Narbey, *Nat Commun*, 2017, 1–8.

18 K. Yao, X. Wang, F. Li and L. Zhou, *Chem. Commun.*, 2015, **51**, 15430–15433.

19 Y. Han, S. Meyer, Y. Dkhissi, K. Weber, J. M. Pringle, U. Bach, L. Spiccia and Y.-B. Cheng, *J. Mater. Chem. A*, 2015, **3**, 8139–8147.

20 T. Salim, S. Sun, Y. Abe, A. Krishna, A. C. Grimsdale and Y. M. Lam, *J. Mater. Chem. A*, 2015, **3**, 8943–8969.

21 S. N. Habisreutinger, T. Leijtens, G. E. Eperon, S. D. Stranks, R. J. Nicholas and H. J. Snaith, *Nano Letters*, 2014, **14**, 5561–5568.

22 F. Bella, G. Griffini, J.-P. Correa-Baena, G. Saracco, M. Grätzel, A. Hagfeldt, S. Turri and C. Gerbaldi, *Science*, 2016, **4046**, year.

23 T. Miyasaka, B. Chaudhary, A. Kulkarni, A. K. Jena, M. Ikegami, Y. Udagawa, H. Kunugita and K. Ema, *ChemSusChem*, 2017, 1–8.

24 S. Yang, Y. Wang, P. Liu, Y.-B. Cheng, H. J. Zhao and H. G. Yang, *Nature Energy*, 2016, **1**, 1–7.

25 B. Li, C. Fei, K. Zheng, X. Qu, T. Pullerits, G. Cao and J. Tian, *J. Mater. Chem. A*, 2016, 17018–17024.

26 M. Sun, F. Zhang, H. Liu, X. Li, Y. Xiao and S. Wang, *J. Mater. Chem. A*, 2017, **5**,

13448–13456.

27 S. Eslava, J. Urrutia, A. N. Busaworv, M. R. Baklanov, F. Iacopi, S. Aldea, K. Maex, J. A. Martens and C. E. A. Kirschhock, *Journal of the American Chemical Society*, 2008, **130**, 17528–17536.

28 C. Sun, Q. Xue, Z. Hu, Z. Chen, F. Huang, H. L. Yip and Y. Cao, *Small*, 2015, **11**, 3344–3350.

29 M. Saliba, T. Matsui, J.-Y. Seo, K. Domanski, J.-P. Correa-Baena, M. K. Nazeeruddin, S. M. Zakeeruddin, W. Tress, A. Abate, A. Hagfeldt and M. Grätzel, *Energy Environ. Sci.*, 2016, **9**, 1989–1997.

30 J. S. Banait, K. S. Sidhu and J. S. Walia, *Canadian journal of chemistry*, 1984, **62**, 303–305.

31 T. Baikie, Y. Fang, J. M. Kadro, M. Schreyer, F. Wei, S. G. Mhaisalkar, M. Graetzel and T. J. White, *Journal of Materials Chemistry A*, 2013, **1**, 5628.

32 K. Sun, J. Chang, F. H. Isikgor, P. Li and J. Ouyang, *Nanoscale*, 2015, **7**, 896–900.

33 Y. Zhao and K. Zhu, *The Journal of Physical Chemistry C*, 2014, **118**, 9412–9418.

34 S. D. Stranks, P. K. Nayak, W. Zhang, T. Stergiopoulos and H. J. Snaith, *Angewandte Chemie - International Edition*, 2015, **54**, 3240–3248.

35 J. Seo, J. H. Noh and S. I. Seok, *Accounts of Chemical Research*, 2016, **49**, 562–572.

36 D. Bi, W. Tress, M. I. Dar, P. Gao, L. Jingshan, C. Renevier, K. Schenk, A. Abate, F. Giordano, J.-P. Correa-Baena, J.-D. Decoppet, S. M. Zakeeruddin, M. K. Nazeeruddin, M. Gratzel and A. Hagfeldt, *Science Advances*, 2016, **2**, 1–7.

37 G. E. Eperon, V. M. Burlakov, A. Goriely and H. J. Snaith, *ACS Nano*, 2014, **8**, 591–598.

38 P. You, Z. Liu, Q. Tai, S. Liu and F. Yan, *Advanced Materials*, 2015, **27**, 3632–3638.

39 I. Lee, J. H. Yun, H. J. Son and T.-S. Kim, *ACS Applied Materials & Interfaces*, 2017, acsami.6b14089.

40 F. Wu and L. Zhu, *Solar Energy Materials and Solar Cells*, 2017, **167**, 1–6.

Supporting Information for

Tetrabutylammonium cations for moisture-resistant and semitransparent perovskite solar cells

Isabella Poli,[§] [‡] *Salvador Eslava,*[¶] [‡] *and Petra Cameron*[§] [‡]

[§]*Department of Chemistry, University of Bath, Bath BA2 7AY, United Kingdom*

[¶]*Department of Chemical Engineering, University of Bath, Bath BA2 7AY, United Kingdom*

[‡]*Centre for Sustainable Chemical Technologies, University of BAth, Bath BA2 7AY, United Kingdom*

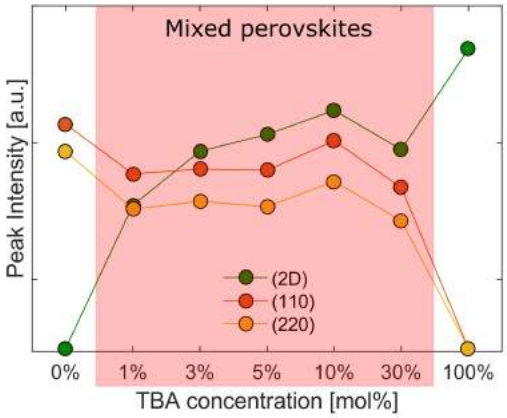

Fig. S1: Intensity of XRD peaks assigned to the 2D phase and 3D phase ([110] and [220]) of $(TBA)_n(MA)_{1-n}PbX_3$ films made from perovskite precursor solutions with n=0 (0%), n=0.01 (1%), n=0.03 (3%), n=0.5 (5%), n=0.1 (10%), n=0.3 (30%) and n=1 (100%)

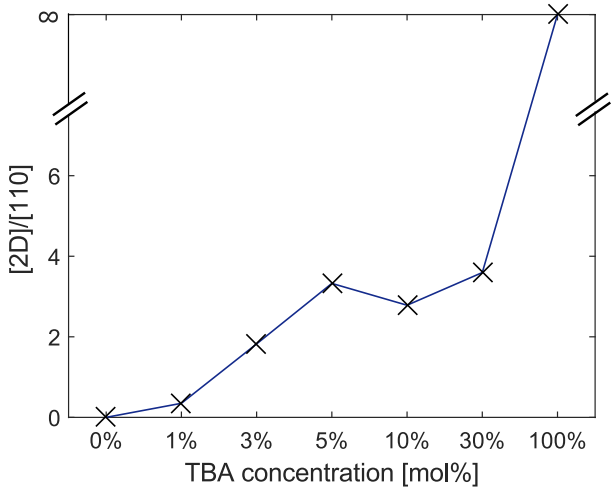

Fig. S2: Ratio between the intensity of XRD peaks assigned to the 2D phase and 3D phase (2D/[110]) of $(TBA)_n(MA)_{1-n}PbX_3$ films made from perovskite precursor solutions with n=0 (0%), n=0.01 (1%), n=0.03 (3%), n=0.5 (5%), n=0.1 (10%), n=0.3 (30%) and n=1 (100%)

Table S1: Position and integrated intensity of XRD peaks assigned to the 2D and 3D ([110] and [220]) perovskite phase. XRD patterns analysed using the MATLAB function PeakFinder

	[2D]		[110]		[220]		
N0	Pos[°]	Area	Pos[°]	Area	Pos[°]	Area	[2D]/[110]
0%	7.9	0	14.825	186.95	29.235	74.92	0
1%	7.9	12.26	14.772	35.073	29.189	10.786	0.35
3%	7.93	75.36	14.773	41.304	29.174	13.955	1.82
5%	7.912	132.16	14.758	39.738	29.152	11.7	3.33
10%	7.89	297.34	14.679	106.8	29.153	27.311	2.78
30%	7.82	79.67	14.72	22.16	29.186	7.28	3.59
100%	7.81	2337.4	14.8	0	29.2	0	∞

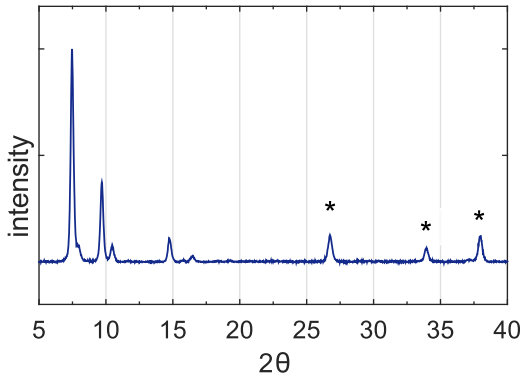

Fig. S3: XRD pattern of perovskite film with 100 % TBAI. Films have been spun onto FTO c-glass substrates. Peaks originated by SnO_2 underlayers are marked by asterisks

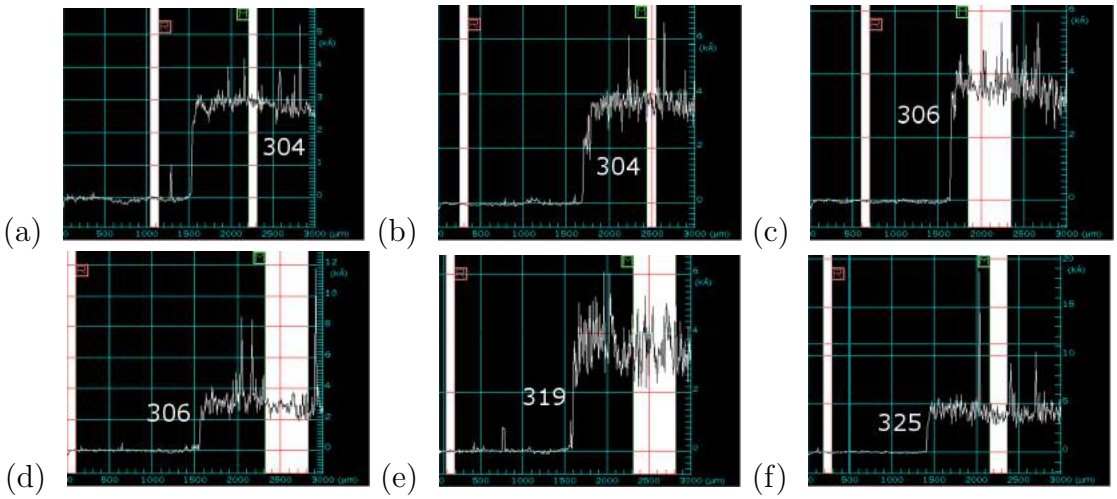

Fig. S4: Profilometry of $(TBA)_nMA_{1-n}PbX_3$ perovskite films deposited on a compact layer of TiO_2 with (a) n=0 (0%), (b) n=0.01 (1%), (c) n=0.03 (3%), (d) n=0.5 (5%), (e) n=0.1 (10%), (f) n=0.3 (30%). The values are calculated by taking the difference between the mean values of the bands R and M respectively

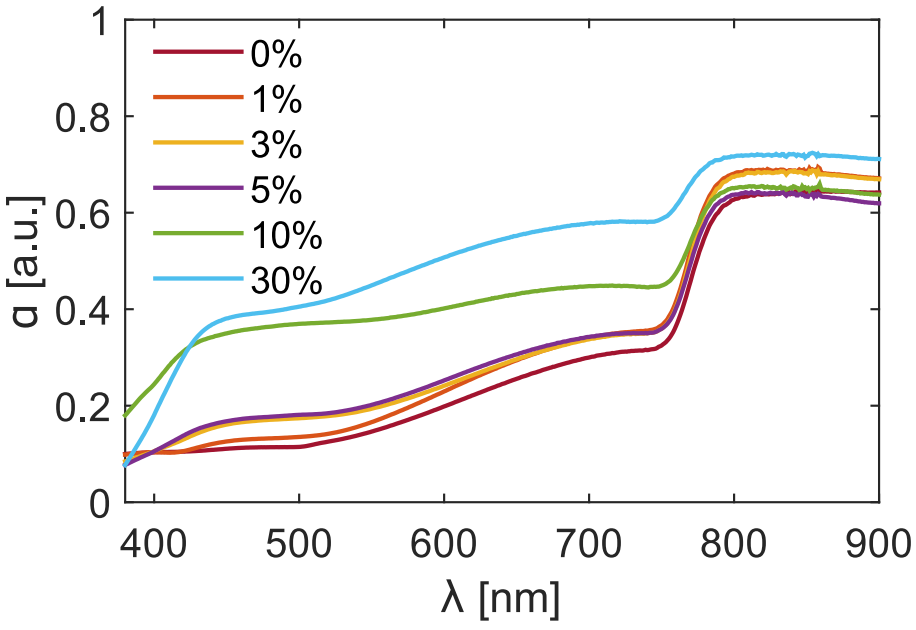

Fig. S5: Transmittance spectra of perovskite films with different concentrations of TBA in the precursor solution

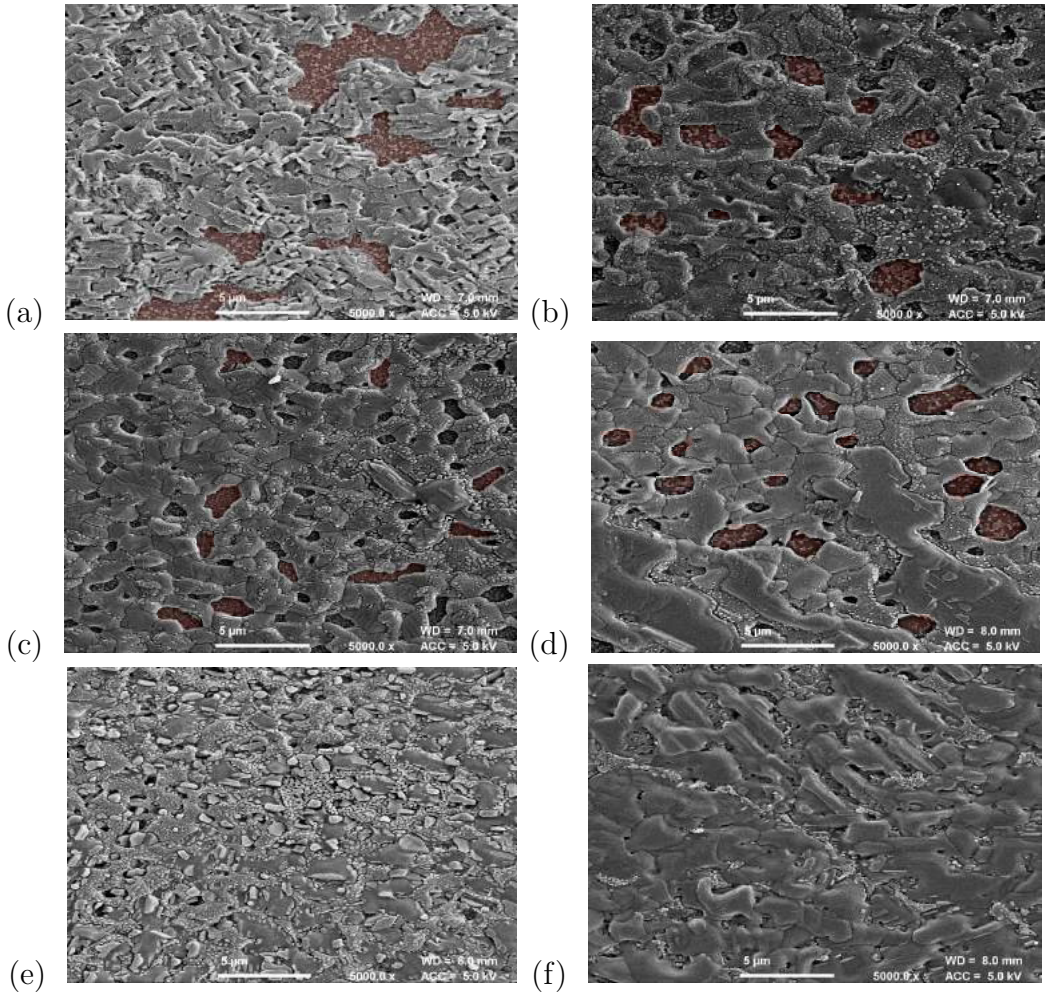

Fig. S6: Top wiew SEM images of $(TBA)_nMA_{1-n}PbX_3$ perovskite films deposited on a compact layer of TiO2. (a)0mol%; (b)1mol%; (c)3mol%; (d)5mol%; (e)10mol%; (f)30mol%. FTO areas have been marked in red using the software Inkscape 0.91 to emphasise the pinholes

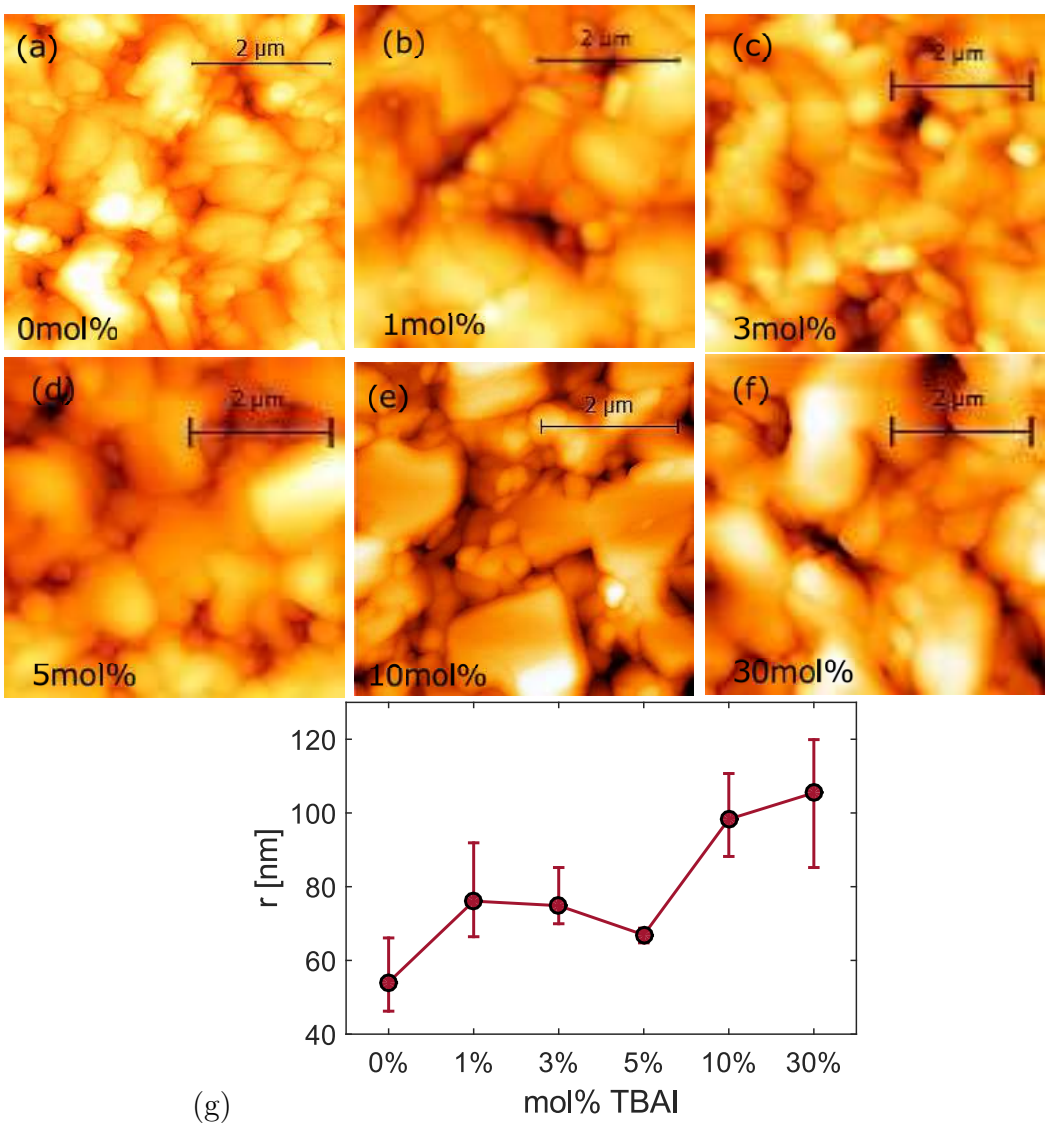

Fig. S7: (a)-(f) AFM images of $(TBA)_n(MA)_{1-n}PbX_3$ perovskite films deposited on a compact layer of TiO_2 with different TBA concentration; (g) Average roughness values extracted using Atomic Force Microscope as a function of TBA concentration in the perovskite precursor solution. Values were measured and averaged over 50*50 μm areas.

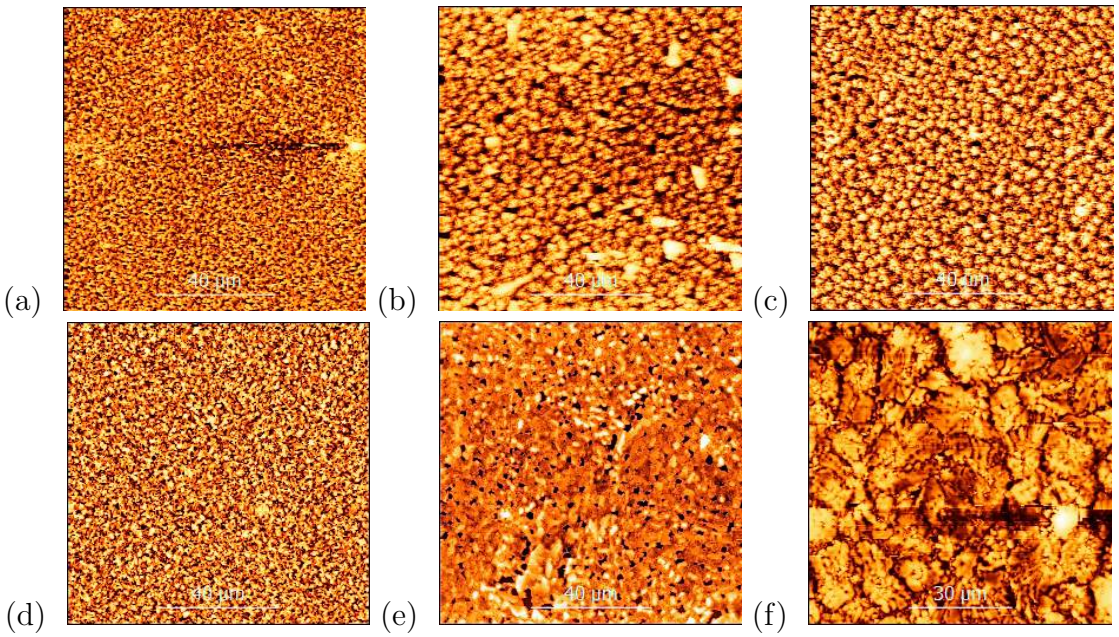

Fig. S8: AFM images of $(TBA)_nMA_{1-n}PbX_3$ perovskite films deposited on a compact layer of TiO2; (a)0mol%; (b)1mol%; (c)3mol%; (d)5mol%; (e)10mol%; (f)30mol%

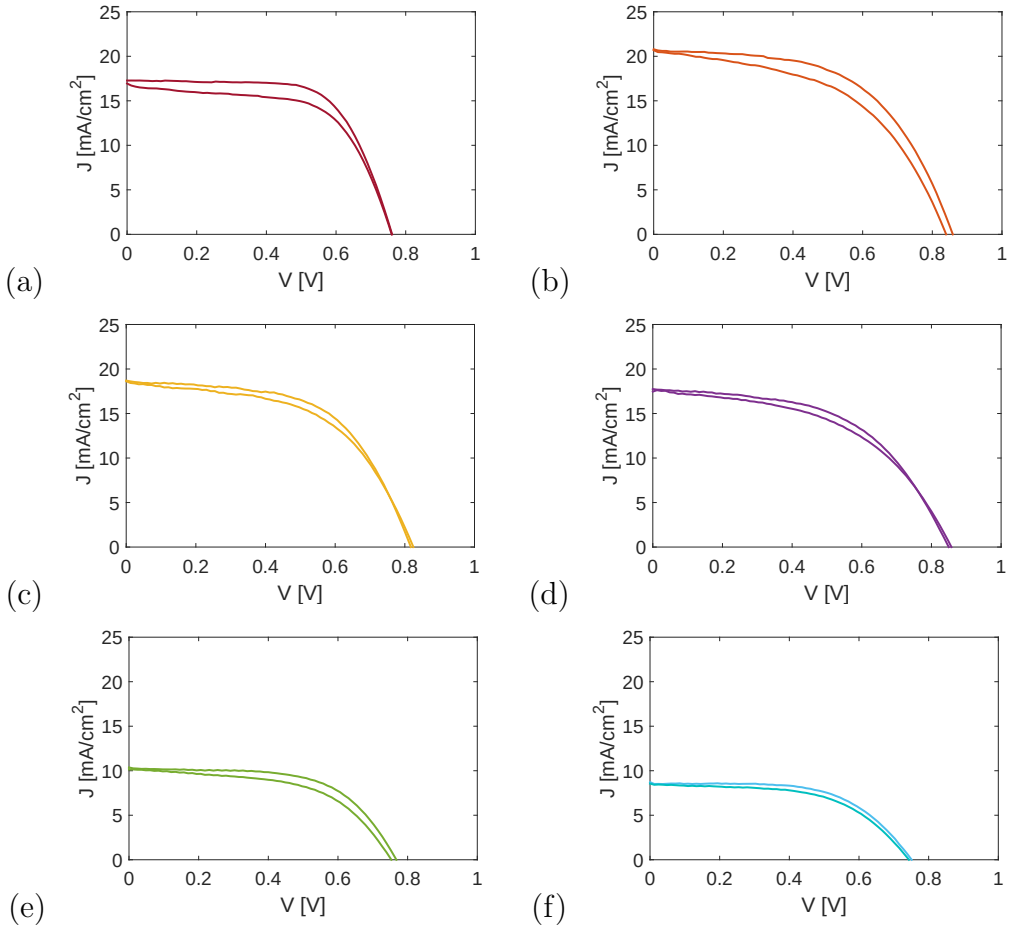

Fig. S9: JV curves in forward and reverse scan of perovskite solar cells made of $(TBA)_nMA_{1-n}PbX_3$ with (a)n=0; (b)n=0.01; (c)n=0.03; (d)n=0.05; (e)n=0.1; (f)n=0.3

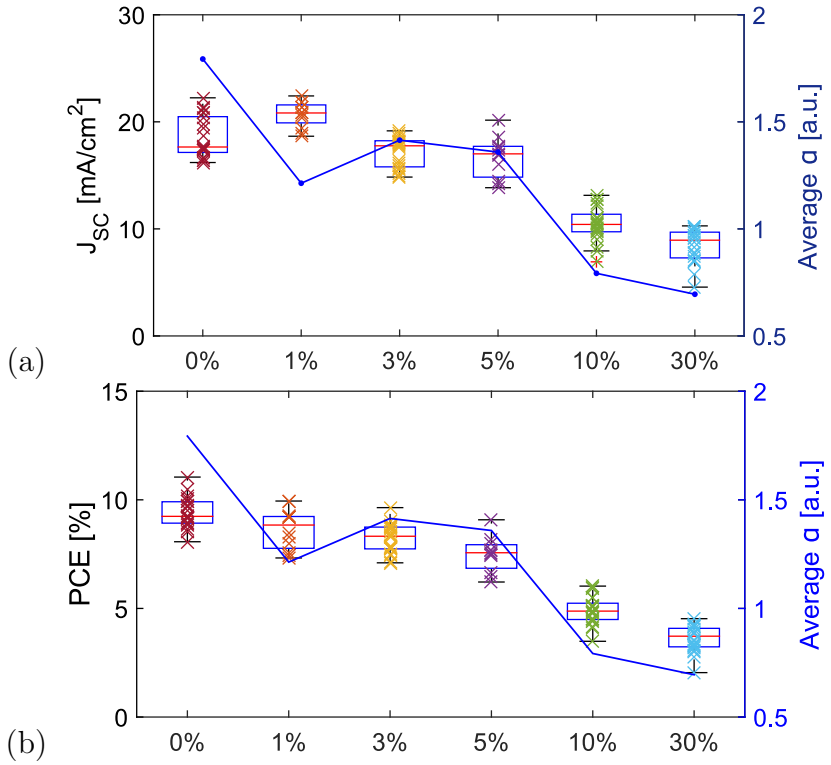

Fig. S10: Trend of photocurrent and PCEs of devices as a function of TBA concentration in the solution precursor. Data are compared to the reduction of absorption measured with UV-Vis. The absorption coefficient has been averaged between 450 and 750 nm.

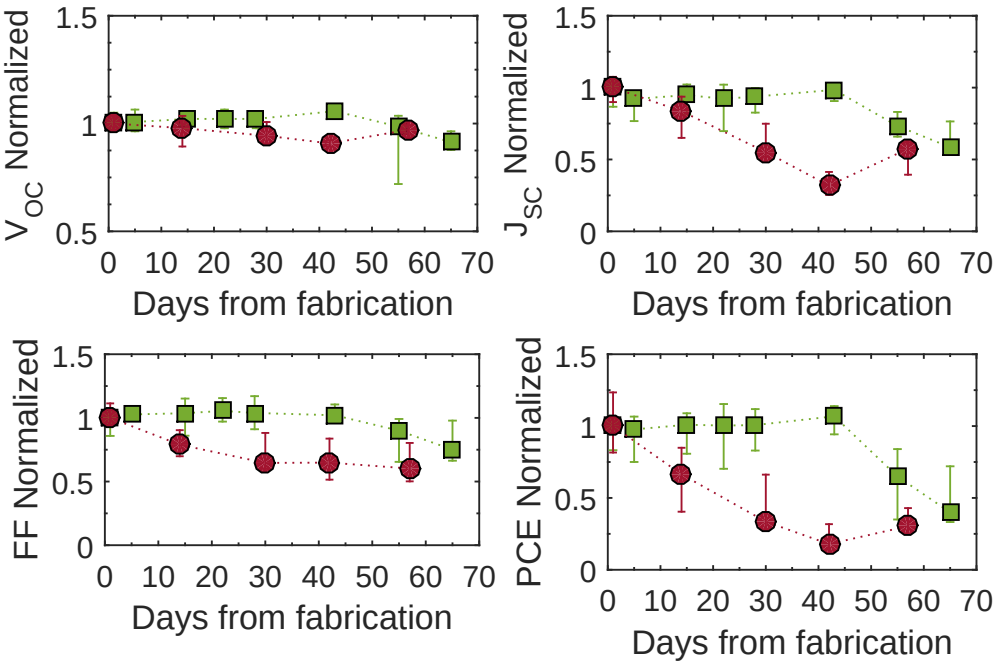

Fig. S11: Evolution of the main photovoltaic parameters over time. All the values have been normalised with respect to the median value obtained after deposition. Square green markers indicate the film with 1mol% of TBA, while red markers indicate the reference solar cell without TBA added. Cells with similar initial PCE have been considered (7.13% and 7.36% for MAPI and MAI/TBAI based cells respectively)

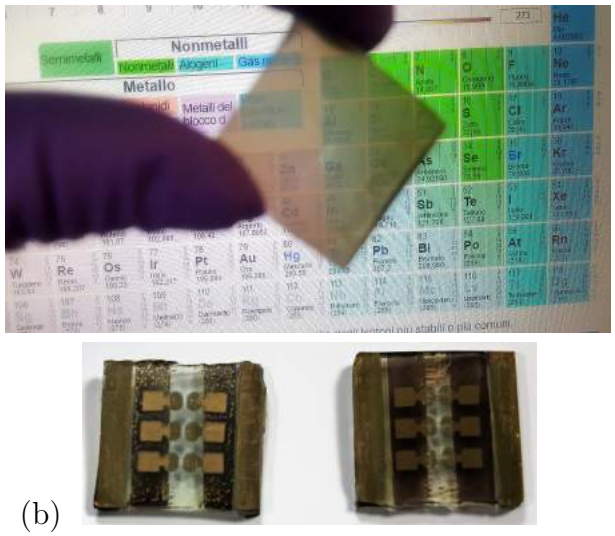

Fig. S12: (a) Image to show the semitransparent film with 30% TBA added into the solution (b) Image to show the degradation in air after over 100 days in ambient condition of films without (left) and with(right) TBA

4.1.2 Post-publication commentary

New studies published after the publication of 'Tetrabutylammonium cations for moisture-resistant and semitransparent perovskite solar cells' by Poli *et al.* shed light on the structural properties of mixed MA/TBA perovskite films. In the published report, it was speculated that the peak at 2θ=7.8° could have been assigned to 2D perovskite structures. This interpretation can not be valid because typical XRD patterns of 2D perovskites show several sharp and equally spaced peaks along 2θ, indicating the (00l) reflections. [17] The peak appearing at 7.8° is most probably associated to the 1 dimensional 1D structure of $TBAPbI_3$, where face sharing [PbI_6] octahedral chains are surrounded by the organic cation TBA^+. Similar structures have been observed for the monohydrate $CH_3NH_3PbI_3{\cdot}H_2O$, $GUAPbI_3$ and (1-methyl-piperidinium)PbI_3 (MPIP). [18, 19, 20]

The XRD data presented in Fig. 3 of the published paper show small shifts in the diffractograms, which are probably due to misalignment of the sample surface. Extensive clarifications are given in section 4.2.2.

4.1.3 Contemporary assessment

The paper 'Tetrabutylammonium cations for moisture-resistant and semitransparent perovskite solar cells' by Poli *et al.* demonstrated a facile technique to enhance the moisture stability of solar cells by incorporating TBA directly in the solution precursor. TBA had previously been used to treat the $MAPbI_3$ surface but it had never been incorporated within the precursor solution and used during crystallisation.

Deep crystallographic analysis of the TBA/MA films has not been provided here. XRD peaks at low 2θ angles have been previously reported in the literature as correspondent to (00l) lattice planes of layered perovskites. [4] However, XRD peaks at low 2θ angles may also be assigned to the crystallisation of different side phases. [21, 19, 22] There is no direct evidence that the diffraction peak observed at 2θ=7.8° in this work corresponds to the formation of 2D layers on 3D $MAPbI_3$ perovskite surface. It may be that the dominant form of TBA on the perovskite surface is the TBAI crystal or the one dimensional (1D) form. A deeper investigation on the diffraction patterns for TBAI, $TBAPbI_3$ and TBA_2PbI_4 films and powders may clarify it.

In 2018, the TBA cation was used in mixed halide perovskite materials to form $TBA_{0.4}MA_{0.6}Pb(I_{0.6}Br_{0.4})_3$. [23] The authors obtained very similar XRD results and attributed the XRD peaks found at low angles to the growth of 2D phases in the film. Thin films fabricated with TBA incorporated in the precursor solution showed improved photostability with considerably decreased halide segregation under illumination.

Soon after the publication of our article, a similar work was published in Nature Energy, where the guanidinium (GUA) cation was incorporated into $MAPbI_3$ perovskites. [24] GUA cation was combined with MA in mixed $MA_{1-x}GUA_xPbI_3$ compositions, with $0 \leq x \leq 1$. Similar to our work, GUA was incorporated within the

precursor solution and the films were deposited via a single-step spin coating procedure. In contrast to our results, new diffraction peaks at low angles of $8.54°$ and $11.31°$ only appeared for x≥0.5 and the authors claimed that for 0≤x≤0.25 GUA was inserted in the crystal unit, forming a 3D perovskite. The presence of GUA improved the open circuit potential of the devices and enhanced stability was observed under continuous illumination and maximum power point tracking. However, samples were stored in an argon atmosphere and the moisture-stability of the devices was not reported. Meanwhile, another report on mixed GUA/MA perovskites was published, reporting new type of layered 2D perovskites with GUA and MA cations alternating in the interlayer spacing. [25]

Recently, diethylammonium iodide (DAI) was incorporated into the three-dimensional $MAPbI_3$ to introduce regions of 2D material. [26] Upon addition of DAI, XRD peaks at 2θ=$7.5°$ were measured, confirming the successful incorporation of 2D material in the structure. The inclusion of DAI improved the crystallisation of the films, reduced defects and improved the stability over time. Solar cells with PCE as high as $19.05\,\%$ were reported when $10\,\%$ DAI was incorporated in the precursor solution.

The interaction between water and a $MAPbI_3$ perovskite film containing PEA was investigated using in situ neutron X-ray scattering earlier this year. [27] The moisture stability of treated $MAPbI_3$ films was improved even though water molecules did interact with the 2D protecting layers and diffused to the $MAPbI_3$ surface. It was proposed that the improved moisture stability was due to suppression of migration of I^- and MA^+ to the surface, preventing their escape and the irreversible formation of PbI_2 in the film.

4.2 Spectroscopy study of TBA in $MAPbI_3$

TBA was added to the precursor solution at molar ratios and XRD structural analysis suggested the coexistence of 3D and 1D phases in the perovskite film. In the article by Poli *et al.* presented in Section 4.1.1, it was speculated that TBA may have segregated towards the surface of 3D perovskite grains due to its large ionic radius, forming TBA-lead halide aggregates at the surface. Indeed higher water contact angles were measured on the surface of the films containing TBA.

More detailed spectroscopic analysis can help in characterising the perovskite films to better understand the phase formation and distribution within the thin film perovskite absorber. For example, UV-Vis spectroscopy can reveal the presence of absorption peaks at low wavelength that can be assigned to low-*n* perovskite phases. [8, 7] FTIR can be used to investigate the presence of intermolecular interactions between the 3D perovskite crystals and TBA crystallites. [28] XRD and XPS can be used to study the bulk and the surface chemistry of MA/TBA mixed films. Finally, PL spectroscopy can be used to identify the specific nature and optoelectronic properties of thin films.

4.2.1 FTIR and UV-Vis spectroscopy

The presence of TBA in the final perovskite film was further confirmed by FTIR characterisation. Figure 4.1 a shows the FTIR spectra of reference $MAPbI_3$ and a thin film with $3\,\%$ of TBA. Both spectra show the N-H stretching vibration typical of $MAPbI_3$ perovskite materials at 3300-3000 cm^{-1}. [14, 29] The TBA-containing film exhibited additional C-H stretching vibrations between 3000-2800 cm^{-1} that can be assigned to the symmetric and asymmetric stretching vibrations of CH_2 and CH_3, indicating the presence of the bulkier TBA cations. [30]

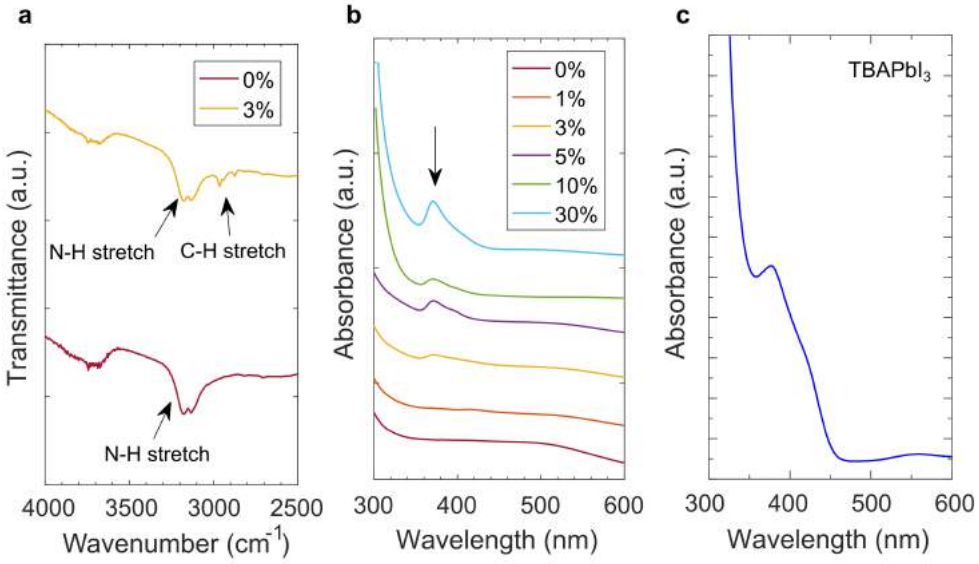

Figure 4.1: a FTIR spectra of $MA_{1-n}TBA_nPbI_3$ with n=0 and n=0.03. **b** UV-Vis spectra of $MA_{1-n}TBA_nPbI_3$ with n=0, 0.01, 0.03, 0.05, 0.1 and 0.3. **c** UV-Vis spectrum of TBA_2PbI_4.

Figure 4.1 b shows the UV-Vis absorbance spectra of reference $MAPbI_3$ and thin films with different molar concentration of TBA (1, 3, 5, 10 and $30\,\%$ of TBA measured at low wavelength of 300-600 nm. Films with TBA concentration $\geq 3\,\%$, an absorption peak at $\sim$380 nm was observed. The intensity of this peak increased with TBA content and it can be assigned to the 1D $TBAPbI_3$ phase. Indeed, $TBAPbI_3$ films prepared without MA exhibited an absorption peak at the same wavelength $\sim$380 nm (Figure 4.1 c).

Both FTIR and UV-Vis spectroscopy provided evidence of the presence of TBA cations within the perovskite thin film.

4.2.2 XPS and XRD spectroscopy

To further verify the presence of TBA, X-ray photoelectron spectroscopy (XPS) measurements were carried out on $MAPbI_3$ films. Figure 4.2 a and b shows a comparison of the elemental concentrations in perovskite films without and with $3\,\%$ of TBA, respectively. Table 4.2 lists the quantification results taken from XPS survey spectra shown in figure 4.2 a and b. The identified elements on the surface are iodine, lead, carbon, nitrogen, oxygen, indium and tin. The presence of carbon, nitrogen, iodine

and lead were expected from the chemical composition of $MAPbI_3$ films. The presence of indium and tin peaks have been previously reported in perovskite samples and indicate migration from the ITO substrate to the top layer with time. [31] Unfortunately, XPS characterisation was not recorded right after sample preparation, but spectra were taken on aged samples (films were aged for few weeks in ambient condition). Therefore, some degradation of the film is expected. However, different films were fabricated at the same time and aged in the same conditions.

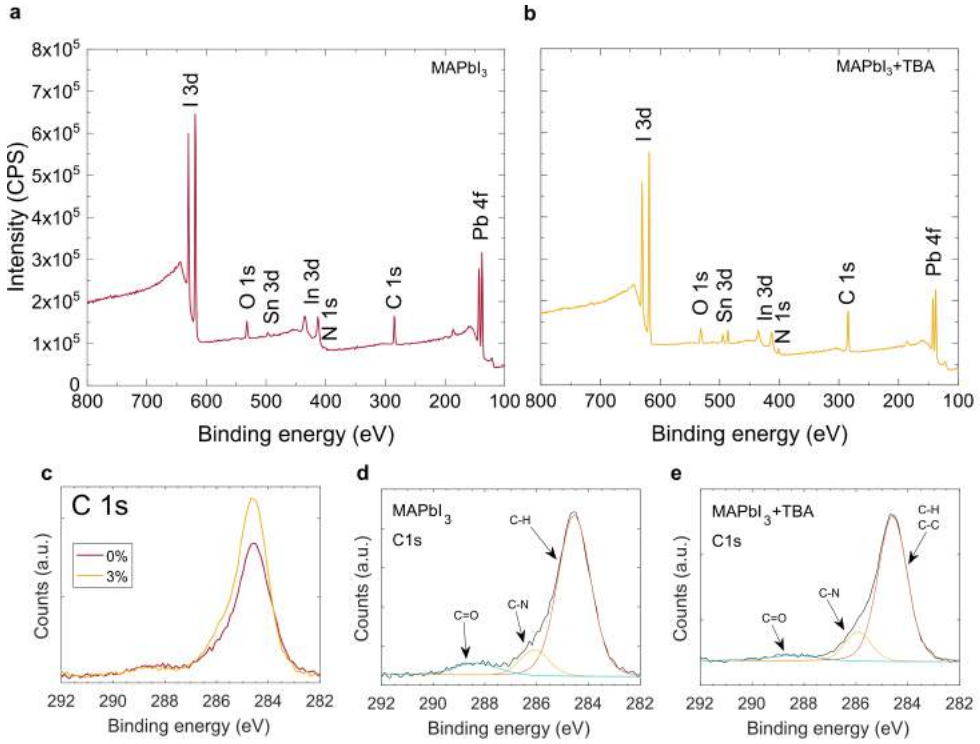

Figure 4.2: **a** XPS survey spectra of a perovskite $MAPbI_3$ film. **b** XPS survey spectra of a perovskite $MAPbI_3$ film with 3 % of TBA. **c** C1s XPS spectra for reference $MAPbI_3$ and for TBA-containing film (3 %). **d** C1s XPS spectrum of reference $MAPbI_3$ with fitted spectral components. **e** C1s XPS spectrum of $MAPbI_3$ with 3 % TBA with fitted spectral components.

Figure 4.2 c shows the C1s XPS spectra of the tested samples, while figures 4.2 d-e show the C1s XPS spectra fitted with different spectral components of reference $MAPbI_3$ and TBA-containing film, respectively. The presence of MA^+ cations was confirmed by the detected hydrocarbon C-H component (284.6 eV) and the amine C-N doublet (286 eV). As expected, the intensity of the hydrocarbon component at 284.6 eV (C-H and C-C) and the C-N^+ bond at 401.9 eV were higher for the TBA-containing film due to partial substitution of MA for TBA. The carbonyl doublet C=O at 288.3 eV may be associated with oxygen and moisture-induced degradation. [32] It is worth noting that the percentage concentration of C=O of reference $MAPbI_3$ and TBA-containing perovskites are 8.12 and 6.43 %, respectively, which may suggest a reduced moisture-induced degradation for TBA-containing films.

XRD analysis of $MAPbI_3$ films with different concentration of TBA confirmed the coexistence of different phases within the material. [16] The low dimensional peaks

Table 4.2: Quantification results extracted from XPS survey spectra of a perovskite $MAPbI_3$ film and a $MAPbI_3$ film with 3 % of TBA.

Material	XPS region	Position (eV)	Area	Atomic concentration %
$MAPbI_3$	I3d	619	2.4×10^6	55.14
	Pb4f	138	1.1×10^6	20.87
	In3d	413	8.2×10^5	16.79
	C1s	285	1.7×10^5	3.38
	O1s	532	1.2×10^5	2.54
	Sn3d	497	4.5×10^4	0.97
	N1s	401	1.5×10^4	0.31
$MAPbI_3$+TBA	I3d	619	1.74×10^6	52.55
	Pb4f	138	7.9×10^5	19.52
	In3d	413	5.0×10^5	13.65
	C1s	285	2.4×10^5	6.16
	O1s	532	1.3×10^5	3.67
	Sn3d	497	1.3×10^5	3.64
	N1s	401	3.0×10^4	0.8

are assigned to 1D $TBAPbI_3$ structures, which coexist with the 3D $MAPbI_3$ phases. The exact position of XRD peaks is an important parameter that may reveal further structural changes in the film. For example, a gradual shift of the 'perovskite 3D peaks' towards smaller angles was observed in $MA_{1-x}GUA_xPbI_3$ on increasing GUA content. [24] Similarly, the XRD perovskite characteristic peaks of $MA_xEA_{1-x}PbBr_3$ (EA=ethylammonium) moved to lower angles at increasing EA contents. [33] Finally, similar XRD results were observed with interstitial occupancy of Rb^+, K^+, Na^+ and Li^+ ions. [34] This phenomenon commonly denotes a gradual expansion of the unit-cell volume and it has been observed after either incorporation of larger cation by direct substitution of methylammonium or extraction of smaller anions (i.e. Br-extraction that leads to I-rich structures). [24, 35, 36]
A closer inspection of the XRD peaks of $MAPbI_3$ films with different concentration of TBA revealed a shift to lower angles of both (110) and (220) lattice planes upon increasing TBA contents (Figure 4.3 a and b, respectively).

Little shifts in (110) XRD peak position may be indication of the expansion of the unit-cell volume. TBA is considerably larger than MA and therefore it is believed to sit preferentially at the interface, without occupying the A site cation. It was also noticed that the (110) and (220) lattice planes had the same shift. Therefore, the observed XRD peaks shift is more probably caused by misalignment of the sample surface.

4.2.3 PL spectroscopy

The presence of TBA led to improved moisture stability for the perovskite solar cells. [16] The higher stability was mainly associated with increased hydrophobicity of the perovskite films, confirmed by the water contact angle measurements. However, the improved stability may also be related to an increased photostability upon addition

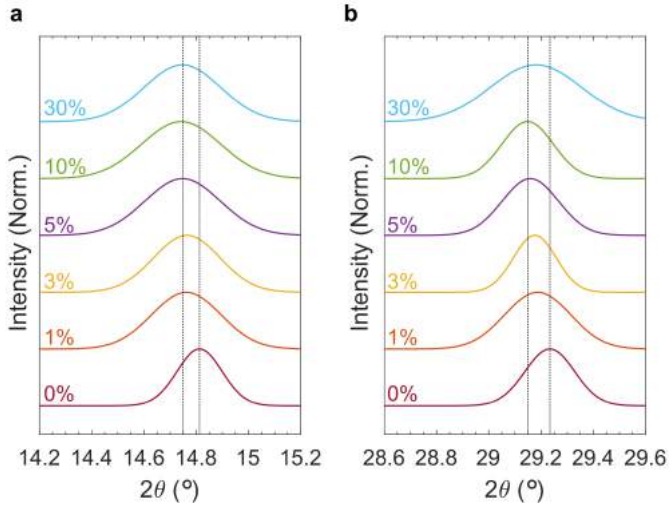

Figure 4.3: **a** Normalised XRD peaks showing the (110) lattice plane on variation of the TBA content (indicated in percentage). **b** Normalised XRD peaks showing the (220) lattice plane on variation of the TBA content (indicated in percentage).

of TBA. Defects in the films affect the radiative and non-radiative recombination pathways, which can be directly observed through photoluminescence dynamics. Figure 4.4 a shows the steady-state PL spectra of a reference $MAPbI_3$ film and a $MAPbI_3$ film containing $3\,\%$ of TBA.

The samples were excited with a monochromatic light of $405\,\mathrm{nm}$, in vacuum, with a power density of $\sim 80\,\mathrm{mW\,cm^{-2}}$. The TBA-containing $MAPbI_3$ film was more emissive than the reference $MAPbI_3$, suggesting a decrease in the density of defects, probably due to effective TBA-passivation. Figure 4.4 b shows the integrated PL measured under continuous illumination over time. The same monochromated light was used but with a lower power density of $\sim 10\,\mathrm{mW\,cm^{-2}}$. The integrated PL of the $MAPbI_3$ film quickly decayed overtime, indicating the generation of photoinduced defects that acted as trapping states, therefore increasing the non-radiative recombination pathways and decreasing the radiative decay paths. In contrast, TBA-containing $MAPbI_3$ film showed considerably higher stability under continuous illumination, suggesting that the mechanisms leading to PL quenching (non-radiative recombination through defects) were delayed by the presence of TBA.

Figure 4.4 c shows the steady state normalised PL spectra of $MAPbI_3$ films with 3, 10 and $30\,\%$ TBA excited with a monochromated light of $530\,\mathrm{nm}$. On increasing the TBA content in the $MAPbI_3$ structure, a gradual blue-shift of PL peaks was observed. A similar shift to lower wavelength of the PL spectrum was previously reported for $MAPbI_3$ films treated with diethylammonium iodide (DAI) and it was associated with incorporation of 2D structures originated by the presence of DAI. [26] PL shifts may also be caused by a variation in the size of thin-film grains, where a decrease in the grain size should be accompanied by a blue-shift of the PL emission. [37, 38] The presence of $TBAPbI_3$ features on the surface may have induced the blue-shift observed in figure 4.4 c.

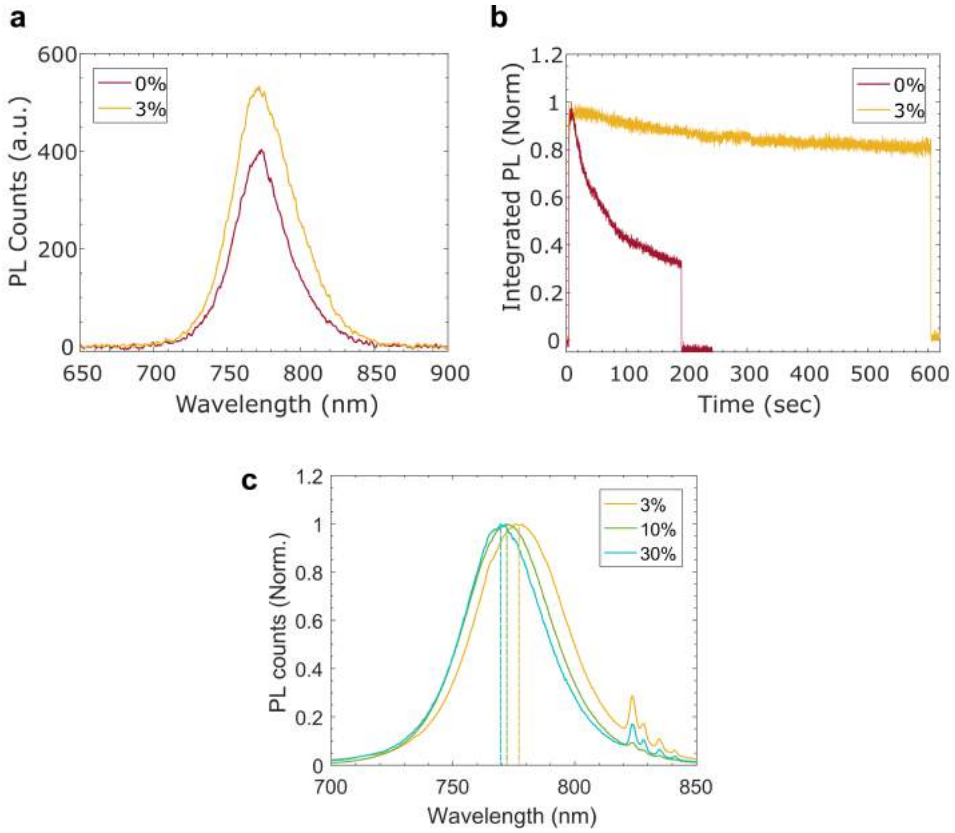

Figure 4.4: **a** Photoluminescence spectra of the $MAPbI_3$ thin films without and with $3\,\%$ of TBA, excited at 405 nm (CW laser, power intensity = $80\,\mathrm{mW\,cm^{-2}}$). **b** Integrated PL measured over time under continuous CW illumination at a power intensity = $10\,\mathrm{mW\,cm^{-2}}$. **c** Steady state photoluminescence spectra of the $MAPbI_3$ thin films without and with 3, 10 and $30\,\%$ of TBA, excited at 530 nm.

4.3 Chapter conclusions

Substituting a much larger cation in perovskites transforms the 3D perovskite into a structure containing regions of low-dimensional phases, which is significantly more stable. Different approaches have been reported to incorporate low-dimensional materials in 3D perovskite structures: adding organic spacers between inorganic sheets of corner-sharing $[BX_6]^{4-}$ octahedra, depositing passivation 2D perovskite layers at the interfaces or coating perovskite grains.

In this chapter we showed how MA can be partly substituted with the large TBA cation. TBA was directly added to the perovskite precursor solution and the thin absorber layer was deposited via a single-step spin coating procedure. XRD analysis showed that low dimensional and 3D phases coexisted within the structure, with diffraction peaks at low angles assigned to 1D $TBAPbI_3$ structures becoming more intense with higher TBA contents. The energy bandgap did not change with different molar percentages of TBA, but mixed MA/TBA films with TBA contents $\geq 10\,\%$ were considerably more transparent, reducing the absorption.
TBA retarded the crystallisation of the absorber and improved the surface coverage.

Top-view SEM images showed segregated small crystallites on the surface, suggesting that TBA may have segregated towards the boundaries of 3D grains. Mixed MA/TBA solar cells showed comparable photovoltaic performances than standard $MAPbI_3$ but enhanced moisture-stability. When aged in the dark, at open circuit, under ambient conditions (RH up to $60\,\%$), the PCE of TBA-containing devices was found very stable for over $1000\,\mathrm{h}$. Indeed, the water contact angle of TBA-based thin films was higher than standard $MAPbI_3$ films, confirming greater hydrophobicity of the absorber.

FTIR, UV-Vis and XPS spectroscopy confirmed the presence of TBA in the thin film. CH_2 and CH_3 stretching vibrations were measured only in TBA-containing films and an additional absorbance peak at $\sim 380\,\mathrm{nm}$ indicated the presence of $TBAPbI_3$ structures in $MAPbI_3$ thin films. TBA-containing $MAPbI_3$ films showed higher PL signal and more stable integrated PL over time, indicating a decrease in defect density and reduced photoinduced defect generation.

4.4 Future work

A bulky alkyl ammonium salt was incorporated in the perovskite thin film by partly substituting the central cation MA for TBA. The presence of TBA improved the morphology of thin films and the device stability by passivating the surface and grain boundaries. XRD showed possible coexistance of low dimensional and 3D phases in the material. However, it also showed that the perovskite crystallinity of thin films decreased upon addition of TBA. This is due to TBA not being incorporated in the 3D perovskite structure because it is too large, causing a deficiency in the A site cation. Future work may look at adding $TBAPbI_3$ directly to the precursor solution $MAPbI_3$, without substituting MA for TBA. This technique may allow the growth of high crystalline 3D thin films with 1D $TBAPbI_3$ structures at the grain boundaries to passivate defects and decrease the adsorption of water at the surface.

The XRD diffraction peaks observed at low 2θ angles is believed to be due to the formation of one dimensional 1D $TBAPbI_3$. Further X-ray diffraction analysis on crystalline powders may elucidate the structure of the materials that have been investigated.

The phase distribution throughout the film thickness could be further investigated using steady-state photoluminescence techniques. Several reports have shown the PL spectra collected under front and back excitation to investigate the distribution of different phases within thin films. 5-ammonium valeric acid (5AVA), phenylethylammonium (PEA) and butylammonium (BA) cations were found to predominantly form low-n phases at the bottom of the superstructure (on the glass surface). [39, 8, 7] In contrast, Li *et al.* reported a two-step deposition technique to grow quasi-2D/3D perovskite structures with different n-phases growing from the top to the bottom of the superstructure. [9] Similarly, it would be interesting to see whether low-n phases originated by the presence of TBA preferentially formed on the bottom or on the top

of the film or homogeneously through the thickness.
Another technique that can be used to study the spatial distribution of different n-regions and obtain the depth profile of different cations is time-of-flight secondary mass spectroscopy (ToF-SIMS). [40]

Bibliography

[1] M. R. Leyden, M. V. Lee, S. R. Raga, and Y. Qi, "Large formamidinium lead trihalide perovskite solar cells using chemical vapor deposition with high reproducibility and tunable chlorine concentrations," *J. Mater. Chem. A*, vol. 3, no. 31, pp. 16097–16103, 2015.

[2] J. W. Lee, D. H. Kim, H. S. Kim, S. W. Seo, S. M. Cho, and N. G. Park, "Formamidinium and cesium hybridization for photo- and moisture-stable perovskite solar cell," *Adv. Energy Mater.*, vol. 5, no. 20, 2015.

[3] I. C. Smith, E. T. Hoke, D. Solis-Ibarra, M. D. McGehee, and H. I. Karunadasa, "A Layered Hybrid Perovskite Solar-Cell Absorber with Enhanced Moisture Stability," *Angew. Chem. Int. Ed.*, vol. 53, no. 42, pp. 11232–11235, 2014.

[4] D. H. Cao, C. C. Stoumpos, O. K. Farha, J. T. Hupp, and M. G. Kanatzidis, "2D Homologous Perovskites as Light-Absorbing Materials for Solar Cell Applications," *J. Am. Chem. Soc.*, vol. 137, no. 24, pp. 7843–7850, 2015.

[5] H. Tsai, W. Nie, J.-C. Blancon, C. C. Stoumpos, R. Asadpour, B. Harutyunyan, A. J. Neukirch, R. Verduzco, J. J. Crochet, S. Tretiak, L. Pedesseau, J. Even, M. A. Alam, G. Gupta, J. Lou, P. M. Ajayan, M. J. Bedzyk, M. G. Kanatzidis, and A. D. Mohite, "High-efficiency two-dimensional Ruddlesden–Popper perovskite solar cells," *Nature*, vol. 536, no. 7616, pp. 312–316, 2016.

[6] R. K. Misra, B. E. Cohen, L. Iagher, and L. Etgar, "Low-Dimensional Organic–Inorganic Halide Perovskite: Structure, Properties, and Applications," *ChemSusChem*, vol. 10, no. 19, pp. 3712–3721, 2017.

[7] Y. Han, S. Park, C. Kim, M. Lee, and I. Hwang, "Phase control of quasi-2D perovskites and improved light-emitting performance by excess organic cations and nanoparticle intercalation," *Nanoscale*, vol. 11, no. 8, pp. 3546–3556, 2019.

[8] J. Liu, J. Leng, K. Wu, J. Zhang, and S. Jin, "Observation of internal photoinduced electron and hole separation in hybrid two-dimentional perovskite films," *J. Am. Chem. Soc.*, vol. 139, no. 4, pp. 1432–1435, 2017.

[9] B. Li, Y. Zhang, L. Fu, T. Yu, S. Zhou, L. Zhang, and L. Yin, "Surface passivation engineering strategy to fully-inorganic cubic $CsPbI_3$ perovskites for high-performance solar cells," *Nat. Commun.*, vol. 9, no. 1, pp. 1–8, 2018.

[10] X. Li, M. I. Dar, C. Yi, J. Luo, M. Tschumi, S. M. Zakeeruddin, M. K. Nazeeruddin, H. Han, and M. Grätzel, "Improved performance and stability of perovskite solar cells by crystal crosslinking with alkylphosphonic acid ω-ammonium chlorides," *Nat. Chem.*, vol. 7, no. 9, pp. 703–711, 2015.

[11] B. Li, C. Fei, K. Zheng, X. Qu, T. Pullerits, G. Cao, and J. Tian, "Constructing water-resistant $CH_3NH_3PbI_3$ perovskite films via coordination interaction," *J. Mater. Chem. A*, vol. 4, pp. 17018–17024, 2016.

[12] L. Zuo, H. Guo, D. W. DeQuilettes, S. Jariwala, N. De Marco, S. Dong, R. DeBlock, D. S. Ginger, B. Dunn, M. Wang, and Y. Yang, "Polymer-modified halide perovskite films for efficient and stable planar heterojunction solar cells," *Sci. Adv.*, vol. 3, no. 8, p. e1700106, 2017.

[13] N. A. Manshor, Q. Wali, K. K. Wong, S. K. Muzakir, A. Fakharuddin, L. Schmidt-Mende, and R. Jose, "Humidity: Versus photo-stability of metal halide perovskite films in a polymer matrix," *Phys. Chem. Chem. Phys.*, vol. 18, no. 31, pp. 21629–21639, 2016.

[14] X. Hou, S. Huang, W. Ou-yang, L. Pan, Z. Sun, and X. Chen, "Constructing Efficient and Stable Perovskite Solar Cells via Interconnecting Perovskite Grains," *ACS Appl. Mater. Interfaces*, vol. 9, no. 40, pp. 35200–35208, 2017.

[15] S. Yang, Y. Wang, P. Liu, Y.-B. Cheng, H. J. Zhao, and H. G. Yang, "Functionalization of perovskite thin films with moisture-tolerant molecules," *Nat. Energy*, vol. 1, pp. 1–7, 2016.

[16] I. Poli, S. Eslava, and P. Cameron, "Tetrabutylammonium cations for moisture-resistant and semitransparent perovskite solar cells," *J. Mater. Chem. A*, vol. 5, pp. 22325–22333, 2017.

[17] P. Cheng, T. Wu, J. Zhang, Y. Li, J. Liu, L. Jiang, X. Mao, R. F. Lu, W. Q. Deng, and K. Han, "$(C_6H_5C_2H_4NH_3)_2GeI_4$: A Layered Two-Dimensional Perovskite with Potential for Photovoltaic Applications," *J. Phys. Chem Lett.*, vol. 8, no. 18, pp. 4402–4406, 2017.

[18] A. M. A. Leguy, Y. Hu, M. Campoy-Quiles, M. I. Alonso, O. J. Weber, P. Azarhoosh, M. van Schilfgaarde, M. T. Weller, T. Bein, J. Nelson, P. Docampo, and P. R. F. Barnes, "Reversible Hydration of $CH_3NH_3PbI_3$ Films, Single Crystals, and Solar Cells," *Chem. Mater.*, vol. 27, no. 9, pp. 3397–3407, 2015.

[19] A. D. Jodlowski, A. Yépez, R. Luque, L. Camacho, and G. de Miguel, "Benign-by-Design Solventless Mechanochemical Synthesis of Three-, Two-, and One-Dimensional Hybrid Perovskites," *Angew. Chem. Int. Ed.*, vol. 55, no. 48, pp. 14972–14977, 2016.

[20] A. Zeb, Z. Sun, A. Khan, S. Zhang, T. Khan, M. A. Asghar, and J. Luo, "$[C_6H_{14}N]PbI_3$: A one-dimensional perovskite-like order-disorder phase transition material with semiconducting and switchable dielectric attributes," *Inorg. Chem. Front.*, vol. 5, no. 4, pp. 897–902, 2018.

[21] Y. Hu, J. Schlipf, M. Wussler, M. L. Petrus, W. Jaegermann, T. Bein, P. Muller-Buschbaum, and P. Docampo, "Hybrid Perovskite/Perovskite Heterojunction Solar Cells," *ACS Nano*, vol. 10, no. 6, pp. 5999–6007, 2016.

[22] Q. Jiang, Y. Zhao, X. Zhang, X. Yang, Y. Chen, Z. Chu, Q. Ye, X. Li, Z. Yin, and J. You, "Surface passivation of perovskite film for efficient solar cells," *Nat. Photonics*, 2019.

[23] P. Kour, M. Chenna Reddy, R. Naphade, and S. Ogale, "Quaternary alkylammonium salt incorporated 2D/3D mixed halide perovskite with highly enhanced photoluminescence and arrested iodide/bromide phase segregation," *APL Materials*, vol. 6, no. 8, p. 086107, 2018.

[24] A. D. Jodlowski, C. Roldán-Carmona, G. Grancini, M. Salado, M. Ralaiarisoa, S. Ahmad, N. Koch, L. Camacho, G. De Miguel, and M. K. Nazeeruddin, "Large guanidinium cation mixed with methylammonium in lead iodide perovskites for 19% efficient solar cells," *Nat. Energy*, vol. 2, no. 12, pp. 972–979, 2017.

[25] C. M. M. Soe, C. C. Stoumpos, M. Kepenekian, B. Traoré, H. Tsai, W. Nie, B. Wang, C. Katan, R. Seshadri, A. D. Mohite, J. Even, T. J. Marks, and M. G. Kanatzidis, "New Type of 2D Perovskites with Alternating Cations in the Interlayer Space, $(C(NH_2)_3)(CH_3NH_3)_nPb_nI_{3n+1}$: Structure, Properties, and Photovoltaic Performance," *J. Am. Chem. Soc.*, vol. 139, no. 45, pp. 16297–16309, 2017.

[26] X. Huang, Q. Cui, W. Bi, L. Li, P. Jia, Y. Hou, Y. Hu, Z. Lou, and F. Teng, "Two-dimensional additive diethylammonium iodide promoting crystal growth for efficient and stable perovskite solar cells," *RSC Adv.*, vol. 9, no. 14, pp. 7984–7991, 2019.

[27] J. Schlipf, Y. Hu, S. Pratap, L. Bießmann, N. Hohn, L. Porcar, T. Bein, P. Docampo, and P. Müller-Buschbaum, "Shedding Light on the Moisture Stability of 3D/2D Hybrid Perovskite Heterojunction Thin Films," *ACS Appl. Energy Mater.*, vol. 2, no. 2, pp. 1011–1018, 2019.

[28] M. Kim, S. G. Motti, R. Sorrentino, and A. Petrozza, "Enhanced Solar Cells Stability by Hygroscopic Polymer Passivation of Metal Halide Perovskite Thin Film," *Energy Environ. Sci.*, vol. 11, pp. 2609–2619, 2018.

[29] Y. Wang, T. Mahmoudi, W. Y. Rho, H. Y. Yang, S. Seo, K. S. Bhat, R. Ahmad, and Y. B. Hahn, "Ambient air solution processed efficient and highly stable perovskite solar cells based on $CH_3NH_3PbI_{3-x}Cl_x$-NiO composite with Al_2O_3/NiO interfacial engineering," *Nano Energy*, vol. 40, pp. 408–417, 2017.

[30] Y. Zhao, X. Xu, and X. You, "Colloidal Organometal Halide Perovskite ($MAPbBr_xI_{3-x}$, 0<x<3) Quantum Dots: Controllable Synthesis and Tunable Photoluminescence," *Sci. Rep.*, vol. 6, no. October, pp. 1–8, 2016.

[31] Z. Ahmad, M. A. Najeeb, R. A. Shakoor, A. Alashraf, S. A. Al-Muhtaseb, A. Soliman, and M. K. Nazeeruddin, "Instability in $CH_3NH_3PbI_3$ perovskite solar cells due to elemental migration and chemical composition changes," *Sci. Rep.*, vol. 7, no. 1, pp. 1–8, 2017.

[32] P. Chen, Y. Bai, S. Wang, M. Lyu, J.-h. Yun, and L. Wang, "In Situ Growth of 2D Perovskite Capping Layer for Stable and Efficient Perovskite Solar Cells," *Adv. Energy Mater.*, p. 10.1002/adfm.201706923, 2018.

[33] S. Gholipour, A. M. Ali, J. P. Correa-Baena, S. H. Turren-Cruz, F. Tajabadi, W. Tress, N. Taghavinia, M. Grätzel, A. Abate, F. De Angelis, C. A. Gaggioli, E. Mosconi, A. Hagfeldt, and M. Saliba, "Globularity-Selected Large Molecules for a New Generation of Multication Perovskites," *Adv. Mater.*, vol. 29, no. 38, pp. 1–9, 2017.

[34] J. Cao, S. X. Tao, P. A. Bobbert, C.-P. Wong, and N. Zhao, "Interstitial Occupancy by Extrinsic Alkali Cations in Perovskites and Its Impact on Ion Migration," *Adv. Mater.*, p. 1707350, 2018.

[35] Y. Hu, M. F. Aygüler, M. L. Petrus, T. Bein, and P. Docampo, "Impact of Rubidium and Cesium Cations on the Moisture Stability of Multiple-Cation Mixed-Halide Perovskites," *ACS Energy Lett.*, vol. 2, no. 10, pp. 2212–2218, 2017.

[36] M. Abdi-Jalebi, Z. Andaji-Garmaroudi, A. J. Pearson, G. Divitini, S. Cacovich, B. Philippe, H. Rensmo, C. Ducati, R. H. Friend, and S. D. Stranks, "Potassium and rubidium passivated alloyed perovskite films: Optoelectronic properties and moisture stability," *ACS Energy Lett.*, vol. 3, no. 11, pp. 2671–2678, 2018.

[37] S. C. Watthage, Z. Song, N. Shrestha, A. B. Phillips, G. K. Liyanage, P. J. Roland, R. J. Ellingson, and M. J. Heben, "Enhanced grain size, photoluminescence, and photoconversion efficiency with cadmium addition during the two-step growth of $CH_3NH_3PbI_3$," *ACS Appl. Mater. Interfaces*, vol. 9, no. 3, pp. 2334–2341, 2017.

[38] S. Rajathi, K. Kirubavathi, and K. Selvaraju, "Structural, morphological, optical, and photoluminescence properties of nanocrystalline PbS thin films grown by chemical bath deposition," *Arabian Journal of Chemistry*, vol. 10, no. 8, pp. 1167–1174, 2017.

[39] G. Grancini, I. Zimmermann, E. Mosconi, D. Martineau, and S. Narbey, "One-Year stable perovskite solar cells by 2D/3D interface engineering," *Nat. Commun.*, vol. 8, pp. 1–8, 2017.

[40] Y. Hu, L. M. Spies, D. Alonso-Álvarez, P. Mocherla, H. Jones, J. Hanisch, T. Bein, P. R. Barnes, and P. Docampo, "Identifying and controlling phase purity in 2D hybrid perovskite thin films," *J. Mater. Chem. A*, vol. 6, no. 44, pp. 22215–22225, 2018.

Chapter 5

Inorganic halide perovskite $CsPbBr_3$ and modification of the solar stack

The most representative halide perovskite absorber $MAPbI_3$ is thermally unstable even at moderate temperatures of $\sim 60\,^{\circ}\mathrm{C}$. Another problem that critically affects the long-term stability of perovskite solar cells is that metals used as top contacts will react with halogens or halide species, particularly in the presence of heat and light. Such reaction can be avoided by developing alternative electrode materials like carbon. This chapter investigates the use of less volatile fully-inorganic halide perovskite materials for the production of solar cells with higher thermal stability. Section 5.1 compares $CsPbBr_3$ halide perovskite materials to the archetypal $MAPbI_3$ and shows how $CsPbBr_3$ can be incorporated in standard planar devices with architecture $TiO_2/CsPbBr_3/Spiro\text{-}OMeTAD/Au$. Section 5.2 presents the use of fully inorganic $CsPbBr_3$ in carbon solar cells for the generation of high voltage metal- and HTM-free devices.

5.1 $CsPbBr_3$ for high open circuit voltage solar cells

Previous chapters investigated two different approaches to increase the moisture stability of perovskite solar cells by treating the absorber surface and by substituting large cations of the A site in ABX_3 structures. Another approach is to totally replace the fragile organic cation MA^+ with more robust inorganic Cs^+. [1]

$CsPbX_3$, where X is either I or Br or a mixture of the two, is an all-inorganic perovskite, which was first reported in 2015 [2] and $CsPbI_3$ cells have now reached efficiencies of $17.1\,\%$. [3] The room temperature stable phase of $CsPbI_3$ is a non perovskite δ-yellow phase that does not make high efficiency solar cells. Different ways have been reported to stabilise the α-black phase of $CsPbI_3$, for example by introducing HI additives to increase strain in the crystal structures, [4] or through phenyltrimethylammonium bromide post-treatment. [3] The instability of the α-

phase of $CsPbI_3$ is mainly due to low tolerance factors t, which can easily be improved by changing the halide I to smaller Br. Indeed, $CsPbBr_3$ is stable at room temperature in the orthorombic γ-phase. [5]

5.1.1 Experimental methods

The substrates were cleaned and etched as described in chapter 2. $CsPbBr_3$ films prepared via a two-step deposition technique is the same procedure described in section 2.2.2. The solution precursor used for the one-step deposition technique of $CsPbBr_3$ was a $0.4\,\mathrm{M}$ equimolar solution of $PbBr_2$ and CsBr in anhydrous DMSO. $100\,\mu\mathrm{l}$ of solution was spin coated on the substrate at 2000 rpm for $30\,\mathrm{s}$ and annealed at $135\,^{\circ}\mathrm{C}$ for $15\,\mathrm{min}$ in air.

Standard architectures were fabricated using TiO_2 and Spiro-OMeTAD as electron transport material and hole transport material, respectively.

5.1.2 Optical and thermal properties

Figure 5.1 a shows the Tauc plots for $MAPbI_3$ and $CsPbBr_3$ films. $CsPbBr_3$ has an energy bandgap of $2.35\,\mathrm{eV}$ (yellow colour), about $0.8\,\mathrm{eV}$ higher than the standard $MAPbI_3$ (black colour).

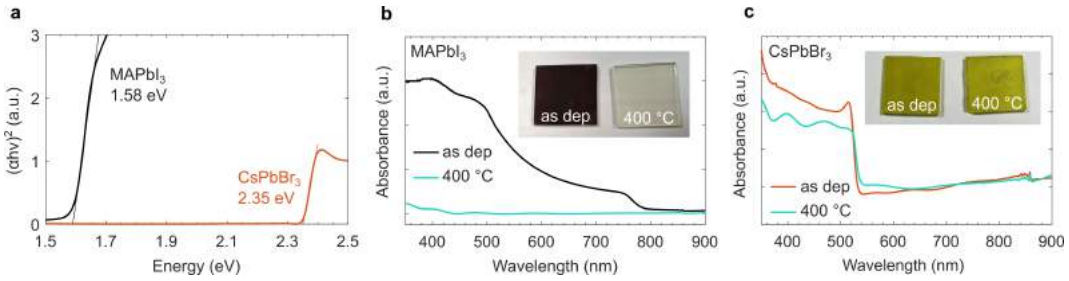

Figure 5.1: **a** Tauc plot of $MAPbI_3$ and $CsPbBr_3$ **b** UV-Vis absorbance of $MAPbI_3$ as deposited ('as dep') and after annealing treatment at $400\,^{\circ}\mathrm{C}$. **c** UV-Vis absorbance of $CsPbBr_3$ as deposited ('as dep') and after annealing treatment at $400\,^{\circ}\mathrm{C}$.

Wider energy bandgap materials absorb smaller parts of the spectrum, therefore leading to lower photocurrents. However, $CsPbBr_3$ is not only more stable towards moisture, but since Cs^+ is much less volatile than MA^+, structures with considerably higher thermal stabilities can be obtained. In fact, $CsPbBr_3$ was found to be thermally stable up to $\sim 550\,^{\circ}\mathrm{C}$ under a N_2 environment. [1] Figure 5.1 b and c show the absorbance of $MAPbI_3$ and $CsPbBr_3$ films, respectively, after deposition ('as dep') and after post-annealing treatment at $400\,^{\circ}\mathrm{C}$ in air for $30\,\mathrm{min}$. While the $MAPbI_3$ sample clearly changed from black to semitransparent due to complete decomposition of the perovskite structure and evaporation of the volatile precursors, the $CsPbBr_3$ film retained its yellow colour after treatment at $400\,^{\circ}\mathrm{C}$, confirming high thermal stability.

5.1.3 Two-step vs one-step solution method

The most common methods used to deposit $CsPbBr_3$ films are solution-based and vacuum-based methods. [2, 6, 7] Solution-based techniques can follow a two-step sequential deposition or one-step method. In the two-step method, $PbBr_2$ is first spin coated to make a layer and then converted to $CsPbBr_3$ by chemical reaction in solution with CsBr. [2, 1] In the one-step method a single spin coating procedure is used to deposit a precursor solution containing $PbBr_2$ and CsBr. [8, 9]

Figure 5.2 a shows the XRD patterns of $CsPbBr_3$ films deposited by the two-step technique after chemical reaction of $PbBr_2$ with CsBr solution ('as dep') and after annealing at $400\,°C$. $CsPbBr_3$ films show distinct (100), (110), (200) and (210) peaks (typical of the orthorombic perovskite structure of $CsPbBr_3$) only after annealing at $400\,°C$, indicating that a post-annealing treatment was crucial to obtain fully-converted $CsPbBr_3$ films. [10] The next section 5.2.2 will investigate the post-annealing temperature dependence of the structure and composition of $CsPbBr_3$ films. Figure 5.2 b shows the XRD patterns of $CsPbBr_3$ films deposited by one-step method after annealing at $135\,°C$ ('as dep') and $400\,°C$. Distinct peaks characteristic of the orthorombic phase appear after annealing at $135\,°C$, the peaks did not change after higher temperature annealing.

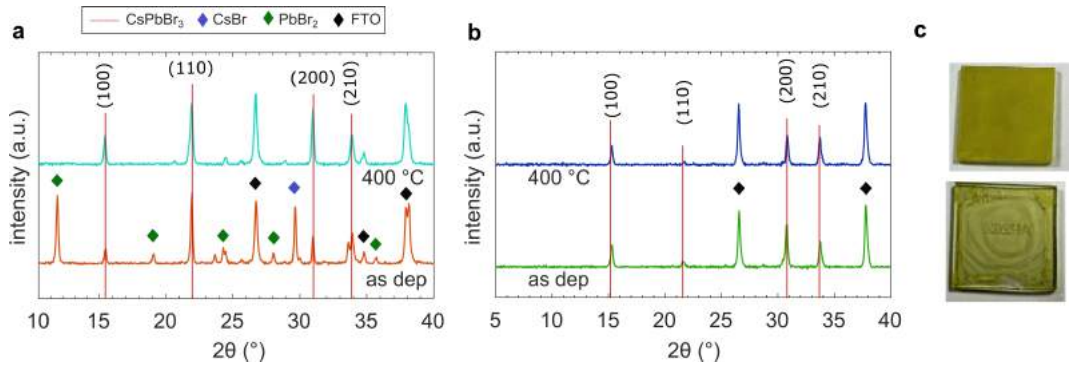

Figure 5.2: **a** XRD patterns of $CsPbBr_3$ films deposited via 2-step technique right after immersion in CsBr and after post-annealing treatment at $400\,°C$ in air. **b** XRD patterns of $CsPbBr_3$ films deposited via 1-step technique after deposition (annealing temperature at $135\,°C$) and after post-annealing at $400\,°C$. The positions of the XRD peaks for $CsPbBr_3$, CsBr, $PbBr_2$ and FTO are marked in the graphs. **c** Photographs of $CsPbBr_3$ films deposited via 2-step (top) and 1-step (bottom) techniques.

The main advantage of using a one-step spin coating methods over two-step ones is higher reproducibility, due to fewer parameters that need to be controlled. [9] However, as shown in figure 5.2 c, films deposited by the one-step technique are considerably thinner due to low solubility of the precursor materials. Films deposited by two-step techniques showed improved coverage and higher absorption, therefore this method was chosen to prepare full devices to investigate the photovoltaic properties of $CsPbBr_3$ based solar cells.

5.1.4 Standard planar solar cells TiO_2/$CsPbBr_3$/spiro-OMeTAD/Au

Standard solar cells with a compact layer of TiO_2 acting as ETM and Spiro-OMeTAD acting as HTM were fabricated. The absorber $CsPbBr_3$ was deposited via a two-step deposition technique. Figure 5.3 a shows the champion current-voltage curve measured under forward and reverse scan (AM 1.5 G, simulated solar light, $100\,\mathrm{mW\,m^{-2}}$), which achieved a PCE of over $5\,\%$ (under reverse scan).

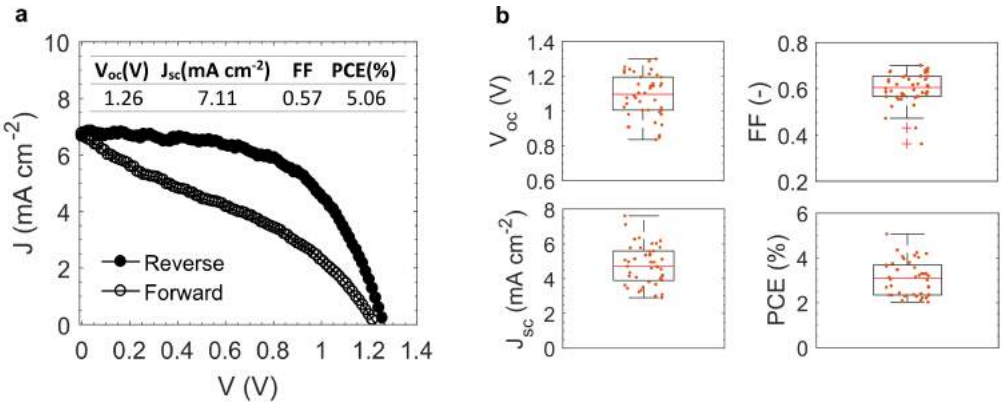

Figure 5.3: a JV curve of the champion TiO_2/$CsPbBr_3$/Spiro-OMeTAD/Au. **b** Box plots of PV parameters of TiO_2/$CsPbBr_3$/Spiro/Au (42 cells, red line indicates the median value, red crosses are outlier values

Figure 5.3 b shows the box plots of the main photovoltaic parameters to indicate high reproducibility of the results. The average PCE was about $3.5\,\%$ and the highest open circuit voltage achieved with such architecture was $\sim 1.3\,\mathrm{V}$.

Low-power but high-voltage solar cells may find potential niche market opportunities like indoor application. [11] Another application of such devices may be found in water splitting applications, where photovoltages higher than the theoretical thermodynamic limit of $1.23\,\mathrm{V}$ are required. [12]

5.2 Metal-induced degradation

One of the widely studied degradation pathways of perovskite solar cells is the reaction of the absorber perovskite material with the metal contacts. Such degradation is accelerated in the presence of heat and light and it can occur for different reasons. First, halogen species and halide products can diffuse through the transport layer to the metal contacts, corroding the metal and causing deficiency of halides in the absorber film. [13] Two of the most widely used metal contacts in perovskite solar cells are silver and gold. Ag is a low-cost candidate, however it has been observed that silver electrodes quickly turn yellow, and the colour change is accompanied by fast decrease in the PCE. The colour change is due to the oxidation of silver to AgI due to reaction with iodine. [14, 15]. Au is considerably more expensive than Ag, however colour changes within days of cell manufacture were not observed. However, it was demonstrated that intense UV-radiation induced the release of I_2 and volatile MAI

that could react with metallic gold at room temperature causing precipitation of new products at the interface that hindered charge extraction. [16]
A second degradation pathway is due to reaction of metals with Pb^{2+} at the surface, which converts $CH_3NH_3PbI_3$ to the monohydrated phase and then to CH_3NH_3I. [17] Such redox chemistry degradation was observed for Al electrodes and $CH_3NH_3PbI_3$ but it is expected to also occur for Cr and Yb metal contacts and $CsPbI_3$ and $CsPbBr_3$ absorber materials.
Finally, metals can diffuse through the transport layer to the perovskite absorber material, forming defect states and insulating the active layer. [18] Gold migration was observed when perovskite solar cells were exposed to temperatures of $70\,^{\circ}C$. [19] Similar results were later observed for Ag and Cu contacts. [20]

5.2.1 Architectures to prevent metal-induced degradation

Several approaches can be used to reduce metal-induced degradation of perovskite solar cells. One approach is through the deposition of barrier layers that can prevent halide species and metals from diffusing through the transport material. Many studies reported the use of solution processed interlayers like MoS_2 and MoO_x, [21, 22] copper phtalocyanine, [23] ITO, [20] and Al:ZnO/SnO_2. [24] The use of such interlayers demonstrated improved PCEs stability over time and under exposure to high temperature.

A second approach consists of designing new metal-free architectures. Carbon is an attractive and promising alternative material because it is cheap, stable and inert to ion migration. [25] Some examples of metal-free perovskite solar cells used carbon nanotubes between the perovskite absorber and the HTM [26, 27] and carbon cloth and fibers on top of the HTM. [28] However, the use of an organic HTM is not particularly effective either, because precursor materials, such as Spiro-OMeTAD, are highly expensive and operationally unstable. [25, 29]
A very promising alternative is a completely new architecture that is HTM-free, metal-free and fully printable. Ku *et al.* introduced a multi-layer mesoporous structure that included TiO_2, ZrO_2 and carbon mesoporous (mC-PSC) for the first time in 2013 (herein called the triple mesoscopic carbon stack). [30] The three layers were assembled by screen printing techniques and the TiO_2 and carbon mesoporous layers acted as electron and hole transport materials, respectively, while the ZrO_2 was used as a spacer layer. Initially, the precursor solution of PbI_2 and MAI was infiltrated through the mesoporous stack via a one-step deposition method. However, very low PCEs were obtained due to poor penetration. [30] Higher pore filling and more uniform morphology could be obtained by using a two-step deposition technique where PbI_2 was first infiltrated through the mesoscopic stack and then converted to $CH_3NH_3PbI_3$ by dipping the substrate into a MAI solution. [31] Another way to improve the pore filling and achieve higher PCEs was demonstrated by Mei *et al.* in 2014. The perovskite cell was produced by infiltrating a solution of PbI_2, MAI and 5AVA into the mesoporous stack via one-step deposition. [32] Later on, perovskite

solar cells stable for over 1 year were reported using such one-step technique, with addition of 5AVA, in these triple mesoscopic carbon cells. [33]

Further optimisation of the mC-PSC pushed the PCE of this kind of architecture to about $15\,\%$. [34, 35, 36] However, using the archetypal $MAPbI_3$ material, low voltages of about $1\,\mathrm{V}$ were achieved due to the difficulties in controlling the quality of the film through the multilayer porous scaffold and the numerous nonradiative recombinations. [37] The use of triple cation precursor solution in fully printable carbon perovskite solar cells pushed the efficiency to a record $17.02\,\%$, however the open circuit voltage was still limited to $1.01\,\mathrm{V}$. [38]

5.2.2 Screen printed carbon $CsPbBr_3$ solar cells with high open-circuit photovoltage

Triple mesoscopic carbon solar cells are fully printable devices which are compatible with large-scale manufacturing. Therefore, these type of cells constitute an attractive solution for the fabrication of scalable perovskite solar cells. Despite the fact that high solar conversion efficiency can be demonstrated, the voltage achieved by the archetypal $MAPbI_3$ is still low. In this work, the use of wider bandgap $CsPbBr_3$ in carbon based devices to achieve high voltage perovskite solar cells was investigated.

$CsPbBr_3$ was infiltrated through the triple-mesoporous layers via a two-step technique to fabricate mesoporous carbon solar cells (mC-PSC). First $PbBr_2$ was infiltrated through the stack and then converted to $CsPbBr_3$ by dipping the substrate into a CsBr solution. EDX characterisation confirmed the presence of Br and Pb throughout the entire scaffold, indicating complete infiltration of the perovskite precursor solution. After infiltration, different annealing temperatures ranging between 100 and $400\,^{\circ}\mathrm{C}$ were tested. It was found that enlarged crystal grains were obtained at higher annealing temperatures. Moreover, both XRD and XPS characterisation demonstrated that higher annealing temperatures promote the conversion of precursor materials $PbBr_2$ and CsBr to the perovskite $CsPbBr_3$. The open-circuit voltage of mC-PSC increased with the annealing temperature, reaching the highest value of $1.44\,\mathrm{V}$ after post-annealing treatment at $400\,^{\circ}\mathrm{C}$. These results were confirmed by impedance spectroscopy analysis, where cells annealed at high temperature (300 and $400\,^{\circ}\mathrm{C}$) reported a higher recombination resistance and lower recombination rate than low-temperature treated cells (100 and $200\,^{\circ}\mathrm{C}$). The champion mC-PSC achieved a PCE of $8.2\,\%$.

Fully-printable mesoporous carbon solar cells mC-PSC were compared to a HTM-free and metal-free planar device (C-PSC). In C-PSC, the absorber material $CsPbBr_3$ was sandwiched between a compact layer of TiO_2, acting as ETM, and a doctor bladed carbon paste layer which acted as HTM and extraction layer. The same post-annealing treatments were studied. In C-PSC thermal treatment at $400\,^{\circ}\mathrm{C}$ was needed to allow complete release of non-conductive nitrocellulose binder in the thick carbon electrode, which was entirely eliminated after $400\,^{\circ}\mathrm{C}$. C-PSC with $CsPbBr_3$

achieved even higher voltages than mC-PSC (champion V_{oc} of $1.45\,\mathrm{V}$) and the highest PCE of $5.7\,\%$ was measured after post-annealing treatment at $400\,^{\circ}\mathrm{C}$.

High voltage and metal-free solar cells were achieved by using $CsPbBr_3$ both infiltrated in mC-PSC and spin coated in C-PSC. Open circuit voltages as high as $1.45\,\mathrm{V}$ were measured, opening the possibility of using such high voltage devices for photovoltaic indoor applications and to drive water splitting reactions.

The results summarised in this section have been published by Poli et al. (2018). [39] The statement of authorship is given below.

This declaration concerns the article entitled:									
Screen printed carbon $CsPbBr_3$ solar cells with high open-circuit photovoltage									
Publication status (tick one)									
Draft manuscript		**Submitted**		**In review**		**Accepted**		**Published**	X
Publication details (reference)	The article has been published in: *J. Mater. Chem. A*, Vol. 6, 18677-18686 (2018)								
Copyright status (tick the appropriate statement)									
I hold the copyright for this material				Copyright is retained by the publisher, but I have been given permission to replicate the material here	X				
Candidate's contribution to the paper (provide details, and also indicate as a percentage)	The candidate **predominantly** executed the work presented in the paper. **Formulation of ideas:** The objectives, analysis and conclusions of the paper were formulated by the candidate, with the support of the lead supervisor Petra Cameron. [IP=85%, JB=0%, JMG=0%, FDR=0%, SE=0%, TW=0%, PJC=15%] **Design of methodology:** The methodology was designed by the candidate with the support of the lead supervisor Dr Petra Cameron and collaborators Jenny Baker and Trystan Watson (Specific, Swansea University). [IP=75%, JB=7%, JMG=0%, FDR=0%, SE=0%, TW=3%, PJC=15%] **Experimental work:** Jenny Baker printed the triple mesoporous stacks with the candidate in Swansea University. The infiltration of mesoporous cells with perovskite solution and optimisation of the fabrication was done by the candidate at the University of Bath. Planar devices were fabricated by the candidate. $CsPbBr_3$ films for XPS characterisation were prepared by the candidate, while XPS was measured by James McGettrick in Swansea University. The stability test was carried out by Francesca De Rossi in Swansea University (with solar cells fabricated by the candidate). The rest of the experimental work was carried out by the candidate in University of Bath. [IP=80%, JB=10%, JMG=5%, FDR=5%, SE=0%, TW=0%, PJC=0%] **Presentation of data in journal format:** Data were analysed by the candidate and plots and figures in journal format were generated by the candidate. The writing of the manuscript was done by the candidate. The lead supervisor Petra Cameron, second supervisor Salvador Eslava and collaborator Jenny Baker reviewed and corrected the writing of the paper. Petra Cameron gave assistance in the submission and peer reviewing process. [IP=70%, JB=4%, JMG=2%, FDR=2%, SE=2%, TW=2%, PJC=18%]								
Statement from Candidate	This paper reports on original research I conducted during the period of my Higher Degree by Research candidature.								
Signed	X Isabella Poli Isabella Poli					**Date**	11/06/2019		

Journal of Materials Chemistry A

PAPER

View Article Online
View Journal | View Issue

Cite this: J. Mater. Chem. A, 2018, 6, 18677

Screen printed carbon $CsPbBr_3$ solar cells with high open-circuit photovoltage†

Isabella Poli, *[ab] Jenny Baker, [c] James McGettrick, [c] Francesca De Rossi, [c] Salvador Eslava, [db] Trystan Watson [c] and Petra J. Cameron *[ab]

Screen printed mesoporous carbon solar cells (mC-PSC) are a promising fully printable technology that does not require organic hole conductors, expensive metal contacts or vacuum processing. However, when infiltrated with the archetypal $CH_3NH_3PbI_3$ perovskite, mC-PSCs show low voltage which limits their use in innovative applications such as indoor light harvesting. Here we investigate both planar (C-PSC) and mesoporous (mC-PSC) carbon cells, based on all-inorganic $CsPbBr_3$. Pure $CsPbBr_3$ is a yellow material with an orthorhombic crystal structure at room temperature and a 2.3 eV band gap, which is not ideal for solar cell applications. However, $CsPbBr_3$ is thermally stable up to over 400 °C and high-voltage planar carbon solar cells, with open circuit voltages of up to 1.29 V and efficiencies up to 6.7% have been reported in the literature. We focus on the effect of the post-annealing temperature on the material properties and photovoltaic activity. XPS and XRD results show a non-linear trend with temperature, with significant improvements in composition between 200 and 300 °C. Both the mesoporous and planar champion devices were obtained after heat processing at 400 °C, reaching PCEs of 8.2% and 5.7% respectively. The average V_{oc} for the planar and mesoporous devices were 1.33 V and 1.27 V respectively with a record 1.44 V for the best mC-PSC.

Received 8th August 2018
Accepted 11th September 2018

DOI: 10.1039/c8ta07694d

rsc.li/materials-a

Introduction

The photovoltaic (PV) market is currently dominated by crystalline silicon (c-Si). The price of c-Si modules has fallen recently, providing cost-competitive power compared to that delivered by fossil fuel technologies.[1] High power conversion efficiencies (PCE), high stability and low-cost are therefore necessary for any new technology that wants to break into the PV market. Halide perovskites emerged as promising new PV material in 2012.[2,3] Perovskite solar cells (PSCs) are composed of Earth-abundant elements and they can be deposited by low-temperature and inexpensive solution-based methods. Most importantly, PCEs have increased to a certified 23.3% in just few years.[4]

Devices with record-efficiency use Au as back contact together with organic conductive polymers acting as hole transport material (HTM). Such architecture strongly limits the long-term stability of perovskite solar cells. Gold migration through the HTM into the perovskite material occurs when PSCs are exposed to high temperatures, irreversibly degrading the layers.[5] Moreover, expensive pure Au is required, dominating the PSCs manufacturing costs.[6] A widely used hole conducting polymer is spiro-OMeTAD ('spiro'). Large-scale production of this material is prohibitive because it requires many synthetic and purification steps and uses expensive catalysts.[7] Moreover, spiro is not highly conducting and additives, such as Li salts, are needed to achieve good device performance.[8] The hygroscopic nature of such additives accelerates the degradation of PSCs.[9] In order to reduce the detrimental effect of using Li salts, PTTA (poly[bis(4-phenyl) (2,4,6-trimethylphenyl)-amine]) was found as an efficient alternative HTM.[10] However PTTA can still cause infiltration problems, as well as increase the fabrication cost.[11]

Solar cells without an organic hole conductor and gold as metal contact have been successfully synthesised.[11,12] PSCs where the contact is a screen printed carbon layer have recently gained wide interest. In the case of mesoporous carbon devices, the perovskite is infiltrated into a 6–10 μm mesoporous carbon layer. This architecture was first demonstrated in 2013 (ref. 13) using methylammonium lead triiodide (MAPI) and very rapidly developed to a certified PCE of 15.6%.[14–20] 5-Ammoniumvaleric acid iodide (5-AVAI) can be used as an additive to obtain better pore filling and lower defect concentration.[14,21] The highest PCEs of 15.6% were achieved by adding ammonium chloride (NH_4Cl) to enable perovskite crystals with preferential growth orientation[20] and replacing the most widely used 5-AVAI with a bifunctional conjugated organic molecule 4-(aminomethyl)

[a]Department of Chemistry, University of Bath, Bath BA2 7AY, UK. E-mail: i.poli@bath.ac.uk; p.j.cameron@bath.ac.uk
[b]Centre for Sustainable Chemical Technologies, University of Bath, Bath BA2 7AY, UK
[c]SPECIFIC, Swansea University Bay Campus, Fabian Way, Swansea, SA1 8EN, UK
[d]Department of Chemical Engineering, University of Bath, Bath BA2 7AY, UK

† Electronic supplementary information (ESI) available. See DOI: 10.1039/c8ta07694d

benzoic acid hydroiodide.[19] Printable solar cells with PCEs as high as 17% were also reported by using triple cation perovskite $TiO_2/Al_2O_3/NiO$ layered framework and carbon counter electrode.[22] Advantages of carbon-based PSCs include good stability, due to the hydrophobic nature of carbon, and a low-cost scalable deposition process compatible with fast printing production.[16,23] Recently, near infrared processing was investigated to further improve the commerciability of the technology by reducing the processing time and allowing the preparation of larger area modules.[24] Infiltration of active materials onto large area carbon surfaces has been demonstrated using a mechanical dispenser and mesh[25] and modules up to 198 cm^2 in size have been reported.[26] One disadvantage of mesoporous carbon cells is that the photovoltage measured in this architecture is still notably low. The highest open circuit voltage reported to date is 1.05 V.[17] In contrast perovskite cells with an organic hole conductor can have open circuit voltages up to 1.4 V.[27] It is therefore crucial to optimise carbon cells to improve the open circuit voltage. High voltage solar cells are essential for a variety of applications, such as charging low-power electronic batteries,[28] indoor applications and photoelectrochemical unassisted water splitting.[29]

Most perovskite devices use methylammonium (MA) and formamidinium (FA) as organic cations. Another limitation in the commercialisation of organo-lead halide perovskites is their thermal and moisture instability. MA and FA are not stable in high humidity ambient conditions and at high temperature, requiring environmental controls during processing and encapsulation later.[23] The most efficient perovskite devices use multi cation materials where organic FA and MA are mixed with the smaller inorganic cation Cs.[30] All inorganic $CsPbI_3$ has a black delta phase and PCEs of 10% have been reported.[31] However, the material tends to form a wide bandgap non-perovskite phase at room temperature.[32] The band gap and phase can be tuned by adding bromide to $CsPbI_3$. The highest reported efficiency in literature on Cs-based perovskite devices with mixed halide is 14.6%;[33] however at certain I : Br ratios the material is unstable and separates into iodide rich and bromide rich regions under illumination.[31,34]

All-inorganic $CsPbBr_3$ perovskites have recently attracted attention due to their high thermal stability. Thermogravimetric analysis (TGA) of $CsPbBr_3$ performed under N_2 flow showed a decomposition onset at about 580 °C and solar cells with mesoporous TiO_2 as electron transport material ETM, spiro as HTM and Au as metal contact based on this material showed PCE of 6.2%.[35,36] Very recently $CsPbBr_3$ was also deposited using a dual-source vacuum evaporation technique achieving a PCE of 6.95%.[37] $CsPbBr_3$ crystallises in the orthorombic space group at room temperature; transitions to the tetragonal and then the cubic phase occur at 88 °C and 130 °C respectively.[38] $CsPbBr_3$ has been recently used in carbon-based architectures as well, showing no performance degradation over 3 months in humid air.[39] Carbon cells with the architecture FTO/c-TiO_2/m-TiO_2/$CsPbBr_3$/C (c: compact, m: mesoporous) achieved PCEs ranging between 5% and 6.7%.[39–41] In these reports the $CsPbBr_3$ films were annealed at 250 °C and the carbon layer was either screen printed or deposited by doctor blade technique. The highest voltage measured using this architecture was 1.29 V.[40] Recently it was shown that by adding carbon and red phosphorus quantum dots at the TiO_2/$CsPbBr_3$ and $CsPbBr_3$/C interfaces, improvements in the V_{oc} up to 1.47 V could be achieved, with the highest PCE measured to be 8.2%.[42,43]

In this work, we report for the first time the preparation of mesoporous carbon $CsPbBr_3$ solar cells (mC-PSC). The mC-PSC architecture consists of c-TiO_2/m-TiO_2/m-ZrO_2/m-carbon with $CsPbBr_3$ infiltrated through the stack. We compare this mC-PSC to planar c-TiO_2/$CsPbBr_3$/m-carbon (C-PSC). $CsPbBr_3$ solar cells with carbon as top contact (C-PSC) have been previously reported in literature. In contrast, the preparation of mC-PSC by infiltration of $CsPbBr_3$ into printable solar cells has not. Cell preparation was carried out under ambient atmosphere and the effect of post-annealing treatment with temperatures ranging between 200 and 400 °C was studied. When annealed at 400 °C enlarged crystal grains and complete conversion of precursor materials to $CsPbBr_3$ was obtained. Our champion mC-PSC and C-PSC reached a PCE of 8.2% and 5.7%, respectively. Most importantly, an extremely high V_{oc} of 1.44 V was achieved for mC-PSC, with an average of 1.27 V over 20 devices. As far as we know, this is the highest voltage ever seen using the c-TiO_2/m-TiO_2/m-ZrO_2/m-carbon structure-based cell, which is notable for its low voltage. In C-PSC the $CsPbBr_3$ crystal size is not constrained by the mesoporous carbon material, allowing free growing of the grains leading to a champion V_{oc} of 1.45 V, with an open circuit voltage of 1.33 V averaged over 40 devices.

Experimental

Schematics of the fabrication process of mC-PSC and C-PSC are shown in Fig. 1.

mC-PSC fabrication

TEC 7 fluorine doped tin oxide (FTO) glass substrates were etched using a Rofin Nd:YVO_4 laser (532 nm) at a speed of 150 nm s^{-1}. Substrates were cleaned with isopropanol (IPA, Sigma-Aldrich) and deionised (DI) water and further treated with O_2 plasma. A compact layer of TiO_2 was deposited *via* spray pyrolysis at 300 °C from a solution 1 : 9 of titanium diisopropoxide bis(acetylacetonate) (Sigma) in IPA. 30 NRD TiO_2 paste (Dyesol) 2 : 3 terpineol (Sigma) by weight was screen printed onto the c-TiO_2 and cells were sintered at 550 °C for 30 min. ZrO_2 paste (Solaronix) was screen printed on top of TiO_2 and sintered at 400 °C for 30 min. A carbon paste (Gwent Electronic Materials) was screen printed on top of the ZrO_2 and sintered at 400 °C for 30 min. 1 M of $PbBr_2$ (98%, Sigma-Aldrich) was dissolved in *N*,*N*-dimethylformamide (DMF, anhydrous, Sigma-Aldrich) at 70 °C and 6 μl dropped onto the active area of each cell while substrates were heated at 70 °C and further sintered at 70 °C for 30 min. The cell was then immersed in CsBr (99.999%, Sigma-Aldrich) solution in methanol (17 mg ml^{-1} kept at 50 °C in a vertical staining jar). After 30 min immersion, the sample was annealed at 150 °C for 30 min.

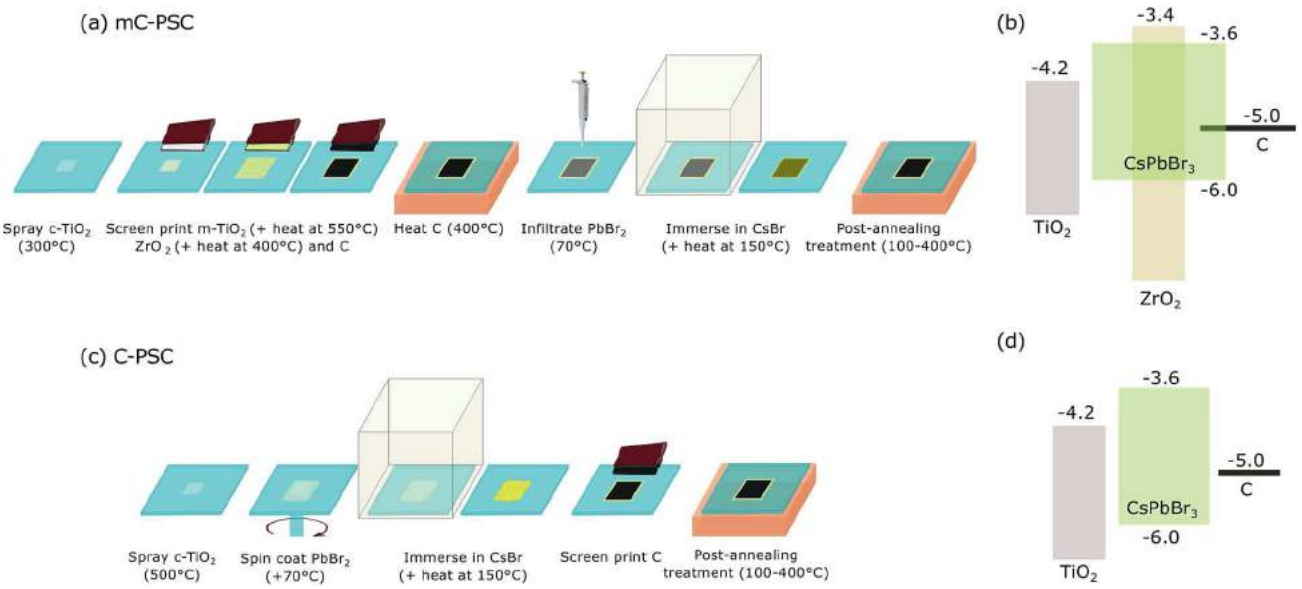

Fig. 1 (a–c) Schematic showing the fabrication of a mesoporous carbon solar cell (mC-PSC) and a planar carbon solar cell (C-PSC). The temperatures within brackets indicate the deposition, sintering and annealing temperatures. The detailed fabrication process is explained in the experimental section; (b and c) energy band diagram of mC-PSC and C-PSC allowing a semiquantitative comparison of the two architectures. Band edge positions of the materials were taken from previous literature data.[13,44]

Devices were further post-annealed at different temperatures ranging between 100 and 400 °C for 30 min.

C-PSC fabrication

FTO glass (TEC 7) (Sigma-Aldrich) was etched with zinc powder and HCl. It was then cleaned in 2 vol% Hellmanex solution in water, followed by DI water, acetone (VWR), IPA (VWR) and ethanol (VWR) before being treated with UV-ozone cleaning. A compact TiO_2 (c-TiO_2) layer was deposited by spray pyrolysis, using a hand held atomiser to spray 20 mM solution of titanium diisopropoxide bis(acetylacetonate) (75 wt%, Sigma-aldrich) in IPA onto the substrates held at 500 °C. Substrates were then annealed at this temperature for 10 minutes. $PbBr_2$ solution was spin coated on top of the substrates held at 70 °C at 2500 rpm for 30 s and each cell was further sintered at 70 °C for 30 min. The cell was then immersed in the CsBr solution kept at 50 °C in a vertical staining jar for 30 min before being annealed at 150 °C for 30 min. A carbon layer was deposited as top contact by doctor blading the carbon paste on top of the $CsPbBr_3$ film. Devices were further post-annealed at different temperatures ranging between 100 and 400 °C for 30 min.

Characterisation

PXRD. Powder diffraction patterns were collected from $CsPbBr_3$ thin films using a Bruker Advance D8 X-ray diffractometer with a Cu Kα source. Measurements were taken from 2θ values of 5 to 80°.

UV/vis spectroscopy. Thin film optical transmission and reflectance measurements were performed on a Perkin-Elmer Lambda 750S UV/Vis spectrometer, from 900 nm to 300 nm. Absorption was calculated as $\alpha = \log\left(\frac{1-R}{T}\right)$.

***J–V* curves.** *J–V* curves were measured using Keithley 2601A potentiostat, under 1 sun intensity and AM 1.5. The voltage was swept at 120 mV s^{-1} from 1.5 V to 0 V and back to 1.5 V. Size of each cell is 0.25 cm^2.

SEM, and AFM images. The cross-section morphology was studied using a JEOL SEM6480LV scanning electron microscope (SEM) (20 kV acceleration voltage and a magnification of 5000). Energy dispersive X-ray spectroscopy (EDX) was used for mapping, line scan, point ID and quantitative analysis of the elemental distribution through an Oxford INCA X-ray analyser. An atomic force microscope (AFM) was used to study the surface profile and measure the sample topography. The images were taken on a Nanosurf easyscan 2 FlexAFM system in Phase Contrast tapping mode using a force of 2 nN. A ContAl-G Tip was used for measurements.

EIS. Electrochemical impedance spectroscopy was measured at open circuit using a Modulab (Solartron analytical AMETEK). Each sample was scanned from 1×10^6 Hz to 0.5 Hz at seven different illumination intensities ranging between 1.47×10^{15} and 1.47×10^{17} cm^{-2} s^{-1}. A single wavelength of light with $\lambda = 465$ nm was used. Impedance data were fitted by using ZView software (Scribner Associates). The theory behind the EIS with ideality factor calculation is detailed in the ESI.†

XPS. XPS was carried out on a Kratos Axis Supra (Kratos Analytical, Manchester) instrument with samples connected to ground. Control XPS spectra of CsBr and $PbBr_2$ powders were also collected. XPS was performed at an X-ray power of 225 W using a monochromated Al Kα source. Step size and pass energy used are 0.1 eV and 20 eV respectively. No X-ray induced degradation was observed on the $CsPbBr_3$ films. XPS data were analysed using CasaXPS and the Kratos sensitivity factor library.

Results and discussion

$CsPbBr_3$ thin films were prepared in air using a 2-step method. $PbBr_2$ was first deposited, then converted to $CsPbBr_3$ by dipping into a CsBr solution, followed by annealing at 150 °C. The precursor films of $PbBr_2$ appeared transparent; the colour of the films changed to bright yellow during the conversion in the CsBr solution. In order to promote the conversion of $PbBr_2$ and CsBr to $CsPbBr_3$, films were post annealed at temperatures between 100 and 400 °C. The morphology, structural properties and surface chemistry were analysed as a function of the processing temperature.

TGA analysis of $CsPbBr_3$ films performed under N_2 flow previously reported in literature showed a decomposition onset at temperatures higher than 500 °C.[36] Our films appeared to be stable after annealing at 400 °C, showing an unaltered absorption window (Fig. S1†) and consistent energy bandgap of 2.35 eV. The effects of post-annealing treatment at different temperatures on the composition and morphology of the $CsPbBr_3$ films were investigated. Fig. 2(a) shows X-ray diffraction (XRD) patterns of a $CsPbBr_3$ thin film post-annealed at 100, 200, 300 and 400 °C. The XRD patterns show obvious $CsPbBr_3$ peaks at 15.2°, 22.1°, 30.9° and 34°, which correspond to (100), (110), (200) and (210) planes respectively, typical of the orthorombic crystal structure of $CsPbBr_3$.[34,40] However, films annealed at 100, 200 and 300 °C show the presence of additional peaks that do not correspond to $CsPbBr_3$. Diffraction peaks marked with the light-blue and red marker in Fig. 2(a) indicate the presence of residual $PbBr_2$ and CsBr indicating that full conversion of $CsPbBr_3$ was not obtained.[45–47] The higher processing temperatures accelerated the conversion. After treatment at 400 °C, the characteristic peaks of $CsPbBr_3$ show higher intensity and the peaks due to residual $PbBr_2$ and CsBr have disappeared. AFM amplitude images of films heat treated at 300 and 400 °C are shown in Fig. 2(b) (AFM images of films annealed at lower temperatures are in Fig. S2†). Films annealed at 300 °C and below show smooth surfaces with crystal grains sizes ranging between 0.3 and 0.9 μm. The crystal size is not uniform on the surface, probably because of the high amount of unconverted $PbBr_2$. Previous literature showed that $PbBr_2$ exhibits a similar smooth surface.[40] The morphology considerably changes when the film is annealed at 400 °C. Enlarged crystal grains are observed with sizes ranging between 3 and 5 μm.

X-Ray photoelectron spectroscopy (XPS) analysis was carried out to study any variations in the surface chemistry of $CsPbBr_3$ films processed at different temperatures. Fig. 3(a) shows the

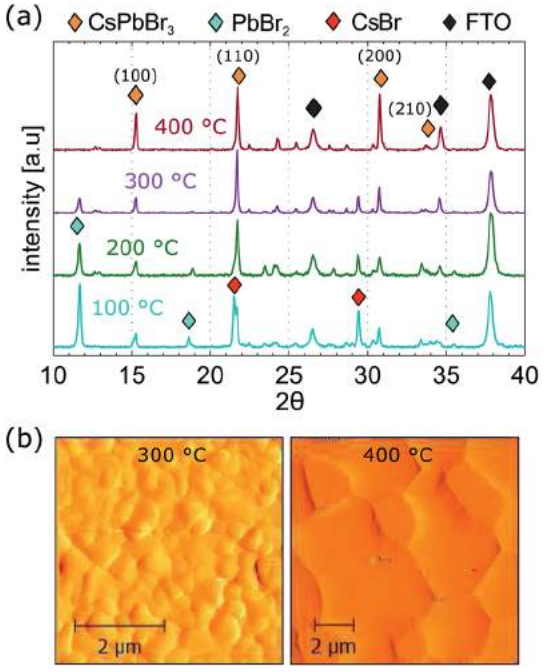

Fig. 2 (a) XRD pattern of $CsPbBr_3$ films post-annealed at 100, 200, 300 and 400 °C. The characteristic peaks of $CsPbBr_3$ are marked with orange. Light blue and red markers indicate the presence of unconverted $PbBr_2$ and CsBr precursor materials. FTO characteristic peaks are indicated by the black marker; (b) AFM amplitude images of $CsPbBr_3$ films annealed at 300 and 400 °C respectively.

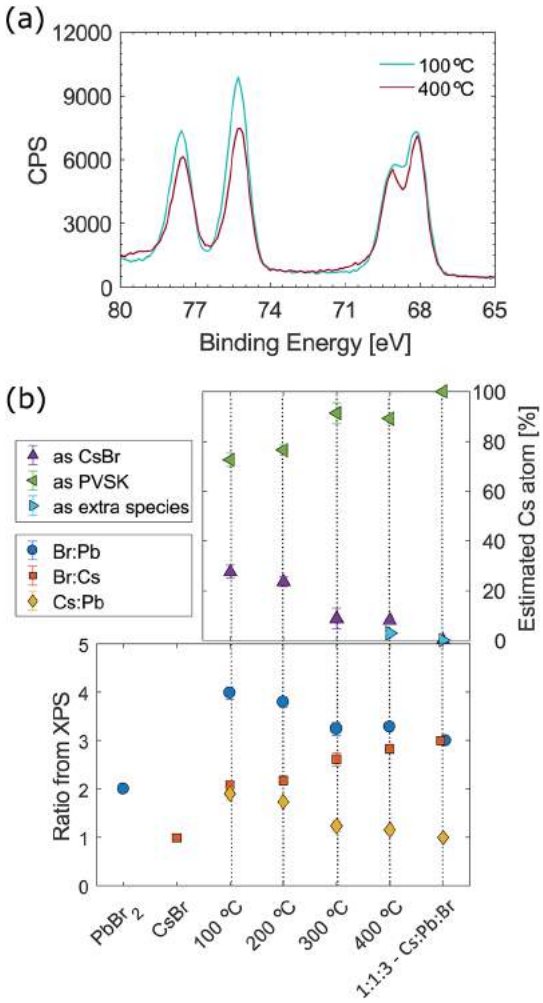

Fig. 3 (a) Comparison of sets of doublets, Cs(4d) and Br(3d), measured by XPS on perovskite (PVSK) $CsPbBr_3$ films processed at 100 and 400 °C; (b) variable surface chemistry of $CsPbBr_3$ as films as a function of process temperature measured by XPS; all data are presented as ratios. Data are the average of three measurements, with error bars indicating the standard deviation.

XPS spectra of $CsPbBr_3$ films processed at 100 and 400 °C. Raw data are fitted with Cs and Br doublets, the fitting spectra are shown in Fig. S3 in the ESI.† The intensity of the Cs(4d) doublet at 75.3 eV and Br(3d) doublet at 68 eV drop from 100 to 400 °C, indicating less unconverted CsBr and suggesting that high temperature annealing is necessary to obtain pure $CsPbBr_3$. Notably, the peaks present after annealing at 400 °C are sharper than the ones measured for the film annealed at 100 °C. Sharp peaks indicate less complex chemistry, as the contribution from CsBr to the Br(3d) envelope drops. As XPS peaks are known to be sensitive to the local electronic environment, broad peaks can indicate disorder or subtle chemical shifts due to multiple similar bonding environments, hence the sharpening of peaks is consistent with the surface being predominantly one species ($CsPbBr_3$) at 400 °C. The bottom graph in Fig. 3(b) shows the elemental ratios measured by XPS on different films. $PbBr_2$ and CsBr ratios were measured directly from small amounts of powders of the precursor materials. The predicted Cs : Pb : Br ratio in the final perovskite films is the stoichiometric 1 : 1 : 3 ratio. The ratio Br : Pb at the surface exceeds 3 : 1 when the film is annealed at low temperatures, this is due to incomplete conversion of the precursors. Overall, an excess of CsBr was measured, especially when films were processed at 100 and 200 °C. When films were synthesised at 300 and 400 °C, the elemental ratio gets closer to the predicted stoichiometric perovskite ratio, suggesting that high temperature allows better conversion of precursors into $CsPbBr_3$. The composition does not show a linear trend with temperature and a significant, non linear improvement in stoichiometry between 200 and 300 °C is observed. The top graph in Fig. 3(b) shows the amount of CsBr present on the top surface of the perovskite. The Cs content as CsBr on the surface decreases from about 30% to less than 10% with increasing annealing temperature. It is important to note that when the film is annealed at 400 °C a new compound develops. This compound is found as a Cs doublet at about 78 and 76 eV and it is present only in the film annealed at 400 °C (see Fig. S3 in the ESI†). The development of extra species is consistent with loss of electron density from the Cs atoms and hence possible oxidation of the material. It might be that 400 °C is a borderline temperature that pushes the $CsPbBr_3$ perovskite very close to the edge of the process window.

To evaluate device performance, solar cells were fabricated. Two different architectures based on carbon as hole transport layer were investigated. The first one is a multi-layer screen printed mesoporous stack with a carbon top electrode (mC-PSC). The mesoscopic layers involved are an n-type TiO_2 layer, a ZrO_2 layer acting as an insulating spacer and a mesoporous carbon top contact. $CsPbBr_3$ is introduced by infiltration through the mesoporous stack. In this architecture, the crystal size of the $CsPbBr_3$ should be determined by the pores of the mesoporous carbon structure, where the smallest were measured to be about 10 nm in width.[24,48] The second architecture is a planar carbon solar cell, where the electron transport layer is TiO_2 prepared by spray pyrolysis and the hole transport layer is carbon layer printed directly onto the $CsPbBr_3$. In this architecture, the $CsPbBr_3$ crystallite size is not limited by the carbon pore size.

Fig. 4 shows cross section SEM/EDX images of a mC-PSC. EDX mapping allows a qualitative analysis of the elements present in the structure, providing details of the solution infiltration. In these devices, $CsPbBr_3$ is homogeneously and uniformly infiltrated through the whole carbon layer. The three different mesoscopic layers are clearly defined and well separated from each other.

J–V curves of four different mC-PSC annealed at 100, 200, 300 and 400 °C measured under reverse scan are shown in Fig. 5(a). The original *J–V* curves measured under forward and reverse scan are shown in Fig. S4 in the ESI.† The current density has been normalised to the J_{sc} to allow easier comparison of the curves. In all of the devices we observed very little change in the photocurrent density with post-annealing temperature. Indeed if the same cell was annealed and then re-measured at each of the four temperatures the short circuit current remained the

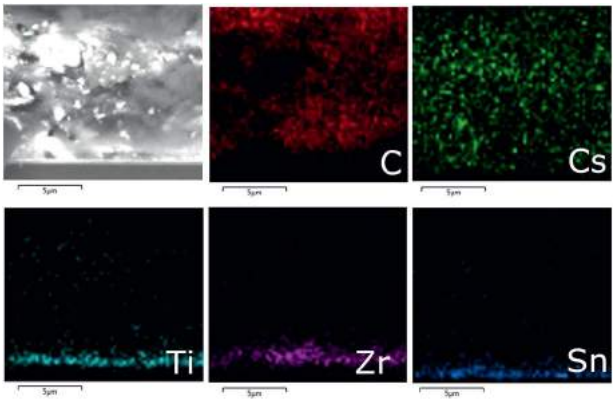

Fig. 4 Cross section SEM/EDX mapping of a mC-PSC device. The mesoscopic layers of TiO_2, ZrO_2 and C are indicated by light blue, purple and red colour respectively. Detection of $CsPbBr_3$ is given by the green colour, which is assigned to Cs. The blue colour shows the presence of coated FTO on glass.

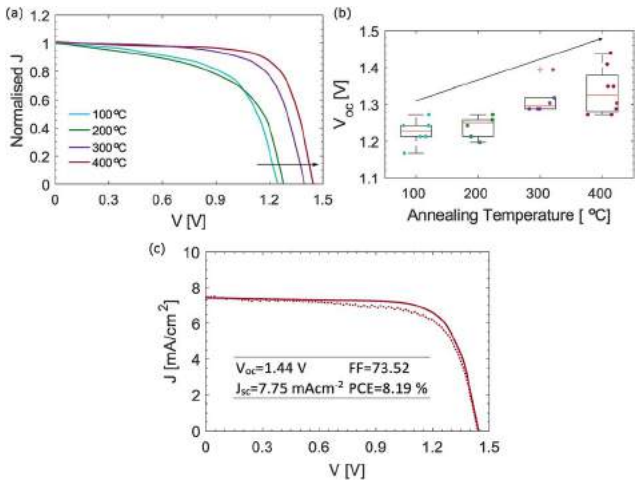

Fig. 5 (a) *J–V* curves of a representative mC-PCS post annealed at different temperatures under reverse scan. The current density has been normalised to the J_{sc}. Original *J–V* curves can be found in Fig. S4 in the ESI; † (b) box-plots of V_{oc} of mC-PSC annealed at different temperatures; (c) champion mC-PSC device post-annealed at 400 °C.

same, but the fill factor was observed to drop due to repeated annealing of the same device (see Fig. S5 in the ESI†). The PV parameter that mainly changes with temperature is the open circuit voltage, as shown by the V_{oc} trend with temperature in Fig. 5(b). The voltage improvement is non-linear as a function of processing temperature, showing a significant improvement between 200 and 300 °C. Interestingly, this trend corresponds well with the information on chemical composition obtained by XRD and XPS shown in Fig. 2 and 3. The composition may influence the recombination rate; unconverted $CsPbBr_3$ species could limit the charge injection and transport, leading to accumulation of charges and higher interfacial recombination, which is reflected in a decreased V_{oc}.[2] Another factor influencing the voltage may be $CsPbBr_3$ grain size. Fig. 2(b) showed that grains become larger when annealed at 400 °C. High temperature processing may push the infiltrated $CsPbBr_3$ material to fully adhere with the carbon particles, improving the charge injection from the perovskite into the mesoporous carbon.

Fig. 5(c) shows the champion mC-PSC device post-annealed at 400 °C, exhibiting V_{oc} = 1.44 V, J_{sc} = 7.75 mA cm^{-2}, FF = 73.52 and PCE = 8.19%. However, on some occasion loss in FF was observed for cells annealed at 400 °C (Fig. S5 and S8†). XPS analysis showed that when the film is processed at 400 °C, additional compounds develop on the surface, which might suggest oxidation and the edge of the process window. When processing $CsPbBr_3$ films at 400 °C, oxidation of the material may be more or less pronounced due to small changes in the annealing temperature and heating and cooling time which may lead to more evident losses in the FF. Fig. S9(a)† shows the *J–V* curve of a mC-PSC post-annealed at 350 °C. No clear oxidation nor loss in FF are observed and high V_{oc} of 1.35 V can be obtained. Stabilised power output measurements were also collected by monitoring the current when the cell was biased to the maximum power point voltage determined by the *J–V* sweep, showing a stable output over 60 s (Fig. S9(b) in the ESI†).

Recently, Liao *et al.* reported a $CsPbBr_3$-based solar cell with quantum dots deposited at the ETM/$CsPbBr_3$ and $CsPbBr_3$/HTM interfaces respectively. They claim that the quantum dots create intermediate energy levels enhancing charge transfer and allowing a champion PCE of 8.2%.[42] In this work we show that using a mesoporous architecture where $CsPbBr_3$ is infiltrated through the mesoporous stack and post-annealed at 400 °C very high PCEs can be obtained without complex passivation of the interfaces.

Photovoltaic parameters shown as box plots for efficiency distributions of over 20 mC-PSC processed at 400 °C are presented in Fig. S10,† showing that very high voltages are consistently measured. Most notably, the average V_{oc} is 1.27 V with the highest being 1.44 V. To our knowledge this is the highest voltage ever seen using the c-TiO_2/m-TiO_2/m-ZrO_2/m-carbon structure-based cell, showing the potential of this architechture. Photocurrent densities for mC-PSC were found to change between 3.5 and 10 mA cm^{-2} over several batches (see Fig. S10†). We believe that the J_{sc} of mC-PSC mainly depends on how good the infiltration of $CsPbBr_3$ into the mesoscopic porous carbon is. Similarly, Wagner *et al.*, who studied the crystallisation of MAPI infiltrated in mesoporous carbon layers, noticed that the most significant increase in photocurrent was observed due to improved alignment of the perovskite surface to the porous carbon.[48] The main parameters affecting the infiltration are believed to be the temperature of CsBr solution and the dipping time.[40] The ramp rate to the high process temperature is another parameter that may play a significant role. Limited performance degradation was observed in mC-PSCs annealed at different temperatures. Fig. S12† shows the variation of the main PV parameters over time. During this time period, the cells were left in an ambient atmosphere without encapsulation, at open circuit (also known as shelf-stability).

Impedance measurements at open circuit were carried out to investigate recombination in mC-PSC when post-annealed at different temperatures. Fig. 6(a) illustrates the impedance response observed at open circuit for two different mC-PSC annealed at 100 and 400 °C. The Nyquist plots obtained for each device at all intensities are shown in Fig S13–S16 in the ESI.† At all intensities three semi-circles were seen in the Nyquist plots. The semicircles centred on 51.4 and 23.5 kHz are attributed to the geometric capacitance C_g and the recombination resistance R_{rec}. The variation of R_{rec} with open circuit voltage is shown in Fig. 6(b). Semilogaritmic plots for mC-PSC annealed at different temperatures have very similar slopes, therefore the cells have similar ideality factors ranging between 2.1 and 2.5.[49] Interestingly, the cells fall into two groups: at the same voltage R_{rec} is lower in the cells annealed at 100 and 200 °C

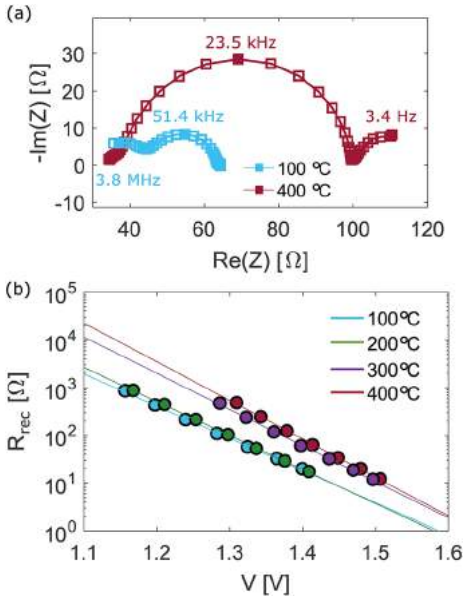

Fig. 6 (a) Example of Nyquist plot of the mC-PSC annealed at 100 and 400 °C measured at 1.41 ± 0.01 V. The response of samples annealed at 100 °C was measured at the highest light intensity (λ = 465 nm, 1.47 × 10^{17} cm^{-2} s^{-1}). While, the response of samples annealed at 400 °C was measured at a lower light intensity (λ = 465 nm, 1.47 × 10^{16} cm^{-2} s^{-1}); (b) recombination resistance for the different type of mC-PSC at open circuit under different illumination intensities. Slopes of the lines shown are 148, 140, 132 and 124 mV per decade for samples annealed at 100, 200, 300 and 400 °C respectively. These values correspond to an ideality factor *m* of 2.5, 2.4, 2.2 and 2.1.

and higher in the cells annealed at 300 and 400 °C. The non-linear trend as a function of temperature corresponds well with the compositional improvement shown by XPS/XRD and the change in open circuit voltage shown in Fig. 3 and 5. These results highlight that the increased open circuit voltage measured for mC-PSC annealed at higher temperatures may be due to a decreased recombination rate.

The spectra were distorted at very high frequencies, with an additional semicircle appearing at the highest illumination intensities. This high frequency response did not change following annealing and we believe it is connected to the carbon contact. This would be expected as all the cells contain a carbon layer of similar thickness which was pre-annealed at 400 °C (Fig. S17 in the ESI† shows the dependence of the resistance extracted from the high frequency response on light intensity and annealing temperature). A third low-frequency (LF) semicircle was observed below 5 Hz, which became more defined for samples processed at higher temperatures. The low frequency response of perovskite solar cells is still hotly debated in the literature and is outside the scope of this paper. A similar low frequency response appeared in the impedance plots of standard planar MAPI cells and they were assigned to changes in the recombination resistance due to the motion of ionic vacancies.[50]

Fig. 7 shows the cross section SEM/EDX images of a C-PSC. In contrast to the mC-PSC, the carbon layer is screen printed on top of the $CsPbBr_3$. Thin layers of c-TiO_2 and $CsPbBr_3$ are both below the thick porous carbon layer, which acts as hole transport material and top contact.

The effect of post-annealing on the planar C-PSC cells was also investigated and the results were compared to those for the mC-PSC. Annealing of C-PSC was carried out after the carbon layer was screen printed on top of the $CsPbBr_3$ absorber layer in order to be consistent with the procedure used for the fabrication of mC-PSC and allow a proper comparison. Each device was systematically annealed at 100, 200, 300 and 400 °C and the same cell re-measured at each of the four temperatures. Fig. 8(a) shows the variation of the main photovoltaic parameters with annealing temperature. Post-annealing treatment at 400 °C is necessary to get high voltage and any performance. The

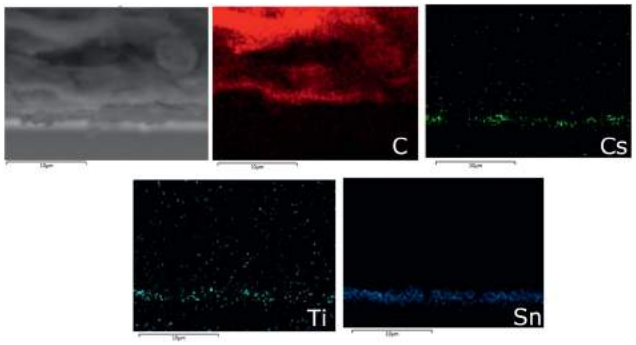

Fig. 7 Cross section SEM/EDX mapping of a C-PSC device. The thin layers of TiO_2 and $CsPbBr_3$ are indicated by light blue and green colour respectively. The thick carbon layer is mapped with the red colour. The blue colour shows the presence of coated FTO on glass.

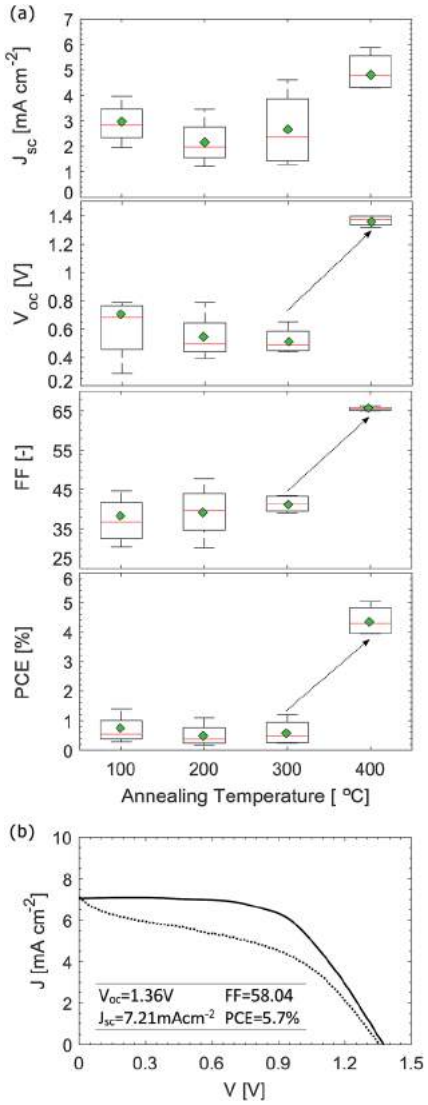

Fig. 8 (a) Box plots of main PV parameters of several C-PSC processed at different temperatures; (b) J–V curves of the champion C-PSC annealed at 400 °C, achieving V_{oc} = 1.36 V, J_{sc} = 7.21 mA cm^{-2}, FF = 58.04 and PCE = 5.7%.

conductivity of the carbon paste at different temperatures was measured using a 4-point probe system (Fig. S18†). The sheet resistance reaches a plateau at about 250 °C. However, the paste is already conducting at 100 °C. Previous TGA and XPS analysis of the sintered carbon paste showed that nitrocellulose binder is entirely eliminated after 400 °C.[24] Baker *et al.* showed that residual non-conductive binder in the carbon layer introduces a band gap at the interface that affects the injection of charges, leading to poor performance.[24] To verify the reproducibility of C-PSC, several batches were fabricated and measured on different days. All cells were made in air with relative humidity (RH) varying between 15 and 40%. The data obtained from 43 devices are shown as box plots in Fig. S19 in the ESI.† Mean and median of all PV parameters have very similar values, indicating that the distribution of data is symmetric. The average open circuit voltage is 1.33 V, with the maximum measured being 1.45 V. Liao *et al.* reported a $CsPbBr_3$ carbon solar cell with a V_{oc} of

1.47 V by depositing quantum dots layers at the ETM/$CsPbBr_3$ and $CsPbBr_3$/HTM interfaces to enhance the charge extraction. In cells with unmodified interfaces a V_{oc} of 1.28 V was reported. In this work, we show that very high voltages can be obtained using $CsPbBr_3$ as absorber material without interface modification.

Fig. 8(b) shows the *J–V* curve of the champion C-PSC, which exhibited $V_{oc} = 1.36$ V, $J_{sc} = 7.21$ mA cm^{-2}, FF = 58.04 and PCE = 5.7% in the reverse direction. The planar device exhibited hysteresis between the two scanning modes, revealing a PCE of 4.2% under forward scan (which leads to an average PCE of 4.95%). Hysteresis in perovskite solar cells is caused by ion migration and the severity of the effect is influenced by the nature of the contact layers.[51,52] Careful selection of the electron transport material can reduce the phenomenon at room temperature. Thin layers of mesoporous TiO_2 between the crystalline perovskite and c-TiO_2 can result in solar cells with low hysteresis.[52,53]

Impedance measurements at open circuit were also carried out on C-PSCs post-annealed at 400 °C. Fig. 9(a) shows the Nyquist plots of a planar carbon cell post-annealed at 400 °C. As above, an additional semi-circle was observed at the highest frequencies which is likely caused by the carbon contact. The semi-circle centred on 2.5 kHz was attributed to C_g and the recombination resistance R_{rec}. The recombination resistance R_{rec} is shown in Fig. 9(b) as a function of V_{oc} and compared to the R_{rec} calculated for a mC-PSC post-annealed at 400 °C. Planar cells show higher R_{rec} than mC-PSC, suggesting that on average planar devices should have lower recombination and higher V_{oc}.

Fig. S21† shows the box plots of the main PV parameters of mC-PSC and C-PSC post-annealed at 400 °C, with the correspondent average values. Only mC-PSC processed at 400 °C were taken into account to allow a proper comparison between the mesoporous and the planar architecture. Overall, C-PSCs show higher open circuit voltage than mC-PSC devices, in agreement with the impedance measurements. On average, an increase of 0.5 V was measured. AFM images showed that $CsPbBr_3$ grains enlarge considerably during the post-annealing treatment, especially at 400 °C. With increasing grain size, trap assisted recombination at the crystallite surface may be reduced and the open circuit voltage improved.[54] In planar devices the growing $CsPbBr_3$ crystallites are less constrained compared to mC-PSCs where the $CsPbBr_3$ is infiltrated in the mesoscopic layers of ZrO_2 and carbon and the matrix is likely to limit the crystallite size.

The average photocurrent is higher in mC-PSC. As reported in previous literature, the morphology of perovskite films strongly influence the performance of C-PSC.[40] At 400 °C the grain size of $CsPbBr_3$ increases and the surface becomes much more rough. High roughness might induce poor contact between the perovskite and the carbon HTM, resulting in a lower photocurrent. In contrast, in mC-PSC the contact between the $CsPbBr_3$ and carbon is expected to be more efficient, as the perovskite material is in intimate contact with the mesoporous layer. However, the photocurrent of the mesoporous devices showed a much wider distribution. Similarly to observations on MAPI graphite-based PSC,[48] the infiltration of $CsPbBr_3$ and right alignment of the perovskite material within the carbon pores are crucial to achieve high photocurrents.

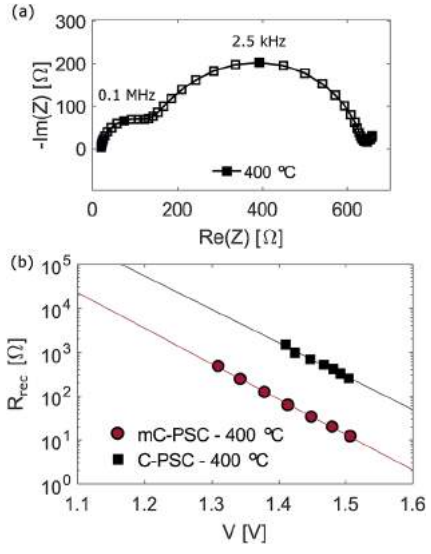

Fig. 9 (a) Example of Nyquist plot of the C-PSC post-annealed at 400 °C measured at open circuit (1.47 V). The response was measured at a light intensity of $\lambda = 465$ nm, 1.47×10^{16} cm^{-2} s^{-1}; (b) recombination resistance for the different type of $CsPbBr_3$ carbon cells at open circuit under different illumination intensities. Slopes of the lines shown are 124 mV per decade for the mC-PSC and 131 mV per decade for the C-PSC, corresponding to ideality factors of 2.1 and 2.2, respectively.

Conclusions

We have investigated planar and mesoporous solar cells using carbon as the hole extraction material and $CsPbBr_3$ as absorber material. All-inorganic $CsPbBr_3$ is much less volatile than the more commonly used organic methylammonium cation, therefore more thermally stable. The properties of $CsPbBr_3$ films were investigated as a function of processing temperature, which was varied between 100 and 400 °C. High temperature annealing was found to be necessary to obtain pure phase materials and a post annealing temperature of 400 °C showed full conversion of the precursor materials $PbBr_2$ and CsBr into $CsPbBr_3$. After post-annealing at 400 °C in air, $CsPbBr_3$ films with larger grains were achieved. XPS analysis suggested that the excess of CsBr decreases (non-linearly) with processing temperature, showing a clear shift to lower amounts of CsBr between 200 and 300 °C. Extra species were present only at 400 °C, suggesting oxidation of the surface and the edge of the process window.

Two different architectures based on different electron transport materials and fabrication methods were compared. mC-PSC devices have a multi-layer screen printed mesoporous stack with $CsPbBr_3$ introduced by infiltration. While in C-PSC a thin film of $CsPbBr_3$ is sandwiched between a compact layer of TiO_2 and a mesoporous thick layer of carbon. The photovoltage of mC-PSC measured from *J–V* curves and the recombination resistance extracted from impedance measurements showed a non-linear trend with processing temperature, with

significant improvements between 200 and 300 °C, corresponding with the compositional improvements observed with XPS. The champion mC-PSC reached a PCE of 8.2% with a remarkable V_{oc} of 1.44 V. C-PSC achieved good performance only when annealed at 400 °C. High temperature processing allows the complete release of non-conductive binder in the thick carbon electrode and higher voltages and FF. The champion C-PSC reached a PCE of 5.7%. Very high V_{oc} were consistently measured on many devices (over 40 cells) fabricated in different batches, with an average of 1.33 V.

This is the first time such high photovoltages have been measured for c-TiO_2/m-TiO_2/m-ZrO_2/m-carbon structure-based cell. Very promising results using $CsPbBr_3$ for solar cell applications have been shown. The possibility of working with fully printable devices that tolerate high temperatures opens up new research to forward the commercialisation of perovskite solar cells.

Conflicts of interest

There are no conflicts to declare.

Acknowledgements

We acknowledge the MAS staff at University of Bath for their assistance in SEM acquisition. I. P., S. E. and P. J. C. would like to thank the EPSRC Centre for Doctoral Training in Sustainable Chemical Technologies (EP/L016354/1). This project has received funding from the European Union's Horizon 2020 research and innovation programme H2020-MSCA-CO-FUND-2014 (# 665992, MSCA FIRE: Fellows with Industrial Research Enhancement). J. B., J. Mc, F. D. R and T. W. would like to thank the Self-Assembling Perovskite Absorbers – Cells Engineered into Modules (SPACE-Modules) (EP/M015254/2) and the SPECIFIC Innovation and Knowledge Centre (EP/N02083/1).

References

1 S. D. Stranks, P. K. Nayak, W. Zhang, T. Stergiopoulos and H. J. Snaith, *Angew. Chem., Int. Ed.*, 2015, **54**, 3240–3248.
2 M. M. Lee, J. Teuscher, T. Miyasaka, T. N. Murakami and H. J. Snaith, *Science*, 2012, **338**, 643–647.
3 H.-S. Kim, C.-R. Lee, J.-H. Im, K.-B. Lee, T. Moehl, A. Marchioro, S.-J. Moon, R. Humphry-Baker, J.-H. Yum, J. E. Moser, M. Grätzel and N.-G. Park, *Sci. Rep.*, 2012, **2**, 591.
4 W. S. Yang, B.-W. Park, E. H. Jung, N. J. Jeon, Y. C. Kim, D. U. Lee, S. S. Shin, J. Seo, E. K. Kim, J. H. Noh and S. I. Seok, *Science*, 2018, **356**, 1376–1379.
5 K. Domanski, J. P. Correa-Baena, N. Mine, M. K. Nazeeruddin, A. Abate, M. Saliba, W. Tress, A. Hagfeldt and M. Grätzel, *ACS Nano*, 2016, **10**, 6306–6314.
6 N. L. Chang, A. W. Yi Ho-Baillie, P. A. Basore, T. L. Young, R. Evans and R. J. Egan, *Prog. Photovoltaics*, 2017, **25**, 390–405.
7 V. Mirruzzo and A. Di Carlo, *Chem*, 2017, **2**, 612–613.
8 A. Abate, T. Leijtens, S. Pathak, J. Teuscher, R. Avolio, M. E. Errico, J. Kirkpatrik, J. M. Ball, P. Docampo, I. McPherson and H. J. Snaith, *Phys. Chem. Chem. Phys.*, 2013, **15**, 2572.
9 I. Lee, J. H. Yun, H. J. Son and T.-S. Kim, *ACS Appl. Mater. Interfaces*, 2017, **9**, 7029–7035.
10 D. Bi, G. Boschloo and A. Hagfeldt, *Nano*, 2014, **09**, 1440001.
11 W. A. Laban and L. Etgar, *Energy Environ. Sci.*, 2013, **6**, 3249.
12 S. D. Stranks, S. D. Stranks, G. E. Eperon, G. Grancini, C. Menelaou, M. J. P. Alcocer, T. Leijtens, L. M. Herz, A. Petrozza and H. J. Snaith, *Science*, 2014, **342**, 341–344.
13 Z. Ku, Y. Rong, M. Xu, T. Liu and H. Han, *Sci. Rep.*, 2013, **3**, 3132.
14 A. Mei, X. Li, L. Liu, Z. Ku, T. Liu, Y. Rong, M. Xu, M. Hu, J. Chen, Y. Yang, M. Gratzel and H. Han, *Science*, 2014, **345**, 295–297.
15 L. Zhang, T. Liu, L. Liu, M. Hu, Y. Yang, A. Mei and H. Han, *J. Mater. Chem. A*, 2015, **3**, 9165–9170.
16 H. N. Chen, Z. H. Wei, H. X. He, X. L. Zheng, K. S. Wong and S. H. Yang, *Adv. Energy Mater.*, 2016, **6**, 1502087.
17 H. Zhang, H. Wang, S. T. Williams, D. Xiong, W. Zhang, C. C. Chueh, W. Chen and A. K. Jen, *Adv. Mater.*, 2017, **29**, 1606608.
18 H. Hu, B. Dong and W. Zhang, *J. Mater. Chem. A*, 2017, **5**, 11436–11449.
19 Y. Hu, Z. Zhang, A. Mei, Y. Jiang, X. Hou, Q. Wang and K. Du, *Adv. Mater.*, 2018, **30**, 1705786.
20 Y. Rong, X. Hou, Y. Hu, A. Mei, L. Liu, P. Wang and H. Han, *Nat. Commun.*, 2017, **33**, 647–648.
21 G. Grancini, I. Zimmermann, E. Mosconi, D. Martineau and S. Narbey, *Nat. Commun.*, 2017, **8**, 1–8.
22 S. Liu, W. Huang, P. Liao, N. Pootrakulchote, H. Li, J. Lu, J. Li, F. Huang, X. Shai, X. Zhao, Y. Shen, Y. B. Cheng and M. Wang, *J. Mater. Chem. A*, 2017, **5**, 22952–22958.
23 F. Matteocci, L. Cinà, E. Lamanna, S. Cacovich, G. Divitini, P. A. Midgley, C. Ducati and A. Di Carlo, *Nano Energy*, 2016, **30**, 162–172.
24 J. Baker, K. Hooper, S. Meroni, A. Pockett, J. McGettrick, Z. Wei, R. Escalante, G. Oskam, M. Carnie and T. Watson, *J. Mater. Chem. A*, 2017, **5**, 18643–18650.
25 S. M. Meroni, Y. Mouhamad, F. De Rossi, A. Pockett, J. Baker, R. Escalante, J. Searle, M. J. Carnie, E. Jewell, G. Oskam and T. M. Watson, *Sci. Technol. Adv. Mater.*, 2018, **19**, 1–9.
26 F. De Rossi, J. Baker, D. Beyon, K. Hooper, S. Meroni, D. Williams, Z. Wei, A. Yasin, C. Charbonneau, E. Jewell and T. M. Watson, *Adv. Mater. Technol.*, 2018, 1800156.
27 S. Ryu, J. H. Noh, N. J. Jeon, Y. Chan Kim, W. S. Yang, J. Seo and S. I. Seok, *Energy Environ. Sci.*, 2014, **7**, 2614–2618.
28 P. Sullivan, S. Schumann, R. Da Campo, T. Howells, A. Duraud, M. Shipman, R. A. Hatton and T. S. Jones, *Adv. Energy Mater.*, 2013, **3**, 239–244.
29 W. S. dos Santos, M. Rodriguez, J. M. Khoury, L. A. Nascimento, R. J. Ribeiro, J. P. Mesquita, A. C. Silva, F. G. Nogueira and M. C. Pereira, *ChemSusChem*, 2018, **11**, 589–597.
30 M. Saliba, T. Matsui, J.-Y. Seo, K. Domanski, J.-P. Correa-Baena, M. K. Nazeeruddin, S. M. Zakeeruddin, W. Tress, A. Abate, A. Hagfeldt and M. Grätzel, *Energy Environ. Sci.*, 2016, **9**, 1989–1997.

31 B. Li, Y. Zhang, L. Fu, T. Yu, S. Zhou, L. Zhang and L. Yin, *Nat. Commun.*, 2018, **9**, 1–8.
32 B. Jeong, H. Han, Y. J. Choi, S. H. Cho, E. H. Kim, S. W. Lee, J. S. Kim, C. Park, D. Kim and C. Park, *Adv. Funct. Mater.*, 2018, **28**, 1–8.
33 L. Yan, Q. Xue, M. Liu, Z. Zhu, J. Tian, Z. Li, Z. Chen, Z. Chen, H. Yan, H.-L. Yip and Y. Cao, *Adv. Mater.*, 2018, 1802509.
34 R. E. Beal, D. J. Slotcavage, T. Leijtens, A. R. Bowring, R. A. Belisle, W. H. Nguyen, G. F. Burkhard, E. T. Hoke and M. D. McGehee, *J. Phys. Chem. Lett.*, 2016, **7**, 746–751.
35 M. Kulbak, D. Cahen and G. Hodes, *J. Phys. Chem. Lett.*, 2015, **6**, 2452–2456.
36 M. Kulbak, S. Gupta, N. Kedem, I. Levine, T. Bendikov, G. Hodes and D. Cahen, *J. Phys. Chem. Lett.*, 2016, **7**, 167–172.
37 J. Lei, F. Gao, H. Wang, J. Li, J. Jiang, X. Wu, R. Gao, Z. Yang and S. Liu, *Sol. Energy Mater. Sol. Cells*, 2018, **187**, 1–8.
38 C. C. Stoumpos, C. D. Malliakas, J. A. Peters, Z. Liu, M. Sebastian, J. Im, T. C. Chasapis, A. C. Wibowo, D. Y. Chung, A. J. Freeman, B. W. Wessels and M. G. Kanatzidis, *Cryst. Growth Des.*, 2013, **13**, 2722–2727.
39 J. Liang, C. Wang, Y. Wang, Z. Xu, Z. Lu, Y. Ma, H. Zhu, Y. Hu, C. Xiao, X. Yi, G. Zhu, H. Lv, L. Ma, T. Chen, Z. Tie, Z. Jin and J. Liu, *J. Am. Chem. Soc.*, 2016, **138**, 15829–15832.
40 X. Chang, W. Li, L. Zhu, H. Liu, H. Geng, S. Xiang, J. Liu and H. Chen, *ACS Appl. Mater. Interfaces*, 2016, **8**, 33649–33655.
41 Z. Liu, B. Sun, X. Liu, J. Han, H. Ye, T. Shi, Z. Tang and G. Liao, *Nano-Micro Lett.*, 2018, **10**, 34.
42 G. Liao, J. Duan, Y. Zhao and Q. Tang, *Sol. Energy*, 2018, **171**, 279–285.
43 H. Yuan, Y. Zhao, J. Duan, B. He, Z. Jiao and Q. Tang, *Electrochim. Acta*, 2018, **279**, 84–90.
44 Q. A. Akkerman, M. Gandini, F. Di Stasio, P. Rastogi, F. Palazon, G. Bertoni, J. M. Ball, M. Prato, A. Petrozza and L. Manna, *Nat. Energy*, 2017, **2**, 1–7.
45 N. K. Kumawat, N. Jain, A. Dey, K. L. Narasimhan and D. Kabra, *Adv. Funct. Mater.*, 2017, **27**, 1603219.
46 S. Ahmad and G. V. Prakash, *Opt. Mater. Express*, 2014, **4**, 101.
47 Lovkush, C. Ravikant, P. Arun and K. Kumar, *Mater. Res. Express*, 2016, **3**, 076403.
48 L. Wagner, L. E. Mundt, G. Mathiazhagan, M. Mundus, M. C. Schubert, S. Mastroianni, U. Würfel, A. Hinsch and S. W. Glunz, *Sci. Rep.*, 2017, **7**, 1–6.
49 A. Pockett, G. E. Eperon, T. Peltola, H. J. Snaith, A. B. Walker, L. M. Peter and P. J. Cameron, *J. Phys. Chem. C*, 2015, **119**, 3456–3465.
50 A. Pockett, G. E. Eperon, N. Sakai, H. J. Snaith, L. M. Peter and P. J. Cameron, *Phys. Chem. Chem. Phys.*, 2017, **19**, 5959–5970.
51 H. J. Snaith, A. Abate, J. M. Ball, G. E. Eperon, T. Leijtens, N. K. Noel, S. D. Stranks, J. T. W. Wang, K. Wojciechowski and W. Zhang, *J. Phys. Chem. Lett.*, 2014, **5**, 1511–1515.
52 S. V. Reenen, M. Kemerink and H. J. Snaith, *J. Phys. Chem. Lett.*, 2015, **6**, 3808–3814.
53 W. S. Yang, J. H. Noh, N. J. Jeon, Y. C. Kim, S. Ryu, J. Seo and S. I. Seok, *Science*, 2015, **348**, 1234–1237.
54 H. D. Kim, H. Ohkita, H. Benten and S. Ito, *Adv. Mater.*, 2016, **28**, 917–922.

Supporting Information for

Screen printed carbon $CsPbBr_3$ solar cells with high open-circuit photovoltage

Isabella Poli,[a b] * *Jenny Baker,*[c] *James McGettrick,*[c] *Francesca De Rossi,*[c] *Salvador Eslava,*[d b] *Trystan Watson,*[c] *and Petra J. Cameron*[a b] *

[a] *Department of Chemistry, University of Bath, Bath BA2 7AY, United Kingdom*

[b] *Centre for Sustainable Chemical Technologies, University of Bath, Bath BA2 7AY, United Kingdom*

[c] *SPECIFIC, Swansea University Bay Campus, Fabian Way, Swansea, SA1 8EN, United Kingdom*

[d] *Department of Chemical Engineering, University of Bath, Bath BA2 7AY, United Kingdom*

Experimental

All data created during this research are openly available from the University of Bath data archive at https://doi.org/10.15125/BATH-00530.

Device fabrication The screen printed mesoporous stacks used in this work were fabricated at SPECIFIC, University of Swansea. The perovskite $CsPbBr_3$ was then infiltrated and cells characterized at University of Bath. Planar devices were fully fabricated in Bath. Both types of cells contained spray pyrolysis titania blocking layers which were deposited using slightly different techniques according to the optimum procedure in each lab.

EIS theory Impedance measurements at open circuit at different illumination intensity were carried out on both mC-PSC and C-PSC.

At all intensities three semi-circles were seen in the Nyquist plots. We believe that the impedance response observed at high frequency is associated to the carbon contact (C_{hf} and R_{hf}). C_g is the geometric capacitance which is voltage-dependent. The parallel resistance that accompanies C_g is attributed to the recombination resistance R_{rec}. Previous studies have shown that the chemical capacitance associated to the photogenerated electrons and holes in the perovskite layer is negligible [1].

Recombination is represented by the voltage-dependent recombination resistance R_{rec}, defined by

$$R_{rec} = (\frac{\delta V}{\delta j_{rec}}) \tag{1}$$

where, J_{rec} is the recombination current density. The variation of the R_{rec} with voltage can be related to the ideality factor m of the device using

$$\frac{\delta log R_{rec}}{\delta V} = -\frac{q}{2.303 m k_B T} \tag{2}$$

where q is the elementary charge, k_B is the Boltzmann constant and T is the temperature.

Optical properties First, we wanted to check the thermal stability of $CsPbBr_3$ at 400 °C by measuring the optical properties of a film before and after annealing treatment at 400 °C. Fig. S1(a) shows the UV-Vis absorption spectrum of $CsPbBr_3$ before and after post-annealing treatment at 400 °C. For comparison, the absorption spectra of $MAPbI_3$ are also shown. The absorption window of $CsPbBr_3$ does not change with the annealing treatment, showing high thermal stability. In contrast, $MAPbI_3$ completely evaporates. $CsPbBr_3$ has an absorption onset of 530 nm, which corresponds to an energy bandgap of 2.35 eV, as confirmed by the Tauc plot showed in Fig. S1(b).

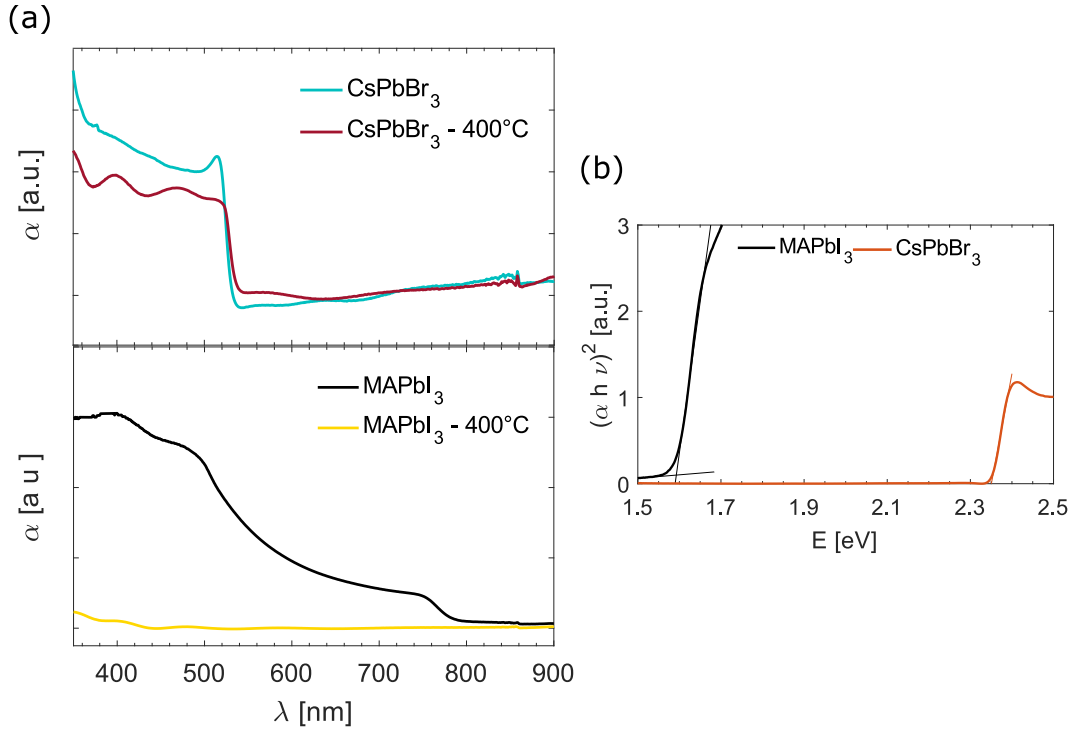

Fig. S1: (a) Absorption spectra of $CsPbBr_3$ and $MAPbI_3$ thin films before and after annealing treatment at 400 °C; (b) Tauc plot of MAPI and $CsPbBr_3$ films. The energy bandgap values measured through the intercepts with the x is are 1.58 and 2.35 eV respectively

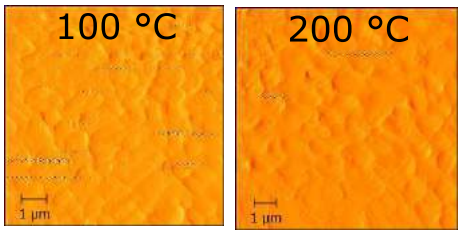

Fig. S2: AFM amplitude images of $CsPbBr_3$ films annealed at 100 and 200 °C respectively

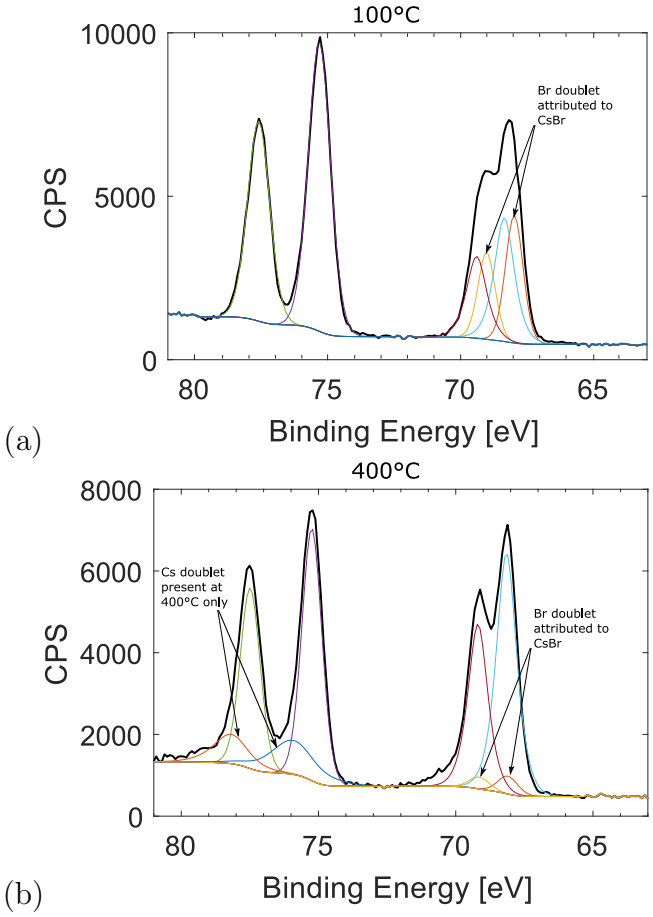

Fig. S3: High resolution XPS spectra of CsPbBr3 films processed at 100 °C (a) and 400 °C (b) for Cs(4d) and Br(3d). CsBr content decreases with temperature. A higher binding energy component appears on the Cs(4d) spectrum when the film is processed at 400 °C, suggesting that the material is close to the edge of its process window. This extra component is consistent with loss of electron density from the Cs atoms and hence possible oxidation of the material. Notably, the peaks present after annealing at 400 °C are sharper than the ones measured for the film annealed at 100 °C. The sharp peaks indicate less complex chemistry, as the contribution from CsBr to the Br(3d) envelope drops, the FWHM of the Cs(4d5/2) peak also drops from 0.97 eV to 0.87 eV, and the FWHM of Pb(4f7/2) peak also drops from 1.00 to 0.81 eV

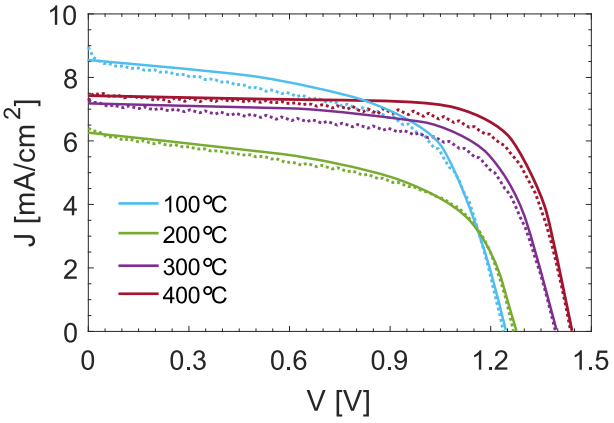

Fig. S4: JV curves of 4 different mC-PSC fabricated in the same batch and each one post-annealed at a different temperature (100, 200, 300 and 400 °C)

JV curves m-PSC JV curves of an average performing mC-PSC are shown in Fig. S5(a). The main PV parameters and the curves measured under forward scan are shown in Table S1 and Fig. S6. The same device was systematically annealed at 100, 200, 300 and 400 °C and tested after each temperature. Four different batches were measured following this procedure. This experiment allowed us to monitor the variation of main PV parameters on the same device as a function of the post-annealing temperature. The PV parameters that mainly change with temperature are the open circuit voltage and the fill factor. The V_{oc} trend with temperature is shown in Fig. S5(b). Box plots of the other PV parameters are shown in Fig. S7. The V_{oc} increases with annealing temperature, while the FF drops-off. Voltage and fill factor compensate each other and the PCE does not change considerably with annealing temperature.

Table S1: Average PV parameters for $CsPbBr_3$ mC-PSC showed in Fig. S6

Parameter	**100**	**200**	**300**	**400**
$\mathbf{J_{sc}}$ **[mA/cm2]**	6.78	6.73	6.58	6.67
$\mathbf{V_{oc}}$ **[V]**	1.21	1.24	1.29	1.35
FF [-]	55.14	59.31	52.79	48.29
PCE [%]	4.53	4.96	4.47	4.35

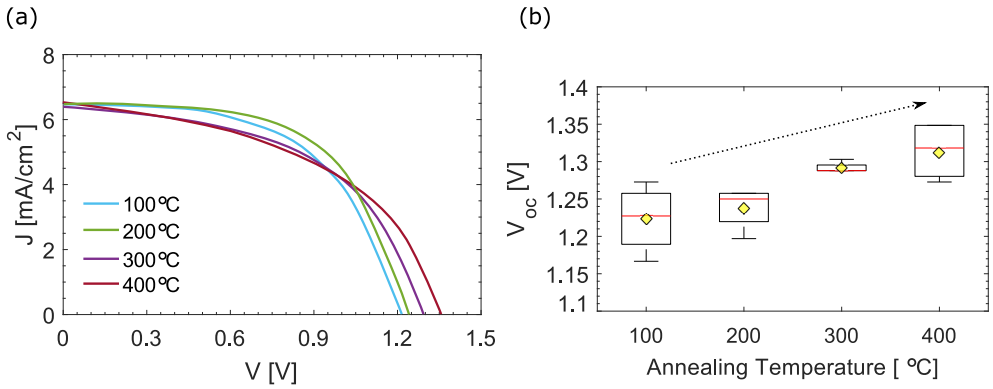

Fig. S5: (a) JV curves of an average performing mC-PCS post annealed at different temperatures; The device with the highest open circuit voltage was post-annealed at 400 °C and exhibited V_{oc}=1.35 V, J_{sc}=7.7 mA cm^{-2}, FF=50.5 and PCE=5.2 %. The most efficient cell was annealed at 200 °C and exhibited V_{oc}=1.26 V, J_{sc}=7.6 mA cm^{-2}, FF=58.7 and PCE=5.6 %.(b) Box-plots of V_{oc} of mC-PSC annealed at different temperatures

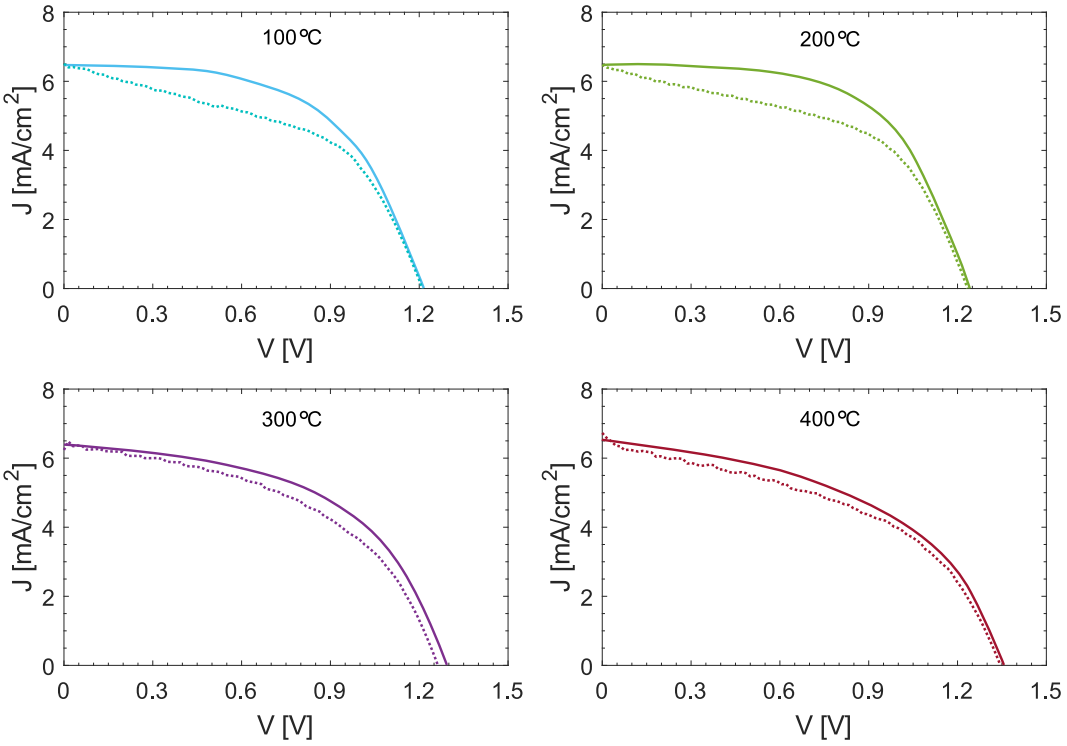

Fig. S6: Forward and reverse scans of a mC-PSC systematically processed at different temperatures (JV curves measured after each annealing step)

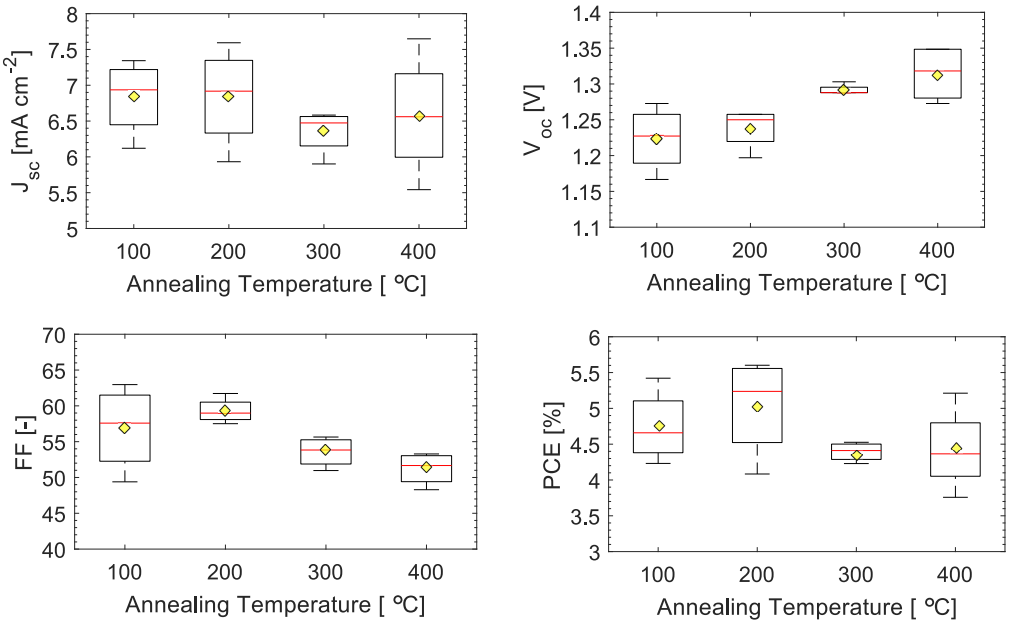

Fig. S7: Box plots of main photovoltaic parameters of mC-PSC. Each cell was sistematically annealed at 100, 200, 300 and 400 °C and measured after each temperature

EQE of mC-PSC Very little changes in photocurrent were observed with post-annealing temperature. This results is further confirmed by the external quantum efficiency (EQE) measurements shown in Fig. S8. The integrated photocurrent of samples processed at different temperatures does not considerably change and very similar short circuit current values are achieved. The EQE spectrum of the sample processed at 400 °C shows lower intensities at 300-350 nm. This can be related to partly oxidation of the $CsPbBr_3$ material due to fast heating that might have damaged the mesescopic layers TiO_2 and ZrO_2.

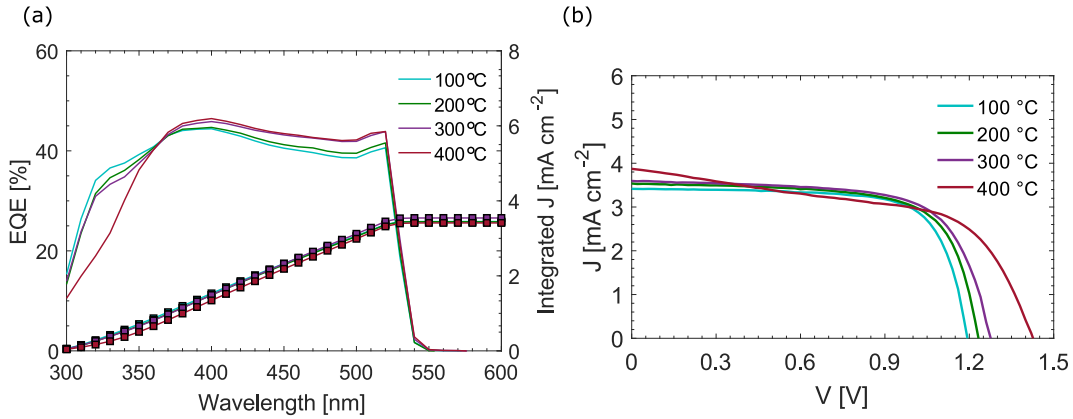

Fig. S8: (a) EQE spectra and integrated current of 4 different mC-PSC devices post-annealed at different temperature after fabrication; (b) JV curves of the mC-PSC devices tested for EQE spectra acquisition

mC-PSC annealed at 350 °C XPS analysis showed that when processing $CsPbBr_3$ films at 400 °C, sometimes oxidation of the material occurred, indicating that the material is close to the edge of its processing window. This phenomenon may be more or less pronounced due to small changes in the annealing temperature and heating and cooling time which may lead to more evident losses in the FF. When processed at an intermediate temperature between 300 and 400 °C, such as 350 °C, the infiltrated $CsPbBr_3$ remains homogeneously yellow through the carbon layer and no sign of clear oxidation is observed. Fig. S9 shows the (a) JV curve of a mC-PSC post-annealed at 350 °C and the (b) stabilised power output measurement over 60 s. The cell was biased to the maximum power point voltage determined by the JV sweep, which is 1.11 V.

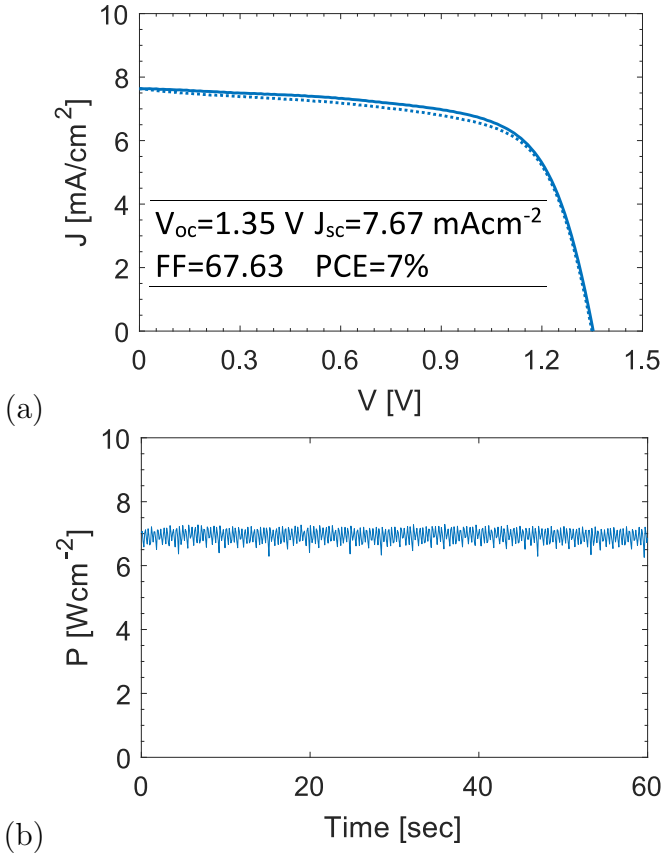

Fig. S9: (a) JV curve of a mC-PSC post-annealed at 350 °C; (b) Stabilised power output measurement over 60 s

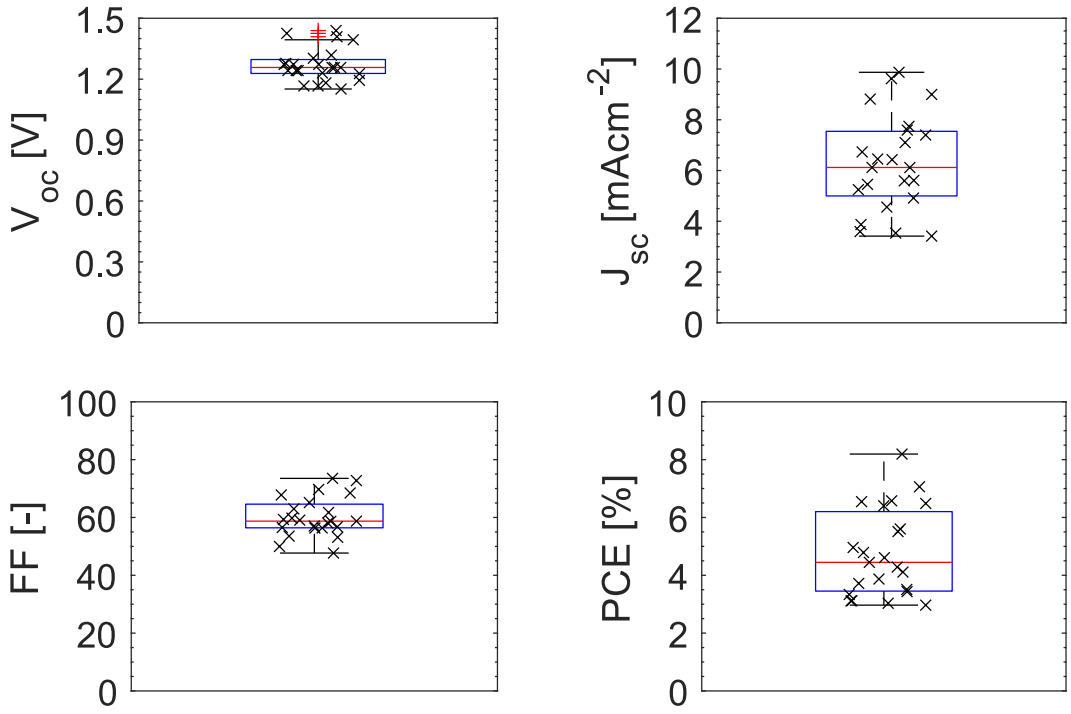

Fig. S10: Box plots of main photovoltaic parameters of mC-PSC post-annealed at 400 °C. Over 20 devices fabricated in different batches were measured

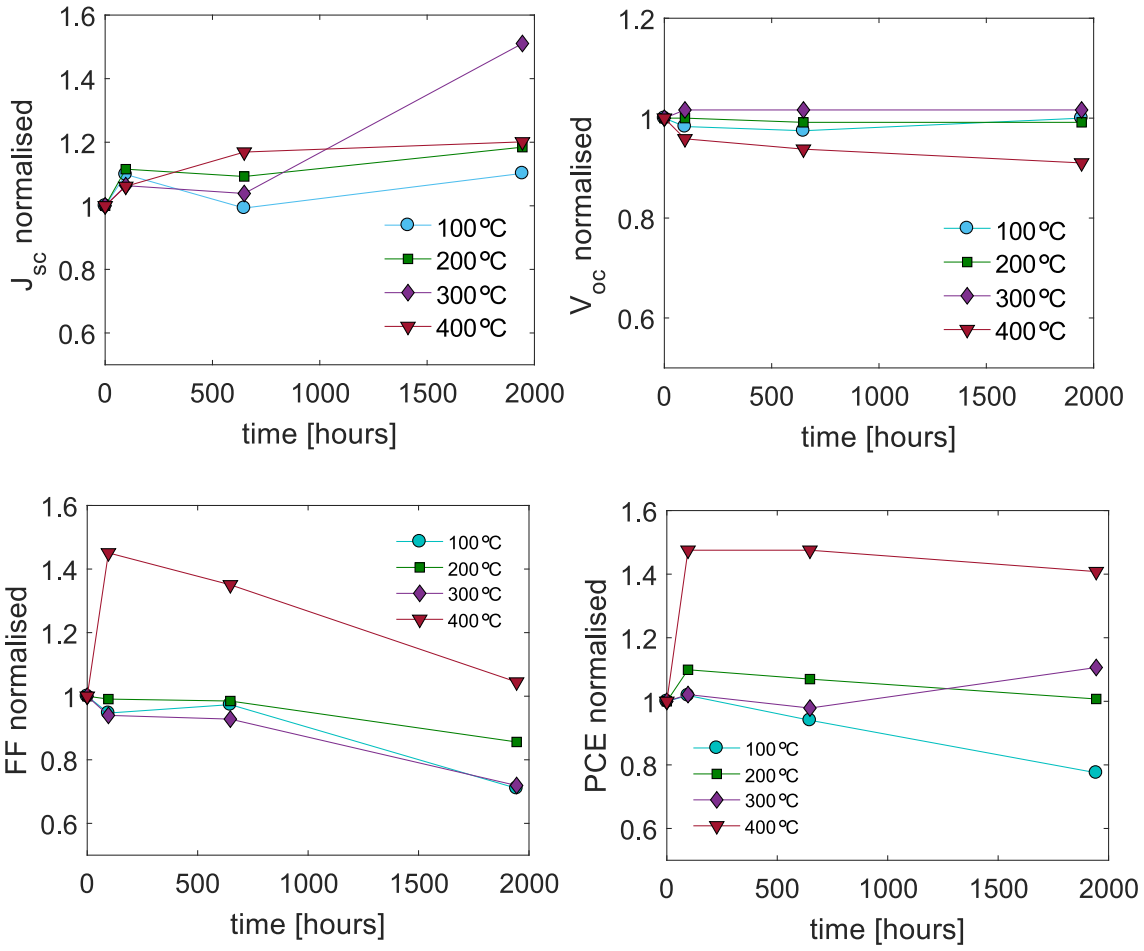

Fig. S11: Variation of the main photovoltaic parameters of mC-PSC annealed at different temperatures overtime. During this time the cells were left in an ambient atmosphere without encapsulation, in the dark, at open circuit (also known as shelf-stability)

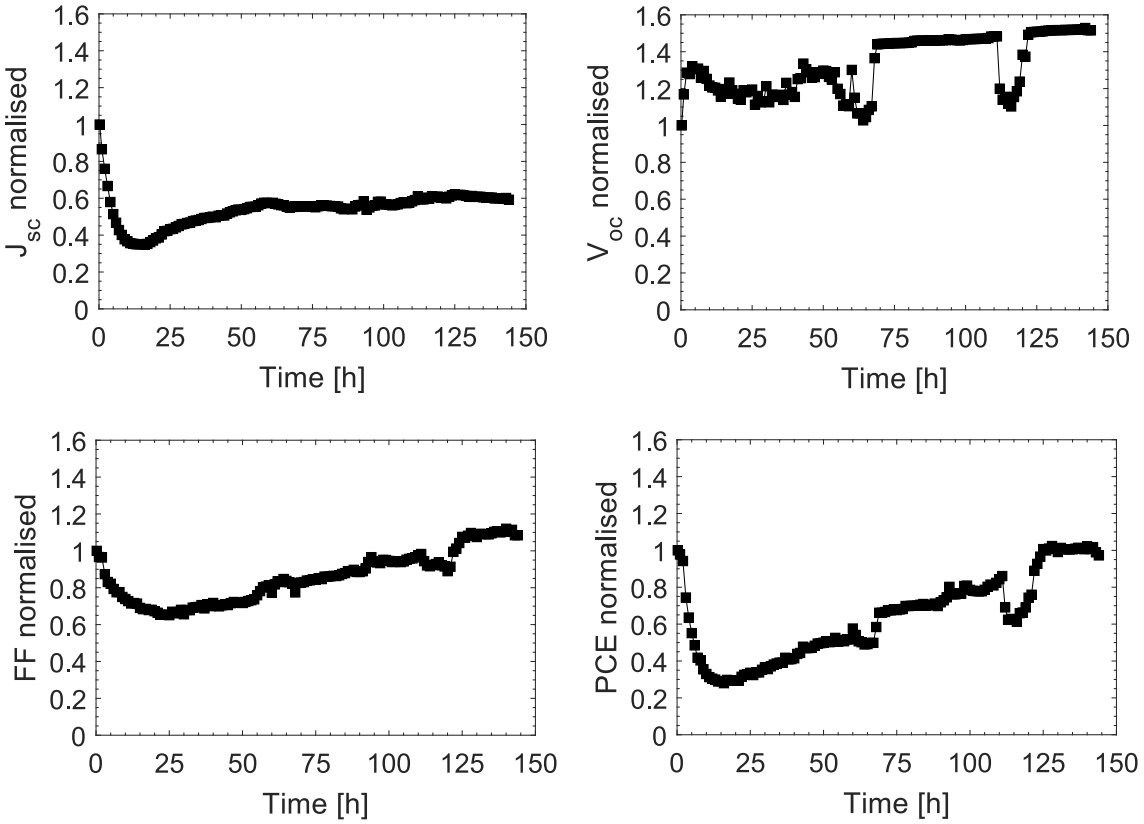

Fig. S12: Variation of the main photovoltaic parameters of a mC-PSC overtime. During this time the unencapsulated cell was monitored under continuous illumination, at short circuit conditions and HR of 50 %

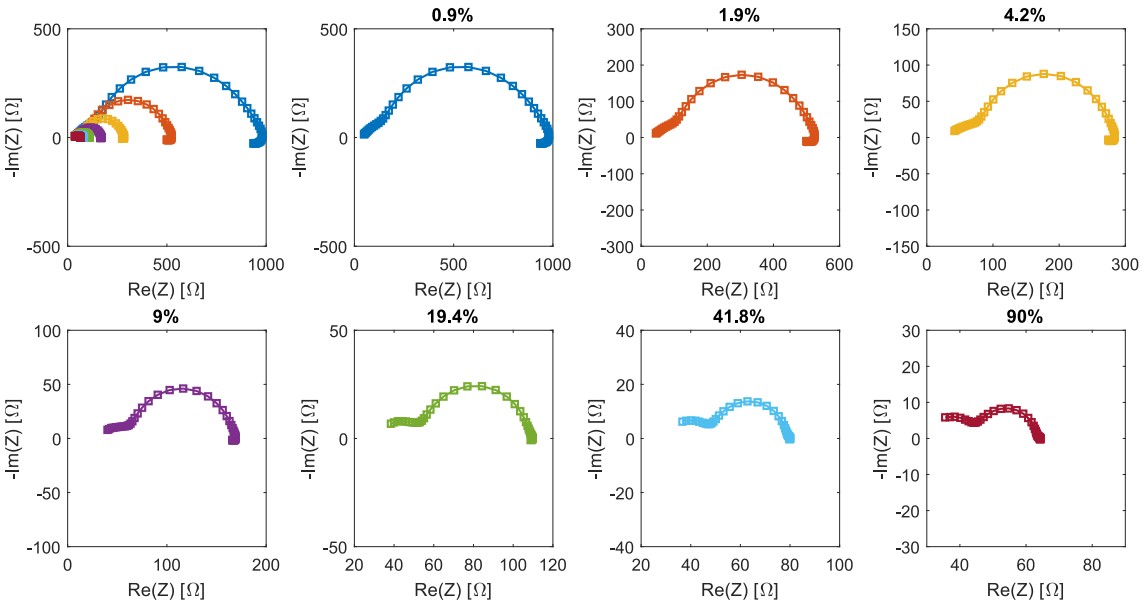

Fig. S13: Nyquist plots measured at open circuit under different illumination intensities for a mC-PSC device post-annealed at 100 °C

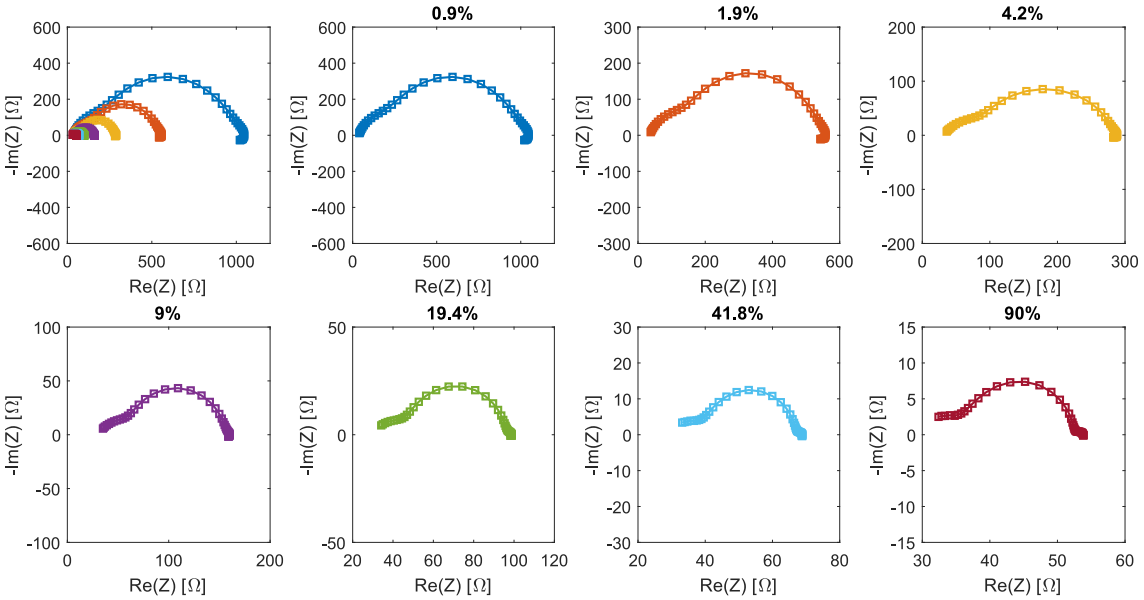

Fig. S14: Nyquist plots measured at open circuit under different illumination intensities for a mC-PSC device post-annealed at 200 °C

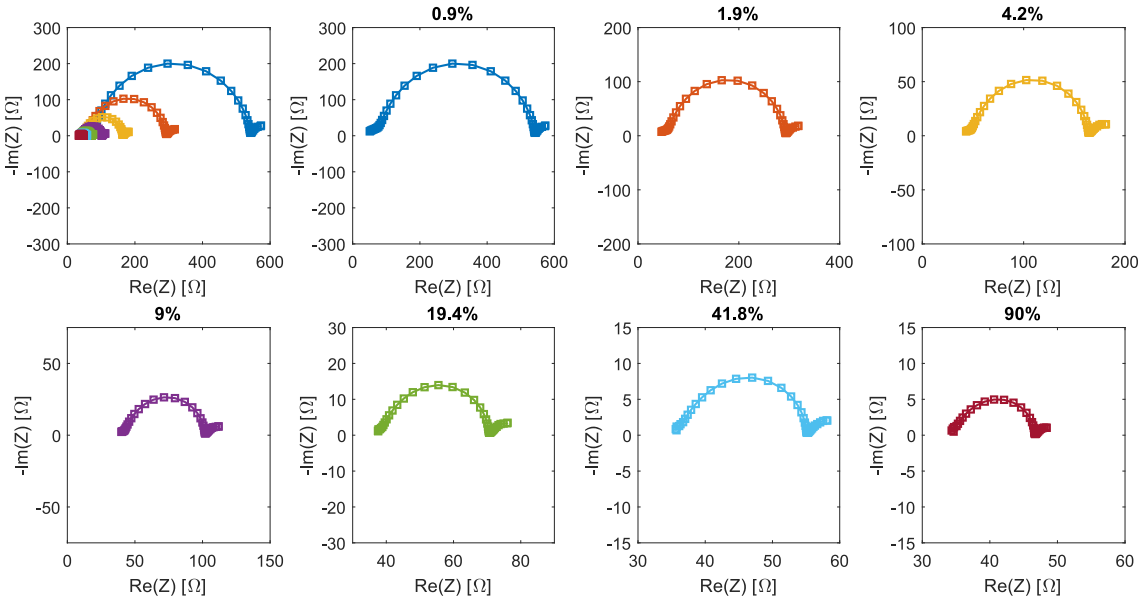

Fig. S15: Nyquist plots measured at open circuit under different illumination intensities for a mC-PSC device post-annealed at 300 °C

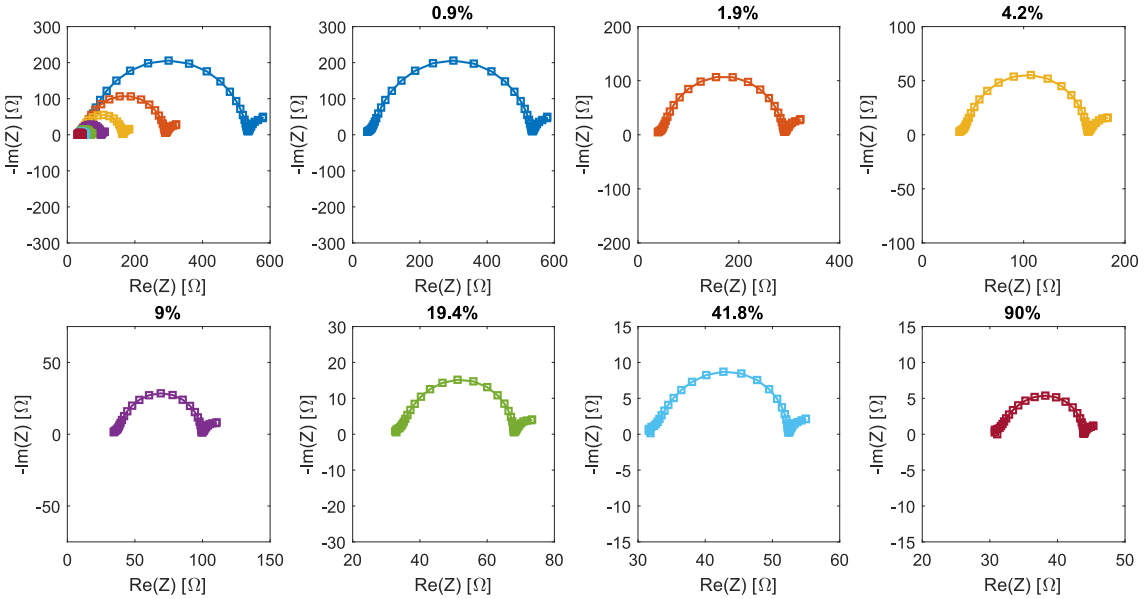

Fig. S16: Nyquist plots measured at open circuit under different illumination intensities for a mC-PSC device post-annealed at 400 °C

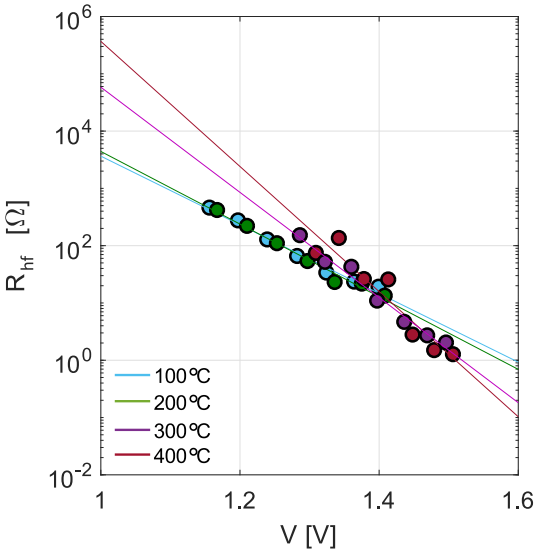

Fig. S17: High frequency recombination obtained by fitting the HF semicircle of EIS measured at open circuit at different illumination intensities of mC-PSC post-annealed at different temperatures

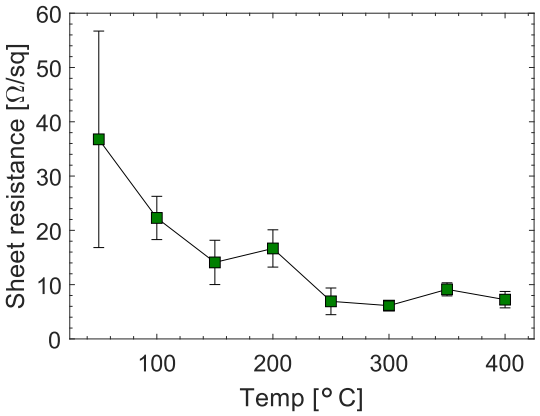

Fig. S18: Sheet resistance of a film of carbon paste measured with a 4-point probe. The resistance was measured after annealing the carbon film at different temperatures

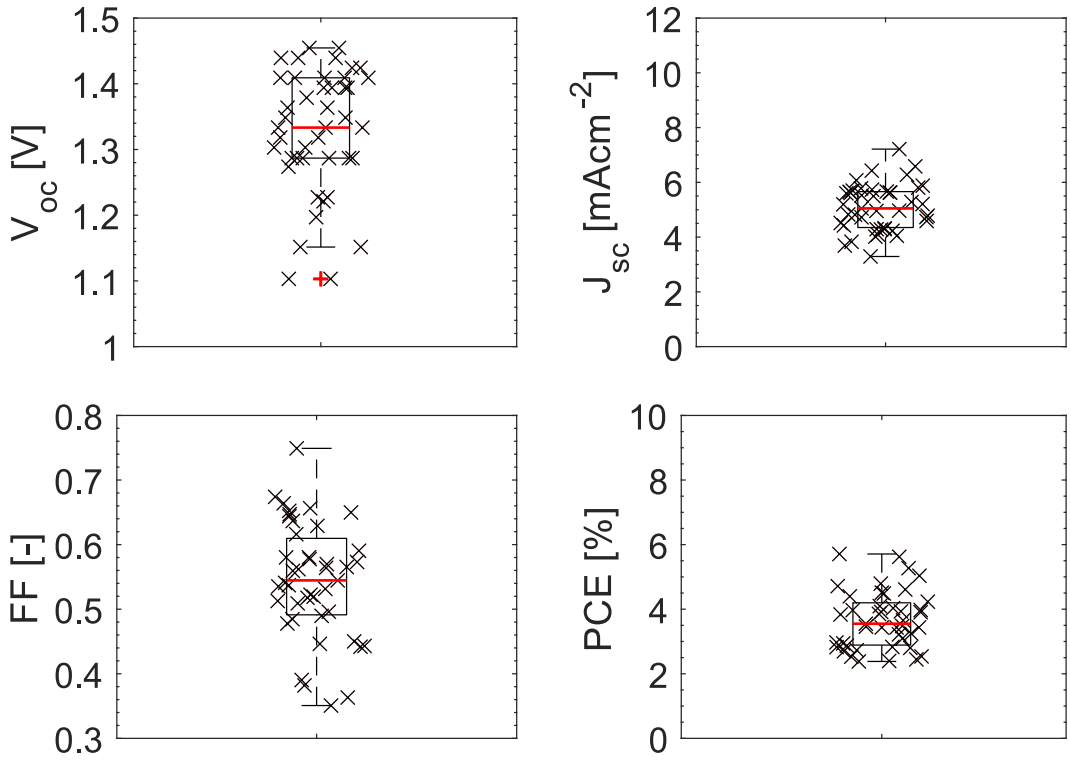

Fig. S19: Box plots of main photovoltaic parameters of C-PSC annealed at 400 °C. Over 40 devices were fabricated in different batches and measured in different days

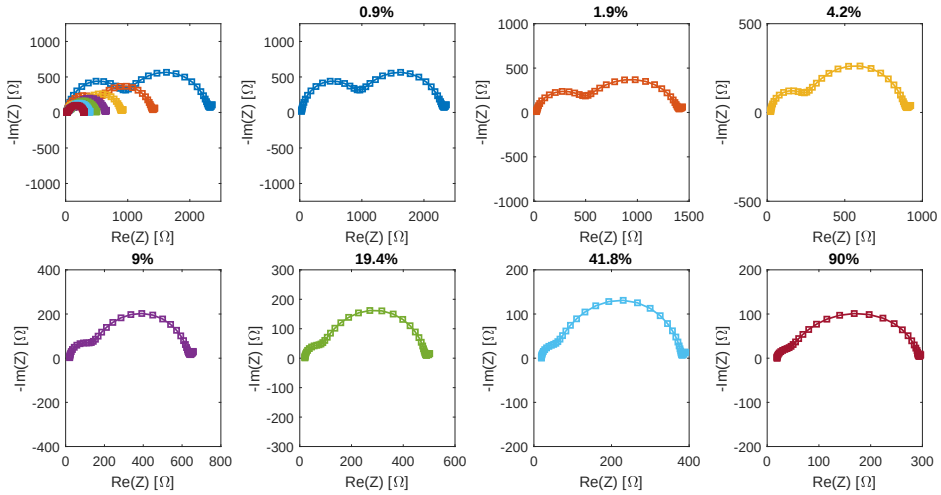

Fig. S20: Nyquist plots measured at open circuit under different illumination intensities for a C-PSC device post-annealed at 400 °C

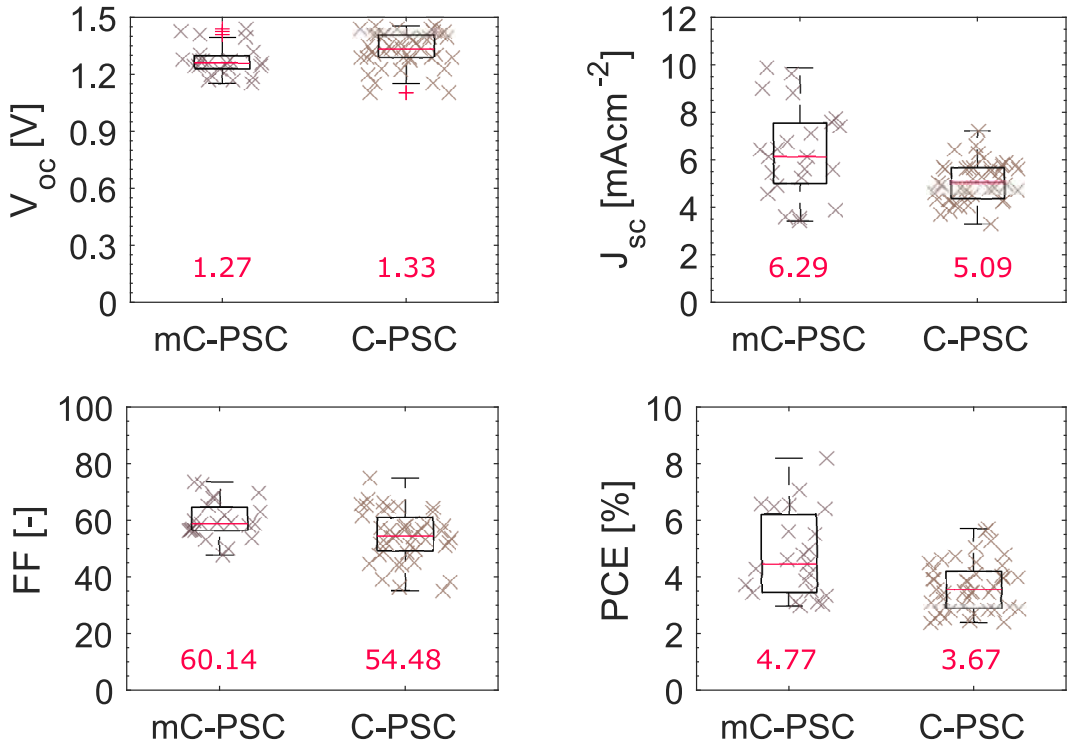

Fig. S21: Box plots of the main PV parameters measured for mC-PSC and C-PSC processed at 400 °C. All devices have been measured under 1 sun with active area of 0.25 cm^2

Bibliography

[1] A. Pockett, G. E. Eperon, T. Peltola, H. J. Snaith, A. B. Walker, L. M. Peter, and P. J. Cameron, "Characterization of Planar Lead Halide Perovskite Solar Cells by Impedance Spectroscopy, Open Circuit Photovoltage Decay and Intensity-Modulated Photovoltage/Photocurrent Spectroscopy," *The Journal of Physical Chemistry C*, vol. 119, no. 7, pp. 3456–3465, 2015.

5.2.3 Contemporary assessment

The paper 'Screen printed carbon $CsPbBr_3$ solar cells with high open-circuit photovoltage' by Poli *et al.* demonstrated for the first time the fabrication of fully-printed mesoporous carbon $CsPbBr_3$ solar cells. [39] The reported mC-PSC with the typical structure TiO_2/ZrO_2/carbon infiltrated with $CsPbBr_3$ achieved the highest open-circuit voltage ($1.44\,\mathrm{V}$) reported with such architecture.

In the publication, we showed that the highest photovoltage was achieved in devices post-annealed at $400\,^{\circ}\mathrm{C}$, however XPS characterisation suggested that such thermal treatment in air may have caused oxidation of the $CsPbBr_3$ surface. In order to avoid oxidation of the material but still allowing high photovoltages, $CsPbBr_3$ films have been later processed at $380\,^{\circ}\mathrm{C}$.

Few months before our publication, Duan *et al.* reported the fabrication of $CsPbBr_3$ planar carbon cells with graphene quantum dots and ternary $CuInS_2/ZnS$ quantum dots deposited at the $TiO_2/CsPbBr_3$ and $CsPbBr_3$/carbon interface, respectively to achieve cells with V_{oc} as high as $1.522\,\mathrm{V}$. [40] Right after the publication of our work, the same group published a $CsPbBr_3$ carbon solar cell with even higher photovoltages. The $CsPbBr_3$ absorber material was sandwiched between the ETM (TiO_2) and the HTM (carbon) and Pb was partly substituted with lanthanide ions. When 3mol% Sm was incorporated in the perovskite crystal structure, solar cells with an impressive V_{oc} of $1.594\,\mathrm{V}$ were achieved. [41]

The paper by Poli *et al.* showed that the average photocurrent density measured in mesoporous carbon devices was higher than the one measured in planar carbon cells, but with much wider distribution. Very recently, our collaborators Dr Trystan Watson *et al.* from SPECIFIC reported an extensive study on the penetration of material and spatial device uniformity in triple mesoscopic carbon solar cells. In order to gain a full picture of the infiltration of perovskite through the stack and its effect on PV parameters, they combined multi-mapping techniques, such as photoluminescence (PL), electroluminescence (EL), Raman and photocurrent mapping, with cross-sectional SEM characterisation. [42] They observed that the penetration of $MAPbI_3$ perovskite via two-step method (similar to the one used for $CsPbBr_3$) was much more complex than the one-step process, leading to much stronger discontinuities in perovskite through the cell volume. Indeed, isolated grains separated by areas with low concentration of perovskite were mapped. In contrast, one-step infiltration was shown to achieve homogeneous and almost full infiltration (up to $98\,\%$ of the cell's area using $MAPbI_3$+5AVA solution). The photocurrent map in two-step infiltrated cells revealed large variations in photocurrent across the cell area. Moreover, it was also observed that dense microscale carbon flakes could prevent perovskite infiltration in some areas, affecting light collection and the generated photocurrent.

Gratzel *et al.* recently reported a detailed study on the kinetics of perovskite formation in sequential deposition techniques. In the latter study it was found that

unconverted PbI_2 was present in the mesoporous layer. [43] It is possible that unreacted $PbBr_2$ is also present in the mC-PSC cells reported in our study (with $\sim 15\,\mu m$ thick mesoporous layers), reducing the converted materials and the absorption of light. The low predictability of this phenomenon may explain the large variability of results reported by Poli *et al.*

5.3 Chapter conclusions

Fully inorganic $CsPbX_3$ perovskite materials are more stable towards moisture and heat due to the use of less volatile and more robust Cs^+ as central cation in the perovskite structure. While the black-phase of $CsPbI_3$ is highly unstable at room temperature, $CsPbBr_3$ has a stable orthorombic structure at room temperature. $CsPbBr_3$ has a wide bandgap of $2.35\,eV$, it has a yellow colour, and it can be stable up to $550\,°C$ under a N_2 environment. Two-step solution-based deposition techniques generated films with good absorption and coverage and complete conversion of precursor materials was achieved after post-annealing treatment at $400\,°C$. Solar cells with the standard architecture $TiO_2/CsPbBr_3/Spiro\text{-}OMeTAD/Au$ achieved average PCEs of $3.5\,\%$ and open-circuit voltages as high as $1.35\,V$.

One of the degradation mechanisms of perovskite solar cells is the reaction of the absorber material with the top metal contacts and subsequent fast degradation of the organic HTM. Therefore, new architectures which were HTM-free and metal-free have been developed. The most widely studied in the literature is the triple mesoscopic carbon cell with the typical architecture $TiO_2/ZrO_2/carbon$ (mC-PSC). When this architecture is infiltrated with the archetypal $MAPbI_3$, low voltages of $\sim 1\,V$ are measured. In this project, the use of inorganic $CsPbBr_3$ in mC-PSC was investigated. The structural properties and morphology of $CsPbBr_3$ films was studied as a function of the post-annealing temperature treatment. Enlarged crystal grains and complete conversion of $PbBr_2$ and CsBr into $CsPbBr_3$ were obtained upon post-annealing treatment at high temperature ($400\,°C$). The champion $CsPbBr_3$-based mC-PSC measured a PCE of $8.2\,\%$. The average V_{oc} was $1.27\,V$ with a record $1.44\,V$ for the best mC-PSC.

5.4 Future work

The effect of post annealing treatment in air of $CsPbBr_3$ films was investigated. XPS analysis showed that the material was partially oxidised after annealing at $400\,°C$, while no oxidation was measured after the material was treated at $300\,°C$. It was therefore concluded that the optimum post-annealing temperature may be between 300 and $400\,°C$. Further XPS analysis should be carried out to precisely measure the limit temperature to avoid oxidation of the material.

The complexity of two-step sequential deposition techniques and the formation of dense flakes in the carbon layer may prevent a proper solution infiltration, leading

to wide distribution of photocurrent densities in $CsPbBr_3$ mesoporous carbon solar cells. The sequential deposition should be better controlled to obtain more uniform $PbBr_2$ clusters through the mesoscopic layers and consecutive $CsPbBr_3$ growth. The use of alternative solvents, like DMSO or GBL, may enhance the infiltration of $PbBr_2$ through the mesoporous pores. Moreover, the conversion of $PbBr_2$ into $CsPbBr_3$ by chemical reaction in solution with CsBr may be optimised looking at different reaction time and solution temperature. One-step technique could also be attempted trying to optimise the penetration by using additives, such as 5AVA in the case of $MAPbI_3$. Finally, the formulation of the carbon layer formation could also be optimised to obtain more uniform flake-free layers.

Bibliography

[1] M. Kulbak, S. Gupta, N. Kedem, I. Levine, T. Bendikov, G. Hodes, and D. Cahen, "Cesium Enhances Long-Term Stability of Lead Bromide Perovskite-Based Solar Cells," *J. Phys. Chem. Lett.*, vol. 7, no. 1, pp. 167–172, 2016.

[2] M. Kulbak, D. Cahen, and G. Hodes, "How Important Is the Organic Part of Lead Halide Perovskite Photovoltaic Cells? Efficient $CsPbBr_3$ Cells," *J. Phys. Chem. Lett.*, vol. 6, no. 13, pp. 2452–2456, 2015.

[3] Y. Wang, T. Zhang, M. Kan, and Y. Zhao, "Bifunctional Stabilization of All-Inorganic α-$CsPbI_3$ Perovskite for 17% Efficiency Photovoltaics," *J. Am. Chem. Soc.*, vol. 140, no. 39, pp. 12345–12348, 2018.

[4] G. E. Eperon, G. M. Paterno, R. J. Sutton, A. Zampetti, A. A. Haghighirad, F. Cacialli, and H. J. Snaith, "Inorganic caesium lead iodide perovskite solar cells," *J. Mater. Chem. A*, vol. 3, no. 39, pp. 19688–19695, 2015.

[5] A. Marronnier, G. Roma, S. Boyer-Richard, L. Pedesseau, J. M. Jancu, V. Bonnassieux, C. Katan, C. C. Stoumpos, M. G. Kanatzidis, and J. Even, "Anharmonicity and Disorder in the Black Phases of $CsPbI_3$ used for Stable Inorganic Perovskite Solar Cells," *ACS Nano*, vol. 12, pp. 3477–3486, 2018.

[6] J. Lei, F. Gao, H. Wang, J. Li, J. Jiang, X. Wu, R. Gao, Z. Yang, and S. Liu, "Efficient planar $CsPbBr_3$ perovskite solar cells by dual-source vacuum evaporation," *Sol. Energy Mater. Sol. Cells*, vol. 187, pp. 1–8, 2018.

[7] J. Zhang, G. Hodes, Z. Jin, and S. Liu, "All-inorganic $CsPbX_3$ Perovskites Solar Cells: Progress and Prospects," *Angew. Chem. Int. Ed.*, 2019.

[8] N. Yantara, S. Bhaumik, F. Yan, D. Sabba, H. A. Dewi, N. Mathews, P. P. Boix, H. V. Demir, and S. Mhaisalkar, "Inorganic Halide Perovskites for Efficient Light-Emitting Diodes," *J. Phys. Chem Lett.*, vol. 6, no. 21, pp. 4360–4364, 2015.

[9] Z. Wei, A. Perumal, R. Su, S. Sushant, J. Xing, Q. Zhang, S. T. Tan, H. V. Demir, and Q. Xiong, "Solution-processed highly bright and durable cesium lead halide perovskite light-emitting diodes," *Nanoscale*, vol. 8, no. 42, pp. 18021–18026, 2016.

[10] R. E. Beal, D. J. Slotcavage, T. Leijtens, A. R. Bowring, R. A. Belisle, W. H. Nguyen, G. F. Burkhard, E. T. Hoke, and M. D. McGehee, "Cesium Lead Halide Perovskites with Improved Stability for Tandem Solar Cells," *J. Phys. Chem Lett.*, vol. 7, no. 5, pp. 746–751, 2016.

[11] S. Yang, Z. Hsieh, M. L. Keshtov, G. D. Sharma, and F. Chen, "Towards High-Performance Polymer Photovoltaic Devices for Low-Power Indoor Applications," *Sol. RRL*, vol. 1, no. 12, p. 1700174, 2017.

[12] C. Jiang, S. J. A. Moniz, A. Wang, T. Zhang, and J. Tang, "Photoelectrochemical devices for solar water splitting-materials and challenges," *Chem. Soc. Rev.*, vol. 46, p. 4645, 2017.

[13] Y. Han, S. Meyer, Y. Dkhissi, K. Weber, J. M. Pringle, U. Bach, L. Spiccia, and Y.-B. Cheng, "Degradation observations of encapsulated planar $CH_3NH_3PbI_3$ perovskite solar cells at high temperatures and humidity," *J. Mater. Chem. A*, vol. 3, no. 15, pp. 8139–8147, 2015.

[14] J. Li, Q. Dong, N. Li, and L. Wang, "Direct Evidence of Ion Diffusion for the Silver-Electrode-Induced Thermal Degradation of Inverted Perovskite Solar Cells," *Adv. Energy Mater.*, vol. 7, no. 14, pp. 1–8, 2017.

[15] Y. Kato, L. K. Ono, M. V. Lee, S. Wang, S. R. Raga, and Y. Qi, "Silver Iodide Formation in Methyl Ammonium Lead Iodide Perovskite Solar Cells with Silver Top Electrodes," *Adv. Mater. Interfaces*, vol. 2, no. 13, pp. 2–7, 2015.

[16] N. N. Shlenskaya, N. A. Belich, M. Grätzel, E. A. Goodilin, and A. B. Tarasov, "Light-induced reactivity of gold and hybrid perovskite as a new possible degradation mechanism in perovskite solar cells," *J. Mater. Chem. A*, vol. 6, no. 4, pp. 1780–1786, 2018.

[17] L. Zhao, R. A. Kerner, Z. Xiao, Y. L. Lin, K. M. Lee, J. . Schwartz, and B. P. Rand, "Redox Chemistry Dominates the Degradation and Decomposition of Metal Halide Perovskite Optoelectronic Devices," *ACS Energy Lett.*, vol. 1, no. 3, pp. 595–602, 2016.

[18] C. C. Boyd, R. Cheacharoen, T. Leijtens, and M. D. McGehee, "Understanding Degradation Mechanisms and Improving Stability of Perovskite Photovoltaics," *Chem. Rev.*, vol. 119, no. 5, pp. 3418–3451, 2019.

[19] K. Domanski, J. P. Correa-Baena, N. Mine, M. K. Nazeeruddin, A. Abate, M. Saliba, W. Tress, A. Hagfeldt, and M. Grätzel, "Not All That Glitters Is Gold: Metal-Migration-Induced Degradation in Perovskite Solar Cells," *ACS Nano*, vol. 10, no. 6, pp. 6306–6314, 2016.

[20] C. C. Boyd, R. Cheacharoen, K. A. Bush, R. Prasanna, T. Leijtens, and M. D. McGehee, "Barrier Design to Prevent Metal-Induced Degradation and Improve Thermal Stability in Perovskite Solar Cells," *ACS Energy Lett.*, vol. 3, no. 7, pp. 1772–1778, 2018.

[21] A. Capasso, F. Matteocci, L. Najafi, M. Prato, J. Buha, L. Cina, V. Pellegrini, A. D. Carlo, and F. Bonaccorso, "Few-Layer MoS_2Flakes as Active Buffer Layer for Stable Perovskite Solar Cells," *Adv. Energy Mater.*, vol. 6, no. 16, pp. 1–12, 2016.

[22] E. M. Sanehira, B. J. Tremolet De Villers, P. Schulz, M. O. Reese, S. Ferrere, K. Zhu, L. Y. Lin, J. J. Berry, and J. M. Luther, "Influence of Electrode Interfaces on the Stability of Perovskite Solar Cells: Reduced Degradation Using MoO_x/Al for Hole Collection," *ACS Energy Lett.*, vol. 1, no. 1, pp. 38–45, 2016.

[23] Y. C. Kim, T. Y. Yang, N. J. Jeon, J. Im, S. Jang, T. J. Shin, H. W. Shin, S. Kim, E. Lee, S. Kim, J. H. Noh, S. I. Seok, and J. Seo, "Engineering interface structures between lead halide perovskite and copper phthalocyanine for efficient and stable perovskite solar cells," *Energy Environ. Sci.*, vol. 10, no. 10, pp. 2109–2116, 2017.

[24] K. Brinkmann, J. Zhao, N. Pourdavoud, T. Becker, T. Hu, S. Olthof, K. Meerholz, L. Hoffmann, T. Gahlmann, R. Heiderhoff, M. F. Oszajca, N. A. Luechinger, D. Rogalla, Y. Chen, B. Cheng, and T. Riedl, "Suppressed decomposition of organometal halide perovskites by impermeable electron-extraction layers in inverted solar cells," *Nat. Commun.*, vol. 8, p. 13938, 2017.

[25] H. Chen and S. Yang, "Carbon-Based Perovskite Solar Cells without Hole Transport Materials : The Front Runner to the Market ?," *Adv. Mater.*, vol. 29, p. 1603994, 2017.

[26] Z. Li, S. A. Kulkarni, P. P. Boix, E. Shi, A. Cao, K. Fu, S. K. Batabyal, J. Zhang, Q. Xiong, L. H. Wong, N. Mathews, and S. G. Mhaisalkar, "Laminated carbon nanotube networks for metal electrode-free efficient perovskite solar cells," *ACS Nano*, vol. 8, no. 7, pp. 6797–6804, 2014.

[27] K. Aitola, K. Domanski, J. P. Correa-Baena, K. Sveinbjörnsson, M. Saliba, A. Abate, M. Grätzel, E. Kauppinen, E. M. Johansson, W. Tress, A. Hagfeldt, and G. Boschloo, "High Temperature-Stable Perovskite Solar Cell Based on Low-Cost Carbon Nanotube Hole Contact," *Adv. Mater.*, vol. 29, no. 17, 2017.

[28] S. Gholipour, J.-P. Correa-Baena, K. Domanski, T. Matsui, L. Steier, F. Giordano, F. Tajabadi, W. Tress, M. Saliba, A. Abate, A. Morteza Ali, N. Taghavinia, M. Grätzel, and A. Hagfeldt, "Highly Efficient and Stable Perovskite Solar Cells based on a Low-Cost Carbon Cloth," *Adv. Energy Mater.*, vol. 6, no. 20, p. 1601116, 2016.

[29] I. Lee, J. H. Yun, H. J. Son, and T.-S. Kim, "Accelerated degradation due to weakened adhesion from Li-TFSI additives in perovskite solar cells," *ACS Appl. Mater. Interfaces*, vol. 9, pp. 7029–7035, 2017.

[30] Z. Ku, Y. Rong, M. Xu, T. Liu, and H. Han, "Full Printable Processed Mesoscopic $CH_3NH_3PbI_3/TiO_2$ Heterojunction Solar Cells with Carbon Counter Electrode," *Sci. Rep.*, vol. 3, no. 1, p. 3132, 2013.

[31] T. Liu, L. Liu, M. Hu, Y. Yang, L. Zhang, A. Mei, and H. Han, "Critical parameters in TiO_2/ZrO_2/Carbon-based mesoscopic perovskite solar cell," *J. Power Sources*, vol. 293, pp. 533–538, 2015.

[32] A. Mei, X. Li, L. Liu, Z. Ku, T. Liu, Y. Rong, M. Xu, M. Hu, J. Chen, Y. Yang, M. Gratzel, and H. Han, "A hole conductor free, fully printable mesoscopic perovskite solar cell with high stability," *Science*, vol. 345, no. 6194, pp. 295–297, 2014.

[33] G. Grancini, I. Zimmermann, E. Mosconi, D. Martineau, and S. Narbey, "One-Year stable perovskite solar cells by 2D/3D interface engineering," *Nat. Commun.*, vol. 8, pp. 1–8, 2017.

[34] Y. Sheng, Y. Hu, A. Mei, P. Jiang, X. Hou, M. Duan, L. Hong, Y. Guan, Y. Rong, Y. Xiong, and H. Han, "Enhanced electronic properties in $CH_3NH_3PbI_3$: Via LiCl mixing for hole-conductor-free printable perovskite solar cells," *J. Mater. Chem. A*, vol. 4, no. 42, pp. 16731–16736, 2016.

[35] C. Tian, S. Zhang, A. Mei, Y. Rong, Y. Hu, K. Du, M. Duan, Y. Sheng, P. Jiang, G. Xu, and H. Han, "A Multifunctional Bis-Adduct Fullerene for Efficient Printable Mesoscopic Perovskite Solar Cells," *ACS Appl. Mater. Interfaces*, vol. 10, no. 13, pp. 10835–10841, 2018.

[36] Y. Hu, Z. Zhang, A. Mei, Y. Jiang, X. Hou, Q. Wang, and K. Du, "Improved Performance of Printable Perovskite Solar Cells with Bifunctional Conjugated Organic Molecule," *Adv. Mater.*, vol. 30, p. 1705786, 2018.

[37] J. Zhao, Y. Zhang, X. Zhao, J. Zhang, H. Wang, Z. Zhu, and Q. Liu, "Band Alignment Strategy for Printable Triple Mesoscopic Perovskite Solar Cells with Enhanced Photovoltage," *ACS Appl. Energy Mater.*, vol. 2, pp. 2034–2042, 2019.

[38] S. Liu, W. Huang, P. Liao, N. Pootrakulchote, H. Li, J. Lu, J. Li, F. Huang, X. Shai, X. Zhao, Y. Shen, Y. B. Cheng, and M. Wang, "17% efficient printable mesoscopic PIN metal oxide framework perovskite solar cells using cesium-containing triple cation perovskite," *J. Mater. Chem. A*, vol. 5, no. 44, pp. 22952–22958, 2017.

[39] I. Poli, J. Baker, J. Mcgettrick, F. D. Rossi, S. Eslava, and P. J. Cameron, "Screen printed carbon $CsPbBr_3$ solar cells with high open-circuit photovoltage," *J. Mater. Chem. A*, vol. 6, pp. 18677–18686, 2018.

[40] J. Duan, T. Hu, Y. Zhao, B. He, and Q. Tang, "Carbon electrode tailored all inorganic perovskite solar cells to harvest solar and water vapor energy," *Angew. Chem. Int. Ed.*, vol. 57, no. 20, pp. 5746–5749, 2018.

[41] J. Duan, Y. Zhao, X. Yang, Y. Wang, B. He, and Q. Tang, "Lanthanide ions doped $CsPbBr_3$ halides for HTM-free 10.14% efficiency inorganic perovskite solar cell

with an ultrahigh open-circuit voltage of 1.594 V," *Adv. Energy Mater.*, vol. 8, p. 1802346, 2018.

[42] H. Lakhiani, T. Dunlop, F. De Rossi, S. Dimitrov, R. Kerremans, C. Charbonneau, T. Watson, J. Barbé, and W. C. Tsoi, "Variations of Infiltration and Electronic Contact in Mesoscopic Perovskite Solar Cells Revealed by High-Resolution Multi-Mapping Techniques," *Adv. Funct. Mater.*, vol. 1900885, pp. 1–10, 2019.

[43] A. Ummadisingu and M. Grätzel, "Revealing the detailed path of sequential deposition for metal halide perovskite formation," *Sci. Adv.*, vol. 4, no. 2, pp. 1–10, 2018.

Chapter 6

Improving tolerance to humidity through encapsulation: graphite sheets to protect halide perovskite devices and drive oxygen evolution in water

Several approaches to protect halide perovskites from water have been investigated, including surface treatments and compositional tuning. This chapter investigates the use of commercial graphite sheets to effectively protect halide perovskite solar cells from high humidity, even when completely submerged in water. As a proof of concept, halide perovskite-based devices have been used in the photoelectrochemical production of oxygen from water. Section 6.1 shows the use of high voltage $CsPbBr_3$-based photoanodes encapsulated with commercial graphite sheets to produce durable and stable photocurrents in water. Furthermore, the versatility of the proposed method is demonstrated with the addition of a water oxidation catalyst to improve the photoelectrochemical performance. Section 6.2 investigates how the same encapsulation technique can be successfully used for the fabrication of $MAPbI_3$-based photoanodes.

6.1 Enhancing water stability of halide perovskite devices

The use of halide perovskites is still limited by their inherently instability in water. The lattice structure can in fact be easily broken by the presence of water leading to irreversible decomposition of the material. [1] The previous chapters of this thesis have shown different approaches to improve the moisture resistivity of halide perovskite solar cells. Other techniques reported in literature included teflon coating, [2] plasma vacuum assisted deposition of ultrathin polymers (adamantane) on top

of Au metal contacts [3] and the use of polymer-functionalised single-walled carbon nanotubes embedded in an insulating polymer matrix as hole transport material. [4] Particularly, the last two techniques showed identical device performance before and after exposure to water for 60 s.

Even though promising water resistant properties have been reported for halide perovskite solar cells, stabilities in water for very limited time were achieved. This limited stability prevented not only the commercialisation of photovoltaic devices but also their use in different applications, like photoelectrochemical water splitting, where intimate contact between the absorber device and the aqueous medium is required. [5] In order to achieve higher stabilities in water, perovskite solar cells require proper thin film encapsulation.

6.1.1 Encapsulation of halide perovskites for photoelectrochemical water splitting

Photoelectrochemical (PEC) water splitting is an attractive pathway to produce solar fuels, such as hydrogen, directly using the energy coming from the sun. PEC systems require the intimate contact of the absorber device with the aqueous electrolyte. Therefore, materials which are stable in water must be found to develop efficient, durable and scalable PEC cells for the generation of solar fuels.

Halide perovskites have been widely investigated for photovoltaic applications. The interest in exploiting such fascinating and promising materials in PEC systems has grown recently. The key challenge is to find an inexpensive and efficient way to protect the unstable halide perovskite absorber in water. Only a few reports have been published so far, showing different protection mechanisms, which have been detailed in the timeline shown in figure 6.1 and in table 6.1.

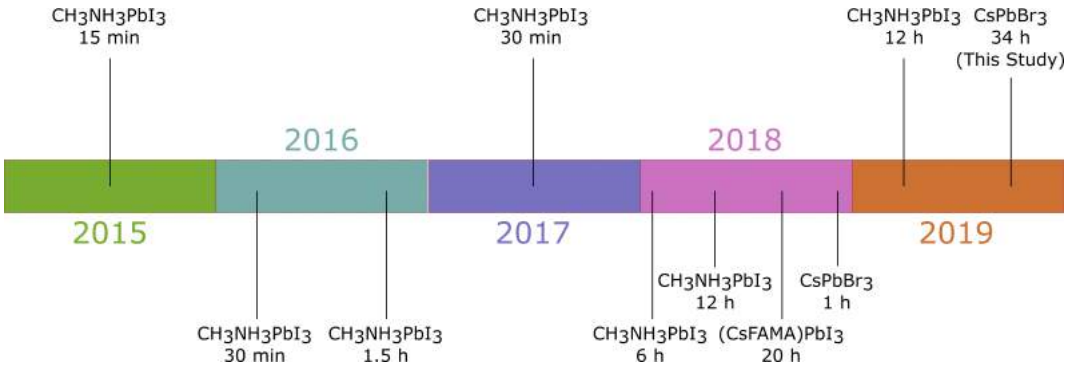

Figure 6.1: Timeline of recent state-of-the-art of halide perovskite photoelectrodes for the generation of solar fuels. The absorber material used and the highest lifetime reported for each study are indicated. See table 6.1 for references.

The first reports used thin layers of Ni deposited by magnetron sputtering, however operation times lower than 30 min under continuous illumination were observed. [6, 7, 9] Later on, other metals have been reported as successfull encapsulation materials, for example field's metal (FM), a fusible InBiSn alloy, and Ti foil

Table 6.1: Encapsulation techniques reported in the literature to use halide perovskites in PEC systems for the generation of solar fuels.

Absorber material	Electrode	Encapsulant	lifetime	ref
$CH_3NH_3PbI_3$	Photoanode	Ni	15 min	[6]
$CH_3NH_3PbI_3$	Photoanode	carbon nanotubes/Ni	30 min	[7]
$CH_3NH_3PbI_3$	Photocathode	FM[1]	1.5 h	[8]
$CH_3NH_3PbI_3$	Photocathode	TEAI[2]/Ni	30 min	[9]
$CH_3NH_3PbI_3$	Photoanode	FM	6 h	[10]
$CH_3NH_3PbI_3$	Photocathode	Ti foil	12 h	[11]
(Cs,FA,MA)PbI_3	Photocathode	FM	20 h	[12]
$CsPbBr_3$	Photocathode	Ag paste/FM	1 h	[13]
$CH_3NH_3PbI_3$-5AVA	Photoanode	C paste/Ag paste/C paste	12 h	[14]
$CsPbBr_3$	Photoanode	C paste/graphite sheet	34 h	This study

1: Field's metals.
2: Tetraethylammonium iodide.

allowed operational time of up to $20\,\mathrm{h}$ and $12\,\mathrm{h}$, respectively. [12, 11] Ag paste, combined with FM or conductive carbon paste has also been employed as protecting and conducting layer for the unstable halide perovskite absorber. [13, 14]

Up to date, most reported studies of halide perovskites for PEC applications have used expensive metals or vacuum-based deposition techniques to protect the sensitive absorber from water. Moreover, the archetypal $CH_3NH_3PbI_3$ and triple cation (Cs,FA,MA)PbI_3 have been mainly employed in PEC systems, achieving high photocurrents but low photovoltages. These systems require high overpotantials to drive the water splitting reactions.

6.1.2 Graphite-protected $CsPbBr_3$ perovskite photoanodes functionalised with water oxidation catalyst for oxygen evolution in water

In this work, an inexpensive, metal-free technique, compatible with large-scale manufacturing was developed to protect halide perovskites from high humidity. This novel coating material consisted of a mesoporous conductive carbon paste and a commercially available conductive graphite sheet (GS). To prove the effectiveness of this encapsulation technique, halide perovskite devices were tested in the harshest condition: submerged under water. Charges were generated and extracted through the electron and hole transport layers even when the device was completely submerged in solution and the photovoltaic parameters measured before and after $2\,\mathrm{h}$ of operation in water were unchanged.

Given the high water resistivity of this architecture, $CsPbBr_3$ protected by layers of carbon paste and GS were used as photoanodes in PEC systems for the evolution of oxygen from water. $1.23\,\mathrm{V}$ is the voltage required to overcome the thermodynamic barrier for water splitting, in practice higher voltages are necessary to compensate for kinetic limitations and losses from solution. For this reason, inorganic $CsPbBr_3$ was chosen as we have been able to make solar cells with open circuit

voltages of up to $1.45\,\mathrm{V}$. [15] Stabilities of over $30\,\mathrm{h}$ of continuous operation in water with currents above $2\,\mathrm{mA\,cm^{-2}}$ at $1.23\,\mathrm{V_{RHE}}$ were achieved. The encapsulated $CsPbBr_3$-based photoanode was very stable across a wide range of pH (3-13) with positive photocurrents that rose steeply from $0.6\,\mathrm{V_{RHE}}$.

The PEC performance of the photoanodes was enhanced by functionalising the electrolyte-facing surface with an Ir-based water oxidation catalyst (WOC). The catalyst was deposited on the surface by simply floating the GS on top of the activated WOC solution at room temperature for $16\,\mathrm{h}$. The presence of the WOC caused the onset potential to shift to lower potentials by $\sim 100\,\mathrm{mV}$ due to accelerated charge transfer and the photocurrent measured at $1.23\,\mathrm{V_{RHE}}$ was about $30\,\%$ higher than the WOC-free device. A faradaic efficiency for O_2 evolution higher than $80\,\%$ was measured (photoanode at applied $1.23\,\mathrm{V_{RHE}}$), indicating that the observed photocurrent was mainly due to O_2 production.

The results summarised in this section have been published by Poli et al. (2019). [16] The statement of authorship is given below.

This declaration concerns the article entitled:										
Graphite-protected $CsPbBr_3$ perovskite photoanodes functionalised with water oxidation catalyst for oxygen evolution in water										
Publication status (tick one)										
Draft manuscript		**Submitted**		**In review**		**Accepted**		**Published**	X	
Publication details (reference)	The article has been published in: *Nat. Commun.*, Vol. 10, 2097 (2019)									
Copyright status (tick the appropriate statement)										
I hold the copyright for this material		Copyright is retained by the publisher, but I have been given permission to replicate the material here	X							
Candidate's contribution to the paper (provide details, and also indicate as a percentage)	The candidate **predominantly** executed the work presented in the paper. **Formulation of ideas:** The objectives, analysis and conclusions of the paper were formulated by the candidate, with the support of the supervisors Petra Cameron, Ulrich Hintermair and Salvador Eslava. [IP=70%, UH=10%, MR=0%, SK=0%, EVS=0%, JB=0%, TMW=0%, SE=5%, PJC=15%] **Design of methodology:** The methodology was conceived and planned by the candidate with the support of the supervisors Petra Cameron, Ulrich Hintermair and Salvador Eslava. [IP=60%, UH=15%, MR=0%, SK=0%, EVS=0%, JB=0%, TMW=0%, SE=5%, PJC=20%] **Experimental work:** The perovskite solar cells and photoanodes were prepared by the candidate. Ulrich Hintermair prepared the iridium WOC and developed the surface functionalization. The candidate conducted all the experimental research, but the tensile strength measurement, which was measured by Santosh Kumar. [IP=88%, UH=6%, MR=3%, SK=2%, EVS=1%, JB=0%, TMW=0%, SE=0%, PJC=0%] **Presentation of data in journal format:** Data were analysed by the candidate and plots and figures in journal format were generated by the candidate. The writing of the manuscript was done by the candidate. The lead supervisor Petra Cameron, second supervisor Salvador Eslava and collaborator Ulrich Hintermair all contributed to analysing and discussing the results, they reviewed and corrected the writing of the paper and gave assistance in the submission and peer reviewing process. [IP=58%, UH=15%, MR=0%, SK=0%, EVS=0%, JB=1%, TMW=1%, SE=5%, PJC=20%]									
Statement from Candidate	This paper reports on original research I conducted during the period of my Higher Degree by Research candidature.									
Signed	X Isabella Poli Isabella Poli						**Date**		16/06/2019	

nature COMMUNICATIONS

ARTICLE

https://doi.org/10.1038/s41467-019-10124-0 OPEN

Graphite-protected $CsPbBr_3$ perovskite photoanodes functionalised with water oxidation catalyst for oxygen evolution in water

Isabella Poli [1,2], Ulrich Hintermair [1,2], Miriam Regue [2,3], Santosh Kumar [3], Emma V. Sackville[1,2], Jenny Baker [4], Trystan M. Watson [4], Salvador Eslava [2,3] & Petra J. Cameron [1,2]

Metal-halide perovskites have been widely investigated in the photovoltaic sector due to their promising optoelectronic properties and inexpensive fabrication techniques based on solution processing. Here we report the development of inorganic $CsPbBr_3$-based photoanodes for direct photoelectrochemical oxygen evolution from aqueous electrolytes. We use a commercial thermal graphite sheet and a mesoporous carbon scaffold to encapsulate $CsPbBr_3$ as an inexpensive and efficient protection strategy. We achieve a record stability of 30 h in aqueous electrolyte under constant simulated solar illumination, with currents above 2 mA cm^{-2} at 1.23 V_{RHE}. We further demonstrate the versatility of our approach by grafting a molecular Ir-based water oxidation catalyst on the electrolyte-facing surface of the sealing graphite sheet, which cathodically shifts the onset potential of the composite photoanode due to accelerated charge transfer. These results suggest an efficient route to develop stable halide perovskite based electrodes for photoelectrochemical solar fuel generation.

[1] Department of Chemistry, University of Bath, Claverton Down, Bath BA2 7AY, UK. [2] Centre for Sustainable Chemical Technologies, University of Bath, Claverton Down, Bath BA2 7AY, UK. [3] Department of Chemical Engineering, University of Bath, Claverton Down, Bath BA2 7AY, UK. [4] SPECIFIC, Swansea University Bay Campus, Fabian Way, Swansea SA1 8EN, UK. Correspondence and requests for materials should be addressed to U.H. (email: u.hintermair@bath.ac.uk) or to S.E. (email: s.eslava@bath.ac.uk) or to P.J.C. (email: p.j.cameron@bath.ac.uk)

About 1 billion people still lack access to electricity, which has significant implications for healthcare, business and food growing[1]. Stand-alone photovoltaic (PV) systems might help electrify geographical areas with no grid access. However, the intermittent nature of solar energy requires the development of systems to store excess energy to be used whenever the sun is not available. Storage in the form of hydrogen has gained wide interest in recent years[2]. At present, hydrogen production still relies on fossil fuels and is mostly based on methane steam reforming and electrolysis[3]. The electricity used to drive conventional electrolysers can come from PV devices or wind turbines, reducing the reliance on fossil fuels. Photoelectrochemical (PEC) water splitting is an emerging technique that uses semiconductors submerged in aqueous solution to directly split water into oxygen and hydrogen using sunlight. The feasibility of both small and large scale PEC water splitting has been shown to be technologically and economically viable[4]. The development of efficient PEC electrodes can save in construction costs as the PV power generator and electrolyser are combined in just one system[5]. However, the development of efficient visible-light absorber materials that are inexpensive and stable in water is still challenging[6,7].

Halide perovskites are promising materials for solar photovoltaic energy conversion thanks to their low cost, easy processability and high efficiency, with the current world-record efficiency standing at 23.7%[8]. Unfortunately, lead halide perovskites are extremely moisture sensitive and need to be protected from high humidity environments[9,10], severely limiting their use for direct PEC water splitting applications. Several approaches have been used to improve the stability of halide perovskite solar cells towards humidity, such as the use of more hydrophobic alkyl ammonium salts[11,12], surface passivation by hygroscopic polymers, carbon nanotubes and long chain ligands[13–16] or through 2D/3D hybrid structures[17–20]. However, none of these techniques have thus far succeeded in protecting perovskite films when submerged in water for extended periods of time as required for application in direct water splitting.

The first example of sunlight-driven water splitting with halide perovskite tandem cells showed a solar-to-hydrogen (STH) efficiency of 12.3%[21]. Two $CH_3NH_3PbI_3$ solar cells were connected in series and combined with Ni electrodes coated in a layer of NiFe. The NiFe was used as bifunctional catalyst for both the oxygen and hydrogen reactions, and in the following years other examples of water splitting driven by halide perovskite solar cells have been reported[22–24]. As a result of the inherent moisture sensitivity of most halide perovskite materials, the use of halide perovskites as photoelectrodes in direct contact with aqueous electrolytes remains less explored. The first example of a halide perovskite solar cell used as a photoanode was reported in 2015, where a $CH_3NH_3PbI_3$ perovskite-based device was protected with a thin Ni layer deposited by magnetron sputtering[25]. Promising initial photocurrents of 12.5 mA cm^{-2} were achieved that gradually dropped to 2.5 mA cm^{-2} within 15 min using S^{2-} as a sacrificial reductant. The same Ni encapsulation technique was later integrated with carbon nanotube/polymer composite protection layers[26] and additional alkyl ammonium salts[27] to extend the operational stability to tens of minutes. A more efficient encapsulation was later demonstrated by Crespo-Quesada et al., who reported a $CH_3NH_3PbI_3$-based photocathode protected by a low-melting alloy of Bi, In and Sn (Field's metal, FM), achieving stability for about 1.5 h under continuous illumination[28]. The same encapsulation technique was then used to fabricate a $CH_3NH_3PbI_3$ halide perovskite-based photoanode that lasted up to 6 h[29]. FM was also used to protect a cesium formamidinium methylammonium (CsFAMA) halide perovskite-based photocathode in tandem with a $BiVO_4$ photoanode that showed stabilities of up to 20 h[30]. Finally, Zhang et al. reported a $CH_3NH_3PbI_3$-based photocathode encapsulated with Ti foil sputtered with Pt, which operated for 12 h under continuous illumination in water[31]. While some of these results appear promising, all of the approaches reported so far rely on expensive materials or sophisticated fabrication techniques.

Initial results on PEC water splitting with halide perovskite materials used the archetypal $CH_3NH_3PbI_3$ and CsFAMA triple-cation mixed halide perovskite that produces photovoltages around 1 V, which alone is below 1.23 V required for water splitting. Wider-bandgap materials can provide higher photovoltages in the range required for water splitting. $CsPbBr_3$ for instance, a fully inorganic compound stable up to 500 °C under N_2, has an energy bandgap of 2.3 eV, and solar cells with very high open-circuit voltages have been reported[32–40]. For example, we have used $CsPbBr_3$ in mesoporous carbon solar cells to obtain efficiencies of 8.2% and open-circuit voltages up to 1.45 V[41]. Recently, $CsPbBr_3$ was used to fabricate a photocathode for hydrogen generation that lasted more than 1 h in water but it used again the expensive Field's metal encapsulation[42].

Here, we present the first report of efficient and stable light-driven water oxidation using $CsPbBr_3$-based photoanodes in aqueous solution. A 20-µm-thick mesoporous carbon (m-c) layer combined with a commercial hydrophobic graphite sheet (GS) is used to effectively protect the highly moisture-sensitive $CsPbBr_3$ from degradation in water. The TiO_2|$CsPbBr_3$|m-c|GS electrodes operate in water across a very wide pH range (2–13), exhibiting photocurrents of up to 3.8 mA cm^{-2} at an applied bias of 1.23 V_{RHE} in acidic solution. Even more impressively they are stable for 30 h of operation with currents above 2 mA cm^{-2} at 1.23 V_{RHE} in aqueous alkaline electrolyte (pH 12.5) under continuous simulated solar illumination of 1 sun (AM 1.5 G). We further show the versatility of our photoanode architecture by functionalising the GS surface with an Ir-based water oxidation catalyst (WOC). The catalyst lowers the onset potential of the photoanode by ~100 mV. The photovoltage measured in aqueous solution is 1.2 V at pH 3.5 and higher than 1.3 V at pH 8.8–12.5. For the first time for a perovskite-based photoanode the Faradaic efficiency of light-driven water oxidation can be assessed, showing our $CsPbBr_3$-based photoanodes to perform photoelectrochemical O_2 evolution from water with a record efficiency of 82.3%.

Results

$CsPbBr_3$ perovskite device preparation. $CsPbBr_3$ is a fully inorganic halide perovskite material, inherently unstable in water like most other organic–inorganic halide perovskites. Supplementary Fig. 1a, b shows the X-ray diffraction (XRD) patterns and UV-vis absorption of a $CsPbBr_3$ film before and after it was dipped in water for 1 s. The initial XRD spectrum was in good agreement with the orthorombic perovskite structure[43], however, after immersion in water, its distinct (100), (110) and (200) diffraction peaks rapidly disappeared and peaks characteristic of the precursor materials $PbBr_2$ and CsBr appeared. While pristine $CsPbBr_3$ has a bandgap of 2.35 eV with an absorption onset corresponding to 530 nm giving rise to its yellow colour, after immersion in water only a semitransparent white material remains ($PbBr_2$). Therefore, in order to use $CsPbBr_3$ in aqueous PEC cells for solar water splitting, effective protection strategies need to be developed as for any other halide perovskite.

We prepared our perovskite photoanodes based on the architecture of a standard carbon perovskite solar cell. Generally, perovskite solar cells are made using an absorber material sandwiched between an electron transport layer (ETL) and a hole transport layer (HTL). In these cells, a compact layer of TiO_2 deposited by spray pyrolysis and a doctor-bladed mesoporous

carbon layer (m-carbon or m-c) were used as the ETL and HTL, respectively, as shown in Fig. 1a (Supplementary Fig. 2 shows a schematic energy band diagram). $CsPbBr_3$ solar cells with similar carbon-based architectures have already shown good stability over 3 months in humid air, thanks to the hydrophobic nature of the m-carbon HTL[44]. Indeed, the water contact angle (WCA) of the mesoporous carbon layer used here exceeded 90° (Supplementary Fig. 3). Figure 1b shows a cross-sectional scanning electron microscopy (SEM) image of the as-prepared $CsPbBr_3$ structure with a 20-µm-thick m-carbon layer acting as conducting contact. Energy dispersive X-ray (EDX) mapping images of the $CsPbBr_3$ solar cell are shown in Supplementary Fig. 4, confirming the formation of a TiO_2|$CsPbBr_3$|m-c stack. Figure 1c shows the FTO|TiO_2|$CsPbBr_3$ interfaces with thin layers of TiO_2 and $CsPbBr_3$ of about 50 and 350 nm, respectively.

We first prepared photoanodes with a TiO_2|$CsPbBr_3$|m-c configuration (schematic illustration in Supplementary Fig. 5a), where the 20 µm-carbon layer aimed to provide waterproof protection to the moisture-sensitive $CsPbBr_3$. Supplementary Fig. 5b shows the current density-voltage (JV) curve of a typical TiO_2|$CsPbBr_3$|m-c solar cell measured under AM 1.5 G. and solar simulated light at 100 mW cm^{-2}. As shown in Supplementary Fig. 5c and Supplementary Note 1, the TiO_2|$CsPbBr_3$|m-c photoanode in pH 9 aqueous electrolyte exhibited a photocurrent density of ~0.4 at 1.23 V_{RHE}. Chronoamperometry was performed at pH 9 and 13 at 1.23 V_{RHE} and is shown in Supplementary Fig. 6a and Supplementary Fig. 7. Promisingly, the photoanode retained 70% of its initial value over 20 min testing and H_2 bubbles were generated on the Pt counter electrode (Supplementary Fig. 6b). The photocurrent density was also measured with monochromatic light, showing that $CsPbBr_3$ was still absorbing visible light at wavelengths $\lambda < 530$ nm after 15 min of immersion in water at pH 9 (see Supplementary Fig. 6c). This photocurrent density could not be assigned to the TiO_2 layer or to the formation of $PbBr_2$ since a control photoanode consisting of TiO_2|$PbBr_2$|m-c generated a maximum of 0.067 mA cm^{-2} at 1.23 V_{RHE} (Supplementary Fig. 8).

Protection of perovskite device in water. In order to more efficiently protect $CsPbBr_3$ from water, a 25 µm self-adhesive graphite sheet (GS) was placed on top of the mesoporous carbon layer, to create TiO_2|$CsPbBr_3$|m-c|GS photoanodes (see Fig. 2a). While the mesoporous carbon acts as an effective HTL due to its intimate contact with the perovskite absorber layer, the GS offers a more compact seal that can protect the halide perovskite more efficiently from liquid water percolation (see Hg porosimetry of m-c and GS in Supplementary Fig. 9 and Supplementary Note 2 showing differences in porosity). Similar to mesoporous carbon, the GS is distinctly hydrophobic (measured WCA is 98°, shown in Supplementary Fig. 10) and it offers excellent thermal and electrical conductivity (1600 $W m^{-1} K^{-1}$ and 20,000 S cm^{-1}, respectively). Figure 2b shows that the JV curves of the TiO_2|$CsPbBr_3$|m-c|GS measured as solar cells before and after 2 h of PEC operation in water were unchanged, indicating extraordinary water stability. As shown from the linear sweep voltammetry (LSV) curve in Fig. 2c, the photocurrent steeply rose from

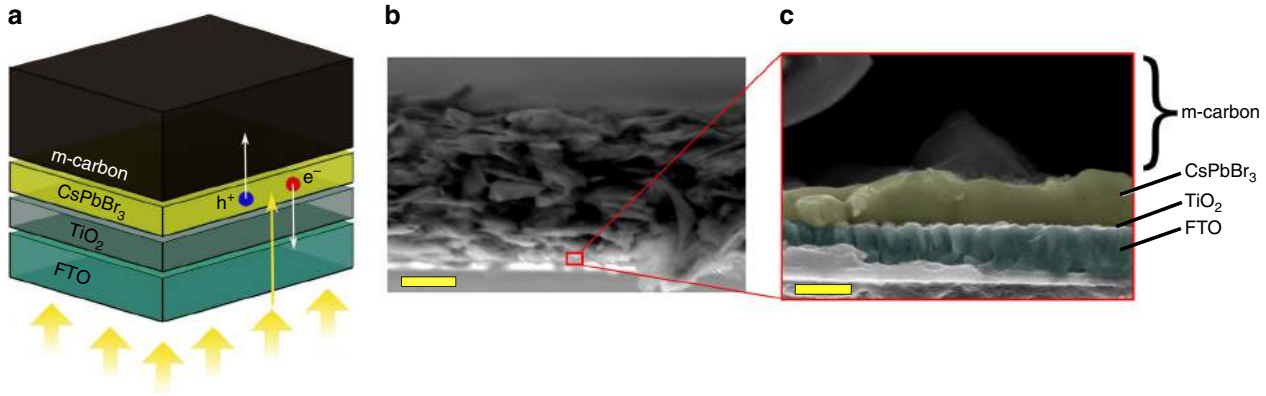

Fig. 1 Configuration of $CsPbBr_3$ devices. **a** Structure of standard carbon solar cell (illuminated through the FTO glass as indicated by the yellow arrows). Electron-hole (e^-/h^+) pairs are generated in the $CsPbBr_3$ thin layer, then e^- and h^+ are collected in the TiO_2 and m-carbon layers, respectively. **b** Cross-sectional scanning electron microscopy (SEM) image of the as-prepared $CsPbBr_3$ perovskite solar cell (scale bar 10 µm). **c** Magnification of the cross-sectional SEM image to show the FTO|TiO_2|$CsPbBr_3$ interfaces (scale bar 500 nm)

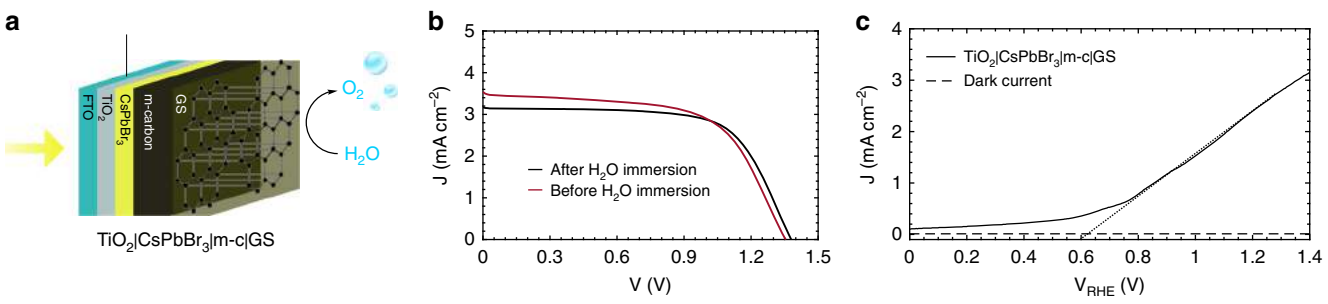

Fig. 2 TiO_2|$CsPbBr_3$|m-c|GS as solar cell and photoanode. **a** Schematic illustration of the $CsPbBr_3$ photoanode for PEC O_2 evolution: TiO_2|$CsPbBr_3$|m-c|GS uses commercial conductive GS on the m-carbon layer; The photoanode is illuminated through the FTO glass. **b** Photovoltaic current density-voltage curves measured under simulated AM 1.5 G solar light (100 mW cm^{-2}) before and after 2 h of immersion in water. Curves shown are measured in reverse scan. **c** Typical linear sweep voltammetry (LSV) measured under PEC conditions at a scan rate of 20 mV s^{-1}, measured in 0.1 M KNO_3 at pH 4.3, under continuous simulated AM 1.5 G solar illumination, 1 sun

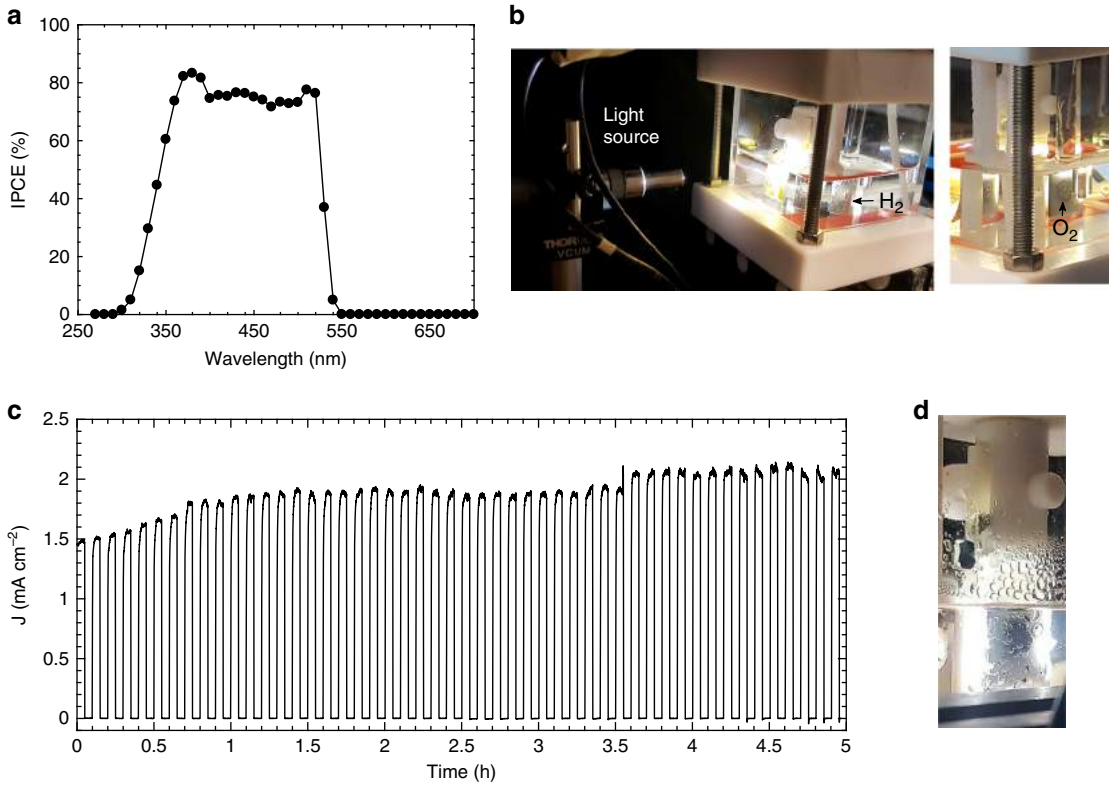

Fig. 3 TiO_2|$CsPbBr_3$|m-c|GS PEC performance in water. **a** Incident photon-to-current efficiency (IPCE) measured in aqueous 0.1 M KNO_3 solution with the pH adjusted to 12 with KOH; electrode was subjected to monochromatic light irradiation at 1.23 V_{RHE}. **b** Photographs of the PEC cell under operation, showing H_2 and O_2 gas bubbles evolving from the counter electrode (Pt) and the photoanode, respectively. **c** Chronoamperometric trace recorded at an applied potential of 1.23 V_{RHE} in KOH electrolyte solution at pH 12.5, under chopped simulated solar light irradiation (AM 1.5 G, 100 mW cm^{-2}). **d** Photographs of the photoanode immersed in the electrolyte solution after 18 h of continuous operation, showing oxygen bubbles evolving from the active area

0.6 V_{RHE} on, achieving a photocurrent density of 2.5 mA cm^{-2} at 1.23 V_{RHE}.

The wavelength dependence of the incident photon-to-current efficiency (IPCE) measured in aqueous solution in Fig. 3a showed an onset wavelength of 530 nm for the TiO_2|$CsPbBr_3$|m-c|GS, which corresponds exactly to the onset light absorption of $CsPbBr_3$ in Supplementary Fig. 1b. An IPCE efficiency of about 70% was measured at 500 nm. In contrast, an IPCE efficiency lower than 10% was measured at 500 nm for the TiO_2|$CsPbBr_3$|m-c in water (Supplementary Fig. 11), suggesting that the $CsPbBr_3$ partially degraded when protected by the m-c layer on its own. The GS, however, proved to be a particularly effective encapsulation layer which did not hinder charge transport. This was confirmed by the JV curves of TiO_2|$CsPbBr_3$|m-c measured before and after applying the GS on the surface, which are shown in Supplementary Fig. 12 and Supplementary Table 1. The V_{oc}, J_{sc} and FF of the device decreased by only about 5% after the GS was applied on the surface, confirming that holes could be properly extracted through the GS layer. Photographs in Fig. 3b show O_2 and H_2 gas bubbles evolving from the GS active area of the $CsPbBr_3$ based photoanode and the Pt counter electrode, respectively.

Figure 3c shows chronoamperometry recorded at an applied potential of 1.23 V_{RHE} in electrolyte at pH 12.5. The TiO_2|$CsPbBr_3$|m-c|GS photoanodes were stable under chopped illumination in basic aqueous electrolyte for more than 5 h and the photoanode's current increased from 1.5 to 2 mA cm^{-2} during this time. This represents the first example of halide perovskite-based photoeletrodes, protected with inexpensive protection layers, which can demonstrate stable photocurrents for hours.

To investigate the long-term stability of the $CsPbBr_3$-based photoanode, chronoamperometry was recorded at a constant applied potential of 1.23 V_{RHE} in aqueous solution (0.1 M KNO_3) under continuous illumination. The evolution of the photocurrent density with time at different pH until the end of life is shown in Supplementary Fig. 13. The device achieved a lifetime of 34 h in an alkaline electrolyte and 23 h in near-neutral solution, while the longest lifetime tested in acidic solutions was 7.8 h. Figure 3d shows a photograph of the PEC cell after 18 h of operation, with oxygen bubbles still emerging from the active area of the photoanode inside the PEC cell. The end of life of all devices tested at different pH was always caused by delamination and fracture of the GS surface (Supplementary Fig. 14). In contrast to previous reports in the literature, which all reported constant decreasing photocurrent under continuous illumination[29,31], we observed an increasing photocurrent during the measurement, especially in near-neutral pH, where the photoanode's current density gradually increased under illumination reaching a peak of 2.5 mA cm^{-2} after 16.7 h (Supplementary Fig. 13). We believe that soaking effects are responsible for causing the increase in photocurrents. Tensile strength measurements showed that the GS material used to encapsulate the moisture-sensitive perovskite layer does experience changes in its mechanical properties when exposed to aqueous electrolyte at pH 7 (as shown in Supplementary Fig. 15). The decrease in stiffness observed likely reflects swelling during soaking that can expose a higher surface area to the electrolyte, thereby increasing water

oxidation performance. To further verify this effect of soaking, we tested a TiO_2|$CsPbBr_3$|m-c|GS photoanode with intermittent electrolyte soaking in the dark at open circuit. The results in Supplementary Fig. 16 show that the photocurrent density increased every time the photoanode was illuminated again following a period of soaking. Another possible explanation for the increase in photocurrent is possible structural modification of the $CsPbBr_3$ due to halide migration under light soaking[45]. Mosconi et al. proposed that Frenkel defects (V_x^+/X_i^-) in halide perovskites heal during irradiation due to lower energy barriers for halide (X) migration in the photoexcited state[46]. Indeed, we previously showed that the efficiency of $CsPbBr_3$ carbon solar cells increased under light soaking[41]. Gradual increase in current over time has been also recently reported for two dimensional/three dimensional perovskite carbon solar cells and triple-cation perovskite devices[47].

In order to further optimise the photoanode and enhance the stability of the GS when exposed to aqueous electrolyte, we measured the performance of TiO_2|$CsPbBr_3$|m-c|GS using a 70-μm-thick GS (GS70). Even though a thicker GS was used, charges were still efficiently extracted when testing the device as a solar cell before PEC testing (Supplementary Fig. 17 and Supplementary Table 2). Figure 4 shows chronoamperometry of TiO_2|$CsPbBr_3$|m-c|GS70 photoanodes recorded at a constant applied potential of 1.23 V_{RHE} in aqueous solution (0.1 M KNO_3, pH 7) under continuous illumination. The photoanode exhibited photocurrents above 2 mA cm^{-2} for about 30 h. Eventually, the silicone-epoxy resin sealing on the slide edges partly degraded in the electrolyte solution, letting some water pass through it, which slowly degraded the $CsPbBr_3$ material to $PbBr_2$ (Supplementary Fig. 18). The GS70 was still intact at the end of the experiment and as mentioned above the failure was due to degradation of the sealant. In contrast, failure in devices with GS25 protecting layers occurred due to fracture of the GS after extended operation in water. This clearly indicates that thicker GS protection layers, along with better sealing materials, can extend the lifetime of these composite photoanodes even further.

Functionalisation of GS with a water oxidation catalyst. To test the versatility of our encapsulated perovskite-based photoanodes and to further improve their efficiency at lower potentials, the addition of an iridium-based water oxidation catalyst (WOC)[48–50] was explored. The $[Ir(\mu O)(pyalk)(H_2O)_2]_2^{2+}$ catalyst chosen has previously been shown to rapidly and irreversibly adsorb to the surface of indium tin oxide (ITO) and α-Fe_2O_3 as a minimally thin molecular monolayer[50–53]. Grafitingly, we also found it to robustly bind to graphitic surfaces after simply floating the GS on an activated WOC solution at room temperature for 16 h (Fig. 5a). Supplementary Fig. 19 shows EDX mapping images and the elemental composition of the GS|WOC, providing direct evidence for the presence of the Ir-WOC on the surface and showing its localisation around oxidic edges on the GS surface[50]. Evidence for the presence of the catalyst was also provided by electrochemical measurements of the GS|WOC sheet. Figure 5b shows cyclic voltammetry (CV) with a clear catalytic wave for water oxidation starting at about 1.4 V_{RHE}[54]. As previously reported for the Ir-WOC in solution[49] and on ITO surfaces[50], the quasi-reversible redox process centred around 1 V_{RHE} appears in acidic media and corresponds to the Ir^{III}/Ir^{IV} redox couple[50]. Comparing CVs of both bare and functionalised GS across a pH range of 2–13 (Supplementary Fig. 20) showed the overpotentials for oxygen evolution to increase with increasing pH for both materials, but with distinctly lower overpotentials in the presence of the Ir-WOC at all pH values (Fig. 5c).

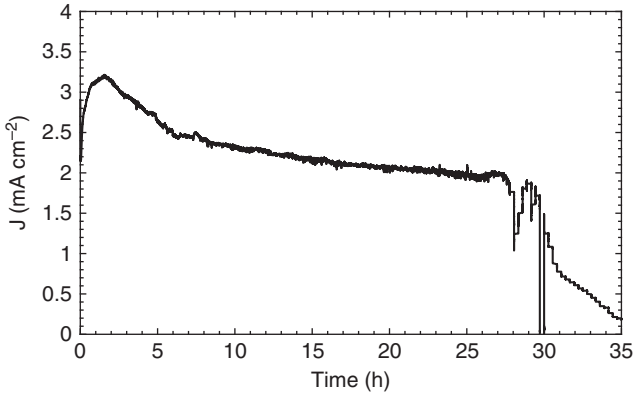

Fig. 4 Long-term stability of TiO_2|$CsPbBr_3$|m-c|GS70 in water. Chronoamperometric trace of TiO_2|$CsPbBr_3$|m-c|GS70 recorded at an applied potential of 1.23 V_{RHE}. 0.1 M KNO_3 electrolyte solution pH 7, under continuous simulated solar light irradiation (AM 1.5 G, 100 mW cm^{-2})

These pre-functionalised GS|WOC sheets could easily be used to fabricate TiO_2|$CsPbBr_3$|m-c|GS|WOC photoanodes as illustrated in Fig. 6a using a straightforward procedure under ambient conditions. When measured as a photoanode in aqueous solution at pH 2.5, a cathodic shift in the onset potential V_{on} of 100 mV was observed with respect to unfunctionalised TiO_2|$CsPbBr_3$|m-c|GS (Fig. 6b). Moreover, the PEC photocurrent density was found to rise faster with applied potential compared with TiO_2|$CsPbBr_3$|m-c|GS, a clear sign of improved hole transport and O_2 evolution kinetics as seen previously for the same Ir-WOC on haematite photoanodes[52]. The shift in the V_{on} to more negative potentials was observed also at higher pHs 4 and 7 (Supplementary Fig. 21 and Supplementary Note 3) and it was in agreement with Tafel plots (Supplementary Fig. 22). Supplementary Fig. 23 shows CVs for complete TiO_2|$CsPbBr_3$|m-c|GS|WOC photoanodes at pH 2.5, 4 and 7. The photocurrent density was higher and the onset potential shifted to more negative values at low pH, as already evidenced by the overpotential trend observed in Fig. 5c as a function of pH.

Open-circuit measurements were performed in the dark and under illumination in different electrolytes (Fig. 7a). The difference between the dark open-circuit voltage and that under illumination determines the photovoltage ΔV_{ph} of the photoanode[52]. TiO_2|$CsPbBr_3$|m-c|GS and TiO_2|$CsPbBr_3$|m-c|GS|WOC showed similar open-circuit potential (OCP) and ΔV_{ph} at equilibrium, showing again that the enhanced activity of TiO_2|$CsPbBr_3$|m-c|GS|WOC is not a thermodynamic effect but the result of enhanced charge transfer kinetics. When 1.23 V_{RHE} were applied in a three-electrode PEC system, similar water oxidation photocurrents for photoanodes with and without WOC were obtained (Supplementary Figs 24 and 25 and Supplementary Note 4). The long-term performance and stability of TiO_2|$CsPbBr_3$|m-c|GS|WOC showed the addition of the WOC to afford almost 20% higher initial photocurrents of 3.5 mA cm^{-2} and nearly three times longer lifetime of 17 h in acidic electrolyte than the bare TiO_2|$CsPbBr_3$|m-c|GS under the same conditions (Fig. 7b).

O_2 production with functionalised perovskite photoanode. The amount of O_2 produced over time by a TiO_2|$CsPbBr_3$|m-c|GS|WOC was enough to be monitored using an oxygen probe in the headspace of a gas-tight PEC cell. Figure 8a shows the detected and predicted O_2 evolution as a function of time under continuous simulated solar light illumination (1 sun, AM 1.5 G) at an applied voltage of 1.23 V_{RHE}, with the predicted amount of O_2 calculated from the photocurrent generated as shown in

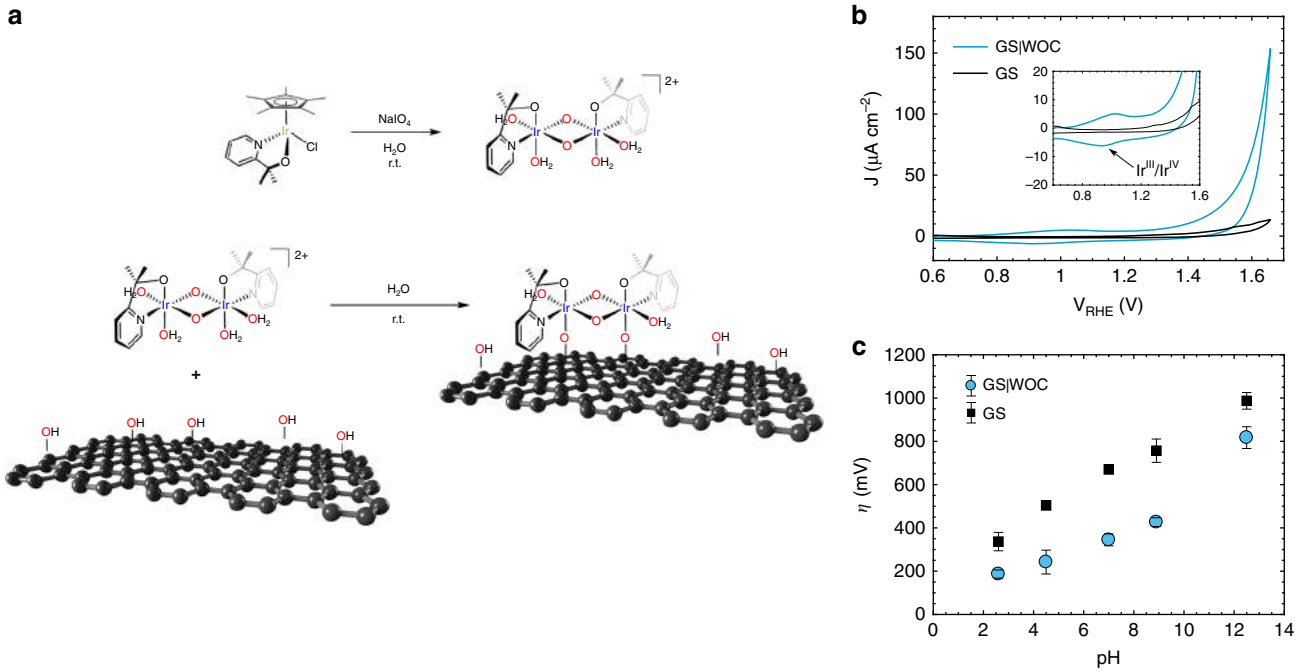

Fig. 5 Formation of the WOC and functionalisation of the GS surface. **a** Oxidative activation of the iridium precursor (top) and functionalisation of the GS surface (bottom). **b** Cyclic voltammetry (CV) scan of GS and GS functionalised with the Ir-WOC measured in 0.1 M KNO_3 at pH 2.6, with scan rate of 50 mV s^{-1}. The inset shows a close-up of the potential axis, where the Ir^{III}/Ir^{IV} couple can be seen. **c** Electrode overpotentials at 10 μA cm^{-2} as a function of the pH of the solution. The error bars represent standard deviation

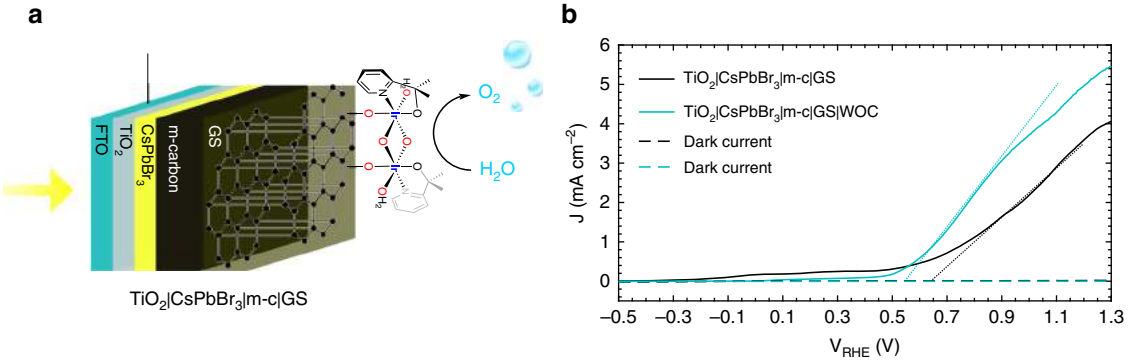

Fig. 6 $TiO_2|CsPbBr_3|m\text{-}c|GS|WOC$ as solar cell and photoanode. **a** Schematic illustration of the $CsPbBr_3$ photoanode for PEC O_2 evolution: $TiO_2|CsPbBr_3|m\text{-}c|GS|WOC$ uses commercial conductive GS functionalised with an Ir-based catalyst. The photoanode is illuminated from the back side. **b** Linear sweep voltammetry (LSV) of a $TiO_2|CsPbBr_3|m\text{-}c|GS$ and a $TiO_2|CsPbBr_3|m\text{-}c|GS|WOC$ measured at a scan rate of 20 mV s^{-1}, in a 0.1 M KNO_3 electrolyte solution with pH 2.5 (pH adjusted with H_2SO_4)

Supplementary Fig. 26 and Supplementary Note 5. Figure 8b shows the Faradaic efficiency of the light-driven water oxidation, which reached values as high as 82.3% using this unoptimised small-scale laboratory setup (Supplementary Discussion). This value compares favourably with other photoanode materials such as WO_3 and TiO_2[55,56], and represents the first successful measurement of a Faradaic efficiency of a stable perovskite-based photoanode in aqueous solution.

The photovoltages of about 1.35 V measured in neutral to alkaline media (pH = 8.8 and 12.5 V) exceeded the thermodynamic 1.23 V required for electrolysis of water. In practice, most PEC devices require photovoltages in the range of 1.7–2 V to effectively overcome the kinetic limitations of proton reduction and water oxidation at the electrolyte interface and drive unbiased solar water splitting[57,58]. Indeed, when an unbiased two-electrode measurement was performed with $TiO_2|CsPbBr_3|m\text{-}c|GS$ and Pt electrodes at pH 2.5, very low photocurrent of 0.05 mA cm^{-2} was measured (Fig. 9a). Excitingly, when a surface functionalised $TiO_2|CsPbBr_3|m\text{-}c|GS|WOC$ was tested under the same conditions, a photocurrent of 0.1 mA cm^{-2} was sustained for more than 5 min (Fig. 9b).

Unfortunately the corresponding amount of O_2 produced was below the detection limit of our oxygen probe (theoretically we generated 28 nmol after 2 h in de-aerated solution, Supplementary Fig. 27), but the photocurrents observed for $TiO_2|CsPbBr_3|m\text{-}c|GS|WOC$ constitute an exciting glimpse at the possibility of unbiased solar water splitting that might become possible with these photoanode architectures after some further optimisation.

In conclusion, we have demonstrated a straightforward versatile and highly effective approach for the fabrication of stable inorganic halide perovskite-based photoanodes using an easily fabricated mesoporous carbon layer and commercially

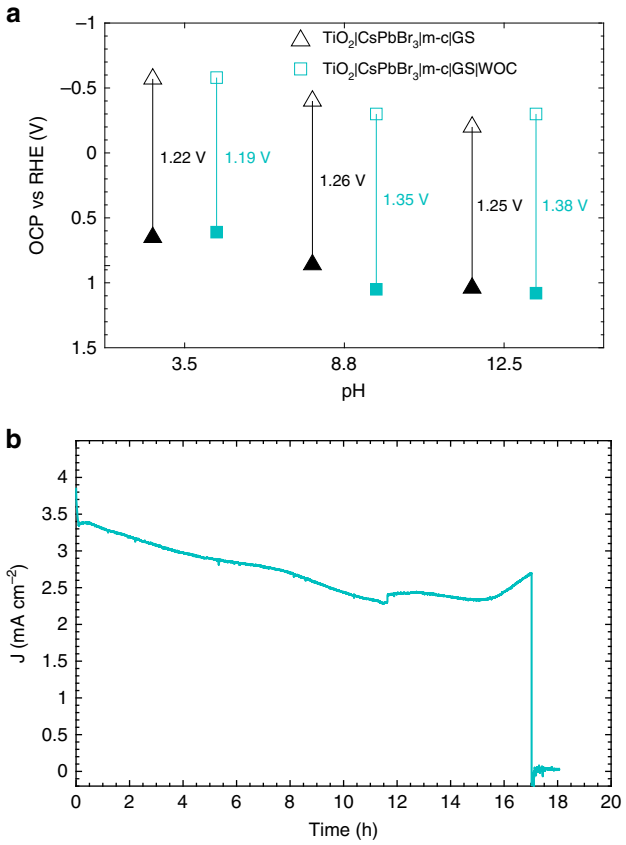

Fig. 7 Comparison of TiO_2|$CsPbBr_3$|m-c|GS with and without Ir-WOC. **a** Open-circuit potential (OCP) of photoanodes measured in 0.1 M KNO_3 solutions with different pH; Measurements performed in the dark are shown with solid symbols, while the ones performed under illumination are shown with open symbols; The photovoltage ΔV_{ph} measured for each sample is given. **b** Chronoamperometric trace of TiO_2|$CsPbBr_3$|m-c|GS|WOC recorded at an applied potential of 1.23 V_{RHE}. The electrolyte was 0.1 M KNO_3 adjusted to pH 2.5 with H_2SO_4, under continuous simulated solar light irradiation (AM 1.5 G, 100 mW cm^{-2})

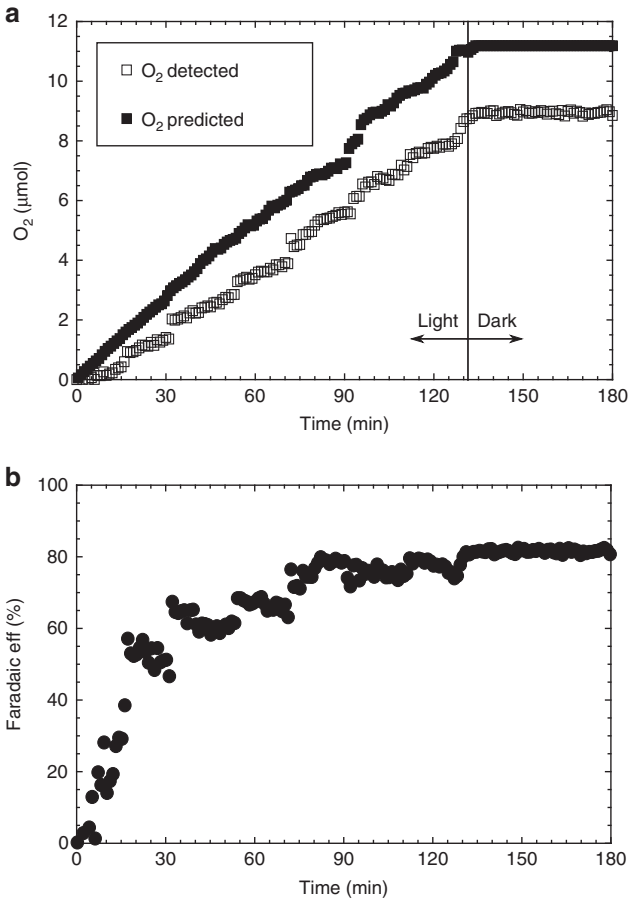

Fig. 8 O_2 evolution performance on TiO_2|$CsPbBr_3$|m-c|GS|WOC. **a** Detected (open square) and predicted (close square) O_2 production under continuous simulated solar light irradiation (AM 1.5 G, 100 mW cm^{-2}), in 0.1 M KNO_3 adjusted to pH 3.5 with H_2SO_4. **b** Faradaic efficiency for O_2 evolution

available graphite sheet as hole transport and protection layers. This encapsulation technique was effective in increasing the photocurrent density of the $CsPbBr_3$-based photoanodes from 0.4 to more than 2 mA cm^{-2} at 1.23 V_{RHE}, and at the same time protected the perovskite from degradation by the aqueous electrolyte. The so-sealed photoanodes worked efficiently in aqueous electrolytes with IPCE values above 70% for direct light-driven water oxidation in aqueous solution, showing good activity over a wide pH range of 2–13. Photocurrents above 2 mA cm^{-2} were obtained for 30 h of continuous illumination in alkaline aqueous solution. We have also demonstrated the versatility of our photoanode device by effectively functionalising the electrolyte-facing surface of the GS with an Ir-based WOC to improve the onset potential of the photoanode by 100 mV in acidic solutions via improved charge transport kinetics. High Faradaic efficiencies for O_2 evolution of up to 82.3% were achieved over 2 h of continuous simulated sunlight irradiation with such a TiO_2|$CsPbBr_3$|m-c|GS|WOC photoanode.

These composite cells are remarkably easy to synthesise without the need for high temperature or vacuum techniques. A working device could be fabricated by a single person using standard laboratory techniques and inexpensive materials and methods. The GS protection strategy used here for oxygen evolution in water can also be used to enhance the lifetime of perovskite solar cells, where the flexible nature of graphite may allow for roll-to-roll processing for efficient large scale manufacturing. We believe that this design represents a promising lead for using inexpensive, high performance but inherently moisture and water-sensitive perovskite materials in integrated photoelectrochemical cells for solar energy conversion. The flexibility of the underlying perovskite material and option of adding matched oxygen-evolution catalysts allows for a high degree of variability that promises application in a wide range of different architectures.

Methods

Photoanode fabrication. FTO glass TEC 7 (Sigma-Aldrich) was etched with zinc powder and HCl (2 M). It was then cleaned in 2 vol% Hellmanex solution in water, followed by de-ionised (DI) water, acetone (VWR), 2-propanol (IPA, VWR) and ethanol (EtOH,VWR) before being treated with UV-Ozone cleaning (in ProCleaner PLUS for 20 min). A compact TiO_2 layer was deposited by spray pyrolysis, using a hand-held atomiser to spray 0.2 M solution of titanium diisopropoxide bis (acetylacetonate) (75 wt%, Sigma-Aldrich) in EtOH onto the substrates held at 500 °C. Substrates were then sintered at this temperature for 10 min. $PbBr_2$ solution (1 M in DMF) was spin coated on top of the substrates held at 70 °C at 2500 rpm for 30 s and each cell was further sintered at 70 °C for 30 min. The cell was then immersed in the CsBr solution (17 mg ml^{-1} in methanol) kept at 50 °C in a vertical staining jar for 30 min before being annealed at 150 °C for 30 min. A carbon paste (black carbon + graphite, Gwent Electronic Materials) was doctor bladed as top contact on top of the $CsPbBr_3$ film. Devices were further post-annealed at 380 °C for 30 min in air for the mesoporous carbon (m-c) layer formation. A graphite thermal sheet (RS, Panasonic, 1600 Wm^{-1} K^{-1}, 180 × 115 mm, 0.025 mm, self-adhesive on one side) was stuck by hand onto the mesoporous carbon top layer. The device was finally sealed (except an active area of 0.25 cm^2) with commercial silicone and epoxy resin left to harden out at room temperature overnight.

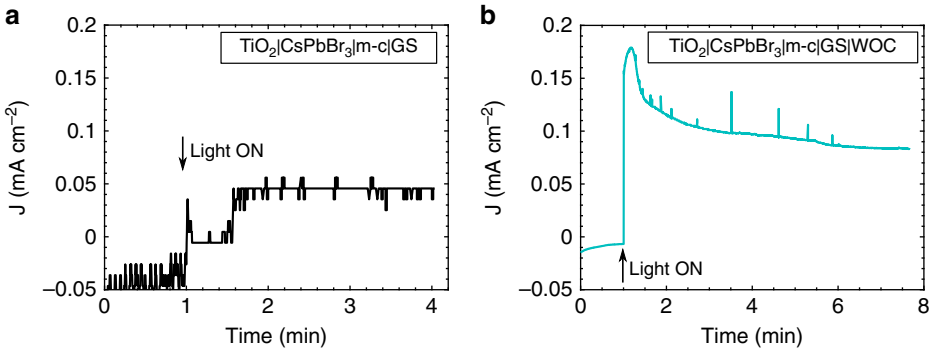

Fig. 9 Unbiased two-electrode performance of TiO_2|$CsPbBr_3$|m-c|GS and TiO_2|$CsPbBr_3$|m-c|GS|WOC. **a** Chronoamperometric trace of TiO_2|$CsPbBr_3$|m-c|GS recorded in a two-electrode cell. **b** Chronoamperometric trace of TiO_2|$CsPbBr_3$|m-c|GS|WOC recorded in a two-electrode cell (0.1 M KNO_3 with pH adjusted to 2.5 with H_2SO_4, with no external bias voltage applied)

Ir catalyst preparation. The iridium precursor [Cp*Ir(pyalc)Cl] was synthesised according to previous literature reports[59]. Forty-eight milligrams of the precursor (0.1 mmol) was added to 20 ml of DI water in an open beaker and a clear orange solution was stirred vigorously for 5 min. Under constant stirring, 540 mg (2.5 mmol) of $NaIO_4$ were added to the beaker and the dark blue solution was allowed to stir overnight at room temperature. A piece of GS was floated on the unstirred, blue Ir-WOC solution overnight to bind the catalyst. It was then rinsed with DI water and left to dry at room temperature.

Device characterisation. Powder X-ray diffraction (XRD) patterns were collected using a Bruker Advance D8 X-ray diffractometer with a Cu Kα source. Measurements were taken from 2θ values in the range 5–80°.

Thin film UV-vis optical transmission and reflectance measurements were performed on a Perkin-Elmer Lambda 750S UV/Vis spectrometer, from 900 to 300 nm. The absorption coefficient was calculated as $\alpha = \ln\left(\frac{(1-R)^2}{T}\right)$.

The cross-sectional microscopy morphology was studied using a JEOL SEM6480LV scanning electron microscope (SEM) (20 kV acceleration voltage and a magnification of 5000) and a JEOL JSM-6301F Field emission scanning electron microscope (FESEM) for high resolution imaging.

Solar cell JV curves were measured using Keithley 2601A potentiostat, under simulated sunlight AM 1.5 G (100 mW cm^{-2}) with a solar simulator Class AAA with a HMI Lamp (200W/70V). A WPVS reference cell (Fraunhofer ISE) in accordance with international standard requirements of IEC 60904-2 was used to calibrate the light. The cell was held at 1.5 V under illumination for 5 s before scanning in reverse. The PV performance was not confirmed from independent certification laboratories. The voltage was swept from 1.5 to 0 V and back to 1.5 V at 100 mV s^{-1}.

The PEC performances of the devices were investigated in aqueous solutions 0.1 M KNO_3, with pH adjusted by using H_2SO_4 or KOH. When specified, a buffered solution of K-borate at pH 9 was used. The measurements were carried out in a three-electrode system with Pt as a counter electrode and Ag/AgCl as a reference electrode. The PEC electrolyte was exposed to air during measurement. The measured potentials versus Ag/AgCl were then converted to the RHE scale using the Nernst equation $E_{RHE} = E_{Ag/AgCl} + 0.059pH + 0.205$. The PEC performance, such as LSV and chronoamperometry, was measured with a Compactstat IVIUM potentiostat under simulated solar illumination (AM 1.5 G filtered 100 mW cm^{-2}) with 300 W Xe source (Lot-QD) from the back side. The intensity of the light at the working electrode position was measured by certified and calibrated SEL033/U photodetector (International Light Technologies). UV or IR light reaching the FTO-coated glass TEC7 is not further filtered but the latter glass may do some UV filtering (absorption spectra of FTO and FTO|TiO_2 are in Supplementary Fig. 28). LSV curves were measured at a scanning rate of 20 mV s^{-1} and chronoamperometry experiments were conducted at 1.23 V_{RHE}.

IPCE measurements were performed from 300 to 900 nm with the same light source passing through a monochromator (MSH-300F LOT QuantumDesign) without the AM 1.5 G filter at an applied bias of 1.23 V_{RHE}. The intensity of the monochromatic light was measured by a SEL033/U photodetector (International Light Technologies).

OCP measurement were performed in a 3-electrode PEC cell. The voltage was measured versus the reference electrode Ag/AgCl when the current flowing through the system was set to be 0. The photovoltage was calculated by subtracting the OCP measured in the dark and under 1 sun illumination (AM 1.5 G filtered 100 mW cm^{-2}).

The O_2 evolution was probed using a compact fibre-optic oxygen metre (FireStingO_2) using a robust oxygen probe (XB7-546-206) in the three-electrode system previously purged with N_2 in a gas-tight quartz cell. TDIP temperature sensor was used to give automatic compensation for minor fluctuation in the PEC cell temperature. The faradaic efficiency was calculated by dividing the experimental O_2 produced and the theoretical O_2 calculated from chronoamperometric traces, assuming that O_2 formation liberates four electrons. The amount of oxygen dissolved in the liquid was calculated according to Henry's law ($K_H = 769.23$ atm M^{-1}) and added to the amount detected in the headspace.

CV scans of GS and GS|WOC were performed using an AUTOLAB potentiostat in H_2SO_4 solution (pH 3.5) with 0.5 M KNO_3 at a scan rate of 20 mV s^{-1}. Ag/AgCl and Pt were used as reference and counter electrodes, respectively.

Ultimate stress and strain was measured using a 50 kN Instron Instrument and samples prepared according to the standard for tensile testing of polymer thin films. Sample was 75 mm long and ~6 mm wide along the working region of the tensile test sample. Stress calculated according to stress = force/area.

Data availability

All relevant data are available from the authors. All data associated with the paper have been deposited online and can be freely and permanently accessed at https://doi.org/10.15125/BATH-00581[60].

Received: 8 December 2018 Accepted: 18 April 2019
Published online: 08 May 2019

References

1. IEA. *World Energy Outlook 2018*. https://www.oecd-ilibrary.org/content/publication/weo-2018-en (International Energy Agency, 2018).
2. Turan, B. et al. Upscaling of integrated photoelectrochemical water-splitting devices to large areas. *Nat. Commun.* **7**, 12681 (2016).
3. Muradov, N. Z. & VeziroÇ$lu, T. N. From hydrocarbon to hydrogen-carbon to hydrogen economy. *Int. J. Hydrog. Energy* **30**, 225–237 (2005).
4. Pinaud, B. A. et al. Technical and economic feasibility of centralized facilities for solar hydrogen production via photocatalysis and photoelectrochemistry. *Energy Environ. Sci.* **6**, 1983–2002 (2013).
5. Krogmeier, B., Staub, F., Grabowski, D., Rau, U. & Kirchartz, T. Quantitative analysis of the transient photoluminescence of CH_3NH_3/PbI_3//PC_{61} BM heterojunctions by numerical simulations. *Sustain. Energ. Fuels* **2**, 1027–1034 (2018).
6. Tilley, S. D., Cornuz, M., Sivula, K. & Grätzel, M. Light-inducedwater splitting with hematite: improved nanostructure and iridium oxide catalysis. *Angew. Chem. Int. Ed.* **49**, 6405–6408 (2010).
7. Bae, D., Seger, B., Vesborg, P. C., Hansen, O. & Chorkendorff, I. Strategies for stable water splitting: via protected photoelectrodes. *Chem. Soc. Rev.* **46**, 1933–1954 (2017).
8. NREL. *Best Research Cell-Efficiencies*. Available at: https://www.nrel.gov/pv/assets/pdfs/best-research-cell-efficiencies-190416.pdf (National Renewable Energy Laboratory (NREL), 2019).
9. Leijtens, T. et al. Stability of metal halide perovskite solar cells. *Adv. Energy Mater.* **5**, 1500963 (2015).
10. Leguy, A. M. A. et al. Reversible hydration of $CH_3NH_3PbI_3$ films, single crystals, and solar cells. *Chem. Mater.* **27**, 3397–3407 (2015).
11. Yang, S. et al. Functionalization of perovskite thin films with moisture-tolerant molecules. *Nat. Energy* **1**, 1–7 (2016).
12. Poli, I., Eslava, S. & Cameron, P. Tetrabutylammonium cations for moisture-resistant and semitransparent perovskite solar cells. *J. Mater. Chem. A* **5**, 22325–22333 (2017).
13. Kim, M., Motti, S. G., Sorrentino, R. & Petrozza, A. Enhanced solar cells stability by hygroscopic polymer passivation of metal halide perovskite thin film. *Energy Environ. Sci.* **11**, 2609–2619 (2018).

14. Poli, I., Liang, X., Baker, R., Eslava, S. & Cameron, P. J. Enhancing the hydrophobicity of perovskite solar cells using C18 capped $CH_3NH_3PbI_3$ nanocrystals. *J. Mater. Chem. C.* **6**, 7149–7156 (2018).
15. Idigoras, J. et al. Enhancing moisture and water resistance in perovskite solar cells by encapsulation with ultrathin plasma polymers. *ACS Appl. Mater. Interfaces* **10**, 11587–11594 (2018).
16. Habisreutinger, S. N. et al. Carbon nanotube/polymer composites as a highly stable hole collection layer in perovskite solar cells. *Nano. Lett.* **14**, 5561–5568 (2014).
17. Ma, C. et al. 2D/3D perovskite hybrids as moisture-tolerant and efficient light absorbers for solar cells. *Nanoscale* **338**, 643–647 (2016).
18. Tsai, H. et al. High-efficiency two-dimensional Ruddlesden–Popper perovskite solar cells. *Nature* **536**, 312–316 (2016).
19. Cao, D. H. et al. Thin films and solar cells based on semiconducting two-dimensional Ruddlesden-Popper $(CH_3(CH_2)_3NH_3)_2(CH_3NH_3)Sn_{n-1}I_{3n+1}$ perovskites. *ACS Energy Lett.* **2**, 982–990 (2017).
20. Smith, I. C., Hoke, E. T., Solis-Ibarra, D., McGehee, M. D. & Karunadasa, H. I. A layered hybrid perovskite solar-cell absorber with enhanced moisture stability. *Angew. Chem. Int. Ed.* **53**, 11232–11235 (2014).
21. Luo, J. et al. Water photolysis at 12.3% efficiency via perovskite photovoltaics and Earth-abundant catalysts. *Science* **345**, 1593–1596 (2014).
22. Gurudayal et al. Perovskite-hematite tandem cells for efficient overall solar driven water splitting. *Nano. Lett.* **15**, 3833–3839 (2015).
23. Kim, J. H. et al. Wireless solar water splitting device with robust cobalt-catalyzed, and perovskite solar cell in tandem: a dual absorber artificial leaf. *ACS Nano* **9**, 11820–11829 (2015).
24. Luo, J. et al. Bipolar membrane-assisted solar water splitting in optimal pH. *Adv. Energy Mater.* **6**, 1600100 (2016).
25. Da, P. et al. High-performance perovskite photoanode enabled by Ni passivation and catalysis. *Nano. Lett.* **15**, 3452–3457 (2015).
26. Hoang, M. T., Pham, N. D., Han, J. H., Gardner, J. M. & Oh, I. Integrated photoelectrolysis of water implemented on organic metal halide perovskite photoelectrode. *ACS Appl. Mater. Interfaces* **8**, 11904–11909 (2016).
27. Wang, C., Yang, S., Chen, X., Wen, T. & Yang, H. G. Surface-functionalized perovskite films for stable photoelectrochemical water splitting. *J. Mater. Chem. A* **5**, 910–913 (2017).
28. Crespo-Quesada, M. et al. Metal-encapsulated organolead halide perovskite photocathode for solar-driven hydrogen evolution in water. *Nat. Commun.* **7**, 12555 (2016).
29. Nam, S., Mai, C. T. K. & Oh, I. Ultrastable photoelectrodes for solar water splitting based on organic metal halide perovskite fabricated by lift-off process. *ACS Appl. Mater. Interfaces* **10**, 14659–14664 (2018).
30. Andrei, V. et al. Scalable triple cation mixed halide perovskite-$BiVO_4$ tandems for bias-free water splitting. *Adv. Energy Mater.* **8**, 1801403 (2018).
31. Zhang, H. et al. A sandwich-like organolead halide perovskite photocathode for efficient and durable photoelectrochemical hydrogen evolution in. *Water Adv. Energy Mater.* **8**, 1800795 (2018).
32. Stoumpos, C. C. et al. Crystal growth of the perovskite semiconductor $CsPbBr_3$: a new material for high-energy radiation detection. *Cryst. Growth Des.* **13**, 2722–2727 (2013).
33. Kulbak, M. et al. Cesium enhances long-term stability of lead bromide perovskite-based solar cells. *J. Phys. Chem. Lett.* **7**, 167–172 (2016).
34. Chang, X. et al. Carbon-based $CsPbBr_3$ Perovskite Solar Cells: All-Ambient Processes and High Thermal Stability. *ACS Appl. Mater. Interfaces* **8**, 33649–33655 (2016).
35. Liu, Z. et al. Efficient Carbon-Based $CsPbBr_3$ inorganic perovskite solar cells by using Cu-phthalocyanine as hole transport material. *Nano-Micro Lett.* **10**, 34 (2018).
36. Kulbak, M., Cahen, D. & Hodes, G. How important is the organic part of lead halide perovskite photovoltaic cells? Efficient $CsPbBr_3$ cells. *J. Phys. Chem. Lett.* **6**, 2452–2456 (2015).
37. Zhang, J., Hodes, G., Jin, Z. & Liu, S. All-inorganic CsPbX3 perovksite solar cells: progress and prospects. Angew. Chem. Int. Ed. https://doi.org/10.1002/anie.201901081 (2019).
38. Duan, J., Hu, T., Zhao, Y., He, B. & Tang, Q. Carbon-electrode-tailored all-inorganic perovskite solar cells to harvest solar and water-vapor energy. *Angew. Chem. Int. Ed.* **57**, 5746–5749 (2018).
39. Yuan, H. et al. All-inorganic $CsPbBr_3$ perovskite solar cell with 10.26% efficiency by spectra engineering. *J. Mater. Chem. A* **6**, 24324–24329 (2018).
40. Duan, J. et al. Lanthanide ions doped $CsPbBr_3$ halides for HTM-free 10.14%-efficiency inorganic perovskite solar cell with an ultrahigh open-circuit voltage of 1.594 V. *Adv. Energy Mater.* **8**, 1802346 (2018).
41. Poli, I. et al. Screen printed carbon $CsPbBr_3$ solar cells with high open-circuit photovoltage. *J. Mater. Chem. A* **6**, 18677–18686 (2018).
42. Gao, L.-f, Luo, W.-J., Yao, Y.-F. & Zou, Z.-G. An all-inorganic lead halide perovskite-based photocathode for stable water reduction. *Chem. Commun.* **54**, 11459 (2018).
43. Beal, R. E. et al. Cesium lead halide perovskites with improved stability for tandem solar cells. *J. Phys. Chem. Lett.* **7**, 746–751 (2016).
44. Liang, J. et al. All-inorganic perovskite solar cells. *J. Am. Chem. Soc.* **138**, 15829–15832 (2016).
45. DeQuilettes, D. W. et al. Photo-induced halide redistribution in organic-inorganic perovskite films. *Nat. Commun.* **7**, 11683 (2016).
46. Mosconi, E., Meggiolaro, D., Snaith, H. J., Stranks, S. D. & De Angelis, F. Light-induced annihilation of Frenkel defects in organo-lead halide perovskites. *Energy Environ. Sci.* **9**, 3180 (2016).
47. Bliss, M. et al. Spectral response measurements of perovskite solar cells. *IEEE J. Photovolt.* **9**, 220–226 (2019).
48. Hintermair, U. et al. Precursor transformation during molecular oxidation catalysis with organometallic iridium complexes. *J. Am. Chem. Soc.* **135**, 10837–10851 (2013).
49. Thomsen, J. M. et al. Electrochemical activation of Cp iridium complexes for electrode-driven water-oxidation catalysis. *J. Am. Chem. Soc.* **136**, 13826–13834 (2014).
50. Sheehan, S. W. et al. A molecular catalyst for water oxidation that binds to metal oxide surfaces. *Nat. Commun.* **6**, 6469 (2015).
51. Li, W. et al. Hematite-based solar water splitting in acidic solutions: functionalization by mono- and multilayers of iridium oxygen-evolution catalysts. *Angew. Chem. Int. Ed.* **54**, 11428–11432 (2015).
52. Moir, J. W., Sackville, E. V., Hintermair, U. & Ozin, G. A. Kinetics versus charge separation: improving the activity of stoichiometric and non-stoichiometric hematite photoanodes using a molecular iridium water oxidation catalyst. *J. Phys. Chem. C.* **120**, 12999–13012 (2016).
53. Zhao, Y. et al. Stable iridium dinuclear heterogeneous catalysts supported on metal-oxide substrate for solar water oxidation. *Proc. Natl Acad. Sci. USA* **115**, 2902–2907 (2018).
54. Sackville, E. V., Marken, F. & Hintermair, U. Electrochemical and kinetic insights into molecular water oxidation catalysts derived from Cp*Ir(pyridine-alkoxide) complexes. *Chem. Cat. Chem.* **10**, 4280–4291 (2018).
55. Fàbrega, C. et al. Efficient WO_3 photoanodes fabricated by pulsed laser deposition for photoelectrochemical water splitting with high faradaic efficiency. *Appl. Catal. B* **189**, 133–140 (2016).
56. Regue, M. et al. Mo-doped TiO_2 photoanodes using $[Ti_4Mo_2O_8(OEt)_{10}]_2$ bimetallic oxo cages as a single source precursor. *Sustain. Energ. Fuels* **2**, 2674–2686 (2018).
57. Smith, W. A., Sharp, I. D., Strandwitz, N. C. & Bisquert, J. Interfacial band-edge energetics for solar fuels production. *Energy Environ. Sci.* **8**, 2851 (2015).
58. Dotan, H., Mathews, N., Hisatomi, T., Grätzel, M. & Rothschild, A. On the solar to hydrogen conversion efficiency of photoelectrodes for water splitting. *J. Phys. Chem. Lett.* **5**, 3330–3334 (2014).
59. Hintermair, U., Hashmi, S. M., Elimelech, M. & Crabtree, R. H. Particle formation during oxidation catalysis with Cp* iridium complexes. *J. Am. Chem. Soc.* **134**, 9785–9795 (2012).
60. Poli, I. et al. Dataset for "Graphite-protected $CsPbBr_3$ perovskite photoanodes functionalised with water oxidation catalyst for oxygen evolution in water". *Univ. Bath*. https://doi.org/10.15125/BATH-00581 (2019).

Acknowledgements

This work was supported by the EPSRC Centre for Doctoral Training in Sustainable Chemical Technologies (EP/L016354/1) at the University of Bath. I.P. thanks the European Union's Horizon 2020 research and innovation programme H2020-MSCA-CO-FUND-2014 (# 665992, MSCA FIRE: Fellows with Industrial Research Enhancement), U.H. thanks the Royal Society for a University research Fellowship (UF160458) and S.E. and S.K. thank the EPSRC for financial support (EP/R035407/1). J.B. and T.W. thank Self-Assembling Perovskite Absorbers Cells Engineered into Modules (SPACE-Modules) (EP/M015254/2) and the SPECIFIC Innovation and Knowledge Centre (EP/N02083/1). All authors thank the MAS staff at the University of Bath Mrs Ursula Potter, Dr Philip Fletcher and Ms Diana Lednitzky for experimental assistance in SEM acquisition and Dr Olivier Camus for Hg porosimetry. The authors thank Prof Steve Tennisson for valuable advice on carbon materials for this project.

Author contributions

I.P., U.H., S.E. and P.J.C. conceived and planned the experiments. I.P. prepared the perovskite solar cells and photoanodes and conducted the experimental research. M.R. helped with IPCE. and oxygen-evolution measurements. S.K. performed the tensile strength measurements. E.V.S. and U.H. prepared the iridium WOC and developed the surface functionalisation. J.B. and T.M.W. provided advice on the mesoporous carbon material used in this project and its characterisation and contributed to the analysis and discussion of the results. IP wrote the manuscript with support of U.H., S.E. and P.J.C. who all contributed to analysing the data and discussing the results.

Additional information

Supplementary Information accompanies this paper at https://doi.org/10.1038/s41467-019-10124-0.

Competing interests: US Patent 9/790/605 by U.H. et al. contains intellectual property described in this article. The other authors declare no competing interest.

Reprints and permission information is available online at http://npg.nature.com/reprintsandpermissions/

Journal peer review information: *Nature Communications* thanks the anonymous reviewers for their contribution to the peer review of this work. Peer reviewer reports are available.

Publisher's note: Springer Nature remains neutral with regard to jurisdictional claims in published maps and institutional affiliations.

Graphite-protected $CsPbBr_3$ Perovskite Photoanodes Functionalised with Water Oxidation Catalyst for Oxygen Evolution in Water

Poli et al.

Supplementary Information

Supplementary Information contains:

- Supplementary Figures 1-28
- Supplementary Tables 1-2
- Supplementary Notes 1-5
- Supplementary Discussion
- Supplementary References

Supplementary Figures

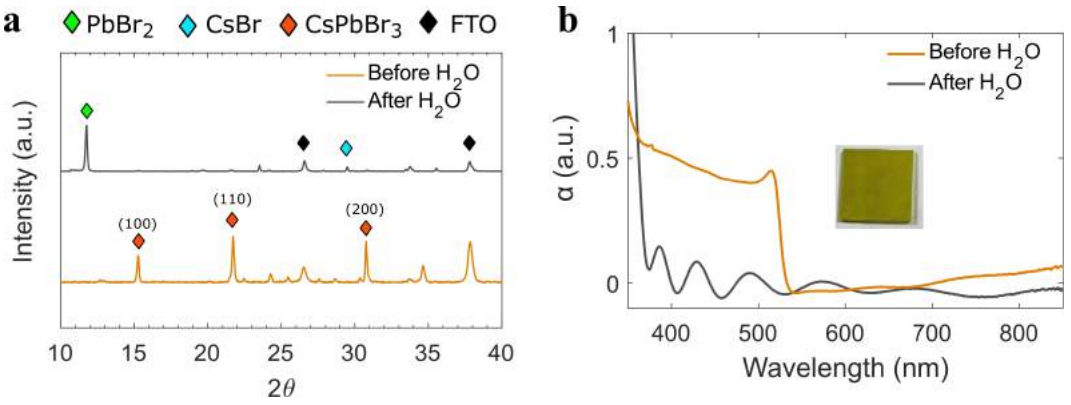

Supplementary Figure 1: Instability of $CsPbBr_3$ in water. a XRD patterns of $CsPbBr_3$ films before and after immersion in water for 1 s. **b** UV-Vis spectra of $CsPbBr_3$ films before and after immersion in water for 1 s; Picture showing the as prepared $CsPbBr_3$ film.

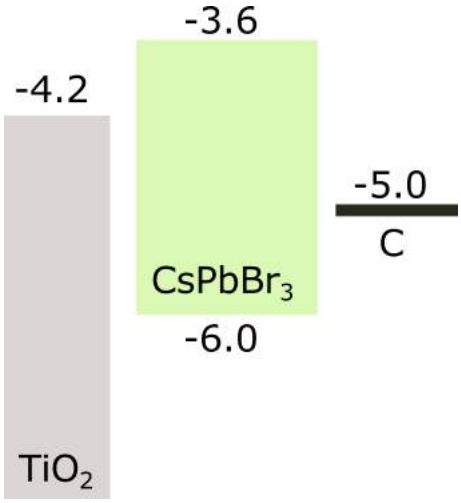

Supplementary Figure 2: Energy band diagram of $CsPbBr_3$-based devices. Schematic of the energy band diagram of $TiO_2|CsPbBr_3|$m-carbon stack used as photoanode in a three-electrode PEC system.

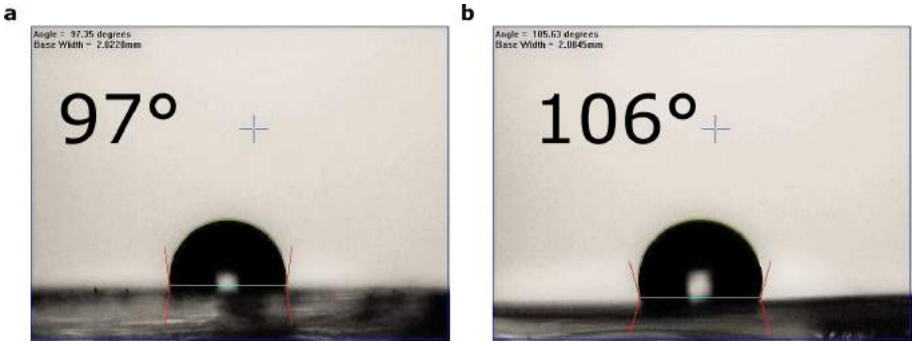

Supplementary Figure 3: Hydrophobicity of the mesoporous carbon HTL. Water contact angle of mesoporous carbon layer **a** doctor bladed and **b** screen printed onto FTO-coated glass.

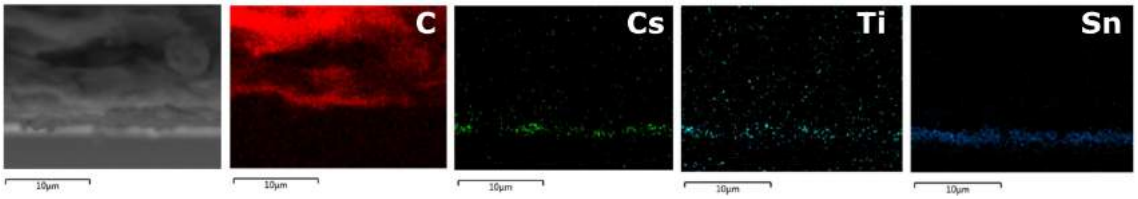

Supplementary Figure 4: Elemental composition of TiO_2|$CsPbBr_3$|m-c. Energy dispersive X-ray (EDX) mapping of the as-prepared TiO_2|$CsPbBr_3$|m-c structure. Red colour indicates C (m-C top contact), green colour is Cs ($CsPbBr_3$ absorber layer), light blue colour is Ti (TiO_2 ETM) and blue colour is Sn (FTO coated glass).

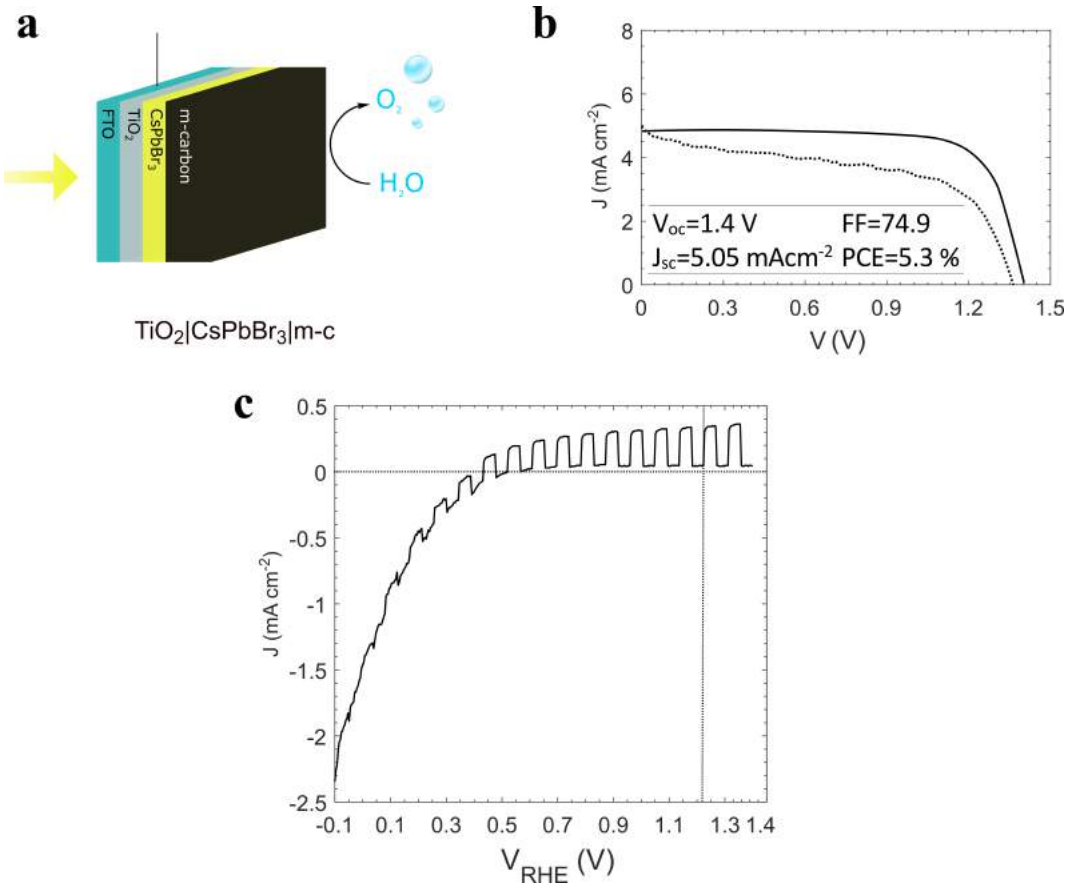

Supplementary Figure 5: $TiO_2|CsPbBr_3|$m-c as solar cell and photoanode. a Schematic illustrations of the $CsPbBr_3$ photoanode for PEC O_2 evolution: $TiO_2|CsPbBr_3|$m-c. **b** Current density-voltage curve measured as a solar cells under simulated AM 1.5 G solar light ($100\,\mathrm{mW\,cm^{-2}}$) before immersion in water. **c** LSV of $TiO_2|CsPbBr_3|$m-c photoanode measured under chopped simulated solar light in a buffer solution (k-borate, pH=9). (See Supplementary Note 1).

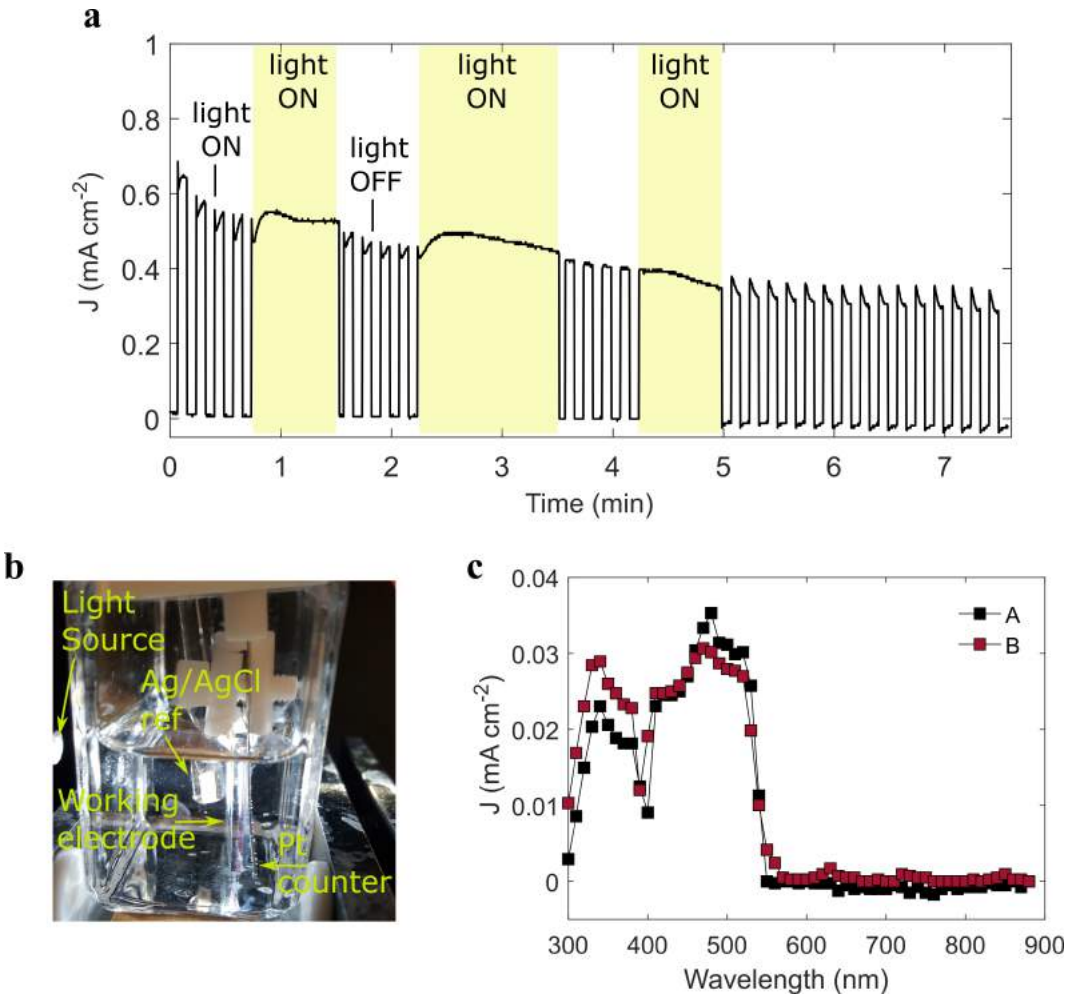

Supplementary Figure 6: TiO_2|$CsPbBr_3$|m-c photoanode stability in water. **a** PEC current density measured over time at an applied voltage of 1.23 V_{RHE} under chopped simulated solar light in buffer solution (k-borate, pH=9). **b** Picture of the three-electrode system setup used during measurement, with H_2 bubbles evolving from the Pt counter electrode. **c** PEC current density under monochromatic light measured in a buffer solution (k-borate, pH=9). Sample B was measured right after immersion while sample A was measured after it has been tested under chopped light in water for 15 min.

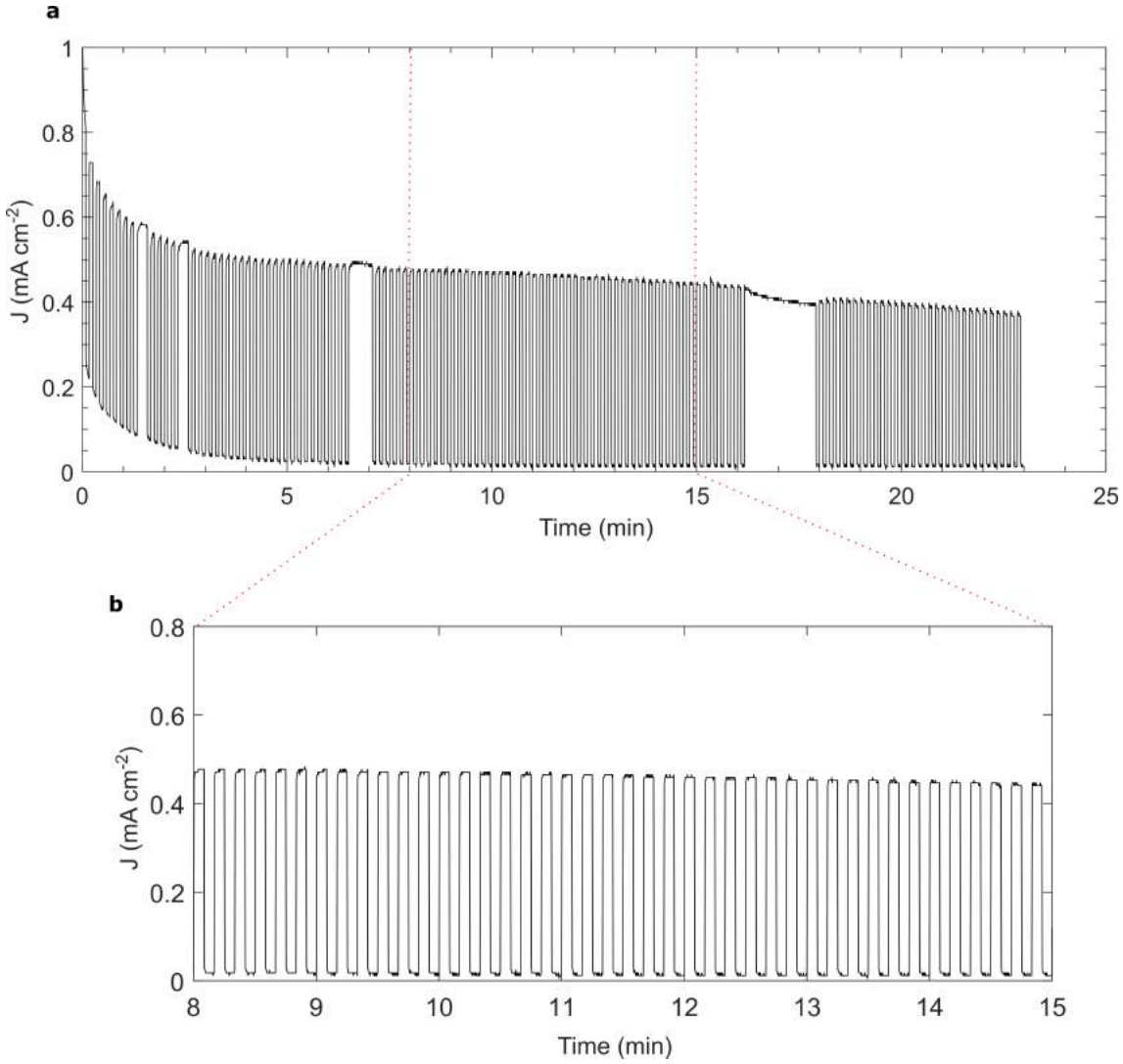

Supplementary Figure 7: $TiO_2|CsPbBr_3|$m-c photoanode stability over time. a PEC current density measured over time at an applied voltage of 1.23 V_{RHE} under chopped simulated solar light in KOH solution pH 13. **b** Magnification of the response under chopped light at minutes 8-15.

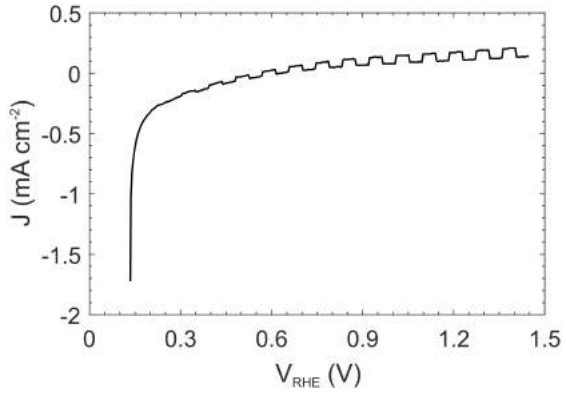

Supplementary Figure 8: $TiO_2|PbBr_2|$m-c as photoanode. LSV of $TiO_2|PbBr_2|$m-c measured under chopped simulated solar light in a buffer solution with pH=9.

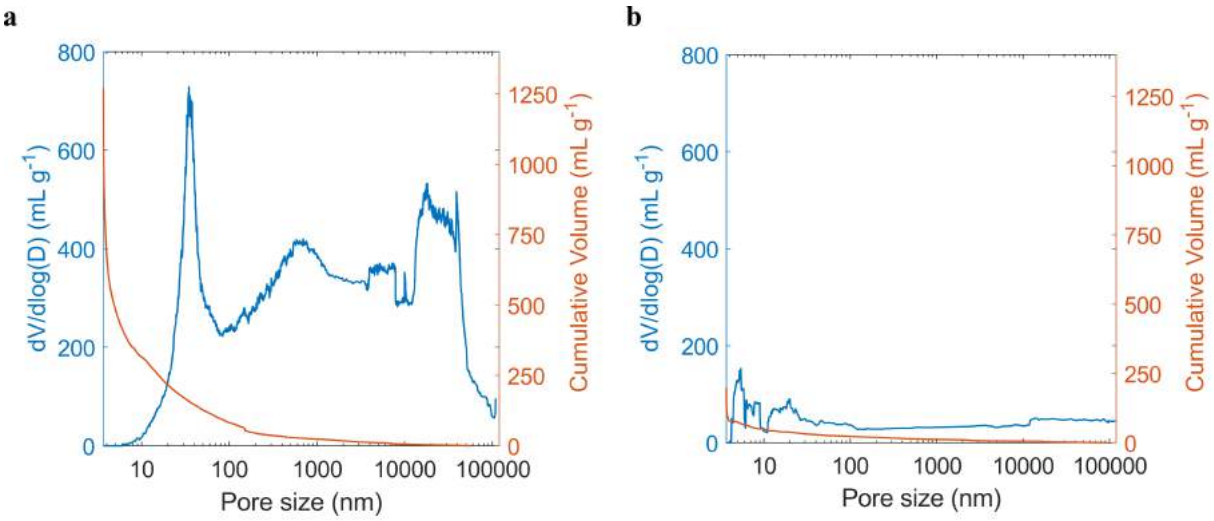

Supplementary Figure 9: Porosity of m-c and GS. Hg porosimetry of **a** m-c and **b** GS showing differences in porosity. (See Supplementary Note 2).

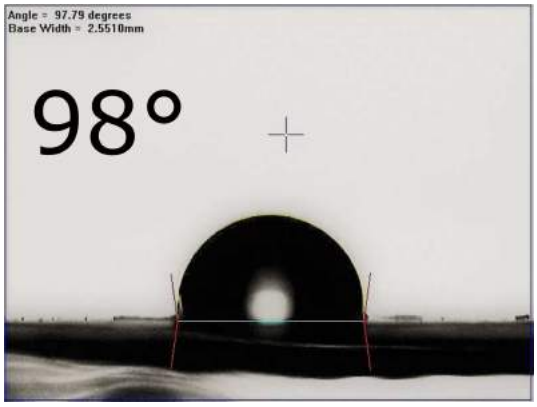

Supplementary Figure 10: Hydrophobicity of GS. Water contact angle of GS.

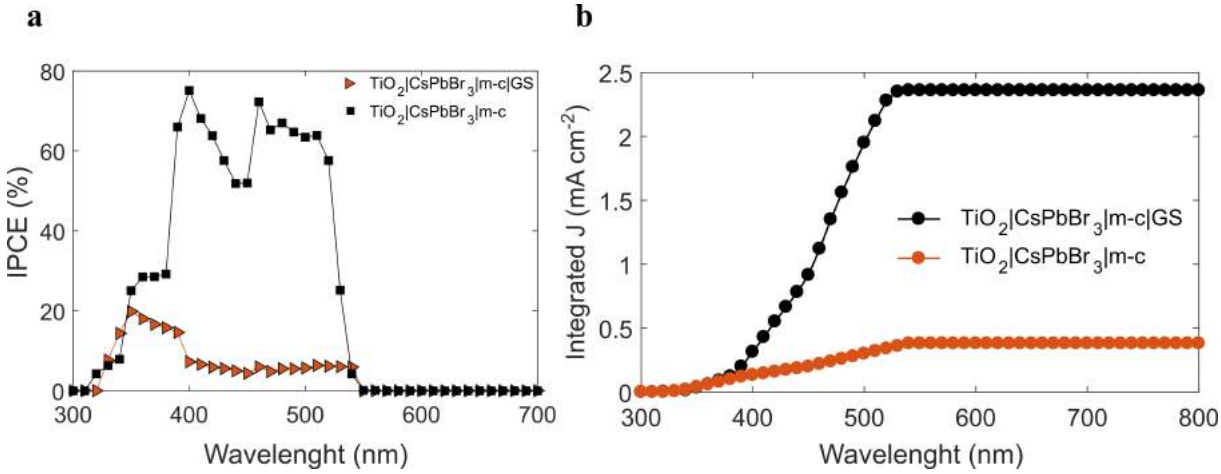

Supplementary Figure 11: Effect of GS encapsulation on PEC performance. **a** Wavelength dependence of the IPCE for $TiO_2|CsPbBr_3|$m-c and $TiO_2|CsPbBr_3|$m-c|GS photoanodes in aqueous buffer solution (k-borate, pH 9) under monochromatic light irradiation at $1.23\,\mathrm{V}$ versus RHE. **b** Theoretical integrated photocurrent density obtained from the IPCE measurement.

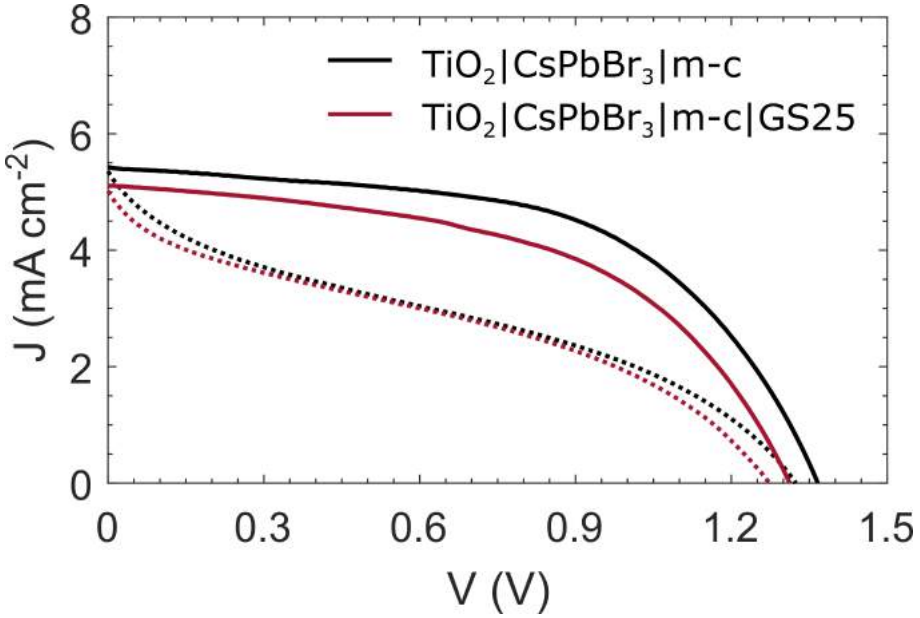

Supplementary Figure 12: Effect of GS25 on photovoltaic proerties. JV curves measured under reverse (solid line) and forward scan (dotted line) of TiO_2|$CsPbBr_3$|m-c (black line) and TiO_2|$CsPbBr_3$|m-c|GS (red line). The same device was measured before and after applying the GS on the surface. Supplementary table 1 lists the main photovoltaic parameters with the relative percentage decrease after GS was applied on the surface.

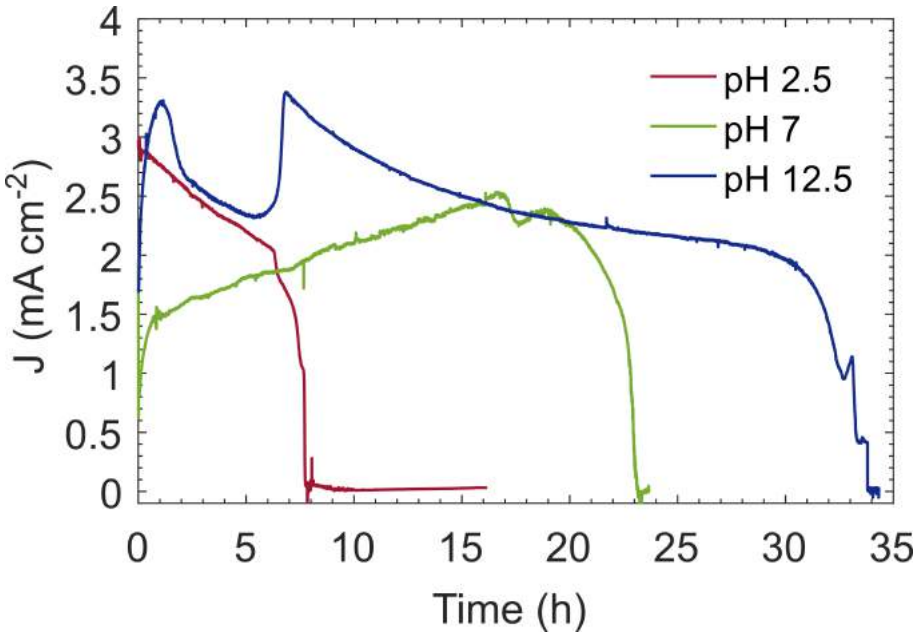

Supplementary Figure 13: Stability as a function of the pH. Chronoamperometric trace of TiO_2|$CsPbBr_3$|m-c|GS recorded at an applied potential of $1.23\,\mathrm{V}_{RHE}$. 0.1 M KNO_3 electrolyte solution at pH adjusted to 2.5, 7 and 12.5 with H_2SO_4 and KOH, under continuous simulated solar light irradiation (AM 1.5 G, $100\,\mathrm{mW\,cm^{-2}}$).

Supplementary Figure 14: Fracture of GS causing water infiltration. Photograph of the device tested at an applied potential of $1.23\,\mathrm{V}$ versus RHE. 0.1 M KNO_3 electrolyte solution pH 7, under continuous simulated solar light irradiation after $23\,\mathrm{h}$ of operation under continuous illumination.

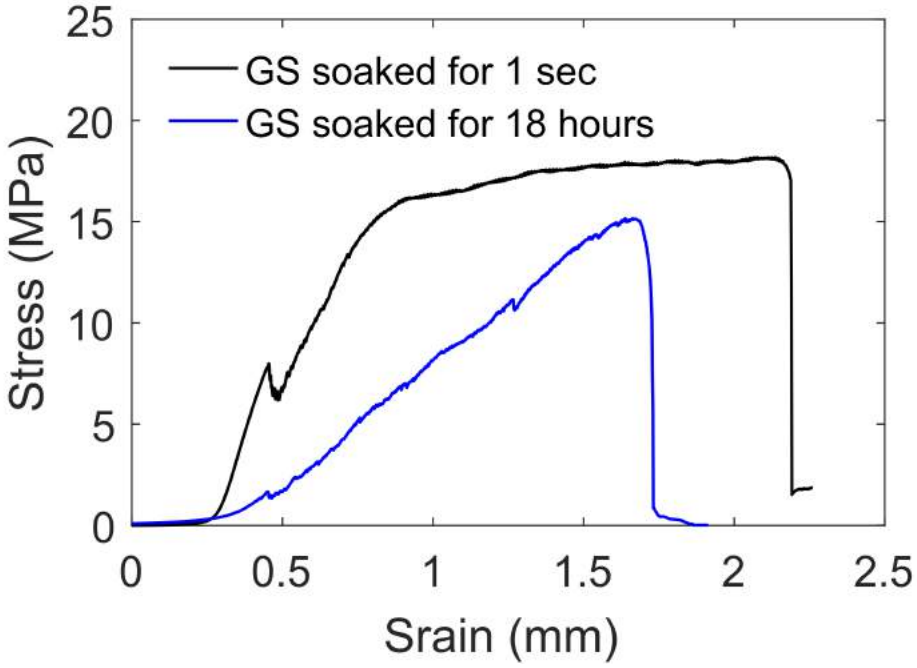

Supplementary Figure 15: Effect of soaking on the mechanical properties of GS. Tensile strength measured for wet GS; The black line indicates GS soaked in aqueous electrolyte for only 1 s. The blue line instead indicates a GS that has been immersed in the aqueous electrolyte (0.1 M KNO_3, pH 7) for 18 h.

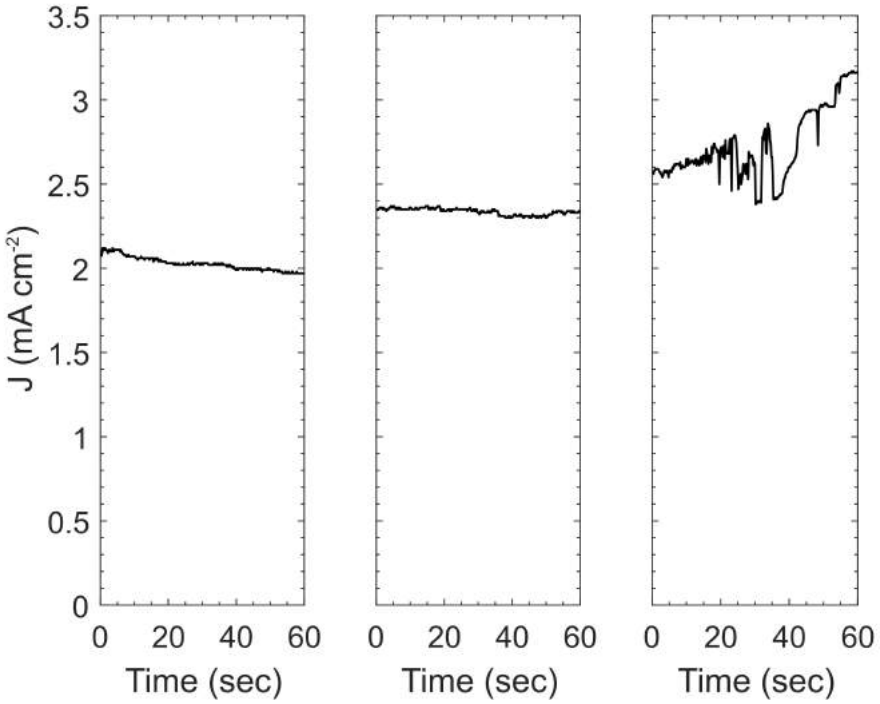

Supplementary Figure 16: Effect of soaking on the photocurrent density. Chronoamperometric trace of $TiO_2|CsPbBr_3|$m-c|GS recorded in 0.1 M KNO_3 solution (pH 7) with an applied potential of 1.23 V_{RHE}. Between each measurement the device was kept in the electrolyte solution for 1 hour in the dark at open circuit.

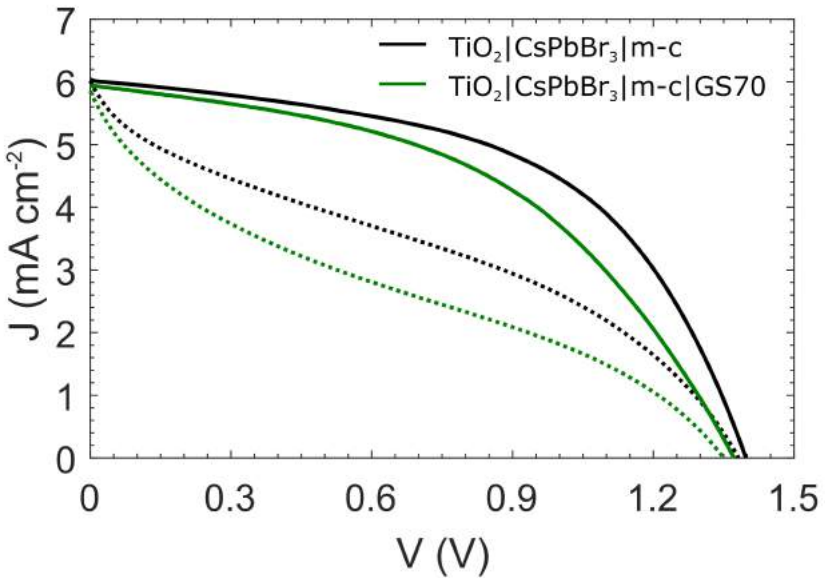

Supplementary Figure 17: Effect of GS70 on the photovoltaic properties. JV curves measured under reverse (solid line) and forward scan (dotted line) of $TiO_2|CsPbBr_3|$m-c (black line) and $TiO_2|CsPbBr_3|$m-c|GS70 (green line). The same device was measured before and after applying the GS70 on the surface. Supplementary table 2 lists the main photovoltaic parameters with the relative percentage decrease after GS70 was applied on the surface.

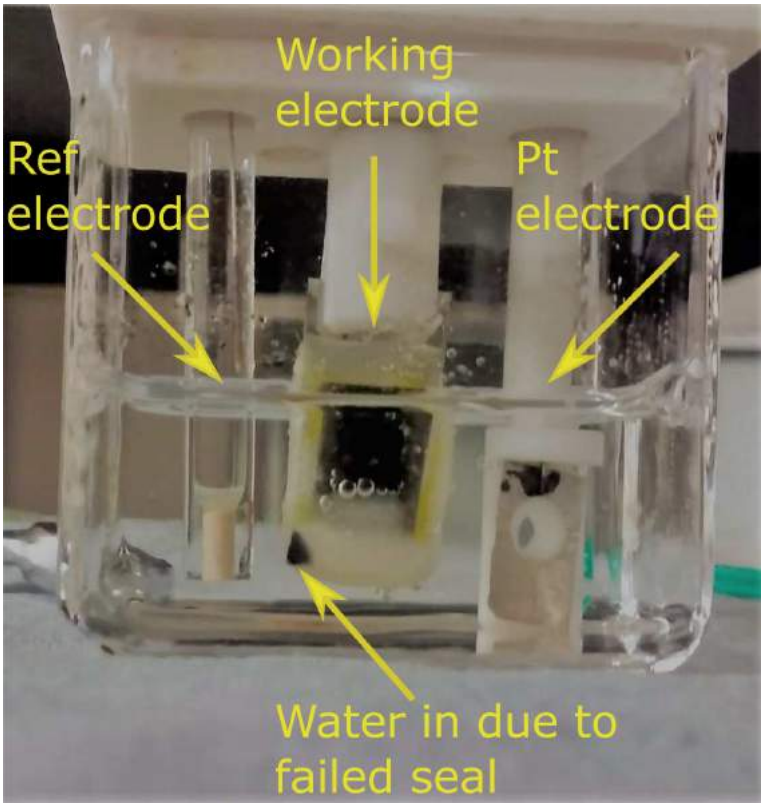

Supplementary Figure 18: PEC cell with three electrode configuration. Photograph of the three-electrode PEC cell with $TiO_2|CsPbBr_3|$m-c|GS70 photoanode used as working electrode. Water got through the device layers, dissolving the absorber material due to a leakage through the seal after the silicone-epoxy resin partially degraded in the electrolyte because of the long time immersion in water.

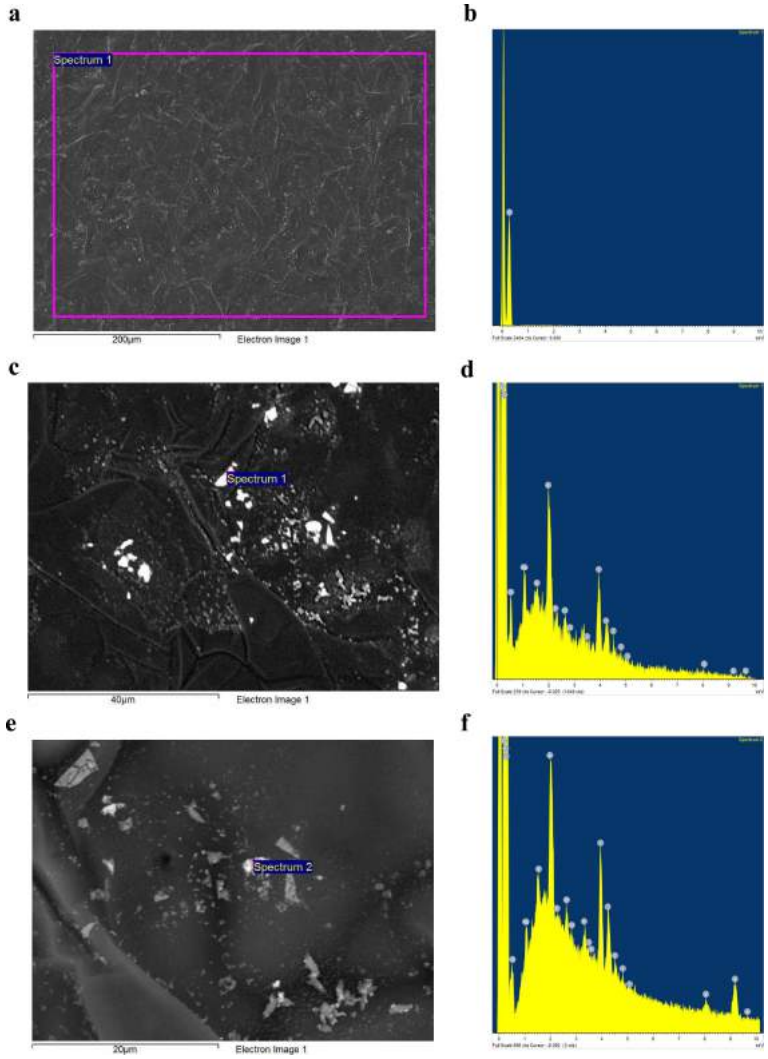

Supplementary Figure 19: Elemental composition of GS|WOC. EDX mapping images and elemental composition of GS|WOC, confirming the presence of Ir on the surface. Top-view SEM images were taken at different magnification. **a** scale bar 200 µm and **b** elemental composition of the area delimited by magenta borders in a (labelled Spectrum 1). **c** scale bar 40 µm and **d** elemental composition of the area delimited by magenta borders in c (labelled Spectrum 1). **e** scale bar 20 µm and **f** elemental composition of the area delimited by magenta borders in e (labelled Spectrum 2).

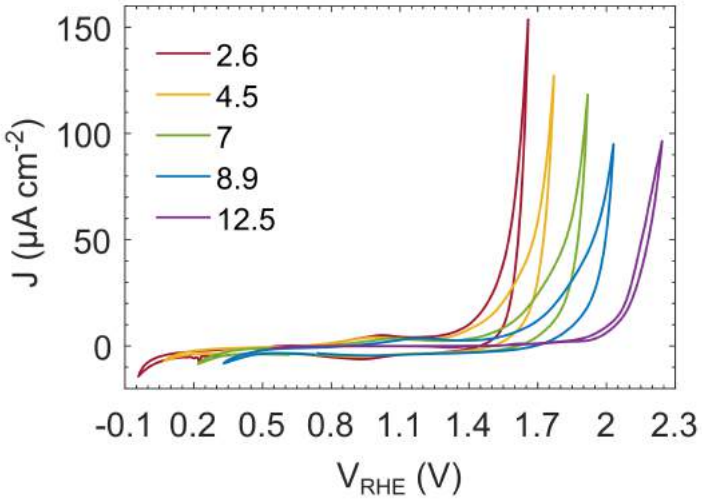

Supplementary Figure 20: Effect of pH on the water oxidation of GS|WOC. CV scans of GS|WOC electrodes performed in 0.1 M KNO_3 solution with pH adjusted with H_2SO_4 and KOH; scan rate of $50\,\mathrm{mV\,s^{-1}}$

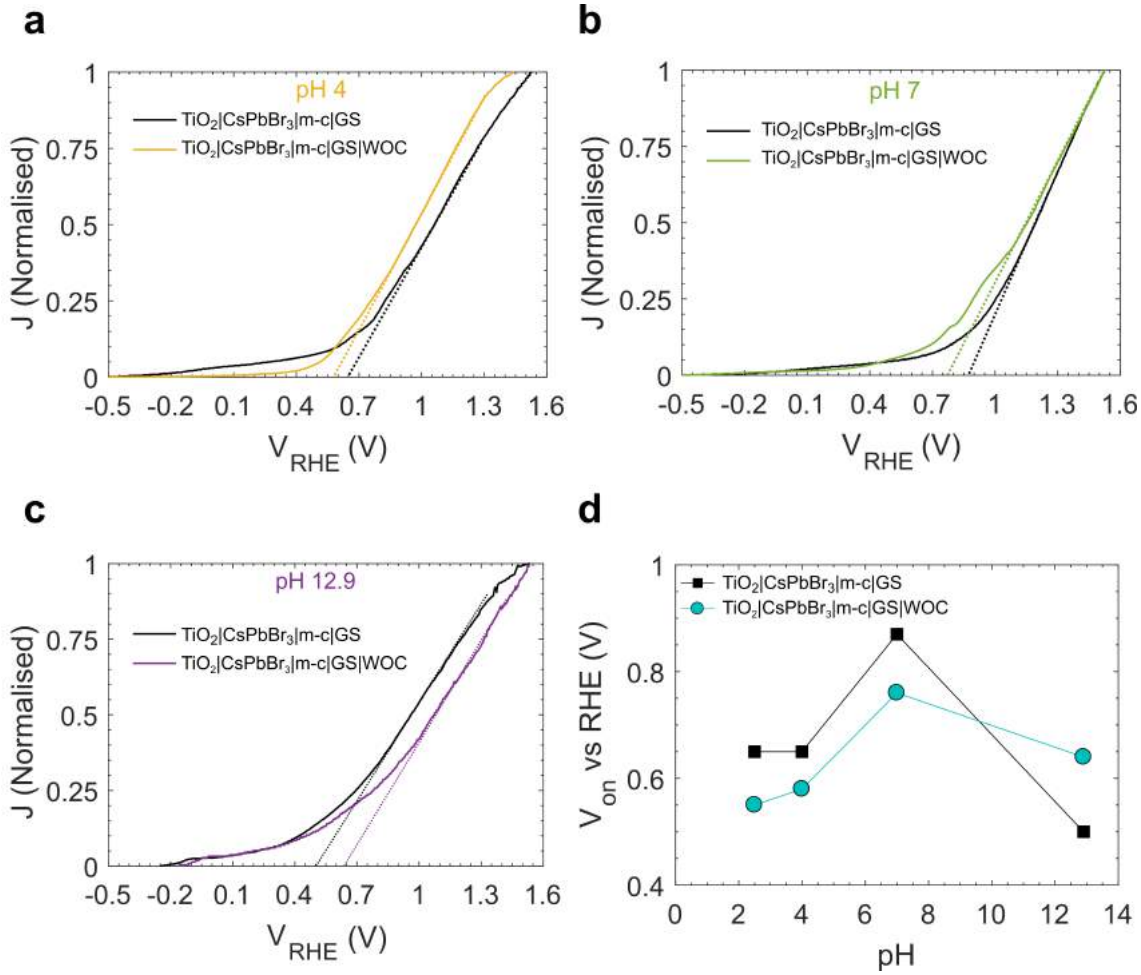

Supplementary Figure 21: Effect of pH on the onset potential. LSV of $TiO_2|CsPbBr_3|$m-c|GS photoanodes with and without functionalised GS measured in 0.1 M KNO_3 with pH adjusted with H_2SO_4 and KOH at **a** 4, **b** 7 and **c** 12.9. The photocurrent density has been normalised with respect to the maximum value obtained. **d** Onset potentials of $TiO_2|CsPbBr_3|$m-c|GS (GS) and $TiO_2|CsPbBr_3|$m-c|GS|WOC (GS|WOC) photoanodes as a function of the pH. (See Supplementary Note 3).

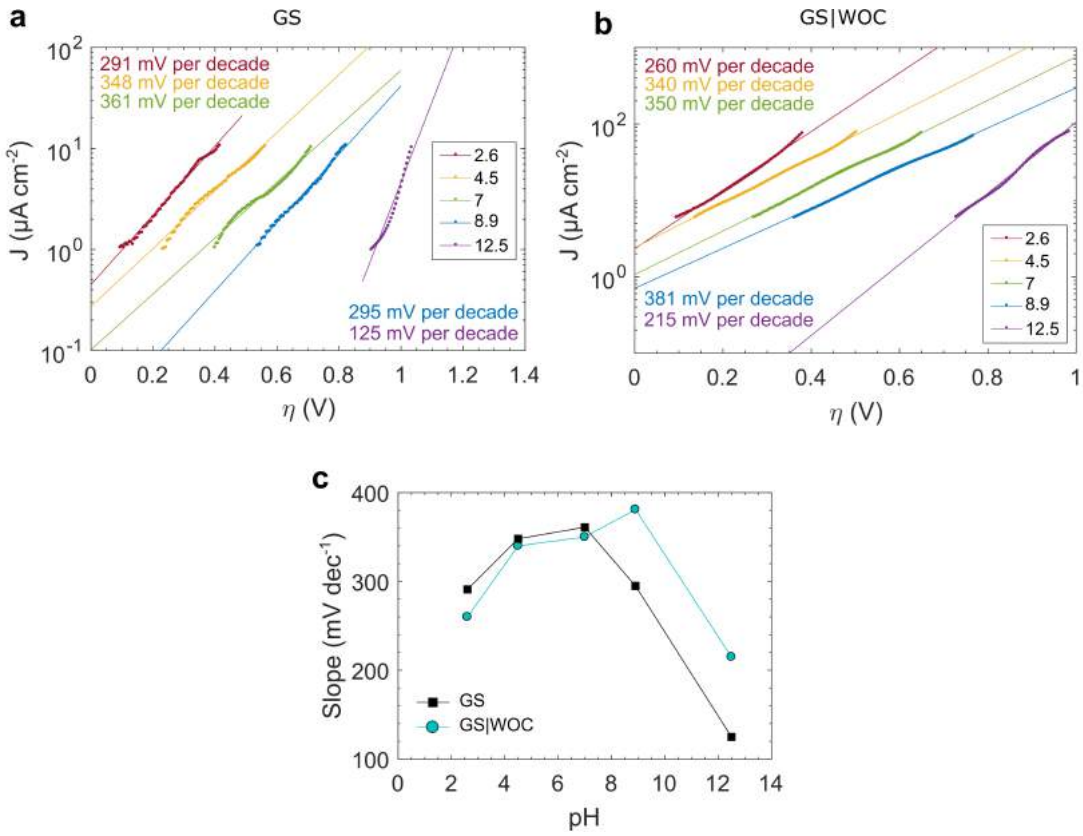

Supplementary Figure 22: Tafel analysis of GS|WOC. Tafel plots of **a** GS and **b** GS|WOC derived from the cyclic voltammograms displayed in Fig 20. **c** Tafel slopes of GS and GS|WOC electrodes as a function of pH of the solution

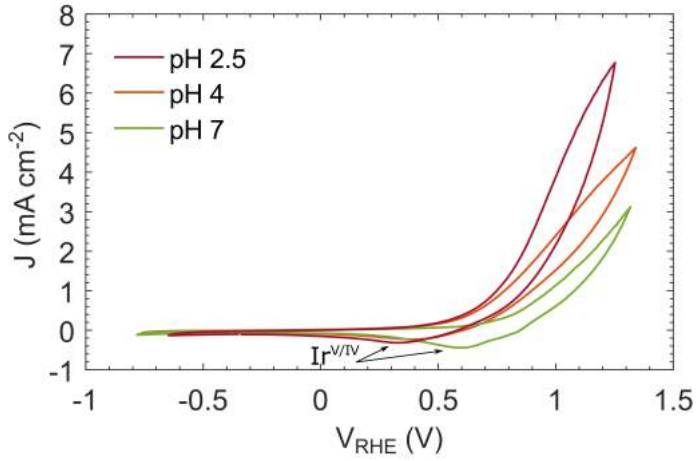

Supplementary Figure 23: Effect of pH on the TiO_2|$CsPbBr_3$|m-c|GS|WOC PEC performance. CV scans of TiO_2|$CsPbBr_3$|m-c|GS|WOC electrodes performed in 0.1 M KNO_3 solution at pH 2.5, 4 and 7 with a scan rate of $50\,\mathrm{mV\,s^{-1}}$. The reduction wave for the $Ir^{V/IV}$ couple can be seen on the reverse scan, while it is not detected in the forward scan. The same behaviour was previously observed on hematite photoanodes functionalised with the same Ir-WOC. [1]

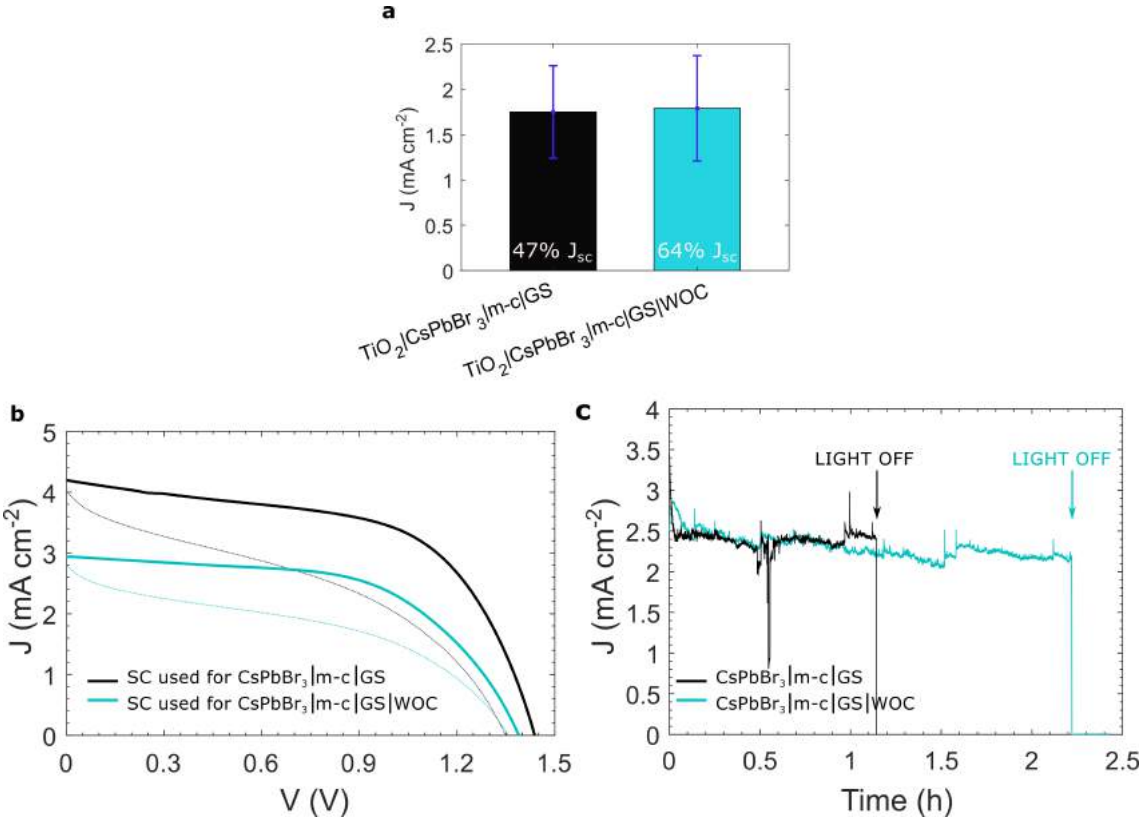

Supplementary Figure 24: PV and PEC performance of $TiO_2|CsPbBr_3|$m-c$|$GS devices. **a** PEC current density measured at 1.23 V versus RHE averaged over 11 and 7 samples respectively (error bars indicate the standard deviation). **b** JV curves of the as-prepared $TiO_2|CsPbBr_3|$m-c solar cells used to prepare the photoanodes for PEC testing. The solid line is measured under reverse scan. The dotted line is measured under forward scan. **c** Chronoamperometric traces of the resulting photoanodes $TiO_2|CsPbBr_3|$m-c$|$GS and $TiO_2|CsPbBr_3|$m-c$|$GS$|$WOC recorded in 0.1 M KNO_3 with pH adjusted to 3.5 with H_2SO_4 under constant illumination. (See Supplementary Note 4).

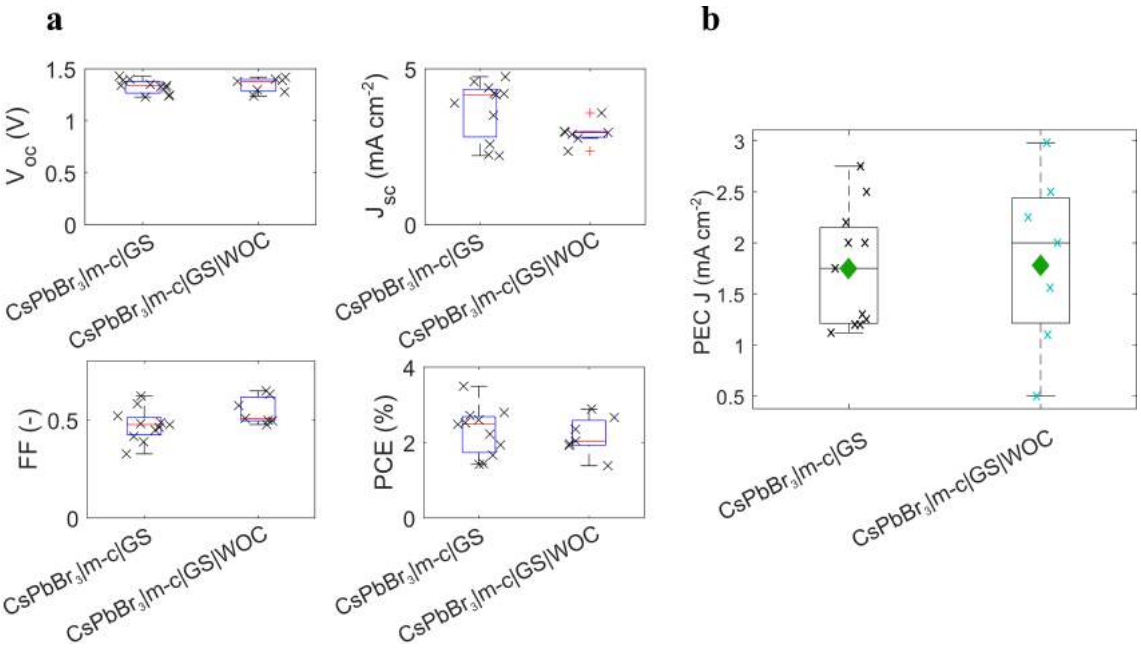

Supplementary Figure 25: Statistical analysis of PV and PEC performance of TiO_2|$CsPbBr_3$|m-c|GS. a Box plots of the main photovoltaic parameters of the as-prepared TiO_2|$CsPbBr_3$|m-c solar cells used to prepare the photoanodes for PEC testing. **b** Box plots of PEC J at 1.23 V versus RHE of TiO_2|$CsPbBr_3$|m-c|GS and TiO_2|$CsPbBr_3$|m-c|GS|WOC. The green markers indicate the average value. (See Supplementary Note 4).

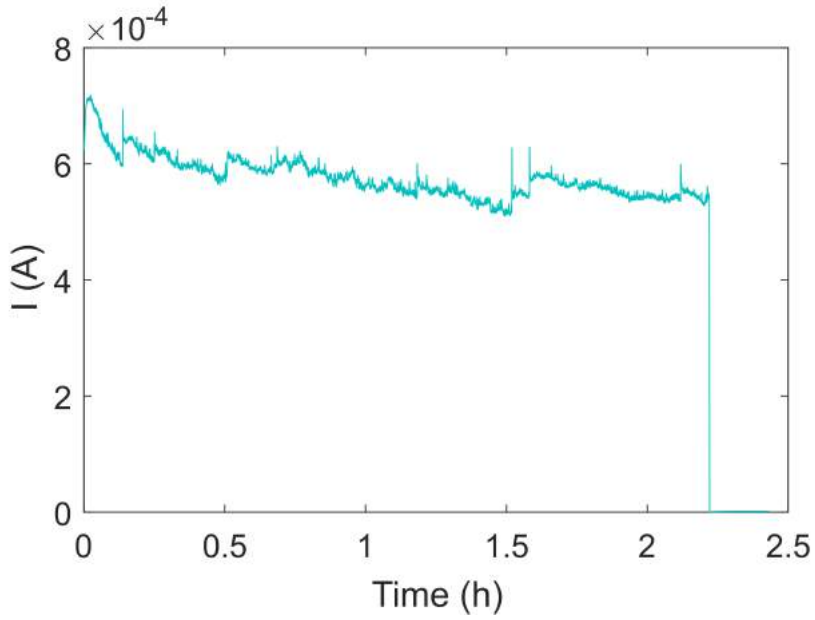

Supplementary Figure 26: Stability of TiO_2|$CsPbBr_3$|m-c|GS|WOC in three-electrode configuration. Chronoamperometric trace of TiO_2|$CsPbBr_3$|m-c|GS|WOC recorded in 0.1 M KNO_3 with pH adjusted to 3.5 with H_2SO_4 under continuous simulated solar light illumination during O_2 evolution detection. (See Supplementary Note 5).

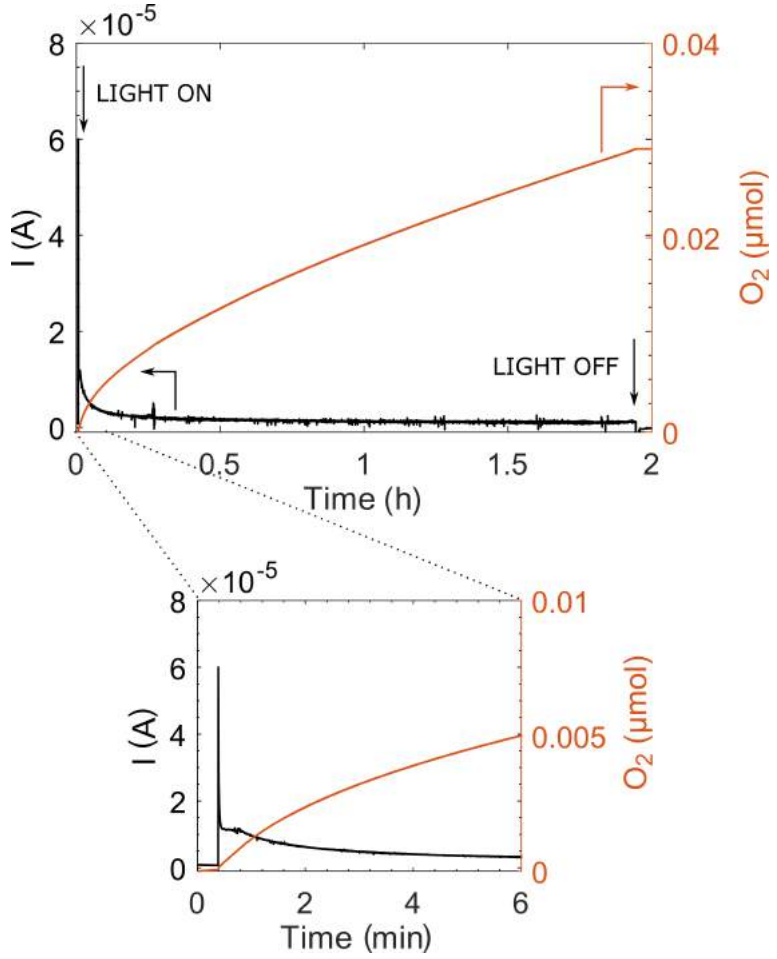

Supplementary Figure 27: Stability of TiO_2|$CsPbBr_3$|m-c|GS|WOC in two-electrode configuration. Chronoamperometric trace of TiO_2|$CsPbBr_3$|m-c|GS|WOC recorded in a two-electrode cell in 0.1 M KNO_3 (pH adjusted to 2.5 with H_2SO_4) without applying any external bias between the working and Pt counter electrode and predicted O_2 production, assuming that O_2 formation liberates 4 electrons.

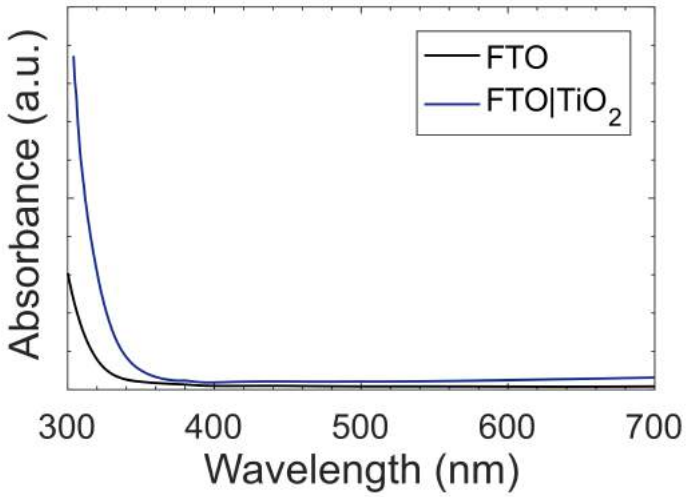

Supplementary Figure 28: Absorbance of FTO c-glass substrates. UV-Vis absorbance of glass coated with FTO and FTO|TiO_2

Supplementary Tables

Supplementary Table 1: Effect of GS25 on the main photovoltaic parameters. Photovoltaic parameters of the TiO_2/$CsPbBr_3$/m-c solar cell shown in Supplementary Figure 12 before and after applying the GS25 on top of m-c layer.

	TiO_2/$CsPbBr_3$/m-c	**TiO_2/$CsPbBr_3$/m-c/GS**	% decrease
J_{sc} ($mA\,cm^{-2}$)	5.43	5.12	5.7
V_{oc} (V)	1.36	1.31	3.7
FF	0.56	0.53	5.3
PCE (%)	4.13	3.50	15.2

Supplementary Table 2: Effect of GS70 on the main photovoltaic parameters. Photovoltaic parameters of the TiO_2/$CsPbBr_3$/m-c solar cell shown in Supplementary Figure 17 before and after applying the GS70 on top of m-c layer.

	TiO_2/$CsPbBr_3$/m-c	**TiO_2/$CsPbBr_3$/m-c/GS70**	% decrease
J_{sc} ($mA\,cm^{-2}$)	6.04	5.94	1.7
V_{oc} (V)	1.39	1.37	1.4
FF	0.53	0.47	11.3
PCE (%)	4.47	3.85	13.9

Supplementary Notes

Supplementary Note 1 Supplementary Fig. 5: Since electrolytes were exposed to air, oxygen reduction taking place at the FTO electrodes explains the dark negative current at cathodic potentials. [2] Indeed, when all the photoanode but the active area was covered with epoxy, avoiding physical contact between the FTO substrate and the electrolyte solution, the dark current at negative potentials was substantially reduced. Similar dark negative currents have been reported in literature [3–5] and they are not particularly relevant to the performance of the photoanode that was studied at higher applied potentials of $1.23\,\mathrm{V}_{RHE}$, where the dark current is in fact zero.

Supplementary Note 2 Supplementary Fig. 9: The porosity of m-c and GS have been measured via mercury porosimetry analysis, which studies the progressive intrusion of mercury into a porous structure under stringently controlled pressures (going from low to high penetration pressure). This technique allows to determine the pore size of the material. The steep part of the curve in Fig. 9a represents the mercury penetration in well-defined pores. The mesoporous carbon layer m-c is highly porous. In contrast, GS is highly compact and dense and has a very poor porosity.

Supplementary Note 3 Supplementary Fig. 21d: The onset potential V_{on} of $TiO_2|CsPbBr_3|$m-c$|$GS and $TiO_2|CsPbBr_3|$m-c$|$GS$|$WOC has been measured in electrolytes with pH ranging between 2.5 and 12. Herein, V_{on} is defined conservatively as the potential that corresponds to the intercept between the dark current and the tangent to the maximum slope of the current rise under illumination. [6]

Supplementary Note 4 Supplementary Fig. 24 and Supplementary Fig. 25: Average PEC current density J measured on 11 $TiO_2|CsPbBr_3|$m-c|GS and 7 $TiO_2|CsPbBr_3|$m-c|GS|WOC photoanodes at $1.23\,\mathrm{V}_{RHE}$. Measurements were taken from distinct samples. The PEC J at $1.23\,\mathrm{V}_{RHE}$ of $TiO_2|CsPbBr_3|$m-c|GS was on average $47\,\%$ of J_{sc} of the as-prepared solar cells, while PEC J of $TiO_2|CsPbBr_3|$m-c|GS|WOC was $64\,\%$ of J_{sc} of the as-prepared solar cells. The average water oxidation photocurrents are equal but the average photovoltaic currents (Jsc) of $TiO_2|CsPbBr_3|$m-c|GS|WOC devices were lower than the ones measured for $TiO_2|CsPbBr_3|$m-c|GS.
Box plots in Supplementary Fig 25: The boxes plot the first and third quartiles, and the band inside the box is the second quartile (the median). The ends of the whiskers represent that the lowest datum is still within 1.5 of the interquartile range (IQR) of the lower quartile, and the highest datum is still within 1.5 IQR of the upper quartile. Red crosses indicate outlier data that are out of the 1.5 IQR.

Supplementary Note 5 The O_2 evolution on the $TiO_2|CsPbBr_3|$m-c$|$GS$|$WOC under constant illumination at $1.23\,\mathrm{V}$ versus RHE was measured. Supplementary Fig. 26 shows the chronoamperometric trace recorded during O_2 evolution detection, which was used to calculate the predicted O_2 production.

Supplementary Discussion

The predicted O_2 value was compared with the measured oxygen level to calculated the Faradaic efficiency. A Faradaic efficiency of $80.9\,\%$ was achieved after $2\,\mathrm{h}$ of testing. Part of the generated oxygen will dissolve in the solution (which is purged for $15\,\mathrm{minute}$ with N_2 before the start of the experiment) and therefore would not be detected by an oxygen probe in the headspace of the cell. The oxygen dissolved in the liquid was estimated according to Henry's law.

The observed delay between the generation of O_2 at the photoanode surface and the actual detection in the headspace of the cell can be assigned to the slow diffusion of oxygen into the membrane of the electrode sensor. [7] In fact, before reaching the probe and be detected, oxygen has to diffuse through any porosity in the graphite layers, saturate the electrolyte, diffuse in the headspace, and finally diffuse through the sensor membrane.

Supplementary References

1. Moir, J. W., Sackville, E. V., Hintermair, U. & Ozin, G. A. Kinetics versus Charge Separation: Improving the Activity of Stoichiometric and Non-Stoichiometric Hematite Photoanodes Using a Molecular Iridium Water Oxidation Catalyst. *J. Phys. Chem. C* **120**, 12999–13012 (2016).

2. Díez-García, M. I. *et al.* $YFeO_3$ Photocathodes for Hydrogen Evolution. *Electrochim. Acta* **246**, 365–371 (2017).

3. Gurudayal *et al.* Core-Shell Hematite Nanorods: A Simple Method To Improve the Charge Transfer in the Photoanode for Photoelectrochemical Water Splitting. *ACS Appl. Mater. Interfaces* **7**, 6852–6859 (2015).

4. Bu, Y. *et al.* Optimization of the Photo-Electrochemical Performance of Mo-Doped $BiVO_4$ Photoanode by Controlling the Metal-Oxygen Bond State on (020) Facet. *Adv. Mater. Interfaces* **4**, 1601235 (2017).

5. Kumar, P. *et al.* Quantum dot activated indium gallium nitride on silicon as photoanode for solar hydrogen generation. *Commun. Chem.* **2**, 4 (2019).

6. Cao, D. *et al.* Cathodic shift of onset potential for water oxidation on a Ti^{4+} doped Fe_2O_3 photoanode by suppressing the back reaction. *Energy and Environmental Science* **7**, 752–759 (2014).

7. Shi, Y. *et al.* CuO-Functionalized Silicon Photoanodes for Photoelectrochemical Water Splitting Devices. *ACS Appl. Mater. Interfaces* **8**, 695–702 (2016).

6.1.3 Contemporary assessment

The paper 'Graphite-protected $CsPbBr_3$ perovskite photoanodes functionalised with water oxidation catalyst for oxygen evolution in water' by Poli *et al.* demonstrated a facile technique to encapsulate $CsPbBr_3$ and develop photoanodes for the photoelectrochemical evolution of oxygen from water. [16] This was the first example of a $CsPbBr_3$-based photoanode and the first time that commercially available graphite sheets were used as protection layers. Most of the works that reported the use of halide perovskites in PEC systems used $CH_3NH_3PbI_3$-based electrodes. The limitation in using the archetypal $MAPbI_3$ is its limited photovoltage that requires high overpotentials to drive water splitting reactions.

The use of a metal-free material to encapsulate and protect the absorber layer was another important aspect of the publication. In fact, previous works only reported the use of Ni, Ti foil and FM to protect the sensitive halide perovskite material. While the paper by Poli *et al.* was under final review and consideration for publication, Tao *et al.* published a $CH_3NH_3PbI_3$ photoanode encapsulated with inexpensive conductive carbon paste and silver conductive paint. [14] Even though the latter technique proved to be effective in protecting the sensitive $CH_3NH_3PbI_3$, more complex architectures were used when compared to the method proposed by Poli *et al.*. A triple mesoporous screen printed cell (TiO_2, ZrO_2 and m-c) infiltrated with a $MAPbI_3$ perovskite solution was used. On top of the m-c layer, an extra conductive carbon paste layer, a silver conductive paint layer and a final conductive carbon paste layer were deposited. A faradaic efficiency $>80\,\%$ was achieved and the photocurrent density decreased by $\sim 30\,\%$ over $12\,\mathrm{h}$ of continuous operation due to water infiltration through existent pinholes. The use of carbon and silver pastes do not allow the creation of a compact hydrophobic protection layer in the way that GS does. Moreover, the method proposed in this thesis demonstrated higher versatility with the addition of a water oxidation catalyst at the photoanode/electrolyte interface, while Tao *et al.* did not use any catalyst.

As of date of publication of this thesis, the lifetime record shown here for an halide perovskite-based device immersed in water still stands.

6.2 Stable $MAPbI_3$ photoanodes for oxygen evolution in water

The GS encapsulation presented in section 6.1 proved to be particularly effective in protecting $CsPbBr_3$ planar carbon cells from water. One of the advantages of such design is the flexibility of the underlying perovskite material. Wide-bandgap materials like $CsPbBr_3$ ($E_g \sim 2.3\,\mathrm{eV}$) have the advantage of generating high voltages under illumination, which are very close to the energy required for unbiased water splitting. In contrast, $MAPbI_3$-based devices ($E_g \sim 1.6\,\mathrm{eV}$) generate considerably lower photovoltages and much higher overpotentials are needed to drive water splitting

reactions. However, much higher photocurrents can be achieved because larger portion of the solar spectrum can be used.

This section investigates the use of GS encapsulation to fabricate $MAPbI_3$ photoanodes to drive oxygen evolution reaction in water in a PEC system.

6.2.1 Experimental methods

The photoanodes discussed in this section consisted of triple mesoporous carbon solar cells containing $MAPbI_3$ with 5AVA as additive. The triple mesoscopic substrates were fabricated by Dr Jenny Baker in Swansea University (SPECIFIC); solar cells were then infiltrated and characterised at the University of Bath. Figure 6.2 shows a schematic of the architecture of the triple mesoscopic carbon solar cell. All layers were printed in air at ambient conditions. A compact TiO_2 layer was deposited by spraying $0.2\,\mathrm{M}$ titanium diidopropoxide bis(acetylacetonate) solution in 2-propanol on FTO substrates kept at $300\,^{\circ}\mathrm{C}$. A TiO_2 paste (Dyesol 30-NRD diluted 1:1 in terpinol) was screen printed on the surface and sintered at $550\,^{\circ}\mathrm{C}$ for $30\,\mathrm{min}$ ($\sim 800\,\mathrm{nm}$). A ZrO_2 layer (Solaronix ZT/SP, $\sim 1.2\,\mu\mathrm{m}$) was screen printed and annealed at $400\,^{\circ}\mathrm{C}$ for $30\,\mathrm{min}$. Finally, a $10\,\mu\mathrm{m}$ thick layer of mesoporous carbon (GEM D3) was screen printed on the surface and annealed at $400\,^{\circ}\mathrm{C}$ for $30\,\mathrm{min}$.
An equimolar perovskite solution of PbI_2 and MAI was prepared in γ-butyrolactone (Sigma-Aldrich) and 5AVA was added to obtain 3mol% ratio between 5AVA and MAI. $6\,\mu\mathrm{l}$ of precursor solution was drop casted through the mesoscopic layers and annealed for $1\,\mathrm{h}$ at $50\,^{\circ}\mathrm{C}$.

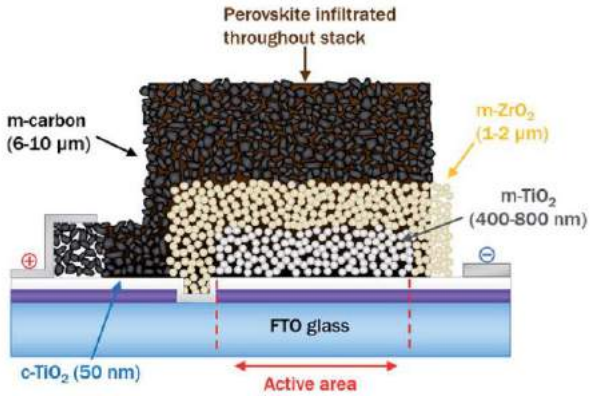

Figure 6.2: Schematic of a triple mesoscopic carbon solar cell. Reproduced from [17].

To fabricate $MAPbI_3$ photoanodes and test them in aqueous solution a graphite thermal sheet (Panasonic, $70\,\mu\mathrm{m}$, selfadhesive on one side) was stuck by hand onto the mesoporous carbon top layer. The device was finally sealed (except an active area of $0.25\,\mathrm{cm}^2$) with commercial silicone and epoxy resin and left to harden out at room temperature overnight.

Masked devices ($0.25\,\mathrm{cm}^2$) were tested under a solar simulator (TS SPACE SYSTEMS) at AM 1.5 G, $100\,\mathrm{mW\,cm}^{-2}$ illumination conditions using a Keithley 2601A

potentiostat. The devices were scanned from $1.2\,\mathrm{V}$ to $0\,\mathrm{V}$ and vice versa at a scan rate of $100\,\mathrm{mV\,s^{-1}}$, after $2\,\mathrm{min}$ of light soaking at $1.2\,\mathrm{V}$.

6.2.2 5AVA-$MAPbI_3$ photoanodes for PEC water splitting

Perovskite photoanodes were prepared infiltrating the perovskite solution through a triple mesoscopic stack of TiO_2/ZrO_2/m-c. 5AVA-$MAPbI_3$ devices were first tested as solar cells. Figure 6.3 a shows the current density-voltage (JV) curve of a typical triple mesoporous carbon cell under forward and reverse scan. The JV curve measured under reverse scan exhibited V_{OC}=0.85 V, J_{SC}=21.7 $\mathrm{mA\,cm^{-2}}$, *FF*=0.54 and *PCE*=9.95 %.

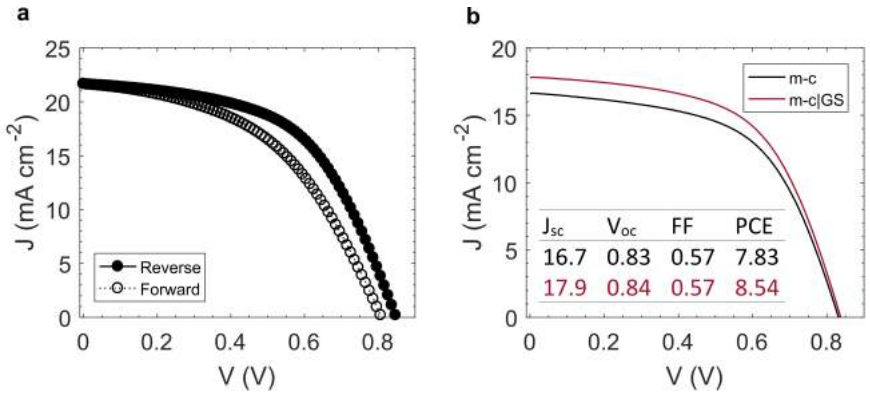

Figure 6.3: a JV curves measured under reverse (close circle) and forward (open circle) scan of 5AVA-$MAPbI_3$ triple mesoporous carbon solar cell. **b** JV curves measured under reverse scan of a 5AVA-$MAPbI_3$ carbon solar cell before and after applying the GS70 on the surface.

The carbon top layer is highly hydrophobic and allows holes to be transported and extracted at the surface. [16] However, it is not sufficiently compact and water would easily penetrate through the pores, irreversibly degrading the active absorber $MAPbI_3$ perovskite. In order to more efficiently protect the perovskite material from water, a $70\,\mu\mathrm{m}$ GS (GS70) sheet was placed on top of the mesoporous carbon top contact. The same GS material had already proved to be a particularly effective encapsulation layer when used on planar $CsPbBr_3$ carbon devices. [16] Figure 6.3 b shows JV curves of a triple mesoscopic carbon solar cell before and after applying GS70 on the surface. The main photovoltaic parameters slightly improved upon addition of the GS on the surface, indicating that GS70 did not hinder transport nor extraction of charges.

Figure 6.4 a shows the linear sweep voltammetry (LSV) curve of a 5AVA-$MAPbI_3$ photoanode measured at pH 2.8. The photocurrent steeply rose from $\sim 1.25\,\mathrm{V_{RHE}}$ on, achieving a photocurrent density of about $6\,\mathrm{mA\,cm^{-2}}$ at $1.5\,\mathrm{V_{RHE}}$. The onset potential measured for 5AVA-$MAPbI_3$ is higher than the one measured for $CsPbBr_3$-based photoanodes by $\sim 0.7\,\mathrm{V}$. This may be due to reduced charge transfer at the interface. It is known that triple mesoporous carbon based cells containing 5AVA-$MAPbI_3$ require extensive periods of preconditioning in order to measure optimum JV curves.

[18] In fact, JV curves shown in figure 6.3 were scanned after $2\,\mathrm{min}$ of light soaking at open circuit conditions. A recent work that investigated photoanodes based on a triple mesoscopic carbon solar cells infiltrated with 5AVA-$MAPbI_3$ reported a lower onset potential of about $1\,\mathrm{V_{RHE}}$. The latter architecture used a $100\,\mu\mathrm{m}$ silver conductive paint layer sandwiched between two conductive carbon paste layers.

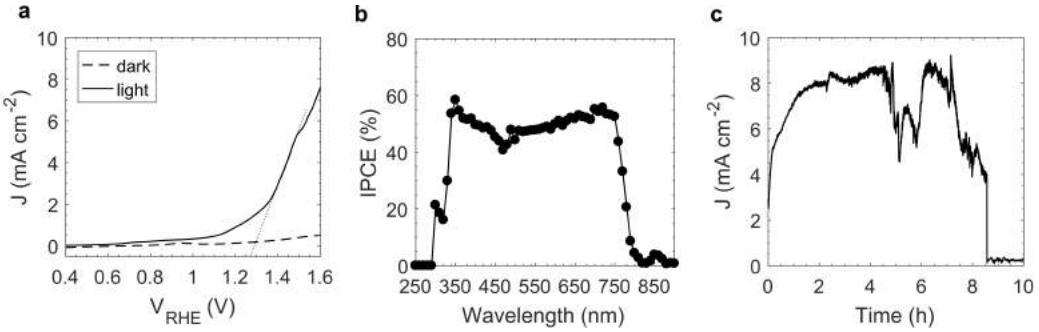

Figure 6.4: a LSV curve of 5AVA-$MAPbI_3$ triple mesoporous carbon photoanode measured in the dark (dashed line) and under simulated solar illumination (solid line), ($0.1\,\mathrm{M}$ KNO_3, pH 2.8 adjusted with H_2SO_4). **b** IPCE curve of 5AVA-$MAPbI_3$ triple mesoporous carbon photoanode measured at $1.5\,\mathrm{V_{RHE}}$ ($0.1\,\mathrm{M}$ KNO_3, pH 2.8 adjusted with H_2SO_4). **c** Chronoamperometric trace of 5AVA-$MAPbI_3$ triple mesoporous carbon photoanode measured at $1.5\,\mathrm{V_{RHE}}$ ($0.1\,\mathrm{M}$ KNO_3, pH 2.8 adjusted with H_2SO_4).

The wavelength dependence of the incident photon-to-current efficiency (IPCE) was measured in aqueous solution, at pH 2.8, at an applied bias of $1.5\,\mathrm{V_{RHE}}$ and it is shown in figure 6.4 b. An onset wavelength of $\sim 800\,\mathrm{nm}$ was measured, indicating that the perovskite absorber material absorbed photons with energy $\geq 1.55\,\mathrm{eV}$. To investigate the long-term stability of 5AVA-$MAPbI_3$ photoanodes, chronoamperometry was recorded at a constant applied potential of $1.5\,\mathrm{V_{RHE}}$ in aqueous solution at pH 2.8, under continuous simulated solar light. The evolution of the photocurrent density until the end of life is shown in figure 6.4 c. The device achieved a lifetime of $9\,\mathrm{h}$ in acidic solutions. It is important to note that the end of life was caused by water infiltration through the slide edges due to failure of the silicone-epoxy resin sealing, suggesting that better sealing materials could easily extend the lifetime of these composite photoanodes.

Similarly to the results for $CsPbBr_3$ photoanodes encapsulated with GS, the photocurrent density was observed to increase from 3 to $9\,\mathrm{mA\,cm^{-2}}$ over the first $5\,\mathrm{h}$ of continuous illumination. Soaking effects of the GS may have been responsible for such increase, in fact the GS material experiences changes in its mechanical properties during soaking for extended periods of time. [16] Another explanation of such slow dynamic behaviour may be linked to the effects of ion migration. [19] Pockett *et al.* recently demonstrated that the extremely slow electrical response of 5AVA-$MAPbI_3$ triple mesoporous carbon solar cells is linked to the migration of iodide vacancies that occurs at much slower rates than the ones measured for pure $MAPbI_3$ or other halide perovskite solar cells (1.1 X $10^4\,\mathrm{s^{-1}}$ *vs* $10^{12}\,\mathrm{s^{-1}}$). [19]

To investigate further the slow response of triple mesoporous carbon solar cells

containing 5AVA-$MAPbI_3$, the evolution of the V_{oc} of a solar cell and the photovoltage ΔV_{ph} generated under illumination in aqueous solution over time were measured.

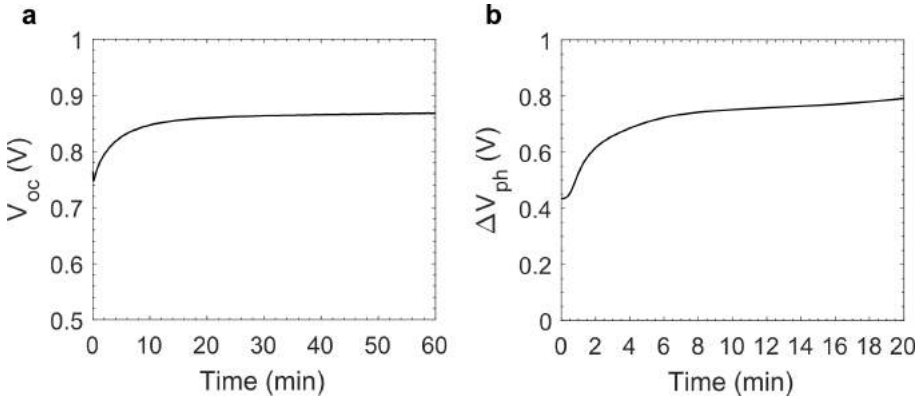

Figure 6.5: **a** Slow rise of V_{oc} of a 5AVA-$MAPbI_3$ triple mesoporous carbon solar cell measured in air under continuous illumination (excitation provided by a single wavelength LED light at $470\,\mathrm{nm}$). **b** Slow rise of ΔV_{ph} of a 5AVA-$MAPbI_3$ triple mesoporous carbon solar cell measured in aqueous solution under continuous illumination (simulated solar light, AM 1.5 G, $100\,\mathrm{mW\,cm^{-2}}$).

Figure 6.5 a shows the V_{oc} of a solar cell monitored in air over time under continuous illumination (single-wavelength laser $470\,\mathrm{nm}$). The V_{oc} increased over time with a very slow rate, reaching a steady state value after about $20\,\mathrm{min}$ of continuous illumination. Figure 6.5 b shows the evolution of the ΔV_{ph} measured in aqueous solution (pH 2.8) over $20\,\mathrm{min}$ of continuous illumination with simulated solar light. Very similar slow dynamic behaviours were observed for devices measured in aqueous solution with GS and in air without GS. These results suggest that the slow increase of the voltage observed in air and water may be linked to intrinsic properties of the 5AVA-$MAPbI_3$ perovskite material.

6.3 Chapter conclusions

Photoelectrochemical water splitting is an attractive approach that uses semiconductors and solar energy to split water into hydrogen and oxygen. Halide perovskites demonstrated exceptional optoelectronic properties like high absorption, high mobilities, long carrier lifetimes and broadly tunable bandgaps. However, their intrinsic instability towards high humidity retained them from being exploited in PEC systems, where the semiconductor needs to be in direct contact with water.

This chapter presented a novel, inexpensive and effective encapsulation technique to protect halide perovskites from high humidity preventing irreversible degradation when completely submerged in water. $CsPbBr_3$ planar carbon solar cells were coated with flexible graphite sheets (25-70 µm thick), offering a compact seal that could protect the halide perovskite from liquid water percolation for very long periods of time. $CsPbBr_3$ devices were used as photoanodes in PEC systems achieving

photocurrent densities higher than $2\,\mathrm{mA\,cm^{-2}}$ in water for over $30\,\mathrm{h}$ under continuous simulated solar illumination. To further demonstrate the versatility of this encapsulation technique, a water oxidation catalyst was added to the surface, improving the charge transport kinetics and achieving higher photocurrents at $1.23\,\mathrm{V_{RHE}}$. The faradaic efficiency for O_2 evolution in water on the photoanode surface was calculated to be higher than $80\,\%$, demonstrating that the observed photocurrent was mainly linked to O_2 production.

Finally, the same encapsulation technique was used to fabricate 5AVA-$MAPbI_3$ triple mesoscopic carbon photoanodes. The lower energy bandgap material ($1.56\,\mathrm{eV}$) allowed to measure photocurrents as high as $9\,\mathrm{mA\,cm^{-2}}$ at $1.5\,\mathrm{V_{RHE}}$ in water. A very slow electrical response under illumination of these composites were demonstrated both in air and water.

6.4 Future work

In the published article, the graphite sheet used to waterproof the $CsPbBr_3$ photoanode was functionalised with an Ir-based water oxidation catalyst. EDX analysis showed that the catalyst did not form a uniform monolayer but it was localised around the oxidic edges of the surface. The catalyst loading on the surface may be improved using electrochemical methods to increase the oxidic edges where the catalyst self-binds to. For example, the use of high anodic potentials may enrich the GS surface in oxygen functional groups. [20]

In this work, a self-adhesive GS was used. Future work may be looking at using different graphite-based materials to simplify the device architecture and enhance the charge extraction process. For example, the same GS is also commercially available without the back-adhesive. Several approaches were attempted to mechanically attach the GS onto the mesoporous carbon scaffold, such as hot-press and electrochemical methods. However, none of the techniques proved to be successful.

$CsPbBr_3$ photoanodes generated a photovoltage of $\sim 1.3\,\mathrm{V}$, which was not sufficient to drive unbiased water splitting. Future work may look at the development of an unbiased PEC water splitting tandem device obtained by matching the $CsPbBr_3$-based photoanode with a photocathode.

Bibliography

[1] A. M. A. Leguy, Y. Hu, M. Campoy-Quiles, M. I. Alonso, O. J. Weber, P. Azarhoosh, M. van Schilfgaarde, M. T. Weller, T. Bein, J. Nelson, P. Docampo, and P. R. F. Barnes, "Reversible Hydration of $CH_3NH_3PbI_3$ Films, Single Crystals, and Solar Cells," *Chem. Mater.*, vol. 27, no. 9, pp. 3397–3407, 2015.

[2] I. Hwang, I. Jeong, J. Lee, M. J. Ko, and K. Yong, "Enhancing Stability of Perovskite Solar Cells to Moisture by the Facile Hydrophobic Passivation," *ACS Appl. Mater. Interfaces*, vol. 7, no. 31, pp. 17330–17336, 2015.

[3] J. Idigoras, F. J. Aparicio, L. Contreras-Bernal, S. Ramos-Terrón, M. Alcaire, J. R. Sanchez-Valencia, A. Borras, A. Barranco, and J. A. Anta, "Enhancing Moisture and Water Resistance in Perovskite Solar Cells by Encapsulation with Ultrathin Plasma Polymers," *ACS Appl. Mater. Interfaces*, vol. 10, pp. 11587–11594, 2018.

[4] S. N. Habisreutinger, T. Leijtens, G. E. Eperon, S. D. Stranks, R. J. Nicholas, and H. J. Snaith, "Carbon nanotube/polymer composites as a highly stable hole collection layer in perovskite solar cells," *Nano Lett.*, vol. 14, no. 10, pp. 5561–5568, 2014.

[5] M. Crespo Quesada and E. Reisner, "Emerging Approaches to Stabilise Photocorrodible Electrodes and Catalysts for Solar Fuel Applications," *Energy Environ. Sci.*, vol. 10, pp. 1116–1127, 2017.

[6] P. Da, M. Cha, L. Sun, Y. Wu, Z. S. Wang, and G. Zheng, "High-performance perovskite photoanode enabled by Ni passivation and catalysis," *Nano Lett.*, vol. 15, no. 5, pp. 3452–3457, 2015.

[7] M. T. Hoang, N. D. Pham, J. H. Han, J. M. Gardner, and I. Oh, "Integrated Photoelectrolysis of Water Implemented on Organic Metal Halide Perovskite Photoelectrode," *ACS Appl. Mater. Interfaces*, vol. 8, no. 19, pp. 11904–11909, 2016.

[8] M. Crespo-Quesada, L. M. Pazos-Outón, J. Warnan, M. F. Kuehnel, R. H. Friend, and E. Reisner, "Metal-encapsulated organolead halide perovskite photocathode for solar-driven hydrogen evolution in water," *Nat. Commun.*, vol. 7, p. 12555, 2016.

[9] C. Wang, S. Yang, X. Chen, T. Wen, and H. G. Yang, "Surface-functionalized perovskite films for stable photoelectrochemical water splitting," *J. Mater. Chem. A*, vol. 5, no. 3, pp. 910–913, 2017.

[10] S. Nam, C. T. K. Mai, and I. Oh, "Ultrastable Photoelectrodes for Solar Water Splitting Based on Organic Metal Halide Perovskite Fabricated by Lift-Off Process," *ACS Appl. Mater. Interfaces*, vol. 10, no. 17, pp. 14659–14664, 2018.

[11] H. Zhang, Z. Yang, W. Yu, H. Wang, W. Ma, X. Zong, and C. Li, "A Sandwich-Like Organolead Halide Perovskite Photocathode for Efficient and Durable Photoelectrochemical Hydrogen Evolution in Water," *Adv. Energy Mater.*, vol. 8, p. 1800795, 2018.

[12] V. Andrei, R. L. Z. Hoye, M. Crespo-Quesada, M. Bajada, S. Ahmad, M. D. Volder, R. Friend, and E. Reisner, "Scalable Triple Cation Mixed Halide Perovskite-$BiVO_4$ Tandems for Bias-Free Water Splitting," *Adv. Energy Mater.*, vol. 8, p. 1801403, 2018.

[13] L.-f. Gao, W.-J. Luo, Y.-F. Yao, and Z.-G. Zou, "An all-inorganic lead halide perovskite-based photocathode for stable water reduction," *Chem. Commun.*, vol. 54, p. 11459, 2018.

[14] R. Tao, Z. Sun, F. Li, W. Fang, and L. Xu, "Achieving Organic Metal Halide Perovskite into a Conventional Photoelectrode: Outstanding Stability in Aqueous Solution and High-Efficient Photoelectrochemical Water Splitting," *ACS Appl. Energy Mater.*, vol. 2, pp. 1969–1976, 2019.

[15] I. Poli, J. Baker, J. Mcgettrick, F. D. Rossi, S. Eslava, and P. J. Cameron, "Screen printed carbon $CsPbBr_3$ solar cells with high open-circuit photovoltage," *J. Mater. Chem. A*, vol. 6, pp. 18677–18686, 2018.

[16] I. Poli, U. Hintermair, M. Regue, S. Kumar, E. V. Sackville, J. Baker, T. M. Watson, S. Eslava, and P. J. Cameron, "Graphite-protected $CsPbBr_3$ perovskite photoanodes functionalised with water oxidation catalyst for oxygen evolution in water," *Nat. Commun.*, vol. 10, no. 2097, 2019.

[17] J. Baker, K. Hooper, S. Meroni, A. Pockett, J. McGettrick, Z. Wei, R. Escalante, G. Oskam, M. Carnie, and T. Watson, "High throughput fabrication of mesoporous carbon perovskite solar cells," *J. Mater. Chem. A*, vol. 5, pp. 18643–18650, 2017.

[18] M. Bliss, A. Smith, T. R. Betts, J. Baker, F. De Rossi, S. Bai, T. Watson, H. Snaith, and R. Gottschalg, "Spectral Response Measurements of Perovskite Solar Cells," *IEEE J. Photovolt.*, vol. 9, pp. 220–226, 2019.

[19] A. Pockett, D. Raptis, S. M. P. Meroni, J. A. Baker, T. M. Watson, and M. Carnie, "The Origin of Exceptionally Slow Light Soaking Effect in Mesoporous Carbon Perovskite Solar Cells with AVA Additive," *J. Phys. Chem. C*, p. acs.jpcc.9b01058, 2019.

[20] A. Ambrosi, C. K. Chua, A. Bonanni, and M. Pumera, "Electrochemistry of graphene and related materials," *Chem. Rev.*, vol. 114, no. 14, pp. 7150–7188, 2014.

Chapter 7

Improving stability under illumination reducing light-induced halide segregation

Semiconductors used for fabricating solar cells should be intrinsically stable to light exposure. However, many studies report that significant changes occur in perovskites under illumination. One very clear example of photoinduced changes observed in perovskites is the case of mixed halide compositions. Light soaking causes segregation into bromine rich and iodine rich crystalline phases due to higher ion movement under illumination, leading to bandgap instabilities. This chapter focuses on photoinduced changes observed in mixed halide triple cation perovskites and investigates the use of 5AVA to passivate halide layers and inhibit the photoinduced halide migration and bandap instabilities.

7.1 Silicon-perovskite tandem solar cells

According to the Shockley-Queisser (SQ) model, the maximum PCE of a solar cell depends on the semiconductor bandgap. Intrinsic losses due to thermalisation and sub-bandgap photons limit the maximum theoretical efficiency of a single-junction solar cell. [1] One approach widely investigated to overcome this limit consists in designing multijunction solar cells (tandem solar cells). This concept has already successfully been proven to overcome the SQ limit, for example PCEs of over $40\,\%$ have been achieved under concentrated light with GaAs/GaInP/Ge triple junction solar cells. [2]

Crystalline silicon-based technologies have dominated the PV market for many years. Currently, the highest efficiency reported for a single crystal Si solar cell under non concentrated light is $26.1\,\%$. [3] Silicon is not only a good material for single junction solar cells, but it is also ideal in multijunction devices. Indeed, its low bandgap of $1.1\,\mathrm{eV}$ and high performance make it an ideal candidate in the role of the low band gap bottom cell in tandem devices. [4]

Halide perovskites have emerged as new PV materials for high efficiency, low cost and easily fabricated solar cells. Some of the properties that make halide perovskites highly fascinating are the band-gap tunability, long diffusion lengths, high charge mobilities and sharp absorption edges. [5, 6] These unique features make halide perovskites a promising top cell for multijunction devices. [7] The first silicon-perovskite tandem solar cell reported in the literature had an efficiency of 17.9%, [8] and recently Oxford PV announced a new PCE world record of $28\,\%$. [3] Optical simulations indicated that the optimum top-cell material in tandem with silicon should have an energy bandgap ranging between 1.7 and $1.8\,\mathrm{eV}$. [9, 4, 10] Therefore, $MAPbI_3$, which has a bandgap of about $1.6\,\mathrm{eV}$, is not optimal as top cell material for the fabrication of perovskite-Si tandem cells. The easiest way to tune the energy bandgap is by using I and Br halide mixtures.

7.1.1 Light induced halide segregation

It is well known that the bandgap of halide perovskites can be tuned by varying the halide composition, covering the whole visible range. This feature would be very interesting to be applied in multijunction devices, but it is rendered impractical by the instability of the lattice. [11] Indeed, the PL spectrum of mixed halide perovskites is observed to split under illumination. [12] This effect is known as Hoke effect, and it was reported for the first time by Hoke *et al.* who suggested segregation of the material into two crystalline phases: a bromine rich and an iodine rich. [13] Later on, it was demonstrated that ion segregation took place via halide defects, resulting in I-rich low-bandgap regions close to the illuminated surface of the film. [14] Experimentally it was observed that upon illumination, $MAPb(I_{1-x}Br_x)_3$ compositions with x>0.2 exhibited phase segregation, resulting in an additional PL peak at $1.68\,\mathrm{eV}$, which indeed corresponds to the energy bandgap of a $MAPb(I_{1-x}Br_x)_3$ material with x=0.2. [13, 15] This phenomenon represents a large problem in the perovskite research community because in order to reach the optimum bandgap for the top cell in tandem silicon-perovskite solar cells, stable $MAPb(I_{1-x}Br_x)_3$ materials with Br contents $x \sim 0.4$ would be preferred.

One approach that has been reported to mitigate photoinduced ion migration in mixed halide perovskite films consists in passivating the surfaces and grain boundaries. Abdi-Jalebi *et al.* demonstrated that photoinduced ion migration could be substantially reduced by decorating the surface and grain boundaries with passivating potassium halide layers. [16] Mixed halide K-passivated compositions with wide bandgaps of 1.7-$1.9\,\mathrm{eV}$ were demonstrated to be stable upon illumination for $30\,\mathrm{min}$. A few months later, tetrabutylammonium (TBA) was incorporated in a perovskite absorber layer showing higher photo-stability and a bandgap material of $1.77\,\mathrm{eV}$ was stabilised for $1\,\mathrm{h}$ under illumination. [17]

7.2 5-aminovaleric acid in halide perovskites

Section 3.2 discussed $MAPbI_3$ surface treatments with 5-aminovaleric acid iodide (5AVA), showing considerably improved PL properties and reduced photo-induced defect formation. Treated perovskite $MAPbI_3$ films with 5AVA showed stabilised integrated PL under illumination for over $30\,\mathrm{min}$. Cao *et al.* recently reported the use of 5AVA in perovskite LEDs, showing that 5AVA additives can effecctively passivate perovskite surface defects, reducing non-radiative recombination pathways. [18]

The 5AVA molecule has been widely used in triple mesoporous carbon-based devices. It was observed that a tiny addition of 5AVA (3mol%) in the perovskite precursor solution infiltrated through the mesoporous scaffold improved both the performance and stability of solar cells. Grancini *et al.* suggested that the addition of 5AVA resulted in a thin 2D layer coating the mesoporous TiO_2 ETM, reducing the recombination at the interface and acting as a template for oriented growth of the 3D layer. [19] Later on, Pockett *et al.* studied the triple mesoscopic carbon cell infiltrated with $MAPbI_3$+5AVA using transient photovoltage measurements. Similarly to what reported by Grancini *et al.*, they observed that 5AVA might have been preferentially absorbed at the TiO_2/ZrO_2 interface. [20] Mesoporous carbon solar cells containing 5AVA require extensive periods of light soaking preconditioning ($\sim 3\,\mathrm{min}$) in order to measure optimum PCEs. [21] Such slow dynamic behaviour was demonstrated to be linked to ion movement and the presence of 5AVA was found to inhibit ion migration. [20]

Recently, the effect of 5AVA on the passivation of grain boundaries in $FASnI_3$ films has been reported. It was proposed that 5AVA interacts with iodide from SnI_6 octahedra forming hydrogen bond interactions. The incorporation of 5AVA allowed the formation of homogeneous and pinhole-free films, with enhanced PL lifetimes with respect to pristine $FASnI_3$ films. Overall, higher PCEs and improved stability under continuous illumination and maximum power point tracking conditions were measured. [22]

In this section, the effects of 5AVA in mixed halide perovskite materials on the halide segregation under illumination is studied.

7.2.1 Experimental Methods

Most of the experiments presented in this section were carried out by the candidate at the Centre for Nano Science and Technology (CNST), Italian Institute of Technology (IIT), Milan. XPS charaterisation was carried out by Dr. Mark Isaacs at HarwellXPS facility. The fabrication and characterisation of solar cell devices instead were carried out at the Chemistry department of the University of Bath.

Perovskite films for UV-Vis, XRD and PL characterisation were deposited on non-conductive glass. Mixed halide $MAPb(Br_{0.4}I_{0.6})_3$ and triple cation (Cs,FA,MA) $Pb(Br_{0.4}I_{0.6})_3$ perovskite thin films were prepared. Br content of $40\,\%$ was chosen in order to obtain materials with energy bandgaps ranging between 1.7-$1.8\,\mathrm{eV}$, which is

the desirable value for the top cell in tandem silicon-perovskite solar cells. The substrates cleaning was done in the same way as descirbed in Chapter 2. $MAPb(Br_{0.4}I_{0.6})_3$ surface were treated by spin coating 25 mM of 5AVA isopropanol solution at 3000 rpm for $30\,\mathrm{s}$ (anhydrous IPA was used). The products were then dried at $30\,^{\circ}\mathrm{C}$ for $2\,\mathrm{min}$ and annealed at $100\,^{\circ}\mathrm{C}$ for $10\,\mathrm{min}$.

$(Cs_{0.05}FA_{0.6}MA_{0.35})Pb(Br_{0.4}I_{0.6})_3$ films were prepared in the same way as described in Chapter 2 (from now on written as $(Cs,FA,MA)Pb(Br_{0.4}I_{0.6})_3$). Different compositions of 5AVA-$(Cs,FA,MA)Pb(Br_{0.4}I_{0.6})_3$ were tested by partly substituting MAI and FAI with 5AVA (1, 3 and 5 mol%).

For the steady-state PL analysis, excitation light was provided by a continuous wave CW diode laser (Oxxius laserboxx, wavelength 450 nm). Perovskite films were mounted inside a vacuum chamber and measured under constant pumping (pressure $< 1 \times 10^{-5}\,\mathrm{mbar}$), and PL was collected in reflection mode and focused into a fiber coupled to a spectrometer (Ocean Optics Maya Pro 2000). PL spectra shown in this chapter were measured at an applied power density of $\sim 20\,\mathrm{mW\,cm^{-2}}$.

The open-circuit voltage of solar cells were monitored using an Autolab PGSTAT30 under continuous illumination. The sample was illuminated with a single wavelength LED light of $470\,\mathrm{nm}$.

7.2.2 5AVA passivated mixed halide perovskites

Surface passivation The use of 5AVA molecule to treat the surface of $MAPbI_3$ thin films was demonstrated to passivate the surface and photostabilise the perovskite surface (see section 3.2). Similarly, 5AVA was used to treat the surface of mixed halide $MAPb(Br_{0.4}I_{0.6})_3$ films. Figure 7.1 a and b show the evolution of PL spectra of $MAPb(Br_{0.4}I_{0.6})_3$ films without and with 5AVA passivation on the surface after $1\,\mathrm{min}$ of continuous illumination, respectively.

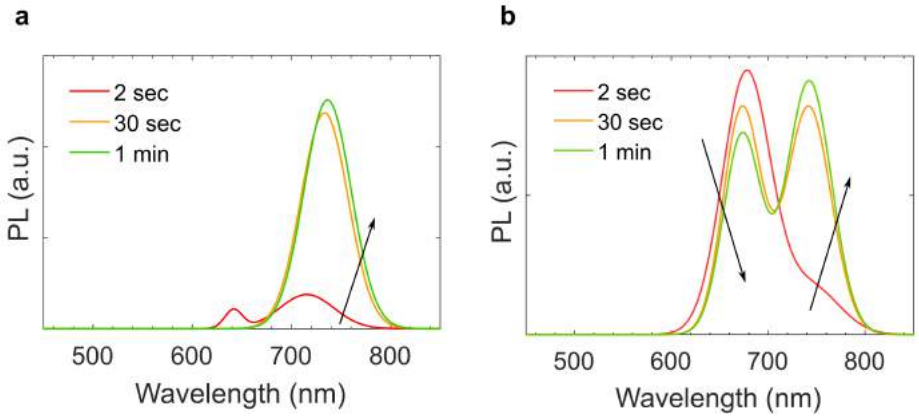

Figure 7.1: a PL spectra of $MAPb(Br_{0.4}I_{0.6})_3$ films over $1\,\mathrm{min}$ of continuous illumination. **b** PL spectra of $MAPb(Br_{0.4}I_{0.6})_3$ films after surface treatment with 5AVA over $1\,\mathrm{min}$ of continuous illumination.

Under illumination, the PL spectrum of the untreated perovskite film red-shifts to $740\,\mathrm{nm}$, which corresponds to $\sim 1.68\,\mathrm{eV}$, the energy bandgap originated by a $MAPb(Br_xI_{1-x})_3$

with x=0.2. After less than 1 minute of continuous light-soaking, the PL intensity of the new peak became about 10 times more intense than the original peak and only a tiny shoulder remained of the original peak at $650\,\mathrm{nm}$. The appearance of this new PL feature was due to the formation of iodide-enriched regions with lower bandgap and it was associated with photoinduced halide migration. The PL intensity of the new peak was found to increase during light soaking. Such phenomenon was reported by Hoke *et al.*, who attributed it to the formation of iodide-enriched domains acting as carrier traps. [13] Under illumination, traps become quickly filled and the evolution gets dominated by bimolecular radiative recombination processes, resulting in increased PL intensity. The PL spectrum of the 5AVA treated film shown in figure 7.1 b was not stable either and an additional PL peak formed at $\sim 740\,\mathrm{nm}$. However, the segregation phase was considerably slower, indicating that the presence of 5AVA on the surface hindered the ion movement and the photoinduced phase segregation slowed down.

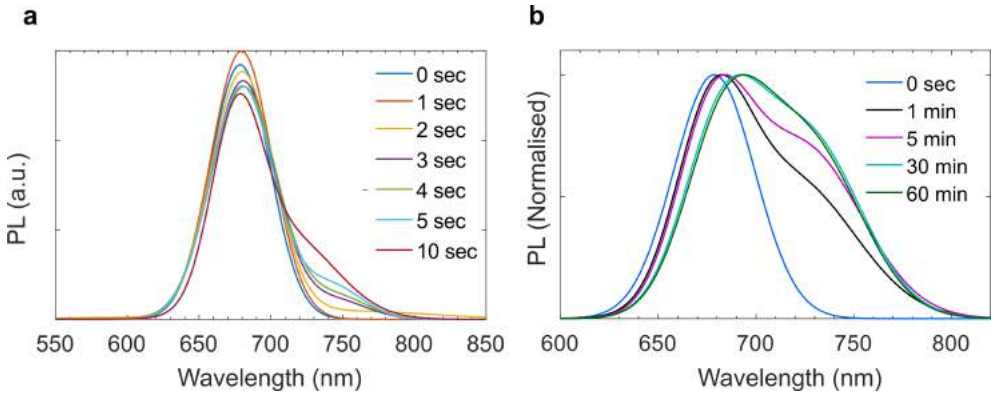

Figure 7.2: PL spectra of surface treated $MAPb(Br_{0.4}I_{0.6})_3$ with 5AVA after 1 month storage in N_2 environment **a** over $10\,\mathrm{s}$ under continuous illumination; **b** over $1\,\mathrm{h}$ under continuous illumination.

The same samples were stored in a solvent-free N_2 environment, in the dark, for 1 month and tested again. Interestingly, while the control untreated film behaved in the same way under illumination, the 5AVA treated film was found to be more stable. Figure 7.2 a shows the evolution of the PL spectrum of the 5AVA treated perovskite film over $10\,\mathrm{s}$ under light soaking. After $10\,\mathrm{s}$ under continuous illumination, a tiny shoulder at higher wavelength appeared and the original PL peak at $660\,\mathrm{nm}$ decreased by only $5\,\%$ with respect to the initial peak at $0\,\mathrm{s}$. Fig 7.2 b shows the normalised photoluminescence from the passivated compositions measured over time under continuous illumination. The PL peak broadened, indicating photoinduced halide segregation and emission from low-bandgap iodide-rich components. However a substantial photoluminescence shift like the one shown in figure 7.1 was not observed. Moreover, after an initial broadening of the peak, after $30\,\mathrm{min}$ no further movement was observed, indicating the effective role of 5AVA in arresting the I/Br segregation phase process.

5AVA in the precursor solution The results showed above suggested that 5AVA may have diffused through the absorber thin film while it was stored in dry N_2 environment, resulting in a more efficient passivation of grain boundaries. In light of these results, 5AVA was directly incorporated within the perovskite precursor solution. Moreover, triple cation perovskites instead of MA-based structures were investigated due to higher intrinsic stability.

Structural characterisation

A series of passivated triple-cation perovskite thin films on glass (Cs,FA,MA)Pb($Br_{0.4}I_{0.6}$)$_3$ were fabricated by adding 5AVA within the precursor solution. Figure 7.3 a shows the Tauc plot (Cs,FA,MA)Pb($Br_{0.4}I_{0.6}$)$_3$ with 0, 3 and 5 mol% of 5AVA added within the precursor solution. The introduction of 5AVA lead to samples with a small increase of the I/Br ratio, which resulted in a slightly lower energy bandgap.

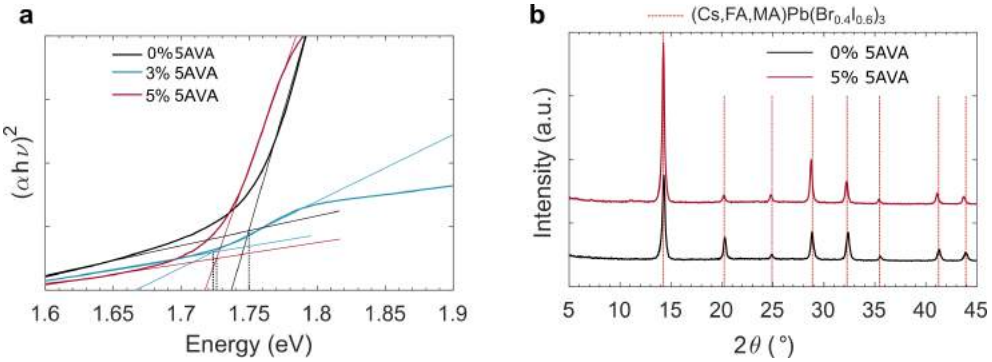

Figure 7.3: a Tauc plot of standard triple-cation and passivated triple-cation films. **b** XRD of standard and passivated (5mol%) (Cs,FA,MA)Pb($Br_{0.4}I_{0.6}$)$_3$ thin films. The positions of the XRD peaks for (Cs,FA,MA)($PbBr_{0.4}I_{0.6}$)$_3$ are marked in the graphs.

Figure 7.3 b shows the diffractograms of the reference perovskite film without 5AVA and the perovskite film containing $5\,\%$ of 5AVA. The incorporation of 5AVA retained the (Cs,FA,MA)Pb($Br_{0.4}I_{0.6}$)$_3$ tetragonal phase, for example indicated by the presence of (110) and (220) lattice planes at $\sim 14.3°$ and $\sim 28.8°$. With the addition of 5AVA, the diffraction intensities increased, indicating a higher vertical orientation. [19]

The presence of 5AVA on the surface of the thin-film was also confirmed by XPS. The XPS survey spectra for reference (Cs,FA,MA)Pb($Br_{0.4}I_{0.6}$)$_3$ and 5AVAI passivated (Cs,FA,MA)Pb($Br_{0.4}I_{0.6}$)$_3$ are given in figure 7.4 a and b, respectively. The presence of carbon, nitrogen, lead, iodine and bromine are predictable from the chemical composition of the perovskite films, while indium and tin may result from migration of these elements from the ITO substrate to the top layer with time. Similar effects with ageing have been previously reported in the literature (see section 4.2.2 for more details on XPS characterisation on aged perovskite films). [23] The XPS regions, with relative atomic concentration extracted from XPS survey spectra are listed in table 7.1. Figure 7.4 c and d show the C *1s* XPS spectra of (Cs,FA,MA)Pb($Br_{0.4}I_{0.6}$)$_3$ without

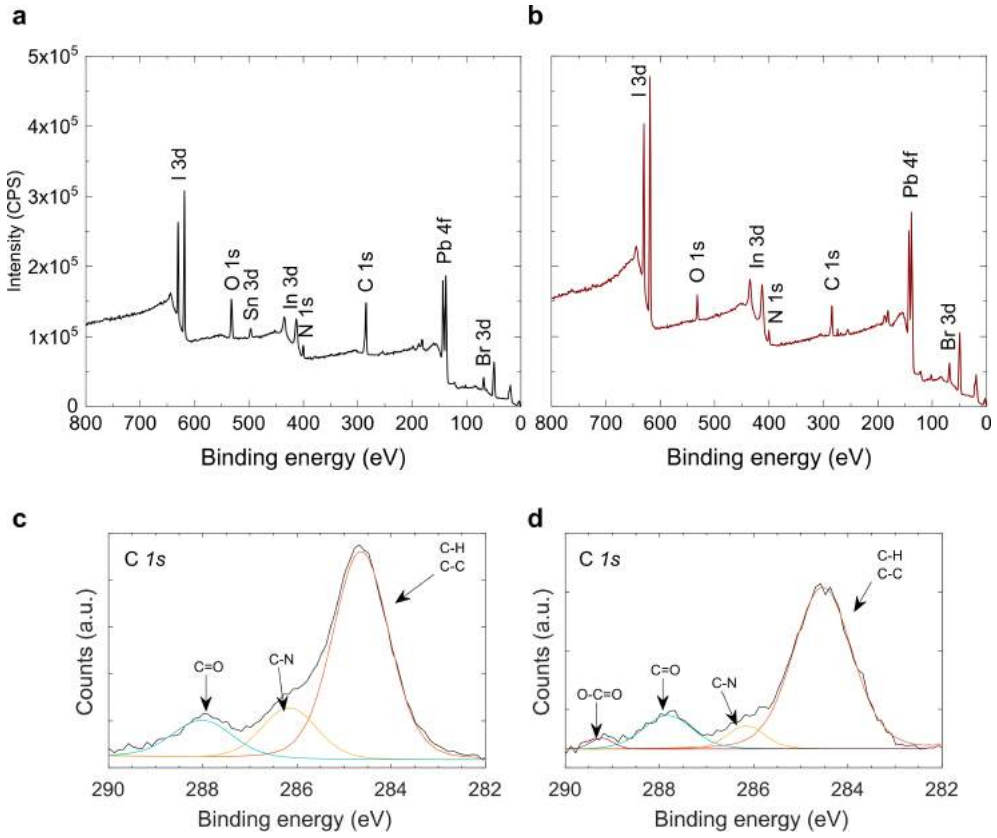

Figure 7.4: **a** XPS survey spectra of a perovskite (Cs,FA,MA)Pb($Br_{0.4}I_{0.6}$)$_3$ film. **b** XPS survey spectra of passivated (Cs,FA,MA)Pb($Br_{0.4}I_{0.6}$)$_3$ film (with 3 % of 5AVAI). **c** C *1s* XPS spectrum of 3D perovskite films fitted with C-H, C-N and C=O components. **d** C *1s* XPS spectrum of 3D perovskite films containing 3 % of 5AVA fitted with C-H, C-N, C=O and O-C=O components.

and with 5AVA, respectively. The presence of MA and FA cations in both spectrum was confirmed by the detected hydrocarbon C-H and C-C (284.6 eV) and the amine C-N (286.1 eV). [24] The emerged carbonyl C=O bond (288 eV) may have come from decomposition of the 3D perovskite induced by absorption of water when the films were exposed to ambient conditions. [25] Figure 7.4 b shows additional species at 289 eV, which could be related to the carboxyl functional group O-C=O, characteristic of 5AVA. [26]

Figure 7.5 a and b show the Pb *4f* and I *3d* XPS spectra of (Cs,FA,MA)Pb($Br_{0.4}I_{0.6}$)$_3$ without and with 5AVA, respectively. According to the peak intensities, which indicate how much of Pb and I is at the surface, it could be estimated that the Pb:I ratio for the bare perovskite film was 1:1.61. The iodine deficit suggests the presence of point defects that may induce halide segregation under illumination. When 5AVA was incorporated, a Pb:I ratio of 1:1.93 was calculated, indicating the presence of more iodine and suggesting that iodine vacancies may have been filled thanks to passivation of the surface and grain boundaries through 5AVA. Similar results were reported by Jian *et al.* who passivated perovskite films with PEA. [27]

Table 7.1: Quantification results extracted from XPS survey spectra of a perovskite (Cs,FA,MA)Pb($Br_{0.4}I_{0.6}$)$_3$ film and a passivated (Cs,FA,MA)Pb($Br_{0.4}I_{0.6}$)$_3$ film with $3\,\%$ of 5AVAI.

Material	XPS region	Position (eV)	Area	Atomic concentration %
(Cs,FA,MA)Pb($Br_{0.4}I_{0.6}$)$_3$	I3d	619	7.9×10^5	32.33
	Pb4f	138	8.3×10^5	27.52
	In3d	413	5.3×10^5	19.27
	C1s	285	2.3×10^5	7.86
	O1s	532	1.7×10^5	6.8
	Br3d	68	8.2×10^4	2.68
	Sn3d	497	5.1×10^4	1.94
	N1s	401	4.4×10^4	1.59
(Cs,FA,MA)Pb($Br_{0.4}I_{0.6}$)$_3$+5AVAI	I3d	619	1.4×10^6	38.67
	Pb4f	138	1.3×10^6	28.58
	In3d	413	9.2×10^5	22.8
	C1s	285	1.4×10^5	3.27
	Br3d	68	1.4×10^5	3.13
	O1s	532	8.5×10^4	2.23
	N1s	401	5.4×10^4	1.33

Stabilised photoluminescence

The photoluminescence from (Cs,FA,MA)Pb($Br_{0.4}I_{0.6}$)$_3$ without passivation and with passivation was measured by continuously illuminating the sample for over $30\,\mathrm{min}$. The PL spectral output of passivated (Cs,FA,MA)Pb($Br_{0.4}I_{0.6}$)$_3$ films (with both 3mol% and 5mol%) was very stable at the optimal bandgap of $1.75\,\mathrm{eV}$ (figure 7.6 b and c). The critical bandgap of $1.75\,\mathrm{eV}$ could be stabilised even at lower passivation levels of 3% for more than $1\,\mathrm{h}$ under continuous illumination. In contrast, the unpassivated sample showed a substantial redshift of the PL peak and the bandgap changed from 1.75 to $1.59\,\mathrm{eV}$ over $30\,\mathrm{min}$ of continuous illumination.

These results showed that 5AVA successfully passivated the surface and grain boundaries of perovskites, inhibiting the photoinduced generation of defects in the bulk and therefore ion migration that would cause halide segregation and photoinstability of the material.

PV solar cell devices

Photoluminescence measurements showed very stable bandgaps of $1.75\,\mathrm{eV}$ when (Cs,FA,MA)Pb($Br_{0.4}I_{0.6}$)$_3$ films were passivated with 5AVA. These results suggest that the presence of 5AVA prevented ion migration through the perovskite film and halide segregation. The open circuit voltage V_{oc} of a solar cell is correlated to the energy bandgap of the material. [28] Therefore solar cells fabricated with passivated (Cs,FA,MA)Pb($Br_{0.4}I_{0.6}$)$_3$ were expected to have higher and more stable V_{oc}

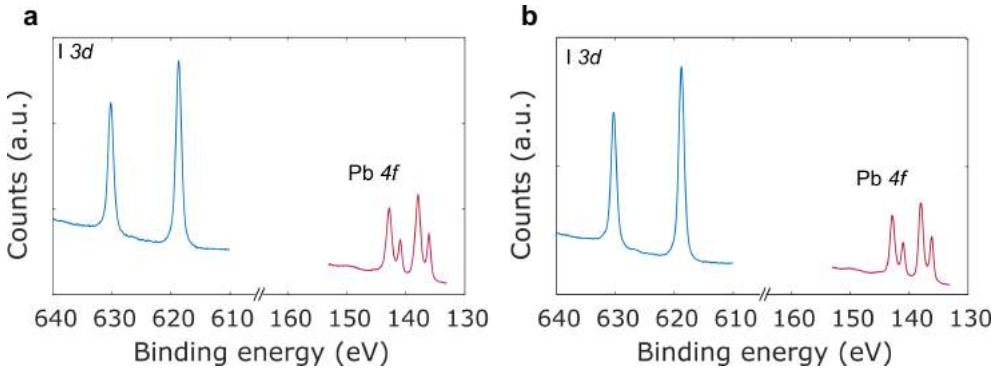

Figure 7.5: **a** Pb *4f* and I *3d* XPS spectra of 3D perovskite films with a calculated Pb:I ratio of 1:1.61. **b** Pb *4f* and I *3d* XPS spectra of 3D perovskite films containing 3 % of 5AVA with a calculated Pb:I ratio of 1:1.93.

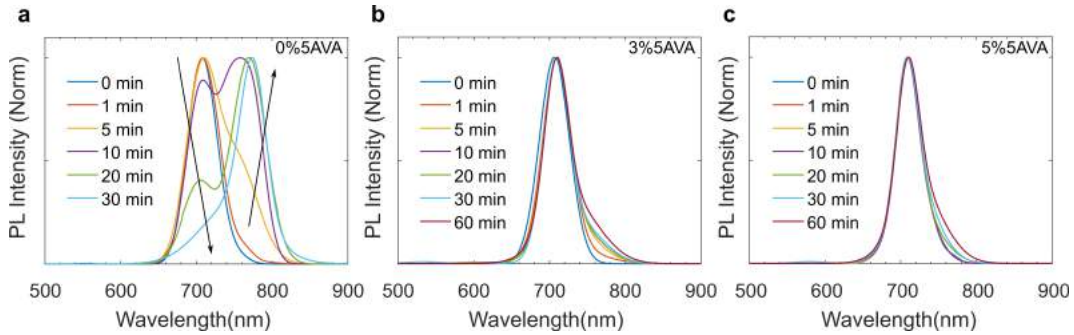

Figure 7.6: Photoluminescence of (Cs,FA,MA)Pb($Br_{0.4}I_{0.6}$)$_3$ **a** without passivation; **b** with 3mol% 5AVA and **c** with 5mol% 5AVA.

than standard triple-cation cells because of the higher stabilised energy bandgap under illumination. Indeed, Abdi-Jalebi *et al.* showed an increase in V_{oc} upon K-passivation. [16]

To validate the advantages of using 5AVA to passivate (Cs,FA,MA)Pb($Br_{0.4}I_{0.6}$)$_3$ perovskite films, full solar cells using the standard device architecture SnO_2/PCBM/perovskite/Spiro-OMeTAD/Au were fabricated. The open circuit of the solar cell was monitored for about 30 min under continuous illumination. Figure 7.7 a shows the V_{oc} variations over time after 3 min of stabilisation. Devices fabricated with passivated (Cs,FA,MA)Pb($Br_{0.4}I_{0.6}$)$_3$ perovskite films showed increased V_{oc}, which is evidence of interface passivation, reduced trap-assisted carrier recombination and higher energy bandgap material. Figure 7.7 b shows the same data but normalised with respect to the initial value to better compare the evolution of V_{oc} over time. While the reference device without passivation showed a gradual decrease in V_{oc} under constant illumination, the V_{oc} of devices with 5AVA was found to be more stable. These results are consistent with the observed instabilities in the energy bandgap measured via PL spectroscopy in figure 7.6.

Figure 7.8 shows the current-voltage curves of (Cs,FA,MA)Pb($Br_{0.4}I_{0.6}$)$_3$ without and with 5AVA passivation, with the extracted parameters given in Table 7.2. The average PCEs of standard triple cation solar cells without passivation and devices

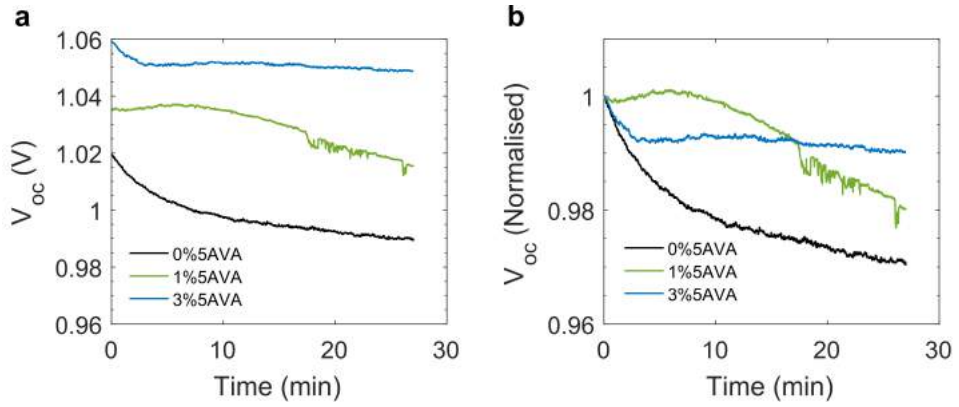

Figure 7.7: **a** V_{oc} of (Cs,FA,MA)Pb($Br_{0.4}I_{0.6}$)$_3$ devices without and with 5AVA passivation over time under constant illumination (monochromatic LED light - $470\,\mathrm{nm}$). **b** Normalised V_{oc} with respect to the initial value.

containing 1mol% of 5AVA did not differ considerably. However, an increase of $\sim$70 mV in the average V_{oc} was observed upon passivation.

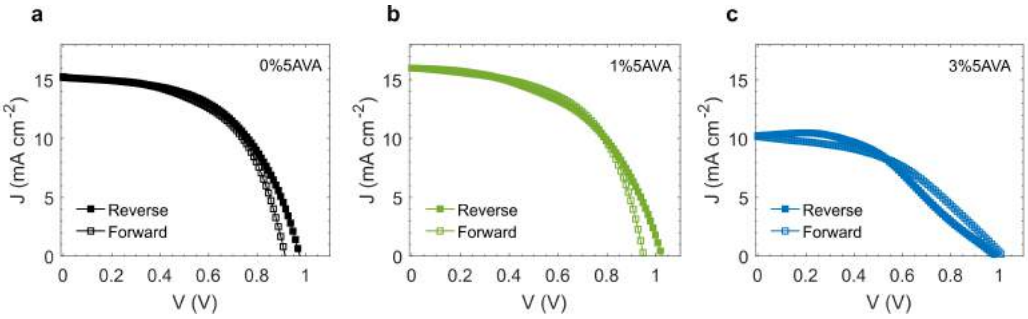

Figure 7.8: JV curves of (Cs,FA,MA)Pb($Br_{0.4}I_{0.6}$)$_3$ devices **a** without passivation, **b** with 1mol% 5AVA and **c** with 3mol% 5AVA

Table 7.2: Average photovoltaic parameters of (Cs,FA,MA)Pb($Br_{0.4}I_{0.6}$)$_3$ with and without 5AVA passivation ($\pm$ 95% confidence interval).

	Scan direction	**J_{sc}** ($\mathrm{mA\,cm^{-2}}$)	**V_{oc}** (V)	FF	PCE (%)
0%5AVA	Reverse	14.95±0.18	0.96±0.05	0.55±0.01	7.91±0.6
	Forward	14.98±0.20	0.91±0.04	0.55±0.01	7.60±0.36
1%5AVA	Reverse	15.11±0.45	1.03±0.01	0.55±0.01	7.99±0.43
	Forward	15.07±0.46	0.97±0.01	0.48±0.02	7.42±0.43
3%5AVA	Reverse	10.00±0.41	0.91±0.06	0.43±0.01	3.90±0.34
	Forward	9.81±0.35	0.93±0.05	0.45±0.01	4.12±0.35

When higher contents of 5AVA were used (figure 7.8 c) the J_{sc}, FF and PCE considerably decreased. 5AVA is a bulky molecule that may cause the formation of 2D layers on the 3D perovskite grain boundaries, hindering the charge transport. High content of 5AVA at the interface may have acted as insulator, hindering the charge transport and causing reduced photocurrents. Loss in J_{sc} has been previously observed in layered perovskite films and caused by electronically insulating sheets formed by the bulky organic cation. [29] Furthermore, the J_{sc} reported for

triple cation solar cells upon K-passivation also decreased for K contents>0.1 due to reduced carrier mobility. [16] Figure 7.8 c shows that high content of 5AVA causes inverted hysteresis, with V_{oc}, FF and PCEs being higher under forward scan. Inverted hysteresis has been previously reported in $MAPbI_3$ solar cells and it may be due to an extraction barrier at the interface, causing reduced charge extraction. [30] This barrier may be caused by the presence of 5AVA.

It is important to note that the solar cell devices presented in this section are not the best-performing devices that can be achieved. Standard triple cation solar cells with a I/Br ratio of 0.6/0.4 can achieve PCEs of $\sim 12\,\%$. However, in order to achieve such high efficiencies, controlled deposition environments (N_2 glove box) and optimised spin coating methods need to be developed. Unfortunately, when these devices were fabricated, the laboratory did not have the optimised equipment to achieve the highest efficiency. Even though more stable and slightly improved V_{oc} was achieved with the addition of 5AVA, the open-circuit voltage was still considerably low considering the wide bandgap of $1.75\,\mathrm{eV}$. [31] Optimised compositions and/or alternative stabilisation strategies need to be developed to fully harvest the potential of these high-bandgap materials.

7.3 Chapter conclusions

Halide perovskites are considered to be one of the most promising material for top-cell in tandem solar cells due to high degree of bandgap tunability. The energy bandgap can be easily tuned by changing the I/Br ratio of the composition. However, for I/Br ratios>4, photoinduced halide segregation and formation of sub-bandgap absorption states are observed, reducing the electronic bandgap of the material and the achievable V_{oc}.

Photoinduced ion migration and bandgap instabilities were reduced by introducing 5AVA within (Cs,FA,MA)$Pb(Br_{0.4}I_{0.6})_3$ perovskite precursor solution. A shift in the XRD characteristic peaks of the tetragonal phase (110) and (220) was observed upon addition of 5AVA, indicating possible expansion of the unit cell and deficiency in the A site cation. XPS characterisation confirmed the presence of 5AVA within the perovskite films and the calculated Pb:I ratio of bare and 5AVA-treated perovskite films inferred passivation of the surface and grain boundaries with 5AVA. Upon addition of 5AVA, the passivation of defects and reduction of halide segregation were observed, leading to stabilised photoluminescence, which allowed to obtain materials with stable $1.75\,\mathrm{eV}$ under continuous illumination for $1\,\mathrm{h}$.
1mol% 5AVA addition did not compromise charge transport nor extraction. Indeed, the presence of 5AVA slightly improved the photovoltaic parameters of triple cation solar cells. On increasing the 5AVA content (3mol%), reduced J_{sc}, V_{oc} and FF occurred, indicating that charge extraction may have been compromised by the presence of large and bulky 5AVA molecules at the grain boundaries which acted as

insulators. Most importantly, the presence of 5AVA stabilised the device V_{oc} upon continuous illumination over time.

7.4 Future work

This work showed that light insuced halide segregation could be prevented by using 5AVA in multi cation mixed halide compositions. Materials with stable optical bandgaps of $\sim 1.75\,\mathrm{eV}$ for over $1\,\mathrm{h}$ under illumination were achieved. Further investigation into 5AVA passivation is required. The photoluminescence response showed to be stable when 5 mol% of 5AVA was added to the precursor solution. However, solar cells fabricated with compositions of 3 mol% showed reduced photocurrent densities, probably due to insulating sheets formed by the bulky cation. The molar composition of the precursor solution should be further optimised in order to achieve the best compromise between reduced ion migration and good charge extraction.

Future work may look at further structural analysis to investigate whether the dominant form of 5AVA in the material is 5AVA crystal itself or 2D layers on the 3D perovskite grain boundaries. Moreover the deposition methods and extraction layers should be further optimised to improve the PCE and stability of the devices.

Bibliography

[1] W. Shockley and H. J. Queisser, "Detailed balance limit of efficiency of p-n junction solar cells," *J. Appl. Phys.*, vol. 32, no. 3, pp. 510–519, 1961.

[2] R. R. King, D. C. Law, K. M. Edmondson, C. M. Fetzer, G. S. Kinsey, H. Yoon, R. A. Sherif, and N. H. Karam, "40% efficient metamorphic GaInPGaInAsGe multijunction solar cells," *Appl. Phys. Lett.*, vol. 90, no. 18, pp. 90–93, 2007.

[3] NREL, "National Renewable Energy Laboratory (NREL)," 2019.

[4] M. H. Futscher and B. Ehrler, "Efficiency Limit of Perovskite/Si Tandem Solar Cells," *ACS Energy Lett.*, vol. 1, pp. 863–868, 2016.

[5] S. De Wolf, J. Holovsky, S. J. Moon, P. Löper, B. Niesen, M. Ledinsky, F. J. Haug, J. H. Yum, and C. Ballif, "Organometallic halide perovskites: Sharp optical absorption edge and its relation to photovoltaic performance," *J. Phys. Chem. Lett.*, vol. 5, no. 6, pp. 1035–1039, 2014.

[6] M. B. Johnston and L. M. Herz, "Hybrid Perovskites for Photovoltaics: Charge-Carrier Recombination, Diffusion, and Radiative Efficiencies," *Acc. Chem. Res*, vol. 49, no. 1, pp. 146–154, 2016.

[7] Z. Wang, Z. Song, Y. Yan, S. F. Liu, and D. Yang, "Perovskite-a Perfect Top Cell for Tandem Devices to Break the S-Q Limit," *Adv. Sci.*, vol. 6, p. 1801704, 2019.

[8] C. D. Bailie, M. G. Christoforo, J. P. Mailoa, A. R. Bowring, E. L. Unger, W. H. Nguyen, J. Burschka, N. Pellet, R. Nou, T. Buonassisi, A. Salleo, and M. D. Mcgehee, "Semi-transparent perovskite solar cells for tandems with silicon and CIGS," *Energy Environ. Sci.*, vol. 8, p. 956, 2015.

[9] M. Filipi, P. Löper, B. Niesen, S. D. Wolf, J. Kr, C. Ballif, and M. Topi, "$CH_3NH_3PbI_3$ perovskite/silicon tandem solar cells : characterization based optical simulations," *Opt. Express*, vol. 23, no. 7, pp. 480–484, 2015.

[10] Y. Jiang, I. Almansouri, S. Huang, T. Young, Y. Li, Y. Peng, Q. Hou, L. Spiccia, U. Bach, Y.-B. Cheng, M. Green, and A. Ho-Baillie, "Optical Analysis of Perovskite/Silicon Tandem Solar Cells," *J. Mater. Chem. C*, vol. 4, pp. 5679–5689, 2016.

[11] C. C. Boyd, R. Cheacharoen, T. Leijtens, and M. D. McGehee, "Understanding Degradation Mechanisms and Improving Stability of Perovskite Photovoltaics," *Chem. Rev.*, vol. 119, no. 5, pp. 3418–3451, 2019.

[12] M. C. Brennan, S. Draguta, P. V. Kamat, and M. Kuno, "Light-Induced Anion Phase Segregation in Mixed Halide Perovskites," *ACS Energy Lett.*, vol. 3, no. 1, pp. 204–213, 2018.

[13] E. T. Hoke, D. J. Slotcavage, E. R. Dohner, A. R. Bowring, H. I. Karunadasa, and M. D. Mcgehee, "Reversible photo-induced trap formation in mixed-halide hybrid perovskites for photovoltaics," *Chem. Sci.*, vol. 6, pp. 613–617, 2015.

[14] A. J. Barker, A. Sadhanala, F. Deschler, M. Gandini, S. P. Senanayak, P. M. Pearce, E. Mosconi, A. J. Pearson, Y. Wu, A. R. Srimath Kandada, T. Leijtens, F. De Angelis, S. E. Dutton, A. Petrozza, and R. H. Friend, "Defect-Assisted Photoinduced Halide Segregation in Mixed-Halide Perovskite Thin Films," *ACS Energy Lett.*, vol. 2, no. 6, pp. 1416–1424, 2017.

[15] F. Brivio, C. Caetano, and A. Walsh, "Thermodynamic Origin of Photoinstability in the $CH_3NH_3Pb(I_{1-x}Br_x)_3$ Hybrid Halide Perovskite Alloy," *J. Phys. Chem. Lett.*, vol. 7, no. 6, pp. 1083–1087, 2016.

[16] M. Abdi-jalebi, Z. Andaji-garmaroudi, S. Cacovich, C. Stavrakas, B. Philippe, E. M. Hutter, A. J. Pearson, S. Lilliu, T. J. Savenije, J. M. Richter, M. Alsari, P. Edward, H. Rensmo, G. Divitini, C. Ducati, R. H. Friend, and S. D. Stranks, "Maximizing and stabilizing luminescence from halide perovskites with potassium passivation," *Nature*, vol. 555, no. 7697, pp. 497–501, 2018.

[17] P. Kour, M. Chenna Reddy, R. Naphade, and S. Ogale, "Quaternary alkylammonium salt incorporated 2D/3D mixed halide perovskite with highly enhanced photoluminescence and arrested iodide/bromide phase segregation," *APL Materials*, vol. 6, no. 8, p. 086107, 2018.

[18] J. Cao, S. X. Tao, P. A. Bobbert, C.-P. Wong, and N. Zhao, "Interstitial Occupancy by Extrinsic Alkali Cations in Perovskites and Its Impact on Ion Migration," *Adv. Mater.*, p. 1707350, 2018.

[19] G. Grancini, I. Zimmermann, E. Mosconi, D. Martineau, and S. Narbey, "One-Year stable perovskite solar cells by 2D/3D interface engineering," *Nat. Commun.*, vol. 8, pp. 1–8, 2017.

[20] A. Pockett, D. Raptis, S. M. P. Meroni, J. A. Baker, T. M. Watson, and M. Carnie, "The Origin of Exceptionally Slow Light Soaking Effect in Mesoporous Carbon Perovskite Solar Cells with AVA Additive," *J. Phys. Chem. C*, p. acs.jpcc.9b01058, 2019.

[21] M. Bliss, A. Smith, T. R. Betts, J. Baker, F. De Rossi, S. Bai, T. Watson, H. Snaith, and R. Gottschalg, "Spectral Response Measurements of Perovskite Solar Cells," *IEEE J. Photovolt.*, vol. 9, pp. 220–226, 2019.

[22] M. E. Kayesh, K. Matsuishi, R. Kaneko, S. Kazaoui, J. J. Lee, T. Noda, and A. Islam, "Coadditive Engineering with 5-Ammonium Valeric Acid Iodide for Efficient and Stable Sn Perovskite Solar Cells," *ACS Energy Letters*, vol. 4, no. 1, pp. 278–284, 2019.

[23] Z. Ahmad, M. A. Najeeb, R. A. Shakoor, A. Alashraf, S. A. Al-Muhtaseb, A. Soliman, and M. K. Nazeeruddin, "Instability in $CH_3NH_3PbI_3$ perovskite solar cells due to elemental migration and chemical composition changes," *Sci. Rep.*, vol. 7, no. 1, pp. 1–8, 2017.

[24] G. Beamson and D. Briggs, *High Resolution XPS of Organic Polymers – The Scienta ESCA300 Database*. Wiley, 1992.

[25] Q. Sun, P. Fassl, D. Becker-koch, A. Bausch, B. Rivkin, S. Bai, P. E. Hopkinson, H. J. Snaith, and Y. Vaynzof, "Role of Microstructure in Oxygen Induced Photodegradation of Methylammonium Lead Triiodide Perovskite Films," *Adv. Energy Mater.*, vol. 7, no. 1700977, 2017.

[26] A. Ganguly, S. Sharma, P. Papakonstantinou, and J. Hamilton, "Probing the Thermal Deoxygenation of Graphene Oxide Using High-Resolution In Situ X-ray-Based Spectroscopies," *J. Phys. Chem. C*, vol. 115, pp. 17009–17019, 2011.

[27] Q. Jiang, Y. Zhao, X. Zhang, X. Yang, Y. Chen, Z. Chu, Q. Ye, X. Li, Z. Yin, and J. You, "Surface passivation of perovskite film for efficient solar cells," *Nat. Photonics*, 2019.

[28] H. Atwater and A. Polman, "Photonic design principles for ultrahigh efficiency photovoltaics," *Nat. Mater.*, vol. 11, pp. 174–177, 2012.

[29] Y. Hu, J. Schlipf, M. Wussler, M. L. Petrus, W. Jaegermann, T. Bein, P. Muller-Buschbaum, and P. Docampo, "Hybrid Perovskite/Perovskite Heterojunction Solar Cells," *ACS Nano*, vol. 10, no. 6, pp. 5999–6007, 2016.

[30] W. Tress, J. P. Correa Baena, M. Saliba, A. Abate, and M. Graetzel, "Inverted Current–Voltage Hysteresis in Mixed Perovskite Solar Cells: Polarization, Energy Barriers, and Defect Recombination," *Adv. Energy Mater.*, vol. 6, no. 19, pp. 1–11, 2016.

[31] T. C. J. Yang, P. Fiala, Q. Jeangros, and C. Ballif, "High-Bandgap Perovskite Materials for Multijunction Solar Cells," *Joule*, vol. 2, no. 8, pp. 1421–1436, 2018.

Chapter 8

Conclusions

The focus of this thesis has been enhancing the stability of halide perovskite solar cells. More specifically, the effect of moisture, heat and light have been studied. Water molecules can easily penetrate through the extraction layers, interacting with and decomposing the perovskite structure. Light exposure induces the formation of defects in the material due to ion-migration. Both the archetypal methylammonium lead iodide ($MAPbI_3$) perovskite structure and organic hole transport materials are prone to thermal instability and degrade upon heating at $80\,°C$ over time. Finally, exposure to light and heat induces side reactions between the metal contacts and the perovskite active material. This work has aimed to investigate different strategies to minimise the degradation of perovskite solar cells and improve their stability.

8.1 Tolerance to humidity

Modification of the top perovskite surface has been investigated to minimise moisture-induced degradation of the perovskite active layer. $MAPbI_3$ nanocrystals (NS) capped with long chain ligands oleic acid (OA) and oleylamine (OLA) have been used to treat the $MAPbI_3$ surface. Thanks to the presence of OA and OLA, the perovskite films become highly hydrophobic and water contact angles higher than $100°$ have been measured. Unencapsulated solar cells fabricated with $MAPbI_3$ NCs treated perovskite absorbers retain the black colour even when completely immersed in water for $30\,s$, confirming that capped $MAPbI_3$ NCs effectively act as a protection capping layer from moisture. Solar cells with $MAPbI_3$ NCs incorporated at the interface have shown enhanced shelf stability with respect to reference $MAPbI_3$ cells for more than $1500\,h$ (unencapsulated devices stored in ambient condition at RH higher than $50\,\%$). Other organic molecules that have been investigated here as hydrophobic materials to modify the top perovskite surface and have shown to effectively slow down the perovskite hydration process are tetrabutylammonium (TBA), phenetylammonium (PEA) and 5-aminovaleric acid (5AVA) cations.

TBA has not only been used to functionalise the $MAPbI_3$ surface, but it has been

directly incorporated in the perovskite solution to passivate grain boundaries. Perovskite films with different TBA contents have been fabricated by partially substituting methylammonium MA with TBA. Higher surface coverage and improved water contact angles have been observed in perovskite films that contain TBA. Films that have been fabricated with TBA as the only cation (MA content=0) have a yellow semi-transparent colour and both XRD and UV-Vis spectroscopy show the presence of low dimensional peaks at low 2θ angles and low wavelengths, respectively. These peaks can be assigned to the formation of 1 dimensional 1D $TBAPbI_3$ structures. Mixed MA/TBA films show the coexistence of the perovskite $MAPbI_3$ 3D phase and a lower dimensional 1D phase originated by the presence of TBA. TBA is believed to preferentially sit at the grain boundaries, generating protecting layers that reduce moisture degradation. Most importantly, unencapsulated solar cells with 3 and $5\,\%$ TBA exhibit negligible degradation over more than $1200\,\mathrm{h}$ when aged in the dark, at open circuit, in ambient condition ($30\,\%$<RH<$60\,\%$).

The modification of the perovskite solar stack has been investigated to enhance the tolerance to humidity. Indeed, moisture can be prevented from getting to the sensitive perovskite absorber by using hydrophobic top charge transport layers. In this work, micrometer-thick hydrophobic carbon based-electrodes have been used to make perovskite solar cells that have shown extraordinary shelf stability for over $2000\,\mathrm{h}$ (unencapsulated devices aged in ambient conditions). Stabilities of over 1 year have been reported in the literature for perovskite solar cells with the same architecture. The hydrophobic nature of carbon minimise the moisture-induced degradation, however the mesoporous structure of the carbon electrode does not completely waterproof the device. In this thesis, the use of flexible graphite sheets (GS) to encapsulate and waterproof perovskite solar cells is demonstrated for the first time. As a proof of concept, GS-protected devices have been used as photoanodes for oxygen evolution in water, showing extraordinary stability for more than $30\,\mathrm{h}$ under continuous operation when entirely dipped in water.

8.2 Thermal stability

The perovskite structure of the archetypal $MAPbI_3$ film is highly sensitive to thermal decomposition due to high volatility of the halide species and the organic cation MA. In this work, the use of fully inorganic perovskite materials has been investigated for the fabrication of solar cells with higher thermal resistance. Yellow perovskite films with an energy bandgap of $\sim 2.3\,\mathrm{eV}$ have been deposited by substituting the organic MA with the inorganic and smaller Cs and I with Br, to obtain $CsPbBr_3$. About $400\,\mathrm{nm}$-thick films were obtained by using a 2-step deposition technique and negligible differences in the UV-Vis spectra are measured after post-annealing treatment at $400\,^{\circ}\mathrm{C}$ in air for $30\,\mathrm{min}$. In contrast, $MAPbI_3$ films completely degrade when subjected to the same treatment. XRD results reveal that high temperature annealing

(300-400 °C) is necessary to obtain full conversion of precursor materials $PbBr_2$ and CsBr into the orthorombic perovskite $CsPbBr_3$. XPS results are in line with XRD, showing less unconverted CsBr after high temperature annealing. The development of extra species, which indicate possible oxidation of the material, are observed after post-annealing treatment at 400 °C in air, suggesting that the optimum annealing temperature to achieve complete conversion and avoid oxidation ranges between 300 and 400 °C.

$CsPbBr_3$ solar cells with different architectures have been fabricated. The highest PCE measured by standard planar devices (TiO_2 and spiro-OMeTAD used as ETM and HTM and Au as top contact) is 5.1 %, with the highest V_{oc} of 1.3 V. Not only the perovskite active layer, but also the commonly used organic hole transport materials, among which spiro-OMeTAD, are particularly sensitive to high temperatures. For this reason, in this work alternative solar stacks that do not use sensitive organic HTM have been investigated, replacing Spiro-OMeTAD/Au top layers with a conductive carbon paste that can be either screen printed or doctor bladed. In this work, carbon based solar cells have achieved even higher photovoltages and efficiencies than standard planar devices that used Spiro-OMeTAD/Au top layers. Two different carbon based devices have been compared: a mesoporous carbon device (mC-PSC), with $CsPbBr_3$ infiltrated through a triple mesoscopic screen printed stack of $TiO_2/ZrO_2/C$, and a planar carbon device (C-PSC), with $CsPbBr_3$ sandwiched between a compact layer of TiO_2 and a doctor bladed layer of C. mC-PSC and C-PSC champion devices have reached PCEs of 8.2 and 5.7 %, respectively, and the highest V_{oc} measured has been 1.45 V.

8.3 Reactions with electrodes

Standard perovskite solar cells use top metal contacts, such as Au and Ag. However, previous reports in the literature have shown that light and heat exposure induce side reactions between the halide species in the perovskite active layer and metals, affecting the long-term stability of the perovskite device as a whole. The use of alternative architectures based on carbon electrodes has been beneficial not only to improve the thermal stability of perovskite solar cells avoiding degradation of the organic HTM, but also to eliminate side reactions with top metal contacts. Previous reports in the literature have shown that triple mesoscopic screen printed $TiO_2/ZrO_2/C$ solar cells infiltrated with the archetypal methylammonium lead iodide can achieve PCEs higher than 15 %. However, notably low open circuit voltages have been measured (<1.1 V). Here, the inorganic $CsPbBr_3$ has been infiltrated through the triple mesoscopic screen printed $TiO_2/ZrO_2/C$ stack for the first time, showing a record V_{oc} of 1.44 V. The V_{oc} of these solar cells improves with the processing temperature, increasing by ∼100 mV after post-annealing treatment at 300 °C.

8.4 Stability under illumination

Lead halide perovskites undergo changes in optoelectronic properties under illumination, mainly due to a light-induced migration of halogen species. Controversial results have been reported in the literature showing the formation of defects in the lattice under illumination, causing a PL intensity decrease, and a light-induced trap annihilation mechanism which leads to a PL intensity enhancement. In this work, the formation of light-induced sub bandgap states is observed in $MAPbI_3$ films. This PL degradation mechanism is minimised by passivating the $MAPbI_3$ thin film top surface with large organic molecules like TBA, PEA and 5AVA. When $MAPbI_3$ films are passivated with 5AVA interlayers, the photostability is considerably improved, the PL intensity does not decay over time under illumination, it increases instead, and longer carrier lifetimes are measured with respect to bare $MAPbI_3$ films. Similarly, TBA/MA perovskite films fabricated by substituting 3 mol% of MA with TBA showed enhanced photostability with respect to the reference $MAPbI_3$. Passivating grain boundaries and the thin film surface prevents the PL intensity degradation mechanism observed in unpassivated perovskite films, favouring the PL intensity enhancement.

One of the most well known and studied effects in the literature, induced by light exposure, is the Hoke effect. The PL spectrum of mixed halide perovskite films (I/Br) has been reported to split under illumination, suggesting segregation into two crystalline phases: a bromide and an iodine rich region. In this work, photo-induced halide segregation has been studied on mixed halide perovskite films with I:Br contents of 0.6:0.4. Halide segregation is suppressed by passivating the grain boundaries with 5AVA molecules. Triple cation mixed halide perovskite thin films with stable energy bandgaps of $1.75\,\mathrm{eV}$ have been measured for over $1\,\mathrm{h}$ under continuous illumination. Most notably, standard planar solar cells (SnO_2 and spiro-OMeTAD used as ETM and HTM, respectively and Au as top metal contact) with 5AVA treated perovskite absorber layers show reduced V_{oc} degradation under illumination over time with respect to the reference untreated perovskite device.

8.5 Solar fuel generation

The use of halide perovskites for photoelectrochemical water splitting applications has been investigated in this work. The waterproofed $CsPbBr_3$ carbon device protected with GS has been used as a photoanode for direct photoelectrochemical oxygen evolution from water. In this work, the photocurrent generated by the $CsPbBr_3$ based device immersed in water is monitored while the applied potential is linearly ramped up and an onset potential of $0.6\,\mathrm{V_{RHE}}$ is measured. This halide perovskite-based photoanode has achieved record stabilities of continuous operation in water under constant 1 sun illumination, with current densities higher than $2\,\mathrm{mA\,cm^{-2}}$

at $1.23\,\mathrm{V_{RHE}}$ sustained for over $24\,\mathrm{h}$. The photoelectrochemical performance was further improved by grafting a molecular Ir-based water oxidation catalyst on the surface of the GS. The presence of the catalyst cathodically shifts the onset potential by $100\,\mathrm{mV}$ due to accelerated charge transfer at the GS/electrolyte interface and faradaic efficiencies of $\sim 82\,\%$ for water oxidation have been measured at $1.23\,\mathrm{V_{RHE}}$.

Publications

1. **Poli, I.**, Eslava, S., Cameron, P. J. "Tetrabutylammonium cations for moisture-resistant and semitransparent perovskite solar cells". *Journal of Materials Chemistry A*, 5, 22325. (2017)

2. **Poli, I.**, Liang, X., Baker, R., Eslava, S., Cameron, P. J. "Enhancing the hydrophobicity of perovskite solar cells using C18 capped $CH_3NH_3PbI_3$ nanocrystals". *Journal of Materials Chemistry C*, 6, 7149. (2018)

3. **Poli, I.**, Baker, J., McGettrick, J., De Rossi, F., Eslava, S., Watson, T. M., Cameron, P. J. "Screen printed carbon $CsPbBr_3$ solar cells with high open-circuit photovoltage". *Journal of Materials Chemistry A*, 6, 18677. (2018)

4. **Poli, I.**, Hintermair, U., Regue, M., Kumar, S., Sackville, E. V., Baker, J., Watson, T. M., Eslava, S., Cameron, P. J. "Graphite-protected $CsPbBr_3$ perovskite photoanodes functionalised with water oxidation catalyst for oxygen evolution in water". *Nature Communications*, 10, 2097. (2019)